THE STABILITY AND CONTROL OF CURVED LIQUID JET BREAK-UP.

by

CHRISTOPHER JAMES GURNEY

UNIVERSITYOF
BIRMINGHAM

University of Birmingham Research Archive

e-theses repository

Acknowledgments

Abstract

An investigation into the break-up dynamics of a curved liquid jet has been studied. A comprehensive review of previous works on straight and curved jet break-up is given, with a detailed comparison between experimental investigation and theoretical models, showing the full uses and limitations of the linear and nonlinear models. A local stability analysis has been developed which can be used to investigate jet stability at any point on the jet at any time. The uses of this model concerning break-up of a ligament and short wave generation at break-up is discussed.

The Needham-Leach method is adopted to obtain the behaviour of linear and nonlinear waves in the large spatial and temporal limits. The onset of nonlinear wave instability as an implication in satellite drop formation is discussed. A solution to the jet equation is obtained which shows an example of Wilton's ripples, a feature of many other areas of fluid dynamics that has, to date, not been seen in liquid jet break-up.

A vibrating nozzle has also been developed which, when vibrating in frequency regimes discovered in this thesis, can control the jet break-up such that satellite droplets are significantly reduced.

Chapter 1

Introduction

Liquid jet break-up is an interesting area of study due to the competing factors bought on by the effects of surface tension; the contraction of a liquid's surface to minimise its energy state and the growth of capillary waves which break the jet. It is an area of considerable interest to the industrial and scientific communities, with the primary focus on the droplets produced post jet break-up, and scientific insights have led to advances in fields such as the quality of ink jet printing.

Despite two hundred years of extensive research in the field of liquid jet break-up, with noticable advances in the classical works of Rayleigh [39] and Weber [47], and more recently Eggers [15], there are many areas not fully understood. With advances in computational techniques and computing power, greater details of jet break-up can be achieved, though mathematical methods remain invaluable in understanding the dynamics behind the numerical solutions.

It is the aim of this thesis to develop a mathematical understanding of curved liquid jets, using similar techniques to those used in examining classical straight jets, as well as developing new methods to shed new insight into the complex dynamics involved.

In Chapter 2 we briefly summarise the results of the aforementioned classical works

on straight jets. We discuss the use of a linear stability analysis in identifying the unstable linear waves involved in jet break-up, and present nonlinear analysis which can be used to simulate break-up.

In Chapter 3, we detail the extension of research on straight jets to include the effects of rotational forces, outlining the models of Wallwork *et al.* [46], Decent *et al.* [12] and Părău *et al.* [36] that form the basis for the work in this thesis. We also present an industrial scenario as motivation for the work.

In Chapter 4 we present some of the experimental work on curved liquid jet break-up, describing the experimental set-up used at the University of Birmingham to replicate the industrial problem. We also detail some methods of droplet control.

In Chapter 5 we fully analyze linear and nonlinear models simulating a curved liquid jet. We classify different types of jet behaviour into different modes of break-up in order to perform the full comparisons with experimental results presented in Chapter 6. In Chapter 6 we also investigate the extent to which a numerical simulation models a jet produced in an experiment, and highlight the uses and limitations of the mathematical model.

In Chapter 7 we investigate the extent to which additional disturbances have an effect on jet break-up. This will be used to explain any discrepancies between the mathematical model and experimental results, and also give an indication of the use of secondary disturbances to control droplet formation. In Chapter 8 we extend the conventional stability analysis in order calculate the stability of a jet at any point in time. This will permit a more detailed analysis of local stability, and will be used to gain insight into jet dynamics during the break-up process.

In Chapters 9 and 10, we develop an asymptotic technique that will be used to analyse the jet equations in the large time and space limit, for a straight and curved inviscid jet respectively. This will give an indication of the behaviour of nonlinear wave

growth, and information about the onset of nonlinear wave instability will be valuable when attempting to regulate droplet production.

In Chapter 11, we use results obtained from the bulk of the thesis to aid the manufacture of a vibrating nozzle that will be added to the experimental setup. We shall present some preliminary results from the experiments. Chapter 12 gives some conclusions and suggestions for further work.

Chapter 2

A Brief review of Straight Jets

A jet is an example of a *free surface flow*, where a free surface is defined as the boundary between two fluids. In free surface flow problems, there is the added complication of calculating the position of the free surface in addition to examining the behaviour of the fluid itself. It is necessary to develop boundary conditions on the fluid to prescribe its position. Consider a free surface given by $F(\mathbf{x}, t) = 0$, where $\mathbf{x}$ are spatial coordinates and t is time. Now a particle which is positioned on the free surface remains there for all time, and we describe this mathematically by the *kinematic condition*

$$\frac{\partial F}{\partial t} + \mathbf{u} \cdot \nabla F = 0,$$

where $\mathbf{u}$ is the velocity of the fluid and ∇ is the gradient operator. *Dynamical conditions* on the free surface arise from the need to balance stresses acting on it. Within a fluid, molecules in contact with their neighbours are in a lower energy state than those that are not. However, surface molecules are in less contact and so are in a higher state of energy. Therefore, the liquid minimizes its surface area to minimize its energy state. It is this contracting of the surface that gives the liquid a *surface tension*, which can be considered as the energy per unit area of the interface [1]. Returning to our free

6

surface problem, equilibrium occurs as stresses caused by pressure and viscous forces acting on the free surface are balanced by stresses caused by surface tension.

We formulate our *normal stress condition* thus

$$\mathbf{n} \cdot \mathbf{T} \cdot \mathbf{n} = \sigma \kappa,$$

where σ is the surface tension, $\mathbf{n}$ is a normal vector to the surface and $\kappa = \nabla \cdot \mathbf{n}$ is the curvature of the surface[1]. $\mathbf{T}$ is a second order stress tensor defined by $p\mathbf{I} + \mu[\nabla\mathbf{u} + (\nabla\mathbf{u})^T]$ where $\mathbf{I}$ is the second order Identity Tensor, p and μ are the pressure and dynamic viscosity of the fluid respectively, and ^{T} denotes the transpose of the vector.

The other form of dynamical condition results in stresses caused by gradients in surface tension acting tangentially to the free surface, and thus our *tangential stress conditions* are

$$\mathbf{n} \cdot \mathbf{T} \cdot \mathbf{t}_i = \nabla\sigma \cdot \mathbf{t}_i, \tag{2.1}$$

where $\mathbf{t}_i$ are vectors tangential to the surface and i indicates there may be more than one tangential vector present. In three dimensions $i = 1, 2$. Gradients in surface tension can be as a result of thermal changes or the presence of surfactants. In the meantime, we shall assume that surface tension is constant throughout and so the right hand side of (2.1) is zero.

2.1 Break-up regimes

The break-up of a liquid jet can be defined as the transition period during which a column of liquid changes into liquid droplets. It is widely believed that this break-up is caused by small perturbations to the surface of the liquid which grow and eventually

---

[1]In some literature, the curvature is given by $\kappa = \left(\frac{1}{R_1} + \frac{1}{R_2} \right)$ where R_1 and R_2 are called the principle radii of curvature.

become large enough such that the radius of the column becomes zero, thus breaking the liquid jet into droplets. The primary source of free surface instabilities are caused by surface tension, and are thus named *capillary instabilities.*

Four different types of break-up regimes of fluid emanating from an orifice have been identified [26], corresponding to combinations of liquid inertia, surface tension and aerodynamical affects. Two lower speed regimes called the *Rayleigh* regime and *first wind-induced* regime are characterized by break-up occurring further down the jet and produce drop sizes of the same order to that of the orifice. The two other regimes occur at higher speeds and are named *second wind-induced* and the *atomization* regime, both of which are typified by break-up lengths close to the orifice and much smaller drop sizes than the orifice radius. It is also important to note that if the exit velocity of the fluid is too low, then the liquid will not jet. This effect dramatically increases if the liquid becomes more viscous. The different break-up regimes can be seen in Figure 2.1.

Although the different regimes have important industrial applications, throughout this thesis we shall consider jet break-up which follows the Rayleigh regime, with the exit velocity sufficiently high speed as to cause jet formation but not so high as to cause atomization. Aerodynamical effects are neglected and the medium in which the jet is dispersed into is taken to be a low density gas.

2.2   Linear Analysis of an Inviscid Straight Jet

Despite liquid jet break-up being a nonlinear occurrence, many aspects can be investigated to a good degree of accuracy using linear theory, such the break-up length of the jet and the size of a main drop produced. (In many cases of liquid-jet break-up, multiple drop sizes are produced and it is necessary to investigate nonlinear aspects
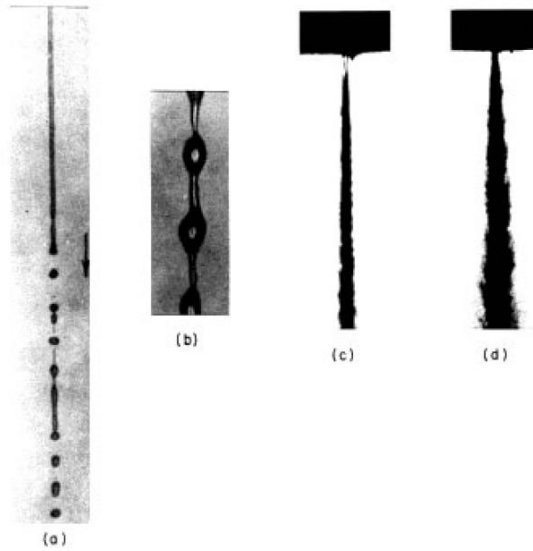
Figure 2.1: Examples of the four jet break-up regimes, (a) Rayleigh regime, (b) first wind-induced regime, (c) second wind-induced regime and (d) atomization regime. Reproduced from Lin & Reitz [28]

to ascertain the details of these secondary droplets. This will be discussed in further detail later).

Rayleigh [39] proposed that capillary jet break-up is caused by the wave mode which grows most quickly with time, or the 'mode of maximum instability'. Consider an infinite axisymmetric cylinder of an incompressible inviscid fluid. Wavelike perturbations of the form $\exp(i(kz - n\theta) + \lambda t)$ are applied to the free surface, where z represents the distance along the central axis of the cylinder and θ the azimuthal coordinate[2]. The amplitude of the disturbance is proportional to $\exp(\lambda t)$. Values of $\mathrm{Re}(\lambda) > 0$ cause the amplitude of the disturbance to grow with time, and so $\mathrm{Re}(\lambda)$ is defined as the *growth rate* of the disturbance. k is denoted the *wavenumber*, where $k = 2\pi/\lambda_w$ where λ_w is the *wavelength* of the disturbance. A prediction for the size of the drop produced on jet break-up can be obtained by assuming a droplet forms over the wavelength of this

---

[2]Note that Rayleigh used cosines to describe this deformation, whilst we have used exponentials here and will throughout the remainder of this thesis for consistency.

disturbance.

A *dispersion relation* is developed describing the relationship between k and λ, given by

$$\lambda^2 = \frac{\sigma}{R^3\rho} \frac{kRI'_n(kR)}{I_n(kR)}(1 - n^2 - k^2R^2) \tag{2.2}$$

where ρ is the density of the liquid, R is the unperturbed radius of the cylinder, I_n is the modified Bessel function of nth order and I'_n is the derivative defined by $I'_n = \left(\frac{d}{dr}I_n(kr)\right)\big|_{r=R}$. Here n is an integer. The derivation of (2.2) follows from a linearisation of the equations of motion. In Chapter 8, we apply this method in a more complex scenario and we will show the details at that point of how these equations are derived. For values of $n \neq 0$, $\lambda^2 < 0$, and this corresponds to waves where λ is purely imaginary with $\text{Re}(\lambda) = 0$. These waves are called *neutrally stable* (waves for which $\text{Re}(\lambda) < 0$ are called *stable*). However, in the case of $n = 0$, (2.2) yields positive values for $\text{Re}(\lambda)$ corresponding to a growing amplitude for $0 < kR < 1$. The desired 'mode of maximum instability', or the *most unstable mode*, corresponds to the maximum value of $\text{Re}(\lambda)$ for all k. Thus Rayleigh's classical formula for the growth rates for an inviscid infinite circular cylinder of fluid are given by

$$\lambda^2 = \frac{\sigma}{R^3\rho} \frac{kRI'_0(kR)}{I_0(kR)}(1 - k^2R^2) \tag{2.3}$$

On examination of (2.3), the disturbance which has the maximum of $\text{Re}(\lambda)$, corresponding to the most unstable wavenumber, takes its value for $kR \approx 0.697$ which gives a wavelength $\lambda_w \approx 2\pi R/0.697 \approx 9R$. The growth rate at this maximum is $\text{Re}(\lambda) \approx 0.3433\sqrt{\sigma/R^3\rho}$, which yields a characteristic time to break-up, $t_b = 1/\text{Re}(\lambda) \approx 2.94\sqrt{R^3\rho/\sigma}$ s. Thus a jet of water of diameter 5mm radius has a wavelength $\lambda_w \approx 45$mm and a characteristic time to break-up $t_b \approx 1/8$ seconds [4]. Also note that $\lambda^2 < 0$ when $k > 1/R$, and so the inviscid cylinder is neutrally stable to

these disturbances.

2.3   The inclusion of viscosity

Viscosity is a damping force on capillary wave growth. Hence the dispersion relation that describes wave behaviour must be dependent on viscosity. This was investigated by Weber [47]. For $n = 0$, the dispersion relation is found to be

$$\lambda^2 + \lambda \frac{2\mu k^2}{I_0(kR)} \left[I_1'(kR) - \frac{2k\tilde{k} I_1(kR) I_1'(\tilde{k}R)}{(k^2 + \tilde{k}^2) I_1(\tilde{k}R)} \right] = \frac{\sigma R}{\rho\mu^2} \frac{kR(k^2 - \tilde{k}^2) I_1(kR)}{(k^2 + \tilde{k}^2) I_0(kR)} (1 - k^2 R^2)$$

(2.4)

where $\tilde{k}^2 = k^2 + \lambda/\mu$. Equation (2.4) can be analysed numerically, looking for the value of k which maximizes $\text{Re}(\lambda)$.

2.4   Instability analysis

In the previous sections, disturbances were of the form $exp(i(kz - n\theta) + \lambda t)$. Positive values of $\text{Re}(\lambda)$ caused perturbations to grow with time. This type of instability is called a *temporal instability*. λ is a complex quantity, denoted $\lambda = \lambda_r + i\lambda_i$. The amplitude of the disturbance will grow or decay depending on whether λ_r is positive or negative respectively, and so λ_r is called the *temporal growth rate*. The imaginary part λ_i represents the (angular) frequency of oscillation and λ_i/k is the *phase speed* of the wave. The wavenumber, k, remains real throughout temporal instability analysis.

However, Keller *et al.* [21] noticed that this form of stability analysis assumes that the disturbances grow everywhere, including at the orifice. In fact disturbances are observed to be minimal in proximity to the orifice and grow as they move down the jet. This is also seen in experimental research involving imposed harmonic disturbances at the orifice to force jet break-up or from technological devices such as the ink jet

printer [23]. These types of instability are called *spatial instabilities*, with a complex wavenumber $k = k_r + ik_i$ and only the imaginary part of λ is non-zero, hence $\lambda = i\lambda_i$. Here k_i is the *spatial growth rate*, k_r is the wavenumber and λ_i the frequency. Keller *et al.* [21] describe that in spatial stability analysis, λ has just two solutions for different values of k and n, but k can have infinitely many solutions for one value of λ and n.

The above spatial instability is a *convective instability*, i.e. an instability which only grows with space away from its point of origin, and not at the point of origin of the disturbance. In other words, the spatial disturbance is small at the orifice where it arises and grows as it moves away.

For very slow jets, a new type of disturbance was discovered which grows more quickly than the Rayleigh mode. It was Leib & Goldstein [23] who formally classified this type of instability in liquid jets, called an *absolute instability*, and discovered that the critical Weber number (a relationship between a jet's inertia and surface tension) below which a jet becomes absolutely unstable is a function of the jet's Reynolds number (a relationship between a jet's inertia and viscosity)[3]. In absolute instability, the disturbance propagates away from its point of origin, but also grows everywhere, including at the point of origin of the disturbance. Lin & Lian [27] extended this to examine the effect of the ambient gas surrounding the jet. In order to describe the differences between convective and absolute instabilities in the context of unstable disturbances to a jet's surface, we shall now give a very brief review of the works of Lin [26, 25].

Lin did not assume that the instabilities take any particular form, and thus allowed both k and λ to be complex. Lin let the variables of the problem be defined by $\mathbf{f}(\mathbf{x}, t)$

---

[3]The Weber number and Reynolds number are formally defined in Section 3.2.1

and took the Laplace-Fourier transform

$$\mathbf{F}(\mathbf{k}, \lambda) = \int_{\infty}^{\infty} \int_{0}^{\infty} e^{-\lambda t} e^{i\mathbf{k}\cdot\mathbf{x}} \mathbf{f}(\mathbf{x}, t) dt d\mathbf{x}$$

in order to model disturbances down the jet (in a similar way previous solutions were of the form $exp(ikz + \lambda t)$).

Lin used residue calculus to solve the resulting inverse transform problem. Taking large time asymptotics to the resulting equations, Lin shows that for a convective instability

$$\lim_{t \to \infty} \mathbf{A}(\mathbf{x}, t) = 0 \tag{2.5}$$

and

$$\lim_{t \to \infty} \mathbf{A}(\mathbf{x} = Ut, t) = \infty. \tag{2.6}$$

where U is the velocity of the wave packet and $\mathbf{A}$ is a vector describing the amplitude of the disturbance at location $\mathbf{x}$. Equation (2.5) shows that the disturbance at a particular point will eventually dissipate, whilst if we move along with the disturbance as in (2.6), it will continue to grow.

Lin analyzed saddle point formation and through long time asymptotics the relationship for an absolute instability is found to be

$$\lim_{t \to \infty} \mathbf{A}(\mathbf{x}, t) = \infty. \qquad \forall \mathbf{x}. \tag{2.7}$$

Equation (2.7) shows that the disturbance will grow at all points along the jet. This is the definition of absolute instability.

In this thesis, we shall consider convective instability of a liquid jet, with disturbances growing as they move away from the orifice.

2.5　Nonlinear analysis

The linear stability analysis predicts drop sizes by assuming a drop forms over the wavelength of the most unstable disturbance. However, jet break-up is seen to be a nonlinear phenomenon and smaller droplets, called satellite droplets, can arise through the nonlinearity of jet break-up. Nonlinear jet break-up is now briefly reviewed.

The full Navier-Stokes equations with a free surface boundary are an extremely complicated set of equations to solve. As of yet, no general analytical solution to this problem exists, and a full numerical solution is very computationally expensive. The reduction of this problem to a one-dimensional approximation using a long-wavelength assumption will help save on this front, whilst maintaining accuracy [16].

Eggers & Dupont [16] adopted a one-dimensional Taylor series expansion in the radial coordinate r,

$$
\begin{aligned}
v(z,r,t) &= v_0(z,t) + r^2 v_2(z,t) + ... \\
u(z,r,t) &= -\tfrac{1}{2} r v_{0z}(z,t) - \tfrac{1}{4} r^3 v_{2z}(z,t) + ... \\
p(z,r,t) &= p_0(z,t) + r^2 p_2(z,t) + ...
\end{aligned}
\tag{2.8}
$$

where v, u and p are the axial velocity, radial velocity and pressure fields respectively in cylindrical polar coordinates, and a subscript represents a derivative with respect to that variable. This allows the derivation of the equations describing the nonlinear system, which are found to be

$$
\begin{aligned}
v_t &= -v v_z - \frac{p_z}{\rho} + \frac{3\nu (h^2 v_z)_z}{h^2}, \\
p &= \sigma \left(\frac{1}{h(1+h_z^2)^{\frac{1}{2}}} - \frac{h_{zz}}{(1+h_z^2)^{\frac{3}{2}}} \right), \\
h_t &= -v h_z - \frac{1}{2} v_z h,
\end{aligned}
$$

where $h(z,t)$ is the position of the free surface, and $\nu = \mu/\rho$ is the kinematic viscosity. This set of equations can be used to generate a numerical simulation of a liquid jet's break-up. Equations similar to the above will be derived later in this thesis for a curved jet. Using Reynolds lubrication theory [40], Eggers & Villermaux [17] used asymptotic Taylor expansions with a small parameter ϵ to derive the leading order (in ϵ) solution to the problem.

2.6   Summary

In this chapter we have given a review of many of the classical works analyzing jet break-up. We presented dispersion relations for both inviscid and viscous jets that could be solved to find the most unstable mode. We then illustrated the differences between convective and absolute instabilities and noted from here on we will be examining disturbances which propagate convectively. We describe the difference between linear and nonlinear analysis of a jet, noting that linear analysis can provide valuable information such as break-up lengths and main drop sizes, but it is the nonlinear methods that fully describe the local dynamics near break-up.

Chapter 3

A Brief review of Theoretical Work on Curved Jets

In the previous chapter, we introduced important aspects concerning liquid jet break-up, focussing on a straight cylindrical jet. However, external forces can cause curvature to a jet's trajectory, such as gravitational or rotational forces. In the next section we shall present an industrial scenario where rotational forces cause a curved liquid jet, whilst the remainder of the chapter details some current research on the break-up of curved liquid jets. The differences to the jet trajectory caused by curvature are discussed in more detail later in the thesis.

3.1   Prilling

Prilling is an industrial process used in the mass manufacture of prills, small spheres of material formed from a molten liquid. For example, *Norsk Hydro* are a Norwegian company who use the prilling process in the production of fertilizer pellets made from

Figure 3.1: Photograph showing multiple jets emerging from a can (dark shape at the bottom of the photograph) in the prilling process. Some droplets can also be seen at the top of the photograph. Reproduced from Wallwork [45].

urea[1]. Their prilling tower is one of the largest in the world, measuring 30m in height and 24m in diameter. At the top of the tower there is a 1m long can, 0.5m in diameter with aprroximately 2000 small holes 4mm in diameter. The can rotates at a rate of 320-450 rpm and the rotational forces cause the molten metal inside the can to emerge from the orifice at high speeds into the atmosphere. Figure 3.1 shows jets forming during the prilling process.

The emerging jets break-up into droplets, which cool and solidify as they fall and are taken away to be processed. Currently, the prilling process produces drops of non-uniform size which causes waste. This waste is due to satellite drop formation. It is

---

[1]Urea, also known as carbamide, is an organic compound with the chemical formula $(NH_2)_2CO$. It reacts with water to form ammonia and carbon dioxide releasing nitrogen, and hence is used as a fertilizer replenishing nitrogen in soils.

the aim of this thesis to gain a thorough understanding of curved liquid jet break-up, focussing on the formation and ultimately the eradication of satellite droplets, reducing waste for companies who use the prilling process in the manufacture of particulate products. This same process is also used in other areas of industry, such as in the production of small spheres of liquid metal in the manufacture of cars, and in some pharmaceutical manufacture. In cases where liquid metals are used, the smaller droplets can be a cause of dust explosion.

3.2 Curved Liquid Jets

In analyzing curved liquid jets we use many of the techniques described for straight jets outlined in Chapter 2. We detail some of the current work on the break-up of curved liquid jets, discussing the calculation of the jet's centreline, linear stability and nonlinear analysis.

3.2.1 The equations of motion

We begin by describing the model and coordinate system for our curved liquid jet, as derived by Wallwork [45].

We consider a circular cylindrical container of radius s_0 rotating about its vertical axis with rotation rate Ω. We work in a rotating frame of reference in which the orifice of radius a is fixed on the surface of the can. The X-axis is directed normal to the surface of the container in the initial direction of the jet and the Y and Z-axes are orthogonal to the X-axis, in the plane of the axis of the cylinder and centreline of the jet respectively. The origin O is at the centre of the can for the X-Y-Z coordinates. This is shown in Figure 3.2.

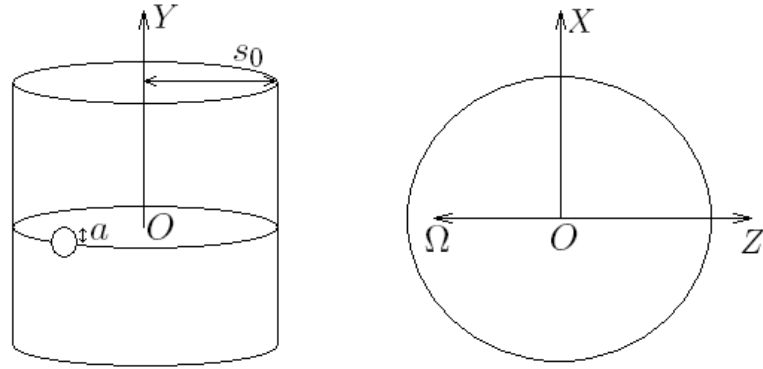The centreline of the jet can be written in summation notation as $\mathbf{r}_{cl} = X_i \mathbf{e}_i$. Here

Figure 3.2: Graphical description of the x, y and z coordinates.

$\mathbf{e}_1 = \mathbf{i}$, $\mathbf{e}_2 = \mathbf{j}$ and $\mathbf{e}_3 = \mathbf{k}$ where $\mathbf{i}$, $\mathbf{j}$ and $\mathbf{k}$ are unit vectors in Cartesian coordinates in the rotating frame, and $X_1 = X, X_2 = Y$ and $X_3 = Z$. We adopt a curvilinear coordinate system (s, n, ϕ) where s is the arclength along the centreline of the jet, and (n, ϕ) are plane polar coordinates in any cross-section of the jet. The origin o for the s-n-ϕ coordinates is at the centre of the orifice on the surface of the cylinder, as demonstrated in Figure 3.3. Also, we let $X_i = X_i(s, t)$ where t is time.

(a) Jet centreline

(b) Jet cross section.
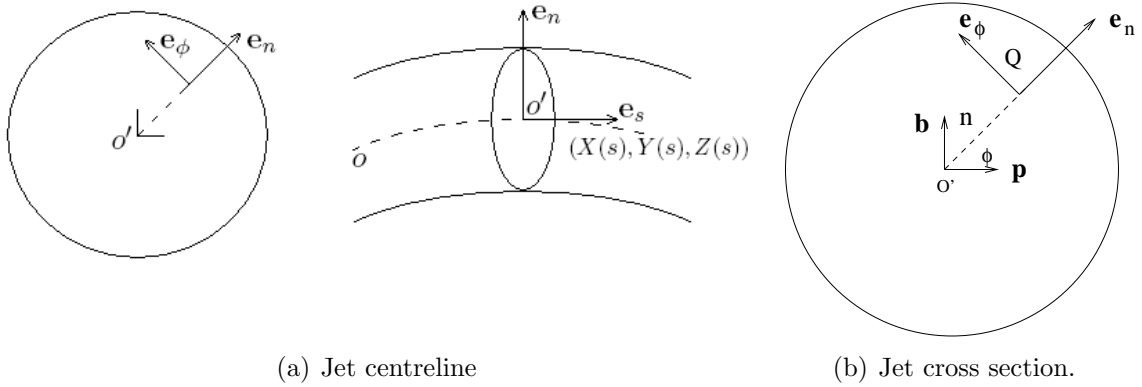
Figure 3.3: Graphical description of the jet's geometry. o is the origin at the centre of the orifice.

We define unit normal vectors in the s, n and ϕ directions as $\mathbf{e}_s$, $\mathbf{e}_n$ and $\mathbf{e}_\phi$ respectively. We use

$$\mathbf{e}_s = X_{i,s}\mathbf{e}_i$$

19

to calculate our principal and binormal vectors, $\mathbf{p}$ and $\mathbf{b}$,

$$\mathbf{p} = \frac{\mathbf{e}_{s,s}}{|\mathbf{e}_{s,s}|} = \frac{X_{i,ss}\mathbf{e}_i}{\sqrt{X_{j,ss}^2}}$$

$$\mathbf{b} = \mathbf{p} \times \mathbf{e}_s = \frac{\varepsilon_{ijk}(X_{j,ss}X_{k,s}\mathbf{e}_i)}{\sqrt{X_{\ell,ss}^2}},$$

where

$$\varepsilon_{ijk} = \begin{cases} 1 & \text{if } (i,j,k) = (1,2,3), (2,3,1) \text{ or } (3,1,2), \\ -1 & \text{if } (i,j,k) = (1,3,2), (3,2,1) \text{ or } (2,1,3), \\ 0 & \text{otherwise}, \end{cases}$$

and for X_i, subscripts in s denote derivatives with respect to s, and subscripts in i, j, k and l are used for summation convention. We describe our plane polar coordinate vectors as

$$\mathbf{e}_n = \cos\phi\,\mathbf{p} + \sin\phi\,\mathbf{b}$$

$$= \frac{1}{\sqrt{X_{\ell,ss}^2}}(\cos\phi X_{i,ss} + \sin\phi\varepsilon_{ijk}X_{j,ss}X_{k,s})\mathbf{e}_i$$

$$\mathbf{e}_\phi = -\sin\phi\,\mathbf{p} + \cos\phi\,\mathbf{b}$$

$$= \frac{1}{\sqrt{X_{\ell,ss}^2}}(-\sin\phi X_{i,ss} + \cos\phi\varepsilon_{ijk}X_{j,ss}X_{k,s})\mathbf{e}_i$$

We also define the position vector of any particle relative to the origin o as

$$\mathbf{r} = \int_0^s \mathbf{e}_s ds + n\mathbf{e}_n.$$

If g is the acceleration due to gravity and if $s_0\Omega^2 \gg g$, then the jets do not fall significantly out of the plane of rotation before breaking up into drops. As we are modelling jets emerging from a rapidly rotating cylinder, the impact of rotation is

20

much larger than that of gravity and so this is a valid assumption most of the time. Hence we set $Y(s,t) = 0$. Further justification on the negation of gravity will be given later when discussing droplet sizes.

We formulate our model thus. In the bulk we have the Continuity Equation and Navier-Stokes Equations

$$\begin{aligned} \nabla \cdot \mathbf{u} &= 0, \\ \frac{\partial \mathbf{u}}{\partial t} + \mathbf{u} \cdot \nabla \mathbf{u} &= -\frac{1}{\rho}\nabla p + \nu\nabla^2\mathbf{u} - 2\omega \times \mathbf{u} - \omega \times (\omega \times \mathbf{r}'), \end{aligned} \tag{3.1}$$

where $\mathbf{u} = u\mathbf{e}_s + v\mathbf{e}_n + w\mathbf{e}_\phi$ is the velocity field, p is the pressure, ρ, $\nu = \mu/\rho$ and μ are the liquid's density, kinematic viscosity and dynamic viscosity respectively, $\mathbf{r}'$ is the position vector in the X-Y-Z system and $\omega = \Omega\mathbf{j}$. The boundary conditions on the free surface $n = R(s, \phi, t)$, as described in Chapter 2, are the kinematic condition

$$\frac{\partial F}{\partial t} + \mathbf{u} \cdot \nabla F = 0$$

where $F(\mathbf{r}, t) = R(s, \phi, t) - n$ describes the free surface, tangential stress conditions

$$\mathbf{n} \cdot \mathbf{T} \cdot \mathbf{t}_i = 0,$$

where $\mathbf{t}_i$ are vectors tangential to the surface and $i = 1, 2$, and the normal stress condition

$$\mathbf{n} \cdot \mathbf{T} \cdot \mathbf{n} = \sigma\kappa, \tag{3.2}$$

where σ is the (constant) surface tension, $\mathbf{n}$ is a normal vector to the free-surface and $\kappa = \nabla \cdot \mathbf{n}$ is the curvature of the free-surface. $\mathbf{T}$ is the stress tensor defined by $p\mathbf{I} + \mu[\nabla\mathbf{u} + (\nabla\mathbf{u})^T]$ where $\mathbf{I}$ is the second order Identity Tensor and ^{T} denotes the

transpose of the vector. We have tangential flow down the centreline,

$$v = w = 0 \qquad \text{on } n = 0,$$

in addition to the arclength condition[2]

$$X_s^2 + Z_s^2 = 1.$$

At this point, to simplify analysis, we move the origin O of the X-Y-Z system to coincide with the origin o of the s-n-ϕ system. In other words we translate the origin of the X-Y-Z system to the centre of the orifice o. We also have orifice conditions

$$X = Z = Z_s = 0, \; X_s = 1, \; R = a \text{ and } u = U \qquad \text{at } s = 0.$$

We wish to examine dimensionless equations and use the following transformations

$$(\bar{u}, \bar{v}, \bar{w}) = \frac{1}{U}(u, v, w), \quad (\bar{X}, \bar{Z}) = \frac{1}{s_0}(X, Z),$$

$$\bar{p} = \frac{p}{\rho U^2}, \quad \bar{n} = \frac{n}{a}, \quad \epsilon = \frac{a}{s_0}, \quad \bar{R} = \frac{R}{a}, \quad \bar{s} = \frac{s}{s_0}, \quad \bar{t} = \frac{tU}{s_0},$$

where U is the exit speed of the jet in the rotating frame at the orifice, and we call ϵ the aspect ratio. We identify the following non-dimensional parameters,

$$We = \frac{\rho U^2 a}{\sigma}, \quad Rb = \frac{U}{s_0 \Omega}, \quad Re = \frac{\rho U a}{\mu}, \quad Oh = \frac{\mu}{\sqrt{\sigma a \rho}},$$

namely the Weber, Rossby, Reynolds, and Ohnesorge numbers respectively. As $a <<$ s_0, $\epsilon << 1$ and can be considered a small parameter, providing the basis for a slender jet assumption. The overbars denote dimensionless quantities in the above.

---

[2]derived from the fact that $ds^2 = dX^2 + dZ^2$ along the centreline,

Dropping overbars, we adopt a slender jet solution method and assume asymptotic expansions of the form

$$
\begin{aligned}
\mathbf{u} &= u_0(s,t)\mathbf{e}_s + \epsilon\mathbf{u}_1(s,n,\phi,t) + O(\epsilon^2) \\
p &= p_0(s,t) + \epsilon p_1(s,n,\phi,t) + O(\epsilon^2) \\
R &= R_0(s,t) + \epsilon R_1(s,n,\phi,t) + O(\epsilon^2) \\
\mathbf{X} &= \mathbf{X}_0(s,t) + \epsilon\mathbf{X}_1(s,n,\phi,t) + O(\epsilon^2).
\end{aligned}
$$

where $\mathbf{u}_1 = u_1\mathbf{e}_s + v_1\mathbf{e}_n + w_1\mathbf{e}_\phi$ and $\mathbf{X}_1 = X\mathbf{i} + Z\mathbf{k}$, as in Wallwork [45]. We can use this to find the steady leading order solution in terms of the pressure, radius, velocity and centreline position by assuming no t dependence. At leading-order, these steady equations are found to be independent of viscosity. These equations are derived in Wallwork [45] and are given below

$$
\begin{aligned}
u_0 &= \left(1 - \frac{1}{Rb^2}\left(X^2 + 2X + Z^2\right) + \frac{2}{We}\left(1 - \frac{1}{R_0}\right)\right)^{1/2} \\
\frac{dR_0}{ds} &= -\frac{WeR_0^2\left((X+1)X_s + ZZ_s\right)}{Rb^2\left(1 + 2WeR_0u_0^2\right)} \\
Z_{ss} &= \frac{WeR_0X_S}{WeR_0u_0^2 - 1}\left(\frac{2u_0}{Rb} + \frac{ZX_s - (X+1)Z_s}{Rb^2}\right) \\
X_s^2 + Z_s^2 &= 1.
\end{aligned}
$$
(3.3)

These ordinary differential equations can be solved subject to the non-dimensional initial conditions $X = Z = Z_s = 0$, $X_s = R_0 = u_0 = 1$ at $s = 0$. X_0 and Z_0 have been relabelled as X and Z in the above. A similar derivation is given in Chapter 8. For the interested reader, the linear derivation of the centreline equations for a jet rotating under the influence of gravity can be found in Wallwork [45]. The expansions presented above can also be used to analyze unsteady time-dependent solutions, giving rise to PDEs in s and t. This will be described in Section 3.2.3. The steady state trajectory
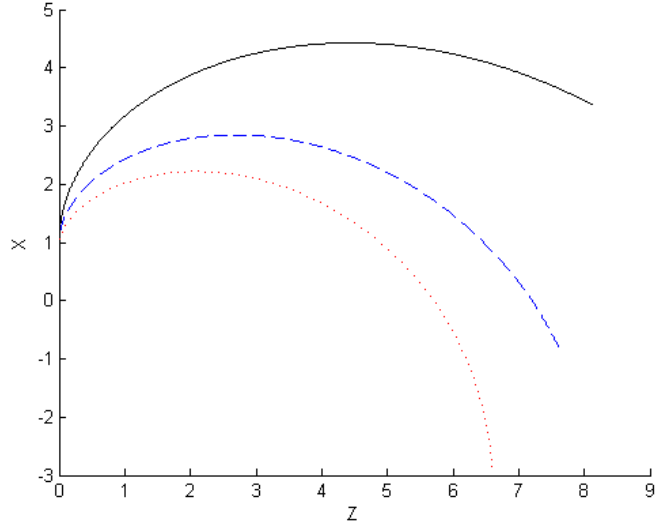
Figure 3.4: Theoretical simulation of the trajectory of the centreline of a curved jet with $Rb = 5(-)$, $2(--)$ and $1(\cdots)$ for $We = 50$.

is solved numerically using a Runge-Kutta scheme and is shown in Figure 3.4.

3.2.2 Linear Stability Analysis

We will now describe linear stability analysis in accordance with the method described in Chapter 2. Wallwork *et al.* [46] studied this for an inviscid rotating jet and Decent *et al.* [12] extended the research to account for viscosity; both were in the absence of gravity. Decent *et al.* [13] incorporated gravity into the linear instability analysis. We outline the method and the results of Decent *et al.* [12] in detail.

We begin by perturbing the steady state using a small dimensionless parameter δ,

$$\mathbf{u} = \bar{\mathbf{u}}(s, n, \phi, \epsilon) + \delta \tilde{\mathbf{u}}(s, \bar{s}, n, \phi, t, \bar{t}) + O(\delta^2)$$

$$p = \bar{p}(s, n, \phi, \epsilon) + \delta \tilde{p}(s, \bar{s}, n, \phi, t, \bar{t}) + O(\delta^2)$$

$$R = \bar{R}(s, n, \phi, \epsilon) + \delta \tilde{R}(s, \bar{s}, n, \phi, t, \bar{t}) + O(\delta^2)$$

$$\mathbf{X} = \bar{\mathbf{X}}(s, \epsilon) + \delta \epsilon \tilde{\mathbf{X}}(s, \bar{s}, t, \bar{t}) + O(\delta^2).$$

24

where $(\bar{\mathbf{u}}, \tilde{\mathbf{u}}) = (\bar{u}, \tilde{u})\mathbf{e}_s + (\bar{v}, \tilde{v})\mathbf{e}_n + (\bar{w}, \tilde{w})\mathbf{e}_\phi$, $(\bar{\mathbf{X}}, \tilde{\mathbf{X}}) = (\bar{X}, \tilde{X})\mathbf{i} + (\bar{Z}, \tilde{Z})\mathbf{k}$[3]. Here $(\bar{\mathbf{u}}, \bar{p}, \bar{R}, \bar{\mathbf{X}})$ are the steady state solutions found in the previous section by solving the ODEs (3.3), whilst $(\tilde{\mathbf{u}}, \tilde{p}, \tilde{R}, \tilde{\mathbf{X}})$ are the unsteady perturbed variables. We have introduced a short length scale, $\bar{s} = s/\epsilon$, and a short timescale, $\bar{t} = t/\epsilon$, with short wave-like disturbances of $O(\epsilon)$. Here s is a long length scale associated with the curving of the trajectory of the jet, while $\bar{s}$ is associated with waves with a much shorter wavelength comparable to the jet's diameter. In Section 2.2, it was these short-wave disturbances that Rayleigh derived.

We retain the terms of $O(\delta)^4$ and look for travelling modes of the form

$$
\begin{aligned}
\tilde{\mathbf{u}} &= \hat{\mathbf{u}}(s, n, \phi, t) \exp\left(ik(s)\bar{s} + \lambda(s)\bar{t}\right) + c.c., \\
\tilde{p} &= \hat{p}(s, n, \phi, t) \exp\left(ik(s)\bar{s} + \lambda(s)\bar{t}\right) + c.c., \\
\tilde{R} &= \hat{R}(s, \phi, t) \exp\left(ik(s)\bar{s} + \lambda(s)\bar{t}\right) + c.c., \\
\tilde{\mathbf{X}} &= \hat{\mathbf{X}}(s, t) \exp\left(ik(s)\bar{s} + \lambda(s)\bar{t}\right) + c.c.,
\end{aligned}
$$

where $\hat{\mathbf{u}} = \hat{u}\mathbf{e_s} + \hat{v}\mathbf{e_n} + \hat{w}\mathbf{e}_\phi$, and $\hat{\mathbf{X}} = \hat{X}\mathbf{i} + \hat{Z}\mathbf{k}$. Here, $k(s)$ is the wavenumber and $\lambda(s)$ is the wave frequency/temporal growth rate and both are made functions of s thus allowing variation down the jet. In addition $c.c.$ denotes the complex conjugate. We expand the velocity, pressure and radius ($\hat{\mathbf{u}}, \hat{p}$ and $\hat{R}$) in Fourier series in ϕ, and find an infinite set of eigenvalue relationships, each associated with $\cos(n\phi)$ or $\sin(n\phi)$ for each integer n. As with straight jets, we have stable modes for $n \geq 1$, plus one unstable mode corresponding to $n = 0$. This calculation is shown in full in Chapter 8.

Wallwork *et al.* [46] derived a relation analogous to (2.3) for inviscid jets, and for

---

[3]We also note that we first tried $\mathbf{X} = \bar{\mathbf{X}}(s, \epsilon) + \delta\tilde{\mathbf{X}}_{\mathbf{0}}(s, \bar{s}, t, \bar{t}) + \delta\epsilon\tilde{\mathbf{X}}(s, \bar{s}, t, \bar{t})$, but $\tilde{\mathbf{X}}_{\mathbf{0}}$ was found to be identically equal to zero

[4]the $O(1)$ equations dropping out naturally as the steady state equations

viscous jets Decent *et al.* [12] derived

$$
\begin{aligned}
We^{3/2}R_0^2\lambda^2 \ k^2 I_0(kR_0)I_1(\tilde{k}R_0) \ &+ \ We^{3/2}R_0^2\lambda^2 \ \tilde{k}^2 I_0(kR_0)I_1(\tilde{k}R_0) \\
+2iWe^{3/2}R_0^2\lambda \ k^3 I_0(kR_0)I_1(\tilde{k}R_0) \ &+ \ 2iWe^{3/2}u_0\lambda R_0^2 \ k\tilde{k}^2 I_0(kR_0)I_1(\tilde{k}R_0) \\
-We^{3/2}R_0^2u_0^2 \ k^4 I_0(kR_0)I_1(\tilde{k}R_0) \ &- \ We^{3/2}R_0^2u_0^2 \ k^2\tilde{k}^2 I_0(kR_0)I_1(\tilde{k}R_0) \\
+2OhWeR_0^2\lambda \ k^4 I_0(kR_0)I_1(\tilde{k}R_0) \ &+ \ 2OhWeR_0\lambda \ k^3 I_1(kR_0)I_1(\tilde{k}R_0) \\
+2OhWeR_0^2\lambda \ k^2\tilde{k}^2 I_0(kR_0)I_1(\tilde{k}R_0) \ &- \ 2OhWeR_0\lambda \ k\tilde{k}^2 I_1(kR_0)I_1(\tilde{k}R_0) \\
-4OhWe\lambda \ k^3\tilde{k} I_1(kR_0)I_0(\tilde{k}R_0) \ &+ \ 2iOhWeR_0^2u_0 \ k^5 I_0(kR_0)I_1(\tilde{k}R_0) \\
+2iOhWeR_0u_0 \ k^4 I_1(kR_0)I_1(\tilde{k}R_0) \ &+ \ 2iOhWeR_0^2u_0 \ k^3\tilde{k}^2 I_0(kR_0)I_1(\tilde{k}R_0) \\
-2iOhWeR_0u_0 \ k^2\tilde{k}^2 I_1(kR_0)I_1(\tilde{k}R_0) \ &- \ 4iOhWeR_0^2u_0 \ k^4\tilde{k} I_1(kR_0)I_0(\tilde{k}R_0) \\
-\sqrt{We} \ k\tilde{k}^2 I_1(kR_0)I_1(\tilde{k}R_0) \ &+ \ \sqrt{We} \ k^3 I_1(kR_0)I_1(\tilde{k}R_0) \\
+\sqrt{We}R_0^2 \ k^3\tilde{k}^2 I_1(kR_0)I_1(\tilde{k}R_0) \ &- \ \sqrt{We}R_0^2 \ k^5 I_1(kR_0)I_1(\tilde{k}R_0) = 0 \quad (3.4)
\end{aligned}
$$

where $\tilde{k}^2 = k^2 + We^{1/2}(\lambda + iku_0)/Oh$. This is equivalent to (2.4) where $u_0 = R_0 = 1$ for a straight jet, whilst (3.4) has the effects of rotation come in via the solutions of u_0 and R_0, obtaining by solving the nonlinear ODEs (3.3). As u_0 and R_0 vary down the jet[5] the most unstable wavenumber generated by (3.4) will also change as s varies. The impact of gravity on growth rates and stability can be found in Decent *et al.* [13].

We shall describe the temporal instability first. As outlined in Section 2.4, for temporal instability we set k real, and let $\lambda = \lambda_r + i\lambda_i$, with $\lambda_r > 0$ generating instability. So the most unstable wavenumber ($k = k^*(s)$) is the value of k at which the growth rate λ_r is at a maximum.

Small Oh number asymptotics yield at leading-order the inviscid temporal insta-

---

[5]as the jet is accelerating and thinning

26

bility result presented in Wallwork *et al.* [46], namely

$$\lambda = -iku_0\left(s\right) + \sqrt{\frac{kI_1\left(kR_0\left(s\right)\right)}{WeI_0\left(kR_0\left(s\right)\right)}\left(\frac{1}{R_0^2\left(s\right)} - k^2\right)},$$

where modes are unstable for $0 < kR_0(s) < 1$. The most unstable wavenumber k^* is found, using this equation, to be

$$k^*(s) = \frac{0.697}{R_0\left(s\right)}$$

where $R_0(s)$ is obtained by the solution of the ODEs presented at the end of the previous section.

The most unstable mode is found by examining a long-wavelength approximation $(k \to 0)$ of (3.4) and is given by

$$k^*(s) = \frac{1}{2^{1/4}R_0^{3/4}\left(s\right)\sqrt{\sqrt{2R_0\left(s\right)} + 3Oh}}. \tag{3.5}$$

We also note that if we take the inviscid limit $Oh = 0$ of (3.5) we obtain

$$k^*(s) = \frac{1}{\sqrt{2}R_0\left(s\right)} = \frac{0.707}{R_0\left(s\right)} \approx \frac{0.697}{R_0\left(s\right)}$$

and so the long wavelength approximation is also a reasonable numerical approximation for the shorter inviscid waves.

For spatial stability, following the method of Keller *et al.* [21], we set $\lambda = -i\omega$ and $k = k_r + ik_i$, and so ω is a real frequency. Instability occurs for $k_i < 0$ since the jet starts at $s = 0$ and propagates to large positive values of s. Comparing the long wave analysis for temporal and spatial instability by writing $k = \omega/u_0 + iK$ and solving the eigenvalue relationship for K in the long-wave limit $\omega \to 0$ and $K \to 0$, it was found

27

that the frequency of the most unstable mode $\omega = \omega^*$ is given by

$$\omega^* = u_0 k^* \tag{3.6}$$

where k^* is given by (3.5) in the long wave limit. Here the spatial instability results coincide with temporal instability for long waves.

Full details of these asymptotics can be found in Decent *et al.* [12], as well as numerical solutions to (3.4). These results are analogous to those results for a straight jet. However, noticeable differences arise through the introduction of rotational forces. For a straight jet the leading-order steady radius and velocity are constant. Spinning jets accelerate and thin as they increase their distance from the orifice. As such, $R_0(s)$ and $u_0(s)$ are introduced as functions of s and this causes the Rayleigh mode to change at different points down the jet.

While asymptotic solutions to (3.4) are useful, it is necessary to solve (3.4) computationally for $O(1)$ values of the parameters to find the most unstable mode as a function of s, as in Decent *et al.* [12]. We will see similar calculations in this thesis, extending [12].

3.2.3   Nonlinearity of Break-up

Whilst linear analysis can be used to examine a jet's stability and calculate the break-up length, we must use nonlinear analysis to investigate the break-up mechanism and satellite drop formation. The nonlinear aspects of a curved jet break-up are described in the works of Părău *et al.* [35, 36], and the full equations and derivations can be found in [35, 36] and in Partridge [33], but we shall present a summary here.

We pose the asymptotic expansions

$$\mathbf{u} = u_0(s,t) + (\epsilon n)\mathbf{u}_1(s,\phi,t) + O((\epsilon n)^2)$$
$$p = p_0(s,t) + (\epsilon n)p_1(s,\phi,t) + O((\epsilon n)^2)$$
$$R = R_0(s,t) + \epsilon R_1(s,\phi,t) + O(\epsilon^2) \qquad (3.7)$$
$$\mathbf{X} = \mathbf{X}_0(s) + \epsilon \mathbf{X}_1(s,\phi,t) + O(\epsilon^2).$$

where we have also assumed a steady centreline at leading order. We obtain the following equations,

$$R_{0t} + u_0 R_{0s} + \frac{u_{0s}R_0}{2} = 0,$$
$$u_{0t} + u_0 u_{0s} = -\frac{1}{We}\kappa_s + \frac{(X+1)X_s + ZZ_s}{Rb^2} + \frac{3}{Re}\frac{(R_0^2 u_{0s})_s}{R_0^2}, \quad (3.8)$$

where κ is the curvature of the free surface as defined in Section 3.2.1. Here $\mathbf{X}_0(s) = X(s)\mathbf{i} + Z(s)\mathbf{k}$.

This system of equations can be solved for our leading order velocity and radius, u_0 and R_0. The initial conditions at $t = 0$ are found to satisfy the following ODEs.

$$u_0 u_{0s} = -\frac{1}{2We}\frac{u_{0s}}{\sqrt{u_0}} + \frac{(X+1)X_s + ZZ_s}{Rb^2} + \frac{3}{Re}\left(u_{0ss} - \frac{u_{0s}^2}{u_0}\right),$$
$$(X_s Z_{ss} - Z_s X_{ss})\left(u_0^2 - \frac{3}{Re}u_{0s} - \frac{\sqrt{u_0}}{We}\right) - \frac{2u_0}{Rb} + \frac{((X+1)Z_s - ZX_s)}{Rb^2} = 0,$$
$$X_s^2 + Z_s^2 = 1, \quad (3.9)$$

where $u_0 = 1/R_0^2$, and the boundary conditions at $s = 0$ are given by $X(0) = Z(0) = Z_s(0) = 0$ and $X_s(0) = u_0(0) = 1$. This is the system of ODEs for the solution at $t = 0$. When $Re = \infty$, this system can be solved using a Runge-Kutta method producing solutions as seen in Figure 3.4 (and also satisfy the steady state equations (3.3) found in section 3.2.1). Părău *et al.* [36] solved the above viscous equations for $Re = O(1)$

29

by using Newton's method. Due to the extra derivatives in s appearing in the viscous term in (3.9), extra boundary conditions at $s = \infty$ were applied corresponding to an assumption that the steady state is bounded at $s = \infty$. Further details of the computational methods used are given in the next section.

Părău *et al.* [36] showed that the viscous steady state and inviscid steady state showed an excellent agreement when these equations are solved numerically, except in cases of very high viscosity. This is verified in Decent *et al.* [12] who showed that the viscous terms appear at higher order, except in the case of high viscosity, using an asymptotic approach by considering the steady state's linear instability. Therefore, it is possible to use the inviscid steady state equations as a good approximation to the viscous steady state equations to calculate the initial conditions at $t = 0$, and some authors have used this assumption in their work [44]. The steady state numerical solution is shown in Figure 3.5, including viscosity. In this thesis we shall use the above viscous steady state equations to calculate the initial conditions at $t = 0$ for added accuracy.

Părău *et al.* [36] also examined the problem of an unsteady centreline, generalizing the asymptotic expansions (3.7) by rewriting the centreline into steady and unsteady parts as

$$\mathbf{X} = \tilde{\mathbf{X}}(s) + \hat{\mathbf{X}}(s, t) + O(\epsilon)$$

and allowing v and w to have extra $O(1)$ components in the velocity expansion. This gave rise to a much larger system of PDEs than equations (3.8). It was shown that the movement of the centreline is very small at experimental and industrial parameter values for all times and for all s, with $\hat{X}$ typically being about 0.1% to 1% of the size of $\tilde{X}$. Therefore, we can assume the centreline remains in its initial state for all times. Therefore in equations (3.8) X and Z can be taken to be equal to their steady state values given by (3.9) for all t.
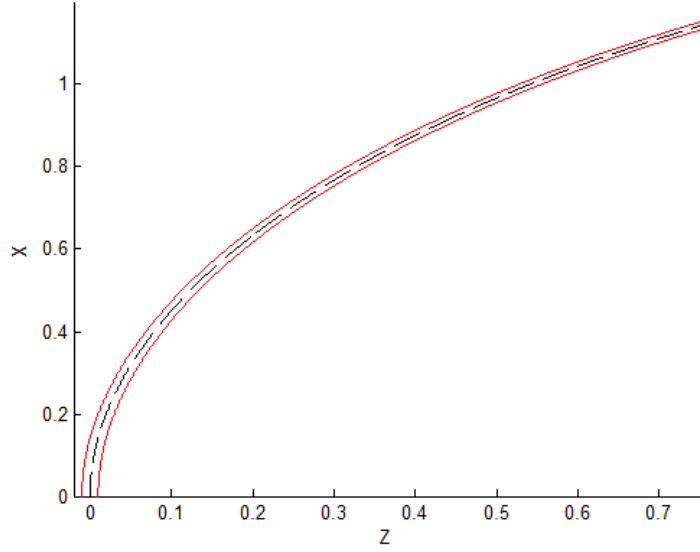
Figure 3.5: Solution of the steady trajectory of the jet. $We = 50$, $Rb = 2$ and $Re = 3000$.

We examine the nonlinear temporal evolution of the jet. In addition to retaining the necessary convective terms in the Navier-Stokes equations, we must retain the full expression for the curvature. When we considered the linear dynamics, the leading order pressure term arising from the curvature in the normal stress condition was given by

$$p_0 = \frac{\kappa}{We} = \frac{1}{nWe} \quad \text{on} \quad n = R_0.$$

However, close to break-up when the surface becomes more deformed it is necessary to retain the full expression for the curvature[6],

$$\kappa = \left(\frac{1}{R_0(1 + \epsilon^2 R_{0s}^2)^{\frac{1}{2}}} - \frac{\epsilon^2 R_{0ss}}{(1 + \epsilon^2 R_{0s}^2)^{\frac{3}{2}}} \right) \tag{3.10}$$

even though the higher order terms in ϵ yield $\sqrt{1 + \epsilon^2 R_{0s}^2} \sim 1$ and $\epsilon^2 R_{0ss} \sim 0$ asymptotically to leading order as $\epsilon \to 0$. However, it is necessary to retain all these extra

---

[6]Note here we still assume no ϕ dependence, as the jet remains axi-symmetric

31

terms in simulations otherwise the equations yield exponential growth to infinitesimally short wavelengths which is not the case physically [3]. The approach of retaining full curvature in simulations has been used by many authors previously for straight jets, for example Eggers and Dupont [16]. Also, Entov and Yarin [18] and Yarin [50] obtained the pressure in terms of the full curvature included here for bending jets in their derivation from physical arguments.

The resulting nonlinear evolution problem is therefore given by

$$
\begin{aligned}
A_t + (Au)_s &= 0 \\
u_t + \left(\frac{u^2}{2}\right)_s &= -\frac{1}{We}\frac{\partial}{\partial s}\left(\frac{4(2A + (\epsilon A_s)^2 - \epsilon^2 A A_{ss})}{(4A + (\epsilon A_s)^2)^{3/2}}\right) + \frac{(X + 1)X_s + ZZ_s}{Rb^2} \\
&+ \frac{3}{Re}\frac{(Au_s)_s}{A},
\end{aligned}
\tag{3.11}
$$

where $A = R_0^2$. The initial conditions at $t = 0$ are obtained from the steady state ODE equations, namely

$$
A(s, t = 0) = R_0^2(s), \qquad u(s, t = 0) = u_0(s)
\tag{3.12}
$$

where $R_0(s)$ and $u_0(s)$ are solutions of the ODEs (3.9). Also $X(s)$ and $Z(s)$ in the above evolution PDEs are obtained from the steady state ODEs (3.9).

To impose the wave disturbance we pose boundary conditions at the orifice $s = 0$

$$
A(s = 0, t) = 1, \qquad u(s = 0, t) = 1 + \delta \sin\left(\frac{\kappa t}{\epsilon}\right),
\tag{3.13}
$$

where δ and κ are the amplitude and frequency of the wave and the introduction of ϵ shows we are searching for fast waves as in Section 3.2.2 because of the non-dimensionalization used. Here δ is a measure of the size of the initial perturbation, and though we have the freedom to choose the size of δ, it is usual to choose a small

perturbation[7]. We can vary κ to simulate disturbances with different frequencies, and by setting $\kappa = k^*$ where

$$k^* = \frac{1}{2^{1/4}\sqrt{\sqrt{2} + 3Oh}},\qquad(3.14)$$

we are imposing the most unstable mode at the orifice from (3.5) since $R_0(s = 0) = 1$. In Chapter 6, we will perform comparisons between a jet excited by this frequency and experimental data. We also impose boundary conditions at the other end of the jet, which involves ensuring that the jet equals the steady state as $s \to \infty$.

Figure 3.6(a) shows the nonlinear temporal solution plotted over the solution of the steady state. Figure 3.6(b) shows $R_0(s, t)$ plotted against s. The simulations are carried out until $R_0(s, t)$ equals 0.05 somewhere along the jet, at which point it is considered to be sufficiently close to break-up. Figure 3.6 shows the solution at this time. It can be seen that the initial sinusoidal disturbance becomes nonlinear at some point down the jet. The onset of this nonlinearity is investigated in Chapters 9 and 10.

Break-up of the jet occurs at $s = s_2$, yielding a break-up length of $s = 1.2215$ non-dimensionalized with respect to s_0. To calculate the drop sizes we take values of R_0 from the numerical simulation, and integrate over a volume of revolution

$$V = \pi \int R_0^2 ds.\qquad(3.15)$$

to get the volume of the drop V. We integrate over a wavelength before break-up from s_1 to s_2 (for the smaller satellite drop in this case) and over a wavelength after break-up from s_2 to s_3 (for the main drop in this case).

---

[7]Decent *et al.* [12] derived this condition as $\delta << 2^{1/4}/\sqrt{3OhWe}$.
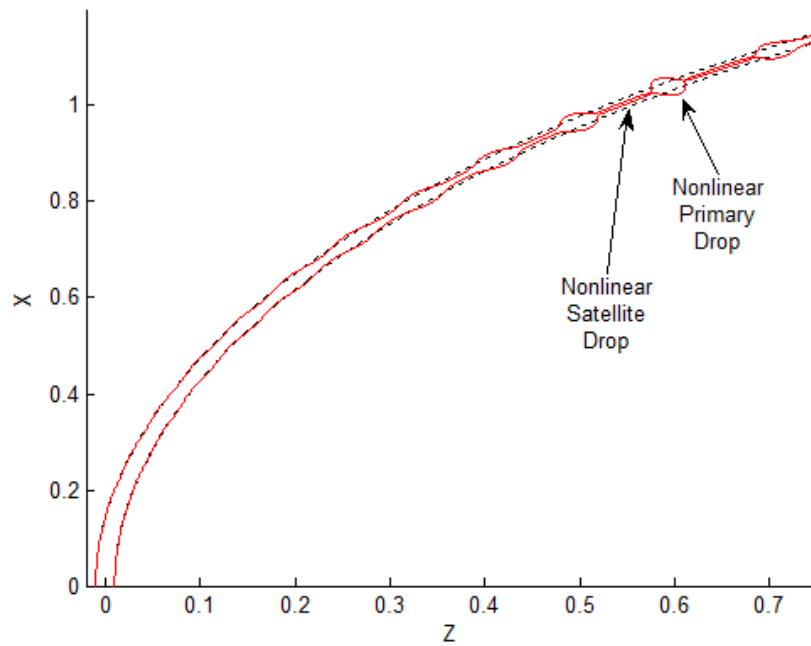
(a) Temporal evolution of the jet superimposed over the steady state initial solution.
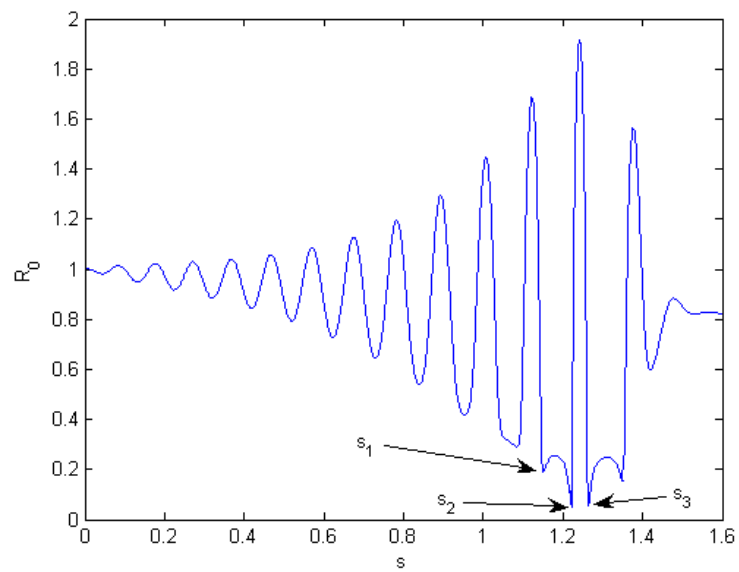
(b) Radius R_0 against arc length s.

Figure 3.6: Nonlinear simulation at the time of break-up. $We = 50$, $Rb = 2$, $Re = 3000$, $\delta = 0.01$ and $\kappa = 0.7053$

34

To calculate the radius of the drop $\hat{R}$ that results from instability, we assume that the resulting drops are spherical (once rupture has occurred), so that

$$V = \frac{4}{3}\pi\hat{R}^3. \tag{3.16}$$

Therefore, we consider a sphere of radius $\hat{R}$ which has volume V. The jet in Figure 3.6 has a main drop with radius of 1.8572 and a satellite drop of radius 0.6413 non-dimensionalized with respect to a. (Note, since s and R_0 are non-dimensionalized with respect to different length scales, we integrate from ϵs_1 to ϵs_2, or ϵs_2 to ϵs_3, and so the resulting drop size $\hat{R}$ is then non-dimensionalized with respect to a.

We note that the jet is assumed to have ruptured when the radius approaches an arbitrarily chosen number (5% in this case). As the radius decreases, a radial dependence becomes more important and the long wavelength analysis less valid. Leppinen and Lister [24] considered an asymptotic nature of inviscid capillary jet break-up in order to get a better understanding of the nature of pinch-off, Sierou and Lister [43] examined the viscous case.

Uddin [44] extended the above by studying Non-Newtonian effects on a spiralling liquid jet by investigating power law fluids. He also provided models for the effect of surfactants on a curved jet, the effect of a periodically heated nozzle and performed investigations into compound jets. This work turned up some interesting results with the potential for further research.

3.2.4 Computational Methods and Numerics

In this section we give a brief outline of the numerical methods used in the simulations, detailing the iterative method used to plot the centreline and the Lax-Wendroff method used to simulate break-up.

Jet Steady State

The steady state is given by the system of equations (3.9), numerically solving for the quantities $X(s)$, $Z(s)$, and $u_0(s)$ subject to the initial conditions $X(0) = Z(0) = Z_s(0) = 0$ and $X_s(0) = u_0(0) = 1$ at the orifice $s = 0$. We use $R_0^2 = 1/u_0$ to obtain $R_0(s)$. In the inviscid case, when $Re = \infty$, we can rewrite (3.9) as a system of five equations to solve for X, Z, X_s, Z_s and u_0, and hence use a Runge-Kutta method. With the inclusion of viscosity, we have an extra derivative of s in the steady equations, and hence we cannot use a Runge-Kutta method.

We therefore use an iterative method, namely Newton's method, solving for X_s, Z_s and u_0 with X and Z obtained using trapezoidal-rule integration. We generate the necessary additional boundary conditions downstream using a quadratic extrapolation of the last internal mesh points. Părău *et al.* [36] show that this method solves the inviscid equations with very good accuracy when compared to the Runge-Kutta method, provided the number of mesh points $M \geq 200$ and the grid interval $ds \leq 0.1$.

Temporal Evolution

To plot the evolution of the jet we solve the system (3.11) where we have the initial conditions given by the solution for the steady state (3.12) and boundary conditions at the orifice (3.13). This system is solved numerically using a two-stage Lax-Wendroff method.

A Lax-Wendroff method solves a system of equations of the form

$$\frac{\partial \mathbf{u}}{\partial t} = -\frac{\partial \mathbf{F}(\mathbf{u})}{\partial s}$$

where in our case the vector $\mathbf{u} = (A, u)^T$ and the conserved flux $\mathbf{F}(\mathbf{u}) = \left(Au, \frac{u^2}{2}\right)^T$.

36

Now the finite difference approximation to this system is

$$\frac{\mathbf{u}_i^{j+1} - \mathbf{u}_i^j}{dt} = \frac{\mathbf{F}_{i+1}^j - \mathbf{F}_{i-1}^j}{2ds}$$

where $\mathbf{u}_i^j = \mathbf{u}(s_0 + ids, t_0 + jdt)$, $\mathbf{F}_i^j = \mathbf{F}(s_0 + ids, t_0 + jdt)$, ds and dt are the space and time intervals and s_0 and t_0 are the initial values for s and t. In our case $s_0 = t_0 = 0$. This approximation can be unstable, and so we introduce half time-steps $t_{j+1/2}$ and half mesh-points $s_{i+1/2}$. Substituting this into the approximation yields the two steps

$$
\begin{aligned}
\mathbf{u}_{i+1/2}^{j+1/2} &= \frac{1}{2}\left(\mathbf{u}_{i+1}^j + \mathbf{u}_i^j\right) - \frac{dt}{2ds}\left(\mathbf{F}_{i+1}^j + \mathbf{F}_i^j\right) \\
\mathbf{u}_i^{j+1} &= \mathbf{u}_i^j - \frac{dt}{ds}\left(\mathbf{F}_{i+1/2}^{j+1/2} + \mathbf{F}_{i+1/2}^{j-1/2}\right)
\end{aligned}
$$

using forward and central differences where the flux $\mathbf{F}_{i+1/2}^{j+1/2}$ is calculated using the values of $\mathbf{u}_{i+1/2}^{j+1/2}$. This is solved at all points down the jet. Jet break-up occurs when the jet radius becomes less than an arbitrarily chosen value (5% of the jet's initial radius). At points downstream of the break-up point, the jet solution no longer has physical meaning as the jet would have broken up into droplets. The spatial and temporal step sizes are decreased until the solutions are found to converge in the simulations.

3.3   Summary

In this chapter we have reviewed current research on a liquid jet emerging from a rotating can. We described methods for plotting the centreline of the jet and detailed the linear stability analysis used to calculate the most unstable mode and we discussed how this differs from a straight jet. We also described the nonlinear analysis used to simulate jet break-up and the method used to work out the corresponding drop sizes. We also detailed the numerical methods used in these simulations.

Chapter 4

A Brief Review on Experimental Investigation of Liquid Jets

In this chapter we detail experimental work on liquid jet break-up. We review previous research into straight jets and droplet control. We then describe in detail the experimental investigation on curved liquid jets at the University of Birmingham.

4.1 Straight Jets and Droplet Control

One of the first to study liquid jet break-up was Savart [42] who noted that liquid jet break-up was a feature of the jet's dynamics. He was able to obtain images, such as the one shown in Figure 4.1, with the jet breaking up into mostly *primary* (or *main*) droplets, the larger droplets which form and are of the same order in size to the radius of the orifice. He also generated *secondary* (or *satellite*) droplets, the droplets much smaller in size which form in between the primary droplets. Savart showed that by varying the frequency at the orifice, disturbances of different frequencies could be seen along the jet, corresponding to different wavelength disturbances. This was also seen by Plateau [38] who found many different unstable wavelengths above a
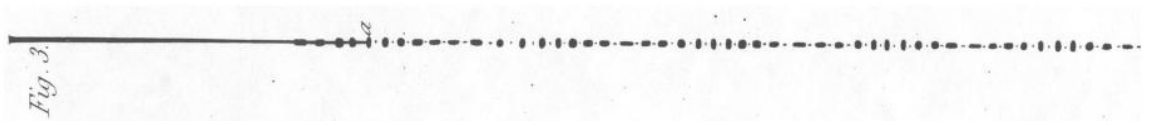
Figure 4.1: A figure from Savart [42] showing the break-up of a straight liquid jet emerging from a 6mm orifice. Reproduced from Eggers and Villermaux [17].

critical wavelength, though it was Rayleigh [39] who noted that it was the mode with highest growth rate that dominates the behaviour (see Chapter 2) and compared well to Savart's experimental results.

Savart's experiments show a high level of accuracy considering the technology available at the time, though with the use of more modern photographic equipment liquid jet break-up can be recorded to a micron scale over a period of microseconds. Peregrine *et al.* [37] investigated the break-up of thin liquid bridges and show clearly the processes involved during drop formation. As drop pinch off is approached, a cylindrical column of fluid (or bridge) forms between the mass of the jet and the drop. At pinch-off, a bifurcation is seen where the column forms into a sharp cone whilst the drop remains spherical. Immediately after pinch-off, very short waves develop on the drop caused by the liquid bridge recoil. A secondary necking and bifurcation appears during the satellite drop formation.

One of the most important aspects of liquid jet break-up is this secondary formation causing the satellite drops, and thus there is a lot of research focussing on reducing their number. By imposing disturbances at the orifice using a piezo-electric transducer, Lindblad and Schneider [29] noted that "droplet size can be precisely controlled and individual droplets produced at will". Chauhan *et al.* [8] used piezo crystal to generate these disturbances, whilst Crane *et al.* [10] used an electrical vibrator to induce mechanical vibrations and Donnelly and Glaberson [14] used a loudspeaker.

Goedde and Yuen [19] investigated a range of induced perturbations at the orifice

and investigated jets falling under gravity. Jets were generated through hydrostatic pressure, as using a pump would cause extra vibrations through the jet. Alongside the theoretical works of Yuen [51], they showed that nonlinear effects dominate the jet break-up, particularly at small wavenumbers, with an initially sinusoidal wave generating higher order harmonics. Rutland and Jameson [41] presented a comparison between the theory and the experiments, where it was shown that a secondary swell can form over a wavelength for a viscous fluid. Chaudhary and Redekopp [7] show theoretically that satellite drops can be reduced by inducing a secondary harmonic, and Chaudhary and Maxworthy [5, 6] compare the theory with experiments using a piezo-electric transducer before and after break-up respectively.

Using the idea of inducing vibrations at the orifice, modifications have been made to the rig at Birmingham involving a vibrating nozzle such that we can attempt to control the liquid jet break-up and produce main droplets of desired size. This is detailed in Chapter 11.

4.2 Laboratory scale Experiments at Birmingham

Experimental investigations into the break-up of curved liquid jets took place in the Chemical Engineering Department at the University of Birmingham. We detail here the investigations on a laboratory scale rig performed by Wong *et al.* [49] simulating the prilling process. A cylindrical can of diameter $D = 0.085$ m and height of 0.115 m was used, with two orifices of diameters $a = 0.001$ m and $a = 0.003$ m. To maintain a constant hydrostatic pressure a peristaltic pump (Waltson-Marlow 505s) kept the fluid at constant height H inside the spinning can. This height was changed from one experimental run to another, with the aspect ratio (H/D) varying from 2/3 to 5/4. The average exit velocities U were calculated by dividing the total volume of liquid

collected over a period of 1 minute by the cross-sectional area of the hole.
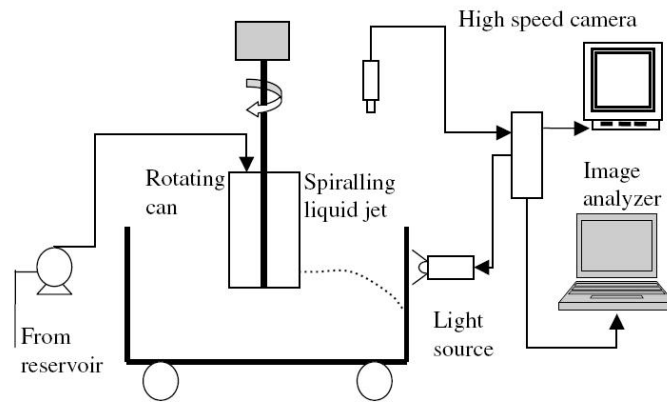
(a) Diagrammatic representation
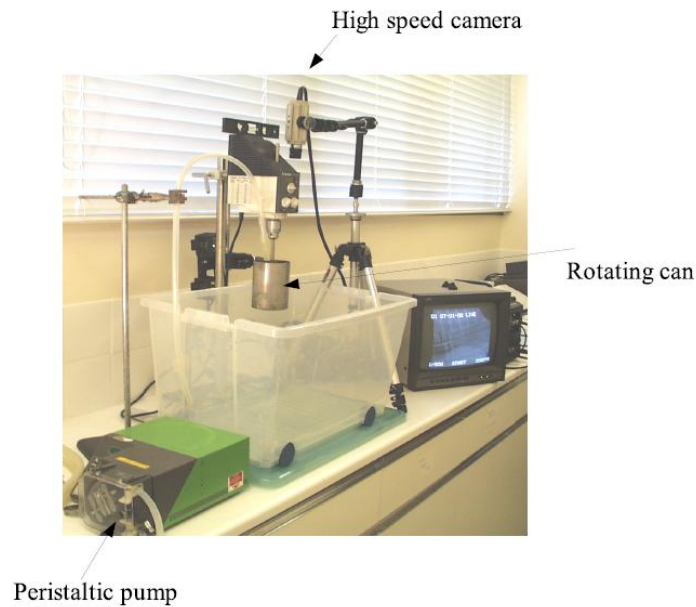
(b) Photographic representation

Figure 4.2: The experimental laboratory scale setup

Images were generated using a high speed digital camera (Photron Fastcam Super 10k) capable of recording up 10,000 frames per second. Using the software Image-Pro Express (Datacell Ltd., UK), Wong *et al.* [49] were able to obtain digital measurements accurate to a tenth of a millimetre, repeating the results three times to generate accuracy. A diagram and photograph of the experimental set-up can be seen in Figure

Liquid dynamic viscosity, μ (Pa s)	0.001-0.081
Liquid density, ρ (kg m^{-3})	1000-1200
Liquid surface tension, σ (N m^{-1})	0.047-0.072
Orifice radius, a (m)	0.0005-0.0015
Liquid aspect ratio, (H/D)	2/3 - 5/4
Can rotation rate, Ω (rad s^{-1})	5.24-31.4
Jet Exit Velocity, U (m s^{-1})	0.318-0.985
Can radius s_0 (m)	0.0425
$Rb = U/\Omega s_0$	0.2 - 4
$Re = \rho U a/\mu$	1 - 1000
$Fr/Rb = \Omega s_0/\sqrt{gH}$	0 - 2
$We = \rho U^2 a/\sigma s_0$	0.5 - 25
$Oh = \mu/\sqrt{\sigma a \rho}$	0.005 - 0.4

Table 4.1: Table summarizing the experimental parameters used for the laboratory scheme.

4.2

Through addition of glycerol (up to 80% of the total fluid mix) to water, Wong *et al.* [49] could obtain fluids of varying rheologies, with dynamic viscosity μ increasing to around 100 times that of water[1]. Through the addition of n-butanol to the mix, surface tension was lowered to a range of 65-100% that of water. The rotational speed of the can was varied from 50 to 300 rpm (corresponding to an angular speed Ω of $5.24 - 31.4$ rad s^{-1}). A summary of the range of the fluid rheologies, the geometry of the experiment and the dimensionless parameters used is given in Table 4.1.

Using different fluids emerging at different exit velocities, Wong *et al.* [49] identified four qualitative types of jet behaviour. These were classified modes 1-4 (denoted M1-M4), with each displaying distinct behaviour which we will now describe in detail. All images are taken from Wong *et al.* [49].

Mode 1 break-up is shown in Figure 4.3, and is characterised by short wavelength disturbances growing quickly causing jet break-up close to the orifice, resulting in primarily main droplets. Few or no satellite droplets are seen. The primary aim of

---

[1]Note η is used throughout Wong *et al.* [49] for dynamic viscosity. μ is used here for consistency.
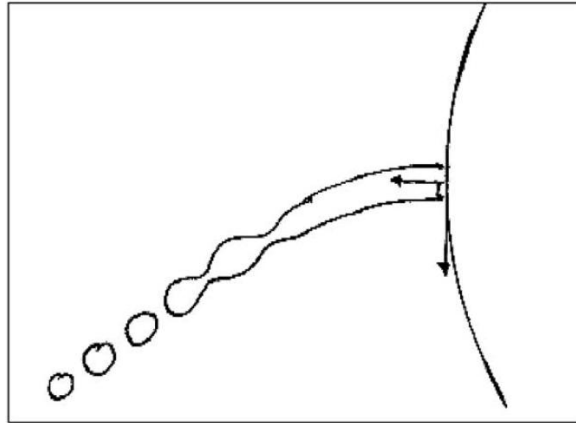
(a) Sketch showing Mode 1 break-up
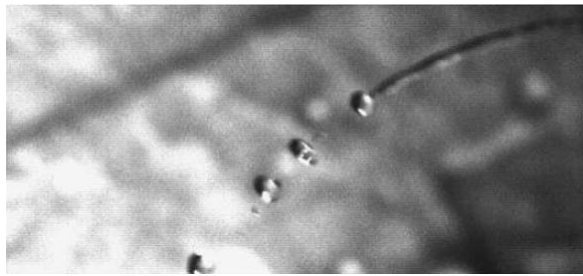
(b) Photograph showing Mode 1 break-up

Figure 4.3: Mode 1 break-up

research into curved liquid jet concerns the formation, and ultimately eradication, of these satellite droplets. As such, Mode 1 break-up is the mode of break-up we wish to generate. Typically, this type of break-up occurs for jets of low exit velocities and so is not seen in the prilling industry due to the large rotation rates present. Wong *et al.* [49] suggest that the presence of the occasional satellite drop could be due to natural vibrations occurring within the experimental set-up. This is an interesting factor which will be investigated in more detail in this thesis.

Mode 2 break-up is shown in Figure 4.4. M2 break-up also consists of short wavelength disturbances, but satellite droplets form in between main droplets. The change from M1 to M2 occurred as the exit velocity of the jet increased, either through increasing the orifice size to 0.003 m or by increasing the rotation rate of the can.

Typical Mode 3 behaviour can be seen in Figure 4.5. M3 occurs as the viscosity of
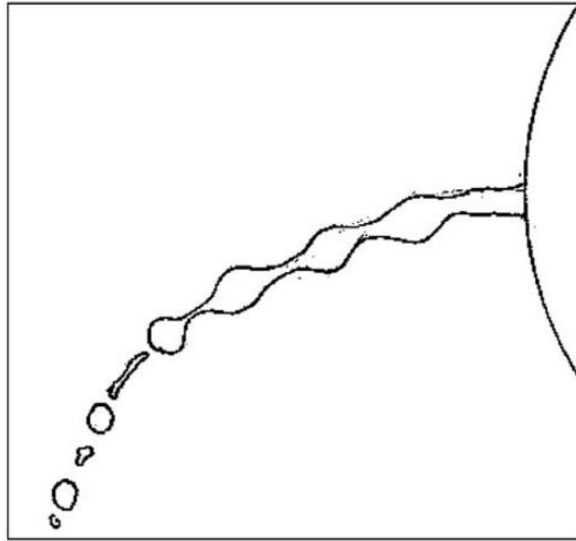
(a) Sketch showing Mode 2 break-up
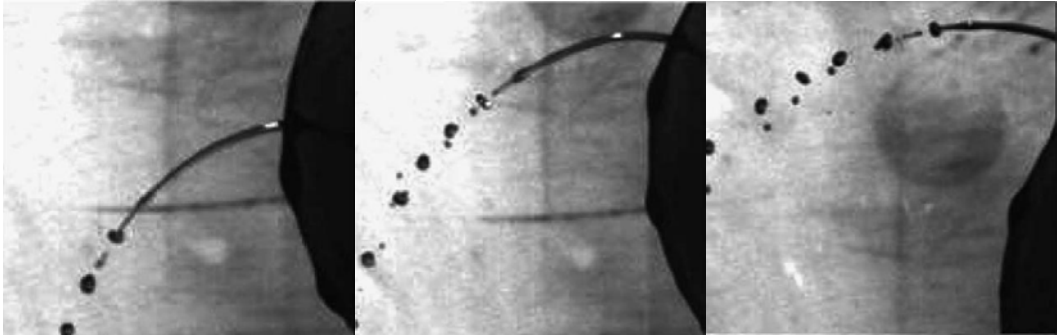
(b) Photograph showing the evolution of Mode 2 break-up

Figure 4.4: Mode 2 break-up

the high velocity jets is increased. The viscous forces dampen the capillary instabilities, and this increased stability causes break-up to occur much further from the orifice. The wavelengths of the disturbances are much longer (around 2-5 times that of the jet diameter) and we see the jet breaking up in several places simultaneously. In between the main droplets we see the formation of *ligaments*, long thin filaments of fluid which subsequently contract and break-up into multiple satellite droplets.

We show Mode 4 break-up in Figure 4.6. M4 break-up is highly nonlinear, occurring for very viscous fluids leaving the orifice at low exit velocities. A swell forms at the end of the jet, and the inertia caused by this swell alters the jet trajectory. Upon
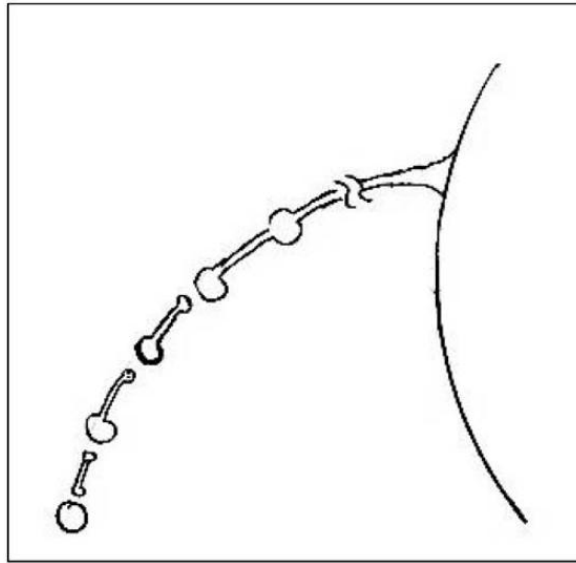
(a) Sketch showing Mode 3 break-up
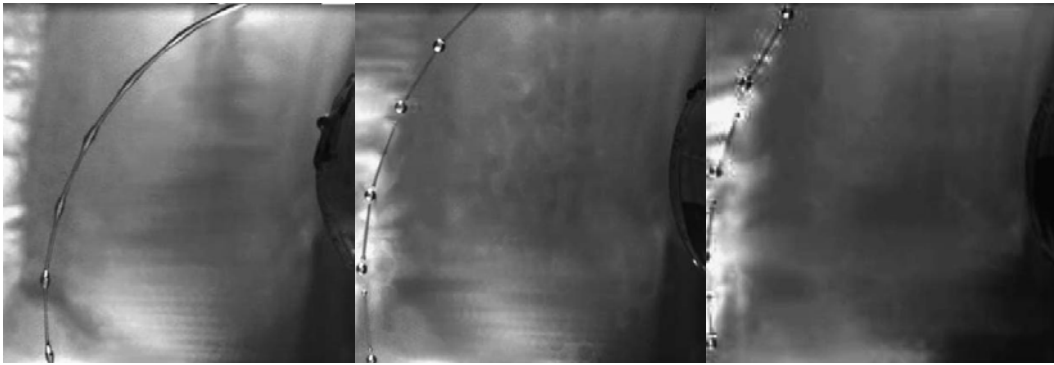
(b) Photograph showing the evolution of Mode 3 break-up

Figure 4.5: Mode 3 break-up

break-up, the jet shatters causing the jet to recoil, and a disturbance propagates back down the jet towards the orifice breaking the upper part of the jet into multiple satellite droplets. A disturbance convecting back upstream is a unique feature of M4 break-up. It is believed there is an element of absolute instability in M4 break-up, and this is currently being investigated in the thesis work of Rachan Bassi.

Wong *et al.* [49] used these mode classifications to develop flow maps showing regions where particular types of behaviour typically occur. One such flow map is shown in Figure 4.7. Four distinct regions showing the modes of jet break-up are
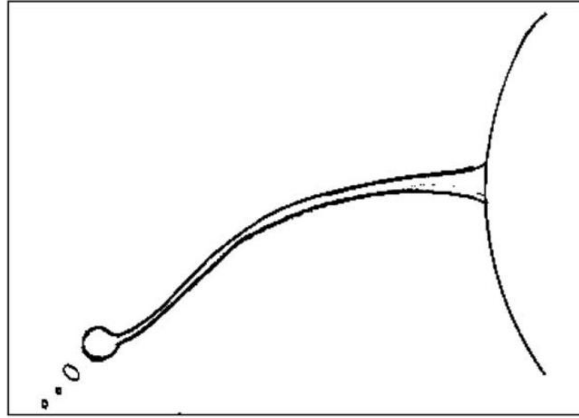
(a) Sketch showing Mode 4 break-up
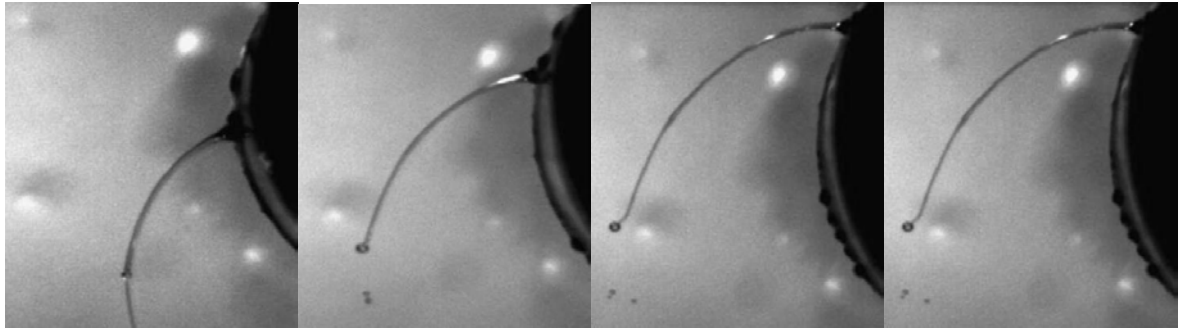
(b) Photograph showing the evolution of Mode 4 break-up

Figure 4.6: Mode 4 break-up

identified, and also a region where the exit velocity is too small to generate a jet. This map illustrates the aforementioned relationships between exit velocity and viscosity, through We and Oh respectively, with the movement through the mode boundaries.

The laboratory scale rig was not only used to identify modes of jet break-up, Wong *et al.* [49] also presented relationships between the various non-dimensional parameters and the length of the jet before break-up and generated several drop size distributions. Three such distributions are presented as examples in Figure 4.8, where the vertical axis measures a frequency $f(n)$ which shows a ratio of the number of drops of diameter n to the total number of drops produced, and the horizontal axis gives the size in a dimensionless quantity. In order to generate reliable results a sample of 200 drops were used, and 35 jets were used to calculate average break-up length.

46
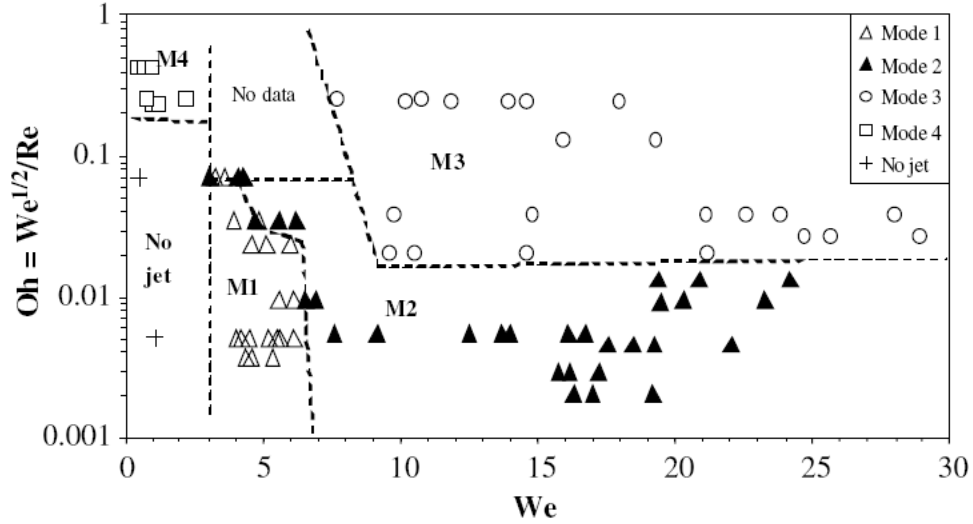
Figure 4.7: Figure showing a map of Ohnesorge number against Weber number displaying regions of break-up regimes.

Figure 4.8(a) shows a typical distribution for M1 break-up. We see a *unimodal* distribution of drop sizes, with a singular maximum where the highest percentage of drop sizes are generated. Not many smaller satellite drops are produced. Figure 4.8(b) displays a distribution for M2 break-up, which is a *bimodal* distribution. There are two local maxima, one with a large number of main droplets, and another with a large number of satellite droplets. Figure 4.8(c) shows the distribution for M3 break-up. Again the distribution is bimodal, but there is a greater quantity of satellite droplets. Further trends and drop size distributions for Mode 4 behaviour and varying orifice sizes are given in Wong *et al.* [49]. We only present typical distributions for Modes 1-3 here.

Though Wong *et al.* [49] were able to identify the four modes on the laboratory scale rig, and identify trends for break-up lengths and drop size distributions, the parameter ranges replicating an industrial problem could not be reached [33]. A larger scale rig was built to obtain dimensionless parameters closer to the industrial regime.

(a) Mode 1 break-up

(b) Mode 2 break-up

(c) Mode 3 break-up
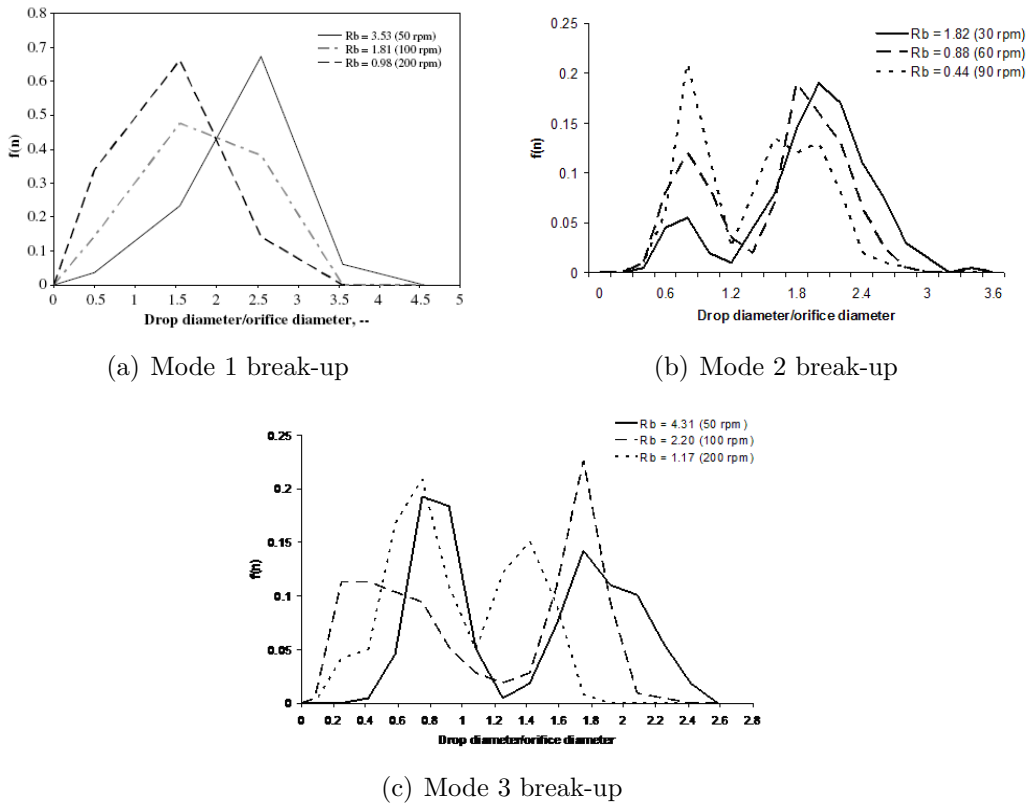
Figure 4.8: Graphs showing drop size distributions for three modes of break-up

4.3 Pilot Scale Experiments at Birmingham

We detail the work of Partridge [33] who obtained results on the larger pilot scale rig in conditions closer to industrial situation, in addition to comparing the results to the smaller laboratory scale rig. These results are summarised in Partridge *et al.* [34]. The rig is situated in the Chemical Engineering Department at the University of Birmingham. The rotating cylinder is 0.285 m in diameter. Orifice diameters were 0.001 m and 0.003 m. The setup can be seen in Figure 4.9. The same mixes of water and glycerol were used as for the laboratory scale rig. The parameter ranges are given in Table 4.2.

Unlike the laboratory scale rig, there was no pump to maintain the same amount of fluid in the can. Instead, after each run of the experiment the fluid was topped back
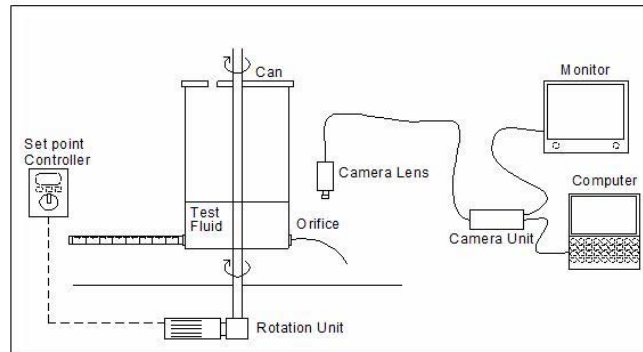
(a) Diagrammatic representation
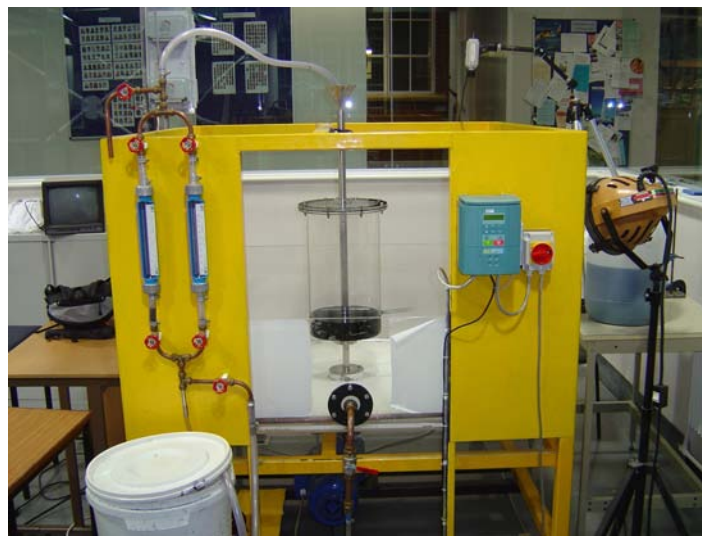
(b) Photographic representation

Figure 4.9: The experimental pilot scale setup

up to the correct aspect ratio. The fall in fluid height in the can dH could be used to calculate the jet exit velocity using the simple formula

$$U = \frac{s_0^2 dH}{a^2 t}$$

where t is the duration of the experiment in seconds. This exit velocity is assumed to be constant as $dH << H$. In order to obtain clear experimental images, Nigrosine (BDH

Liquid dynamic viscosity, μ (Pa s)	0.001-0.081
Liquid density, ρ (kg m^{-3})	1000-1215
Liquid surface tension, σ (N m^{-1})	0.047-0.072
Orifice radius, a (m)	0.0005-0.0015
Liquid aspect ratio, (H/D)	1/4 - 1/2
Can rotation rate, Ω (rad s^{-1})	3.14-31.4
Jet Exit Velocity, U (m s^{-1})	0.1-6.3
Can radius s_0 (m)	0.1425
$Rb = U/\Omega s_0$	0.13 - 7
$Re = \rho U a/\mu$	2 - 4200
$We = \rho U^2 a/\sigma s_0$	0.36 - 170.2
$Oh = \mu/\sqrt{\sigma a \rho}$	0.0031 - 0.3091

Table 4.2: Table summarizing the experimental parameters used for the pilot scheme.

Chemical Suppliers) dye was stirred into the mixture and allowed to set[2]. The same high speed camera (Photron Fastcam Super 10k) was used to generate the images, and a ruler attached to the side of the can to allow for calibration when calculating jet break-up length from the images obtained from the camera.

Partridge [33] investigated a range of parameters in similar ranges to those used by Wong *et al.* [49] to see a comparison between the two rigs, investigating whether the fluid has the same break-up mode classification for particular parameter ranges. This is shown in Figure 4.10.

There are distinct regions where the two rigs have good agreement for M2 and M3 break-up, though there is a parameter region where both M2 break-up and M3 break-up is encountered. This overlap is partially due to the subjective nature in classifying the mode of jet break-up, and so classifying break-up into the laboratory scale regime was difficult. A new type of break-up was identified, called Mode 2/3 break-up and examples are shown in Figure 4.11(a). It is a short wavelength disturbance with one satellite droplet forming in between main droplets, features identified as Mode 2 break-

---

[2]This has minimal effect on the jet rheology. Viscosity, density and surface tension were calculated before and after the dye was added with little change noted.
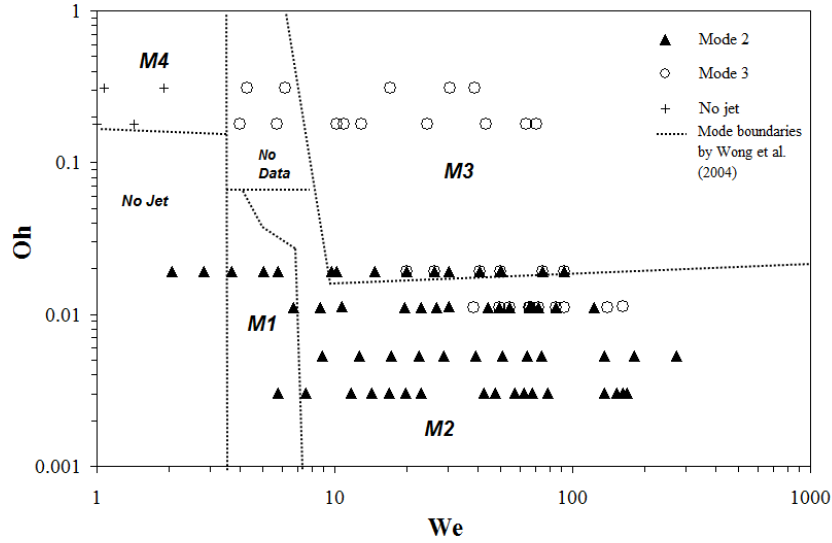
Figure 4.10: Figure showing a map of Ohnesorge number against Weber number displaying regions of break-up regimes found on the pilot scale rig plotted over the boundaries derived by Wong *et al.* [49].

up. There are also multiple break-up points, as typified by Mode 3 behaviour, though there is no ligament formation.

Partridge [33] also highlights another interesting feature, the presence of anti-symmetric (or kink) disturbances. This is shown in Figure 4.11(b). These were also not seen on the laboratory scale rig where only axisymmetric (or varicose) disturbances were seen for Modes 1-3. Partridge [33] suggested these features could be because of air resistance or greater mechanical vibrations at higher rotation rates. We also see in Figure 4.10 no areas of M1 behaviour on the pilot scale rig.

4.4   Present Day and Future Work

In Uddin [44], nonlinear models were presented detailing non-Newtonian jet break-up, both for shear thinning and shear thickening liquids. Victoria Hawkins is a research

(a) Multiple break-up points   (b) Non-axisymmetric disturbances
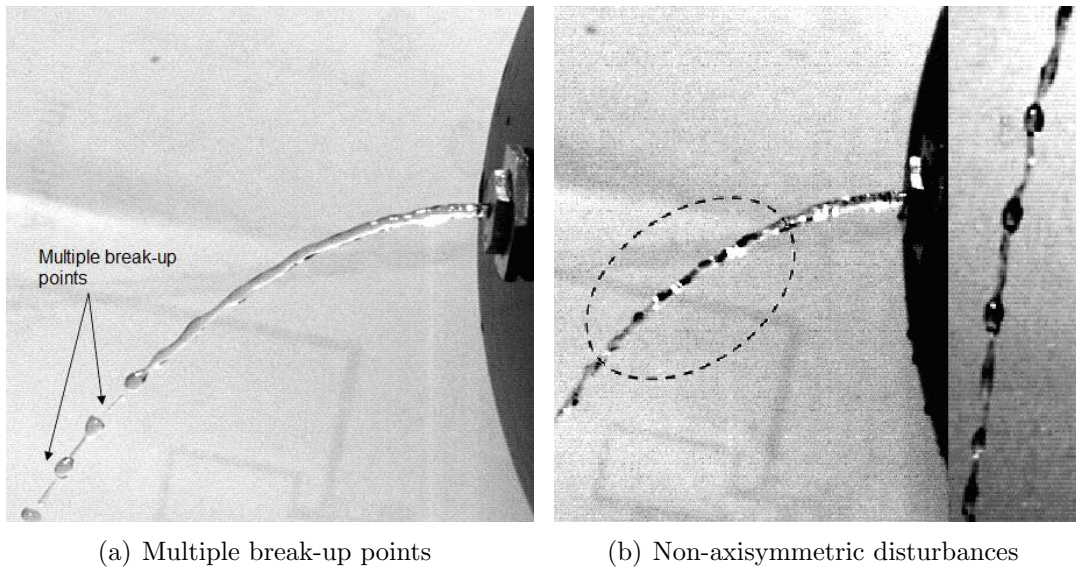
Figure 4.11: Figure showing features of M2/3 break-up, identified by Partridge [33].

student in the Chemical Engineering Department at Birmingham and much of her experimental research investigates non-Newtonian jets and jets under the influence of surfactants.

4.4.1 Non-Newtonian Jets

The earlier experiments by Wong and Partridge involved the use of Newtonian fluids, namely fluids which continue to flow in the same manner despite external forces or stresses acting upon it, such as water (or glycerol) and air. Mathematically, the primary factor which identifies a Newtonian fluid is the linear relationship between the stress and rate of strain, and thus as a result a constant viscosity. Many fluids industrially, biologically and chemically do not display this relationship and these fluids are entitled *non-Newtonian.*

For non-Newtonian fluids, the viscosity changes as external stresses are applied to the fluid. As such rotational forces will have a major effect on a non-Newtonian fluid's rheology, and the corresponding liquid jet could show some very interesting
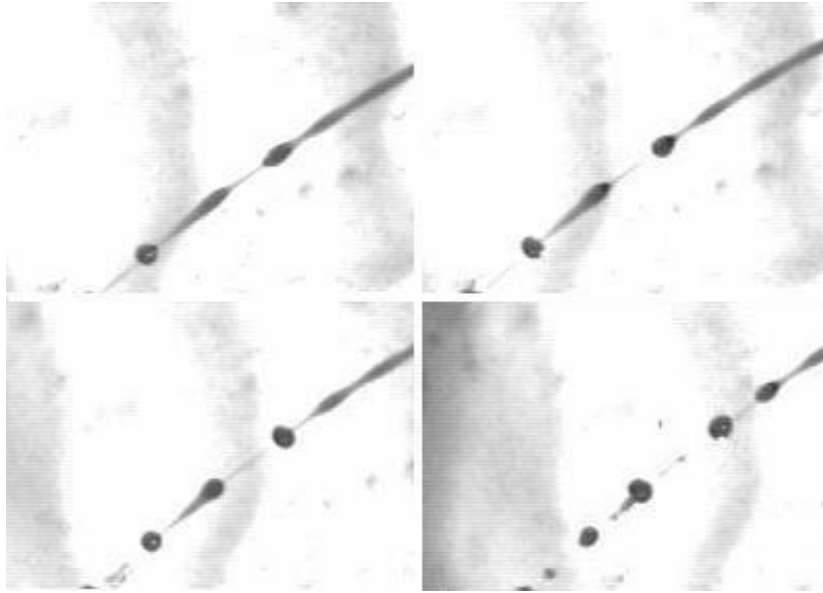
Figure 4.12: Figure showing typical pendant drop formation.

behaviour. There are two types of non-Newtonian fluids, those displaying no elastic (or *inelastic*) properties, and those which do, *viscoelastic* fluids. We present some of Victoria Hawkins' research on experimental break-up of a non-Newtonian jet with inelastic properties using the pilot-scale rig.

There are two main types of inelastic fluids, *shear-thinning fluids* with viscosity decreasing with the rate of shear applied, and *shear-thickening fluids* with viscosity increasing with the rate of shear. The next series of results we present are for shear-thinning fluids, namely an aqueous-carboxymethylcellulose (CMC) mixtures of three different concentrations, 0.1% CMC, 0.2% CMC and 0.3% CMC.

The first distinct feature seen are *pendant* drops, which form instead of ligament in between the main drops. A 'tear-shaped' drop forms with the head forming at pinch-off. The tail contracts yielding a drop larger than the adjacent primary drops. We show this formation in Figure 4.12.

Further features are presented in Figure 4.13, showing extremely long jets which

break-up at many places simultaneously. The corresponding ligaments are completely displaced from the jet centreline. Although these multiple break-up points and non-axisymmetric disturbances were seen for a viscous fluid, their effect is far more noticeable here. For Newtonian fluids, this non-axisymmetry was attributed to wind resistance, whereas here it would suggest that this bending is also a function of the fluid rheology.

(a) Multiple break-up points   (b) Non-axisymmetric disturbances
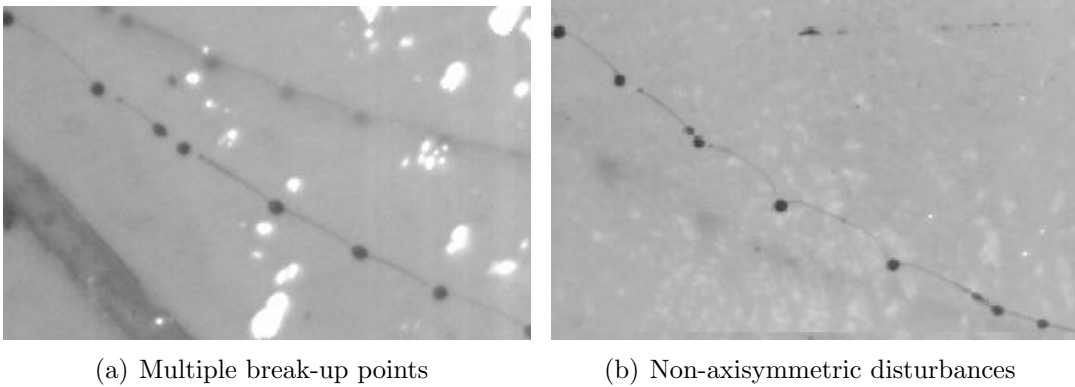
Figure 4.13: Figure showing Non-Newtonian jet break-up.

Presented in Figure 4.14 is a flow map illustrating the regions where pendant drop formation and the non-axisymmetric disturbances are typically observed. It suggests that as velocity is increased the ligaments no longer form into pendant drops and start showing non-axisymmetry. Shear-thickening fluids are the subject of current research with no results available at this time.

4.4.2 Surfactants

Also present in Uddin [44] is a mathematical model describing the influence of surfactants on a jet. A surfactant is a substance which is added to a fluid and will change the surface tension, without changing other properties of the fluid too drastically. With liquid jet break-up, the instabilities are driven by capillary forces, so a substance which affects surface tension will naturally have an effect on these in-
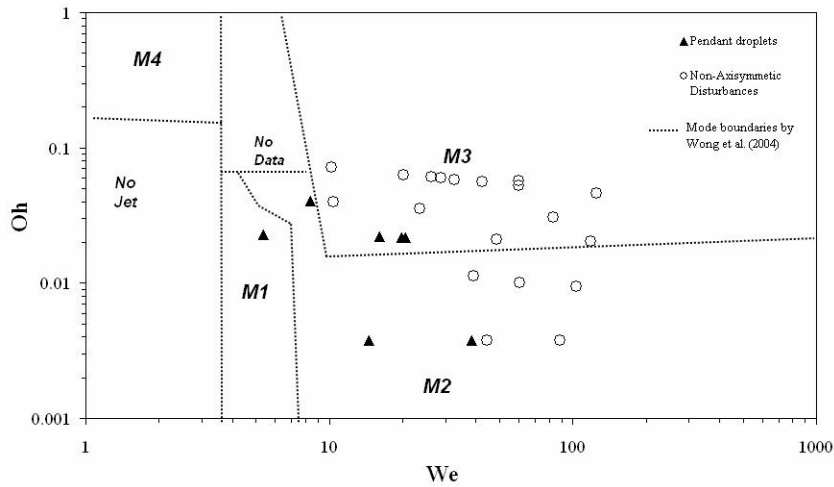
Figure 4.14: Figure showing a map of Ohnesorge number against Weber number displaying regions of break-up regimes for a non-Newtonian rig plotted over the boundaries derived by Wong *et al.* [49].

stabilities. Victoria Hawkins added a soluble surfactant to the fluid, sodium dodecyl sulfate (SDS) in 0.1%, 0.2% and 0.3% of the total fluid, and examined the effect on the resulting jet.

Figure 4.15 shows the effect of 0.1% surfactant concentration compared to a jet with no surfactant present, for 4 different rotation rates. The surfactant has a greater effect on the jet trajectory for higher rotation rates. Wallwork [45] discovered that jets with a higher surface tension are more curved. This surfactant lowers the surface tension and this explains why the jet has less curvature. More 'blobby' behaviour with surfactants is observed, with neither distinct primary or secondary drop formation at the time of break-up. Also, a longer break-up length is noted as the surface tension driven instabilities have been reduced. We note this has changed for 180 rpm, break-up is shorter for the surfactant laden jet. With decreased surface tension, there is a smaller force holding the jet together and so increased mechanical instabilities caused

by higher rotation rates could have a larger effect.

4.5   Summary

In this chapter we have documented current work on the experimental research into the break-up of liquid jets. There are many interesting aspects left to be examined however. The effect of shear-thickening liquids is yet to be resolved, and perhaps viscoelastic fluids could also be examined. Following on from research presented in Chapter 7 in this thesis, a device which generates mechanical vibrations in the nozzle has been developed. This will be discussed in greater detail in Chapter 11.
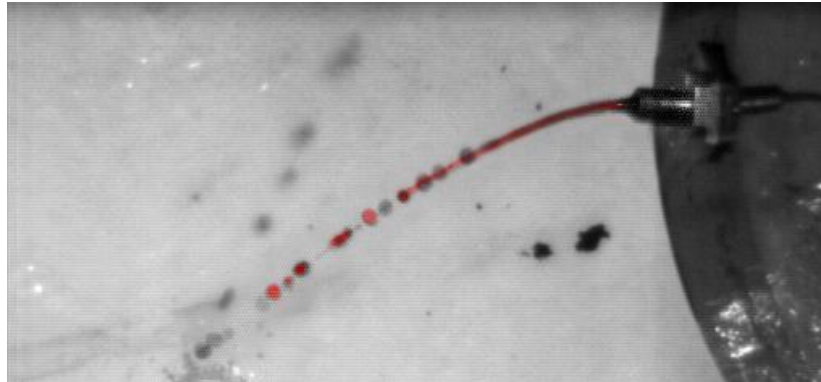
(a) 30 rpm
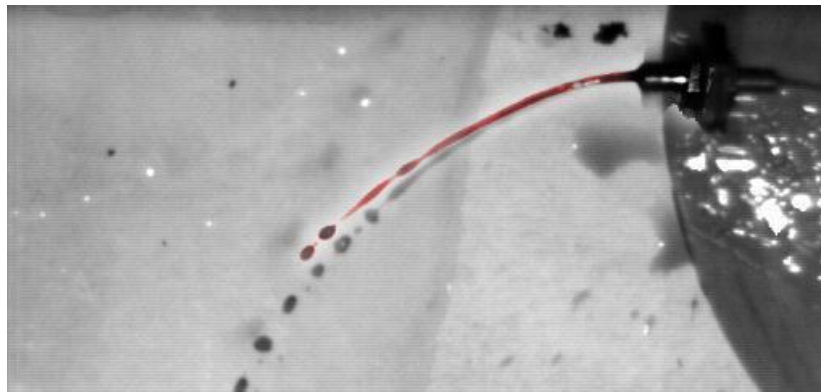
(b) 60 rpm
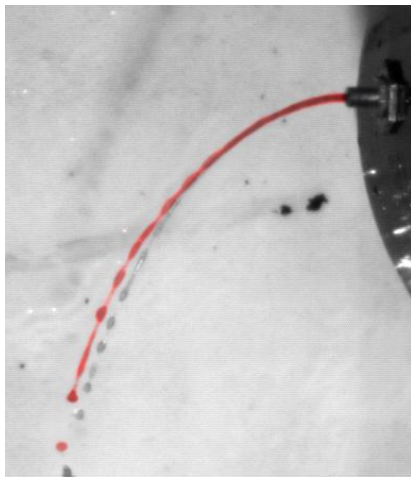
(c) 120 rpm
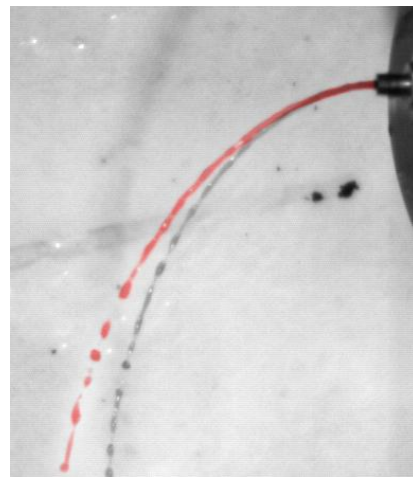
(d) 180 rpm

Figure 4.15: Figure showing a jet of 0.1% SDS(red) compared to a jet with no surfactant.

Chapter 5

Mode Classification of Numerical Jet Simulations

In Chapter 3 we discussed theoretical research developed to model a curved viscous jet. We presented discussions on both the linear and nonlinear theories. However, we did not analyzed the differences (if any) between different models. We intend to perform here a more in-depth comparison between the models in parameter ranges we would typically see in experiments. This chapter extends previous work reviewed in Chapter 3.

5.1   Linear and Nonlinear Theories

As the break-up of the jet is a nonlinear phenomenon, only the nonlinear theory predicts the impact of satellite droplets. Therefore, we shall focus our comparison around the prediction of main droplet sizes between linear and nonlinear theories. Linear theory states that we can predict the size of the main droplet by integrating over a wavelength about the point of break-up. Now the dimensional wavelength of the disturbance is given by $\lambda_w = 2\pi a/k^*(s)$ where $k^*(s)$ is the most unstable wavenumber

given by (3.4). Therefore, it is necessary to calculate the most unstable wavenumber at the point of break-up, $k^*(s_b)$, where s_b is the length of break-up. Nonlinear theory is used to calculate s_b.

As outlined in Chapter 3, the steady state equations (3.9) are solved, yielding the initial conditions for the temporal PDEs (3.11) subject to the boundary condition

$$A(s = 0, t) = 1, \qquad u(s = 0, t) = 1 + \delta \sin\left(\frac{\kappa t}{\epsilon}\right),$$

where δ is the amplitude of the disturbance and $\kappa = k^*(s = 0)$ is the most unstable wavenumber at the orifice given by

$$k^* = \frac{1}{2^{1/4}\sqrt{\sqrt{2} + 3Oh}}.$$

This yields values for the main drop radius, satellite drop radius and break-up length s_b. Using values of $R_0(s_b)$ and $u_0(s_b)$, obtained from (3.9), the linear dispersion relation (3.4) is solved for k computationally, adopting the view of a spatial instability with $\lambda = -i\omega$. An example is shown in Figure 5.1. The curve displays the roots for which k_i is most negative, since (3.4) has more than one solution.

The most unstable wavenumber is the real part of the wavenumber k_r corresponding to the most negative growth rate k_i[1]. In this case $k^*(s_b) = k_r = 0.765$, and hence integrate over the wavelength $\lambda_w = 2\pi a/k^*(s_b)$ in the same way as for nonlinear break-up (using (3.15) and (3.16)). We obtain a drop radius of 1.7205 in non-dimensional units in this case. The nonlinear simulation gives a main drop radius of 1.8246 in non-dimensional units at the same parameter values, so differs only slightly from the linear prediction.

---

[1]With a complex wavenumber $k = k_r + ik_i$ waves are of the form $e^{-k_i\bar{s}}e^{i(k_r\bar{s} + \lambda\bar{t})}$, and so we need the growth rate $k_i < 0$ yields an increase in amplitude as $\bar{s}$ increases from 0.
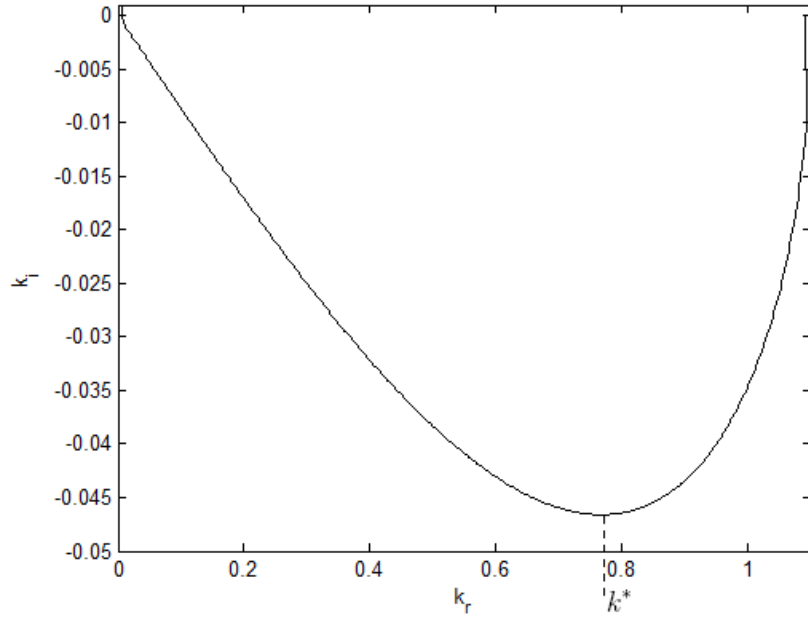
Figure 5.1: Dispersion relation solved for k for $0 < \omega < 2$. $R_0(s_b) = 1.2022$, $u_0(s_b) = 0.912$, $We = 50$, $Rb = 2$ and $Oh = 0.001$.

We compare the two models for a variety of parameters, investigating the degree to which the two results differ. The nonlinear results show similar trends to those presented in Părău *et al.* [35, 36] whilst linear theory results are equivalent to those in Wallwork *et al* [46] and Decent *et al.* [12]. However, comparisons between these theories has, as of yet, not been performed in detail. Figure 5.2 shows the differences in sizes between the two theories for main drop radii.

Figure 5.2(a) shows a comparison between the nonlinear and linear theory as the Weber number is increased for varying Rossby numbers. It can be seen that nonlinear theory predicts very little variation in size as the Weber number changes, whilst linear theory predicts smaller droplets for larger Weber numbers. As the Rossby number is decreased (corresponding to an increasing rotation rate) there is a decrease in drop sizes for both theories, as expected. However, for smaller Rossby number the discrepancies between the two theories becomes more noticeable. In the case of higher Weber

numbers and lower Rossby number the nonlinear theory can predict a droplet over twice the size of the linear theory.

Similar results are noted for other parameters. Figure 5.2(b) shows the impact of the Ohnesorge number on the two theories. Increasing the Ohnesorge number (increasing viscosity) causes the difference between the two theories to become more noticeable at higher Weber numbers. Perhaps most noticeably, using nonlinear theory results in increasing main drop sizes with increasing Ohnesorge number, whilst linear theory predicts a decreasing main droplets for a increasing Ohnesorge number. Figure 5.3(a) shows that the theories differ to their greatest extent for larger Ohnesorge and smaller Rossby number, in other words in the case of a more viscous fluid at a higher rotation rate.

Close to pinch-off the nonlinear wavepacket could 'bunch-up' as the jet thins. This nonlinear wave supposition could increase the radius of the droplet. This effect would be more noticeable for a thinner jet, which would explain why this occurs for high viscosities at high rotation rates. Linear theory however, does not account for the nonlinearity of break-up, so this effect would not be seen. Figure 5.3(b) shows that the difference between the two theories has a greater effect for smaller δ, i.e. if the initial imposed amplitude of the disturbance is smaller and hence the jet is longer.

5.2 Classifying Jet break-up

We must clarify our typical mode behaviour of a theoretical jet, and investigate whether numerical simulations can generate the modes identified by Wong *et al.* [49]. We cannot simulate Mode 4 break-up as this would probably involve absolute instabilities; this is studied in the PhD thesis of Rachan Bassi. We vary the parameters to generate different modes and classify these on a theoretical scale, fully describing their

behaviour.

Figure 5.4 shows how changing δ has an effect on the nonlinear dynamics of the jet. When δ is smaller the jet has a larger break-up length. This is intuitive, since if we perturb the initial disturbance by a greater amount then it needs less time to grow to the amplitude necessary to generate break-up. We can see from Figures 5.4 that qualitatively, jet break-up is not affected by changes in δ. However, if the main drop does not form clearly after break-up, such as in Figures 5.4, we investigate the main drop before the satellite drop or ligament.

Figures 5.5 and 5.6 show numerical simulations using parameters from the experimental regime, illustrating three modes of theoretical jet break-up with similar characteristics to the experimental modes M1-M3. Identifying the mode of break-up from the simulations can be relatively straight forward, such as in Figure 5.5(a) and (b); the break-up is distinctively M1 and M2 behaviour respectively where clear formation of the primary droplet occurs, and in the case of M2 break-up clear formation of the satellite droplet on the other side of the break-up point. However, as the transition period between M2 and M3 break-up is approached, classifying the mode of break-up becomes more difficult and largely subjective. In cases where the simulation does not show a secondary pinch-off such as in Figure 5.6(a), or when it is unclear whether there is a ligament or a large satellite droplet, the jet is assumed to break-up under the M2/3 regime. In situations when it appears that multiple primary droplets may form, such as in Figure 5.6(b), the jet is said to undergo M3 break-up, where a ligament forms in between two primary droplets. As the numerical model breaks down at the point of break-up, further ligament behaviour cannot be ascertained [35]. As such, for M2/3 and M3 break-up, the frequency and size of any satellite droplets cannot be obtained and drop size analysis is limited to examining primary drops.

5.3 Summary

In this chapter we have compared primary drop sizes generated by linear and nonlinear theories. The models compare well for jets with low exit velocity and low viscosity. As velocity is increased (decreased Rb) or viscosity increases (increasing Oh), a more noticeable difference occurs between drop sizes.

The nonlinear model was used to simulate jet break-up, and the modes of break-up were identified through the similarity in their behaviour to experimental modes. We identified that satellite droplets can not be generated from a ligament. In the next chapter we compare drop sizes produced from these theories to experimental data.
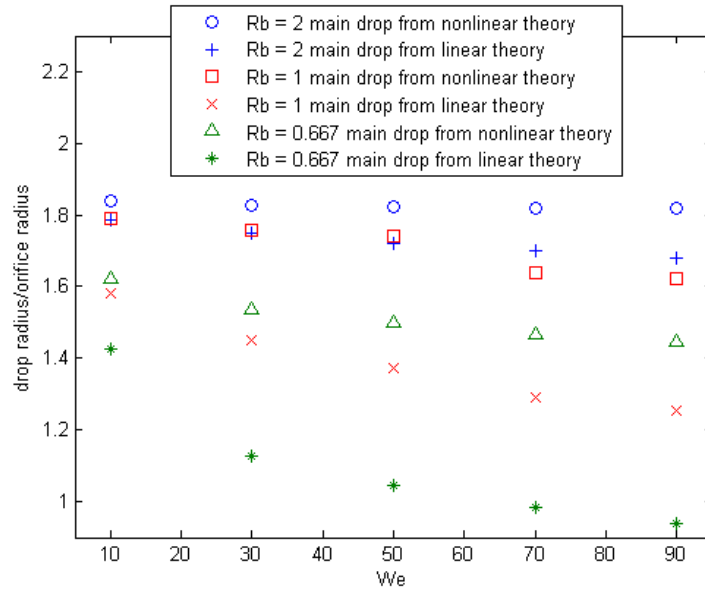
(a) Varying Weber numbers for different Rossby numbers, $Oh = 0.001$, $\delta = 0.01$
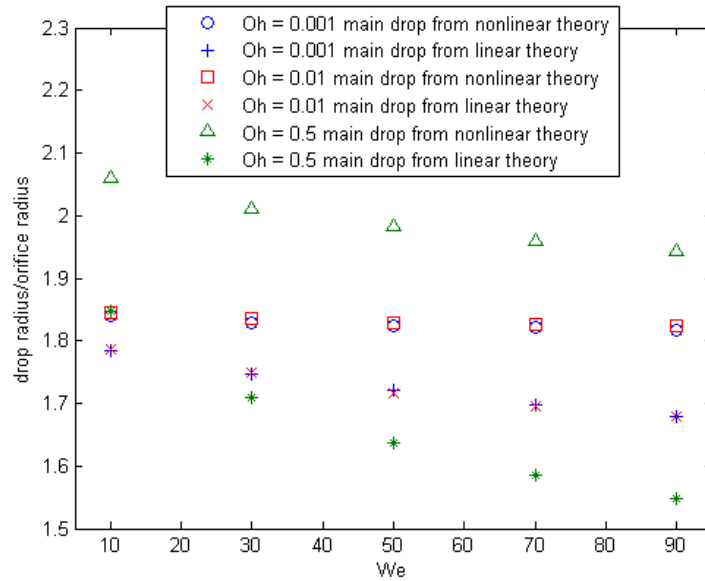
(b) Varying Weber numbers for different Ohnesorge numbers, $Rb = 2$, $\delta = 0.01$

Figure 5.2: Graph showing a comparison between main drop radii predictions using nonlinear theory and linear theory. $\epsilon = 0.01$ and κ varies accordingly since $k = k^*(s = 0)$ which is a function of Oh.
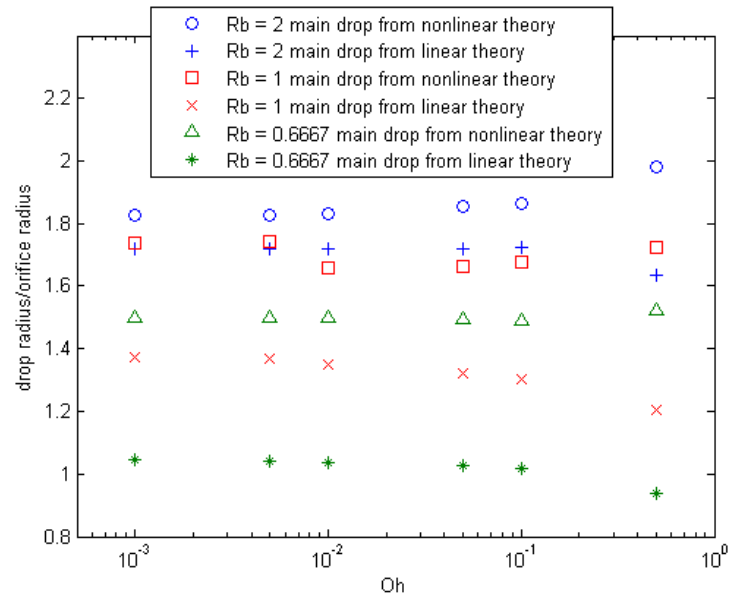
(a) Varying Ohnesorge numbers for different Rossby numbers, $We = 50$ and $\delta = 0.01$
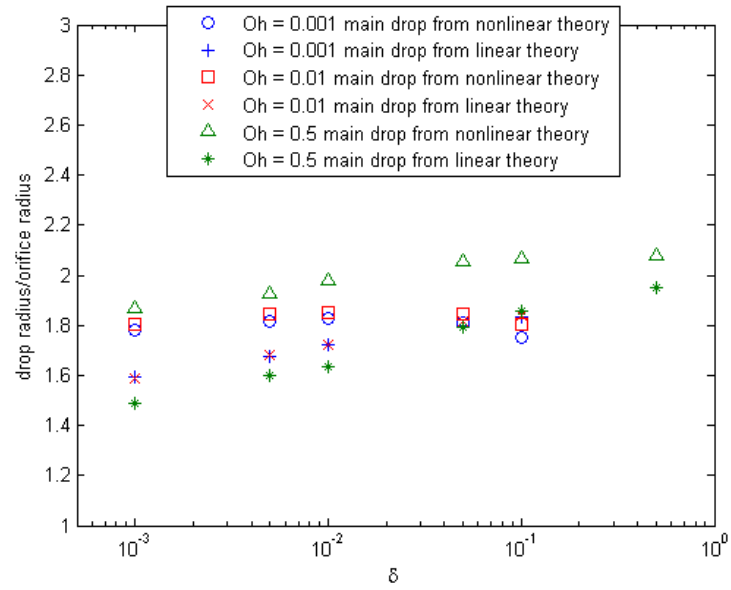
(b) Varying δ for different Ohnesorge numbers, $We = 50$ and $Rb = 2$

Figure 5.3: Graph showing a comparison between main drop radii predictions using nonlinear theory and linear theory. $\epsilon = 0.01$ and κ varies accordingly.
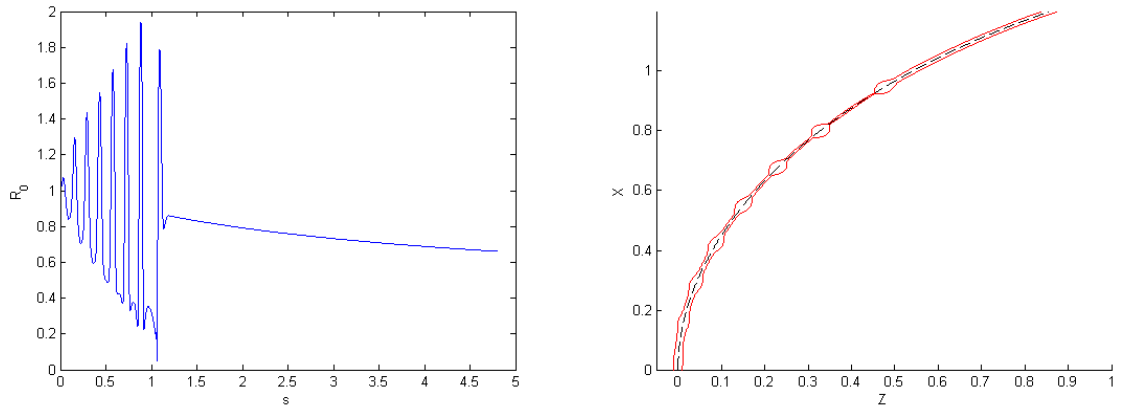
(a) $\delta = 0.1$
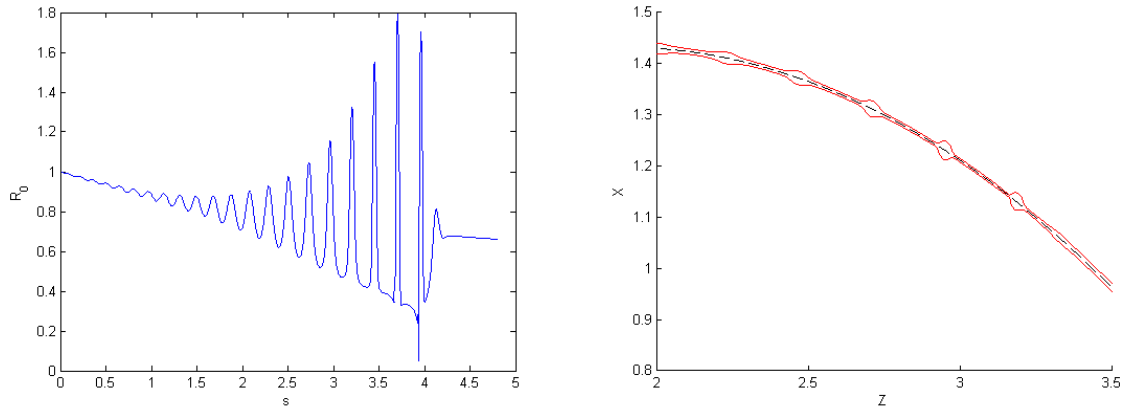
(b) $\delta = 0.001$

Figure 5.4: Nonlinear simulation showing the effect of changing δ on a jet. $We = 50$, $Rb = 2$, $Oh = 0.5$, $\kappa = 0.4926$ and $\epsilon = 0.01$. In (d) the orifice is at $X = Z = 0$, off the edge of the figure.

66
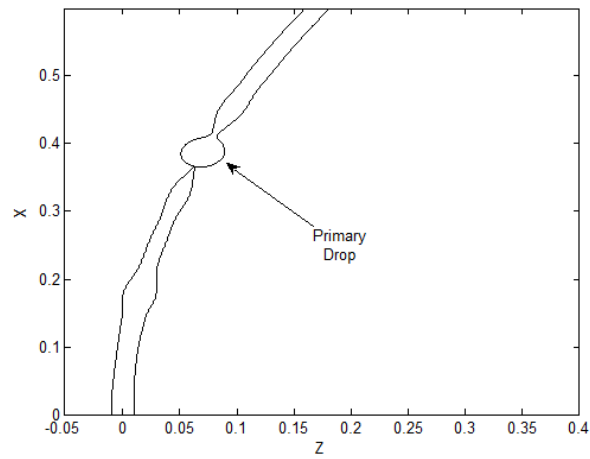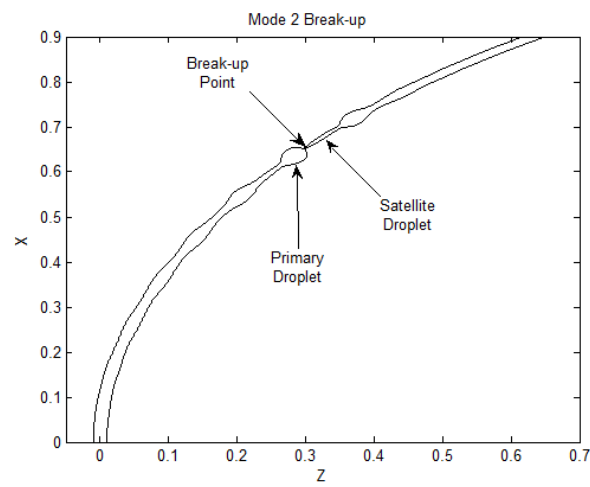
(a) Mode 1

(b) Mode 2

Figure 5.5: Theoretical Mode Classification

67
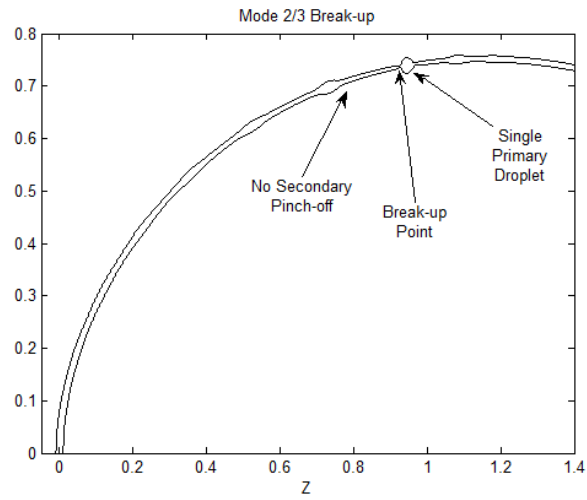
(a) Mode 2/3
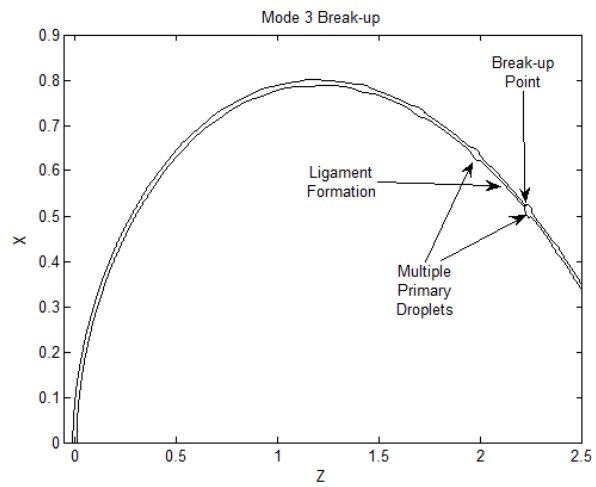
(b) Mode 3

Figure 5.6: Theoretical Mode Classification

68

Chapter 6

Comparison between Theory and Experiments

In the previous chapter we compared the linear model and nonlinear model for a curved viscous jet, focussing on main drop sizes. We noticed differences in the size of droplets produced by those models when we have a more viscous fluid at higher rotation rates, with the nonlinear model predicting a drop over twice the size of the linear model. These differences and their implications can only be fully discussed once a detailed comparison with experimental data had been performed.

We shall compare the theory with the experiments in this chapter in order to truly appreciate the uses and limitations of the mathematical model. We wish to see if the numerical simulations exhibit the same behaviour and generate droplets of the same size identified on the experimental stage.

6.1 Comparison of Theoretical Mode Classifications with Experimental Data

6.1.1 Parameter Maps

In Chapter 4, we discussed the use of flow maps to characterize jet break-up in given parameter ranges. We wish to see if the same thing can be done on a theoretical scale. Parameter maps were used to illustrate the relationship between viscosity and jet velocity in describing mode type. As the surface tension changes only slightly between different liquids in the experiments, necessary experimental changes in Weber number came through changes in the velocity of the jet, and so to generate this change in inertia we must change the rotation rate of the can, thus impacting upon the Rossby number in experimental runs. This illustrates an inter-dependence of the non-dimensional parameters within the problem when carrying out experimental parameter searches.

The nonlinear model is used to predict the mode boundaries of Partridge *et al.* [34] and the results are presented in Figure 6.1. Each simulation point uses values of dimensionless parameters obtained from the experiments. The hollow symbols denote theoretical mode break-up which matches the experimental modes of break-up, whilst the solid symbols indicate a different mode. In this analysis, δ was kept as constant due to the large number of break-up points, hence not optimised to match the break-up length. This does not affect the nature of break-up (as shown by Figure 5.4). All discrepancies between modes occur at the same viscosity ($\mu = 0.00418$ Pa s) in the transition period between M2 and M3 break-up. Due to the subjective nature of classifying the mode of break-up (both theoretically and experimentally), comparing experimental and theoretical modes is difficult in the transition period between modes. Discrepancies in this region more typically occur at higher Weber numbers suggesting the nonlinear model is more sensitive to rotation rate.
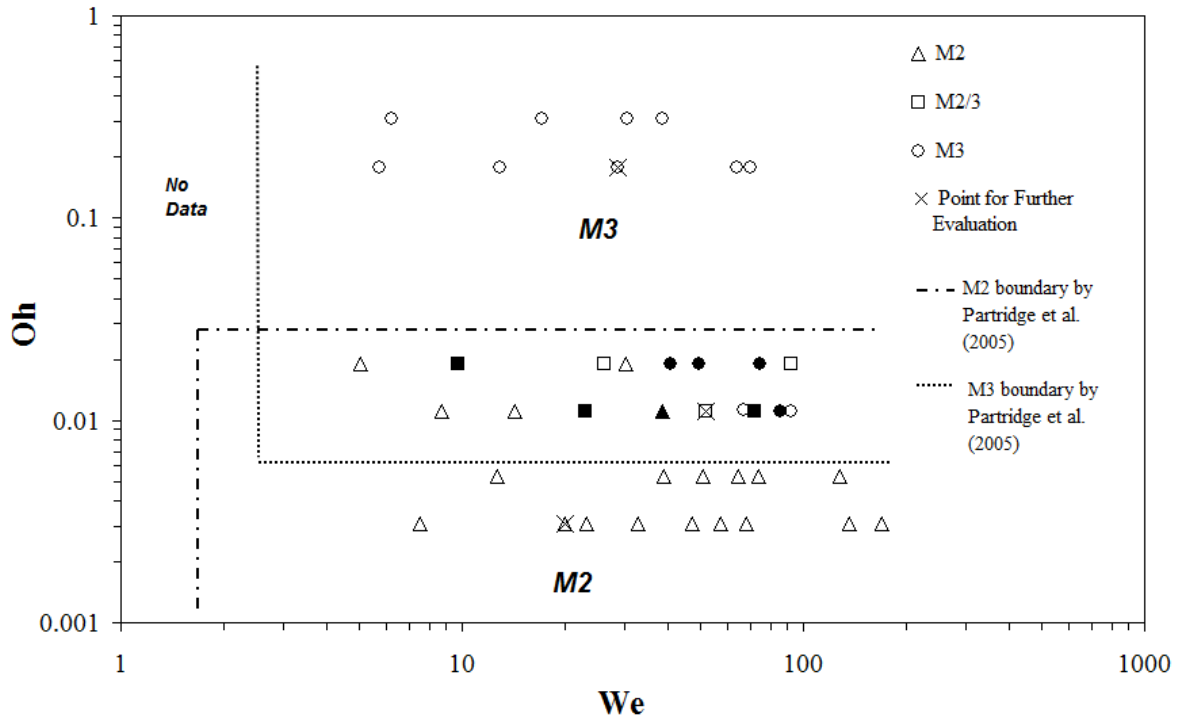
70

Figure 6.1: Map of Weber number against Ohnesorge number to illustrate a comparison between theoretical data and experimental data. Theoretical data obtained for $\delta = 0.01$, $\epsilon = 0.01$ and κ varies accordingly with Oh. Rb is taken from the experimental data obtained from the pilot scale rig. Also plotted are the mode boundaries derived by Wong *et al.* [49].

Nine data points (marked by crosses) have been chosen in Figure 6.1 for further evaluation. These data points are chosen since they exhibit M2, M2/3 and M3 break-up. The theoretical results for these data points are compared to experimental images, with δ optimised to match the break-up lengths. Drop size distributions will also be compared. These data points will be referred to as Jets 1-9. The parameters for each jet are given in Table 6.1.

Jet	Glycerol Concentration (%)	Mode	μ (Pa s)	Ω(rad/s)	ρ (kg/m^3)	σ (N/m)
1	0	2	0.001	3.14	997.5	0.0718
2	0	2	0.001	6.28	997.5	0.0718
3	0	2	0.001	12.56	997.5	0.0718
4	40	2/3	0.00418	12.56	1140	0.065
5	40	2/3	0.00418	18.84	1140	0.065
6	40	2/3	0.00418	31.4	1140	0.065
7	80	3	0.0722	12.56	1244	0.0665
8	80	3	0.0722	18.84	1244	0.0665
9	80	3	0.0722	31.4	1244	0.0665

Jet	H/D	U	We	Rb	Re	Oh	κ
1	1/2	0.9804	20.03	2.189	1462	0.003051	0.7048
2	1/2	1.153	27.75	1.289	1600	0.003051	0.7048
3	1/2	1.203	32.82	0.672	1800	0.003051	0.7048
4	1/4	0.9428	22.26	0.512	375	0.01253	0.6979
5	1/4	1.404	51.86	0.522	574	0.01253	0.6979
6	1/4	2.231	128.7	0.494	905	0.01253	0.6979
7	1/4	2.231	28.676	0.336	30	0.1785	0.6022
8	1/4	2.231	28.676	0.332	30	0.1785	0.6022
9	1/4	2.231	28.676	0.269	30	0.1785	0.6022

Table 6.1: Table detailing the jets which will undergo further evaluation. The parameters which are similar to all the jets are $a = 0.0015$ m, $s_0 = 0.1425$ m and $\epsilon = 0.01$

6.2 Comparing Jet images

We modify the amplitude δ of the unstable wave at the orifice in order to obtain a break-up length in the simulations which corresponds to that observed in experiments. We then measure the simulations' predicted drop sizes and compare to experiments for identical parameter values. We take this route since δ is difficult to measure in experiments.

Figure 6.2 shows the numerical simulation for Jet 1, and this is overlayed onto the experimental photograph in Figure 6.3. There is excellent agreement between the model and the experimental jet, in terms of the trajectory, shape and point of break-up. Figure 6.4 presents the drop size distribution obtained from the experiments, with
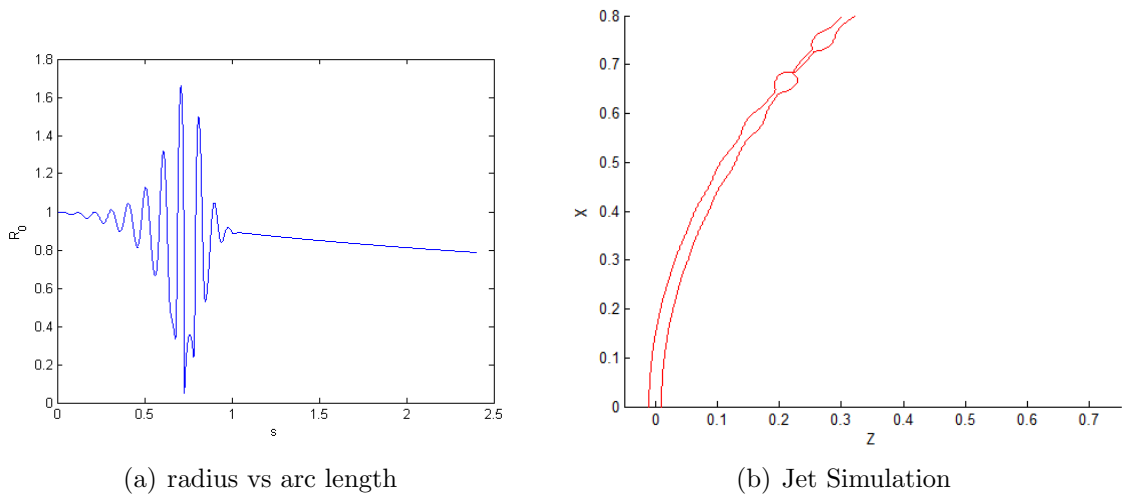
(a) radius vs arc length

(b) Jet Simulation

Figure 6.2: Theoretical results for Jet 1. $\delta = 0.00199$ and $\epsilon = 0.01$.

added predictions for theoretical drop sizes. Primary drop sizes show little discrepancy between the two theories and correspond almost exactly to the experimental mean drop size.
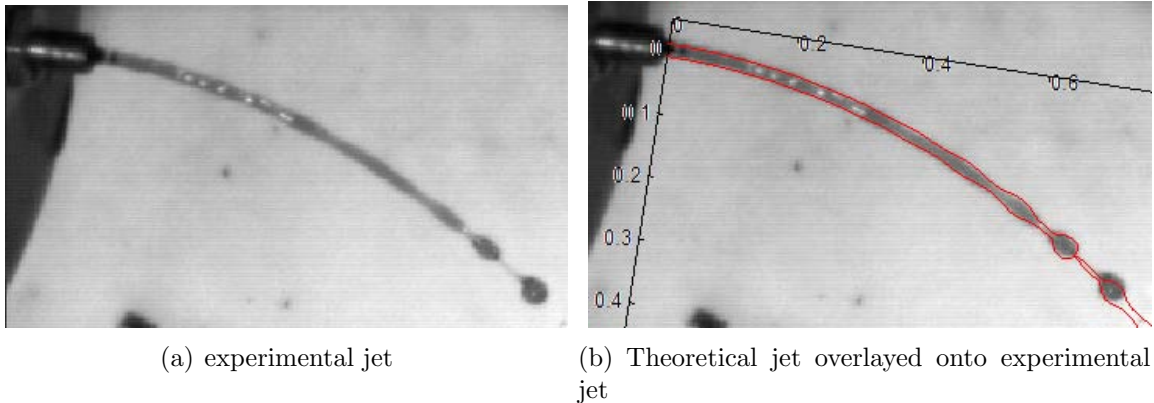

(a) experimental jet

(b) Theoretical jet overlayed onto experimental jet

Figure 6.3: Results for Jet 1. $\delta = 0.00199$ and $\epsilon = 0.01$.

Similar results can be noted for Jets 2 and 3, as shown by Figures 6.5 - 6.7 and Figures 6.8 - 6.10 respectively. The nonlinear theory does appear to provide a very good prediction of the behaviour in the Mode 2 regime. We note that as we increase the rotation rate, δ increases to match break-up lengths with the experimental images.
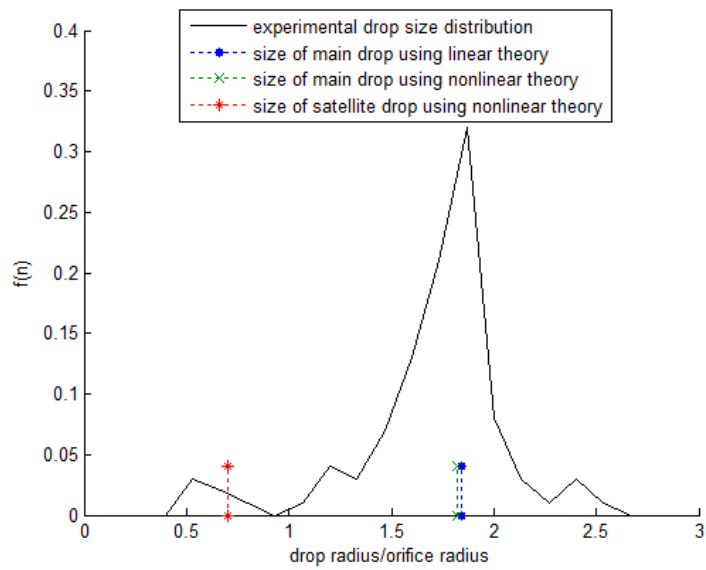
Figure 6.4: Graphs showing the experimental drop size distribution forJet 1, with theoretical drop size predictions from linear and nonlinear theory. $\delta = 0.00199$ and $\epsilon = 0.01$.
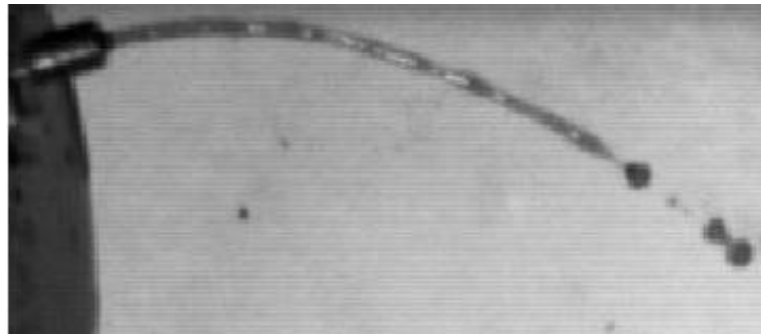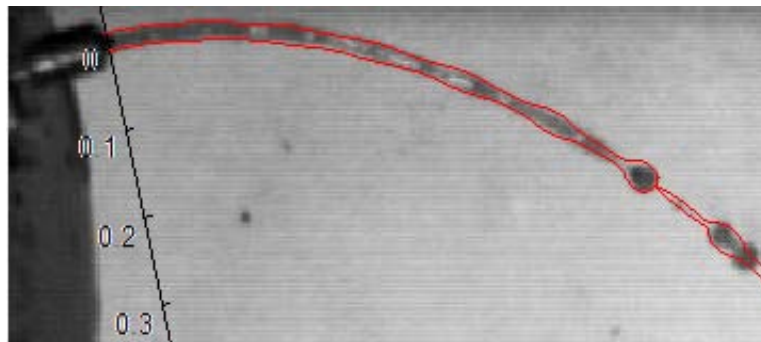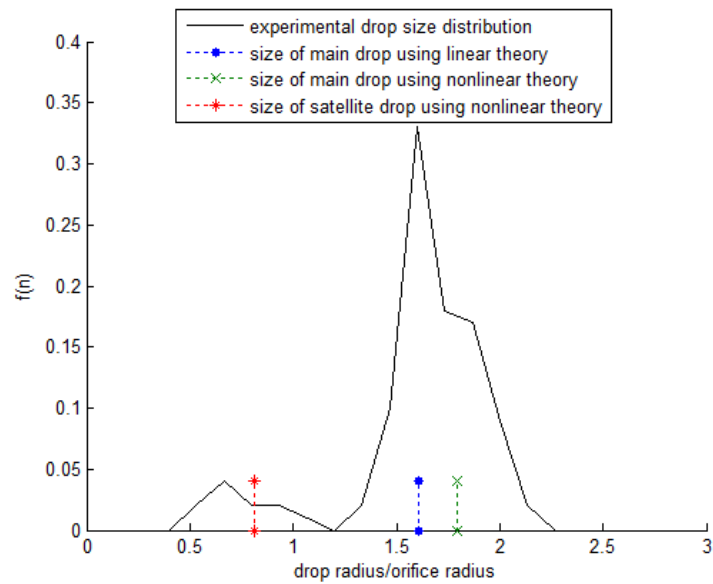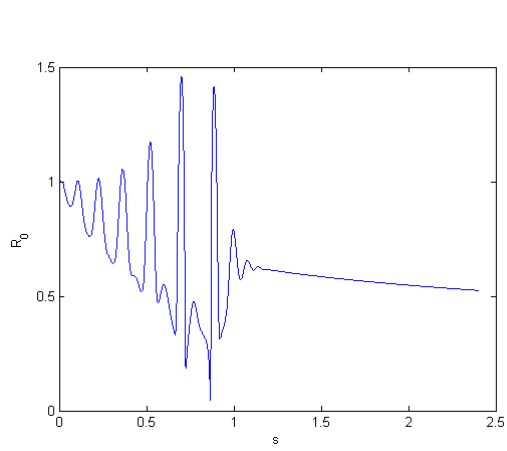

(a) radius vs arc length

(b) Jet Simulation
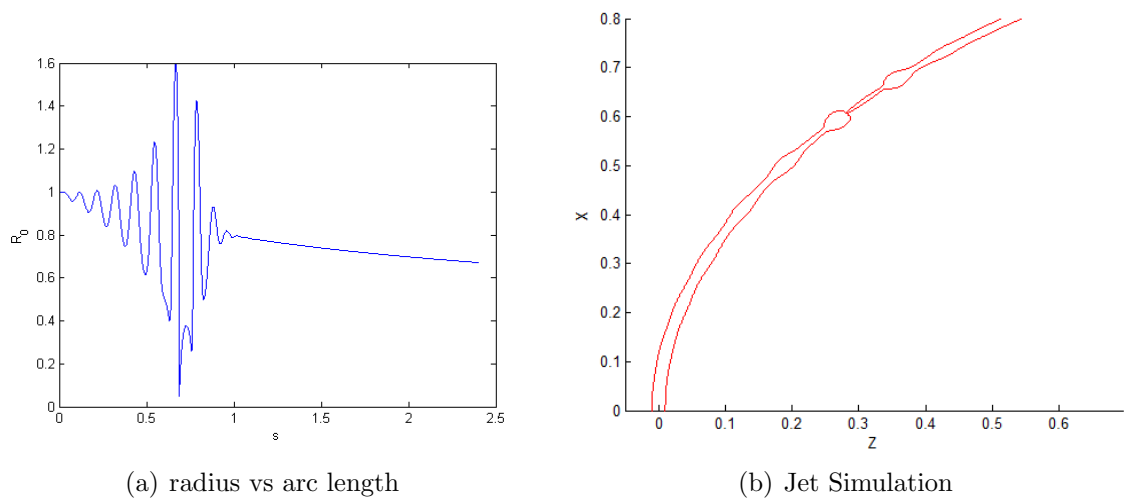
Figure 6.5: Theoretical results for Jet 2. $\delta = 0.00803$ and $\epsilon = 0.01$.

(a) experimental jet

(b) Theoretical jet overlayed onto experimental jet

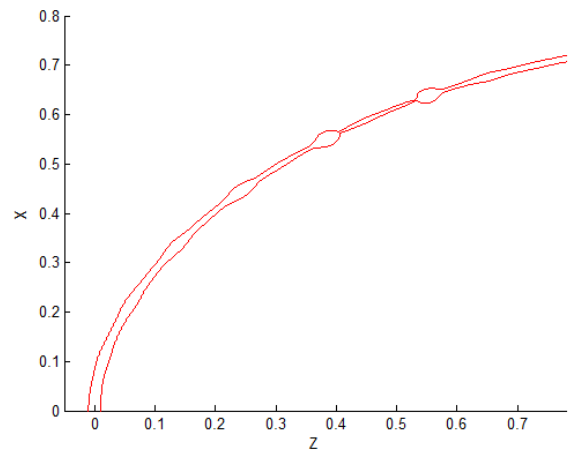Figure 6.6: Results for Jet 2. $\delta = 0.00803$ and $\epsilon = 0.01$.

Figure 6.7: Graphs showing the experimental drop size distribution for Jet 2, with theoretical drop size predictions for linear and nonlinear theory. $\delta = 0.00803$ and $\epsilon = 0.01$.
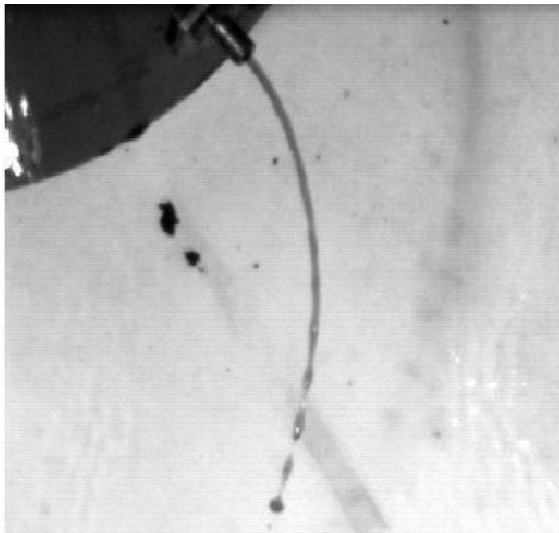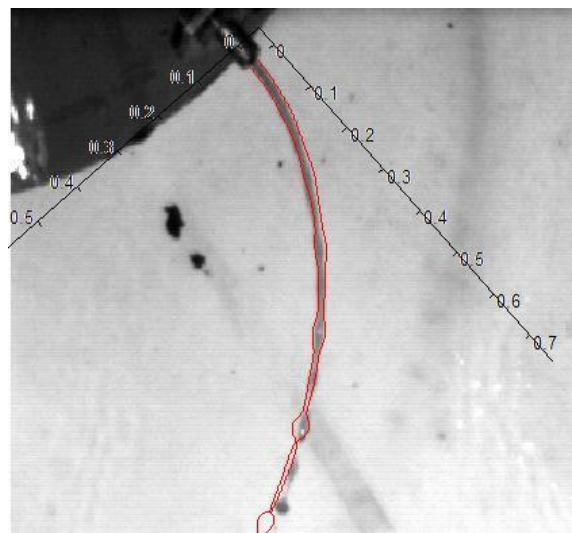
(a) radius vs arc length

(b) Jet Simulation

Figure 6.8: Theoretical results for Jet 3. $\delta = 0.0325$ and $\epsilon = 0.01$.

(a) experimental jet

(b) Theoretical jet overlayed onto experimental jet

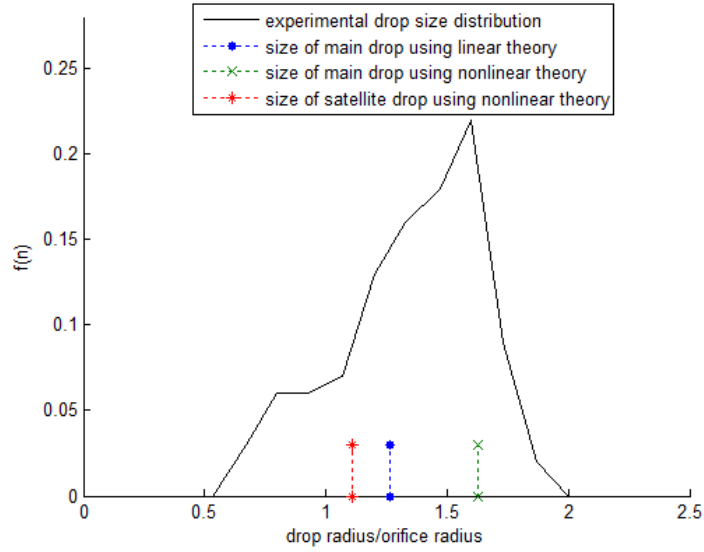Figure 6.9: Results for Jet 3. $\delta = 0.0325$ and $\epsilon = 0.01$.

Figure 6.10: Graphs showing experimental drop size distribution for Jet 3, with theoretical drop size predictions for linear and nonlinear theory. $\delta = 0.0325$ and $\epsilon = 0.01$.

We investigate the Mode 2/3 regime next. Figure 6.11 shows two numerical solutions for Jet 4, with slightly different values of δ. It illustrates, as an example, that when a fluid is more viscous, and we have ligament formation, break-up can occur on either side of the ligament for two different values of δ. For $\delta = 0.0052$, assuming one drop/ligament before break-up and one after break-up, gives a break-up length of 2.208 and a main drop of radius 1.0376 in nondimensional units, and for $\delta = 0.0053$ break-up length is 2.0032 and main drop radius is 1.369. These are two markedly different lengths and drop sizes, though the amplitude of orifice disturbance δ is changed by only a small amount and there is little difference in qualitative jet break-up.

The comparison with the experimental image is made in Figure 6.12, where $\delta = 0.0052$ as this yields the value which corresponds to the experimental break-up length. Initially the numerical simulation accurately models the jet trajectory, but as the jet length increases there is a noticeable difference between the two trajectories. This could be because the trajectory of the jet falls out of the $Z - X$ plane through gravitational

77
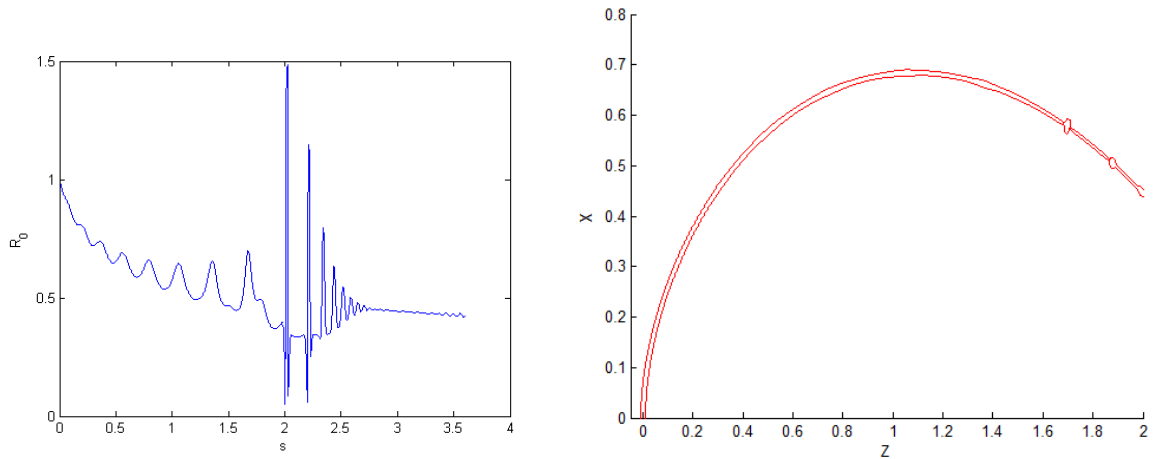
(a) $\delta = 0.0053$
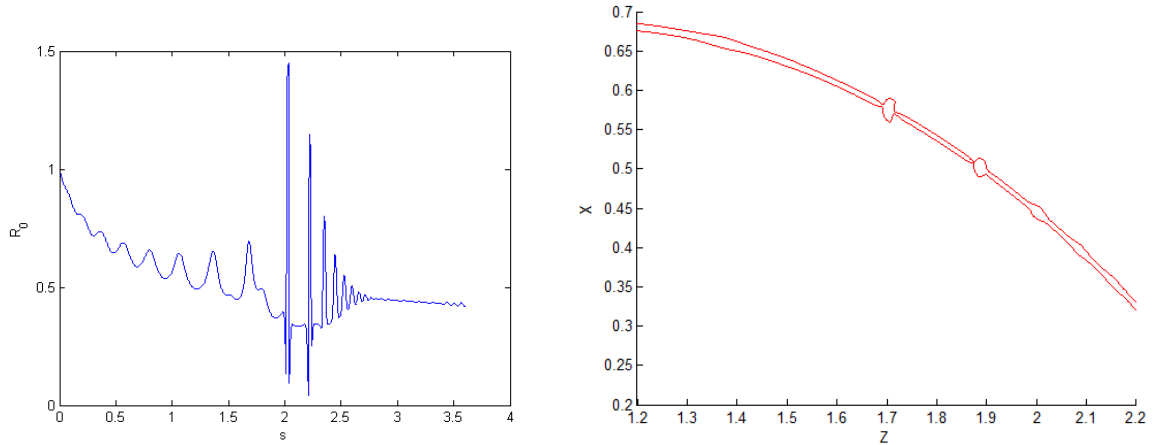
(b) $\delta = 0.0052$

Figure 6.11: Theoretical results for Jet 4. $\epsilon = 0.01$.

forces which are neglected in the simulations. This is illustrated in Figure 6.12(a) where the droplets towards the end of the jet are 'blurry' and so are not in focus, unlike the upper part of the jet. Whilst the calculation of the trajectory in three dimensions is possible, a 2D experimental image can not be compared with a 3D numerical simulation. It would be necessary to use multiple cameras in different planes to accurately measure the trajectory of the jet in three dimensions. Then the 3D nonlinear simulation could be compared.

The results are compared to the experimental photographs and drop size distribu-

tions in Figures 6.12 and 6.13 . The larger drop predicted by $\delta = 0.0053$ is not in the experimental drop size distribution, whilst the drop produced for $\delta = 0.0052$ and the linear theory result are both very similar and fall in the centre of the distribution. This shows that with multiple break-up points, there may be droplets of varying size though the nonlinear simulation can only be used to predict one droplet as the solution is not valid after break-up point. There are no satellite droplets for the more viscous fluid predicted by these simulations.
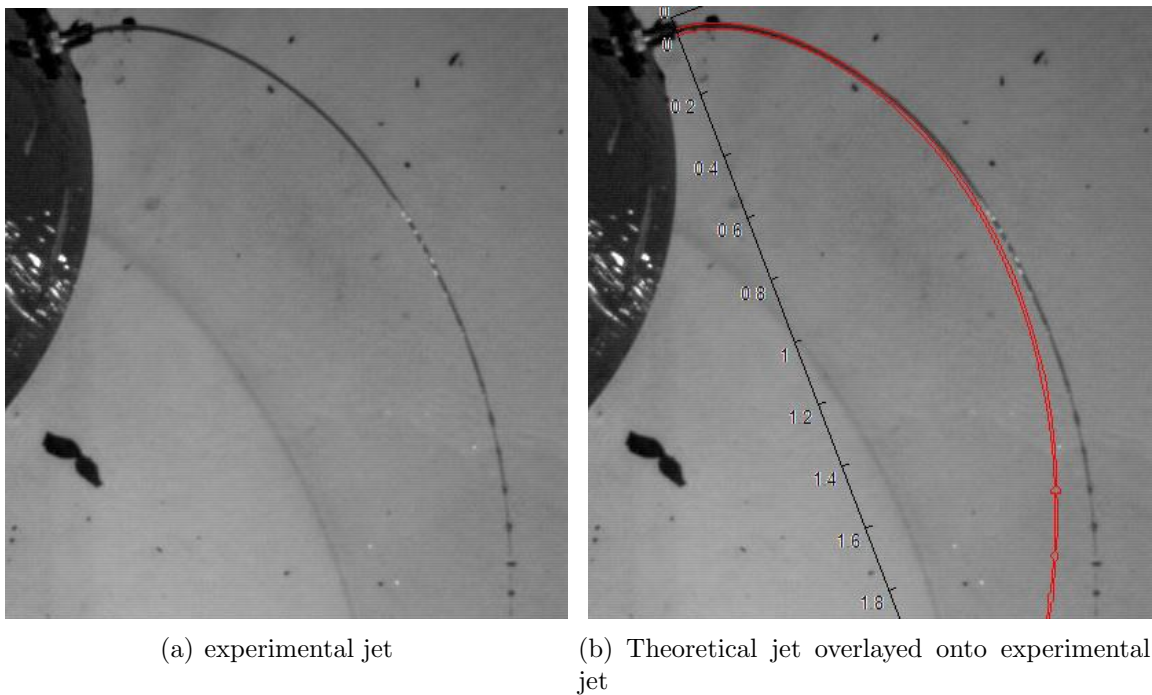

(a) experimental jet

(b) Theoretical jet overlayed onto experimental jet

Figure 6.12: Results for Jet 4. $\delta = 0.0052$ and $\epsilon = 0.01$.

Figures 6.14 - 6.16 shows the results for Jet 5. Gravity appears to have less of an affect on the trajectory of the jet[1], although the trajectory is not as accurately modelled as for Mode 2 break-up for Jets 1-3. Figure 6.16 shows that the nonlinear theory predicts a drop which falls within the upper end of the distribution for main drops, while the linear theory predicts smaller drops.

---

[1]Note that although it appears the numerical simulation moves away from the experimental image, this is in fact due to post break-up droplets falling after the break away from the jet.
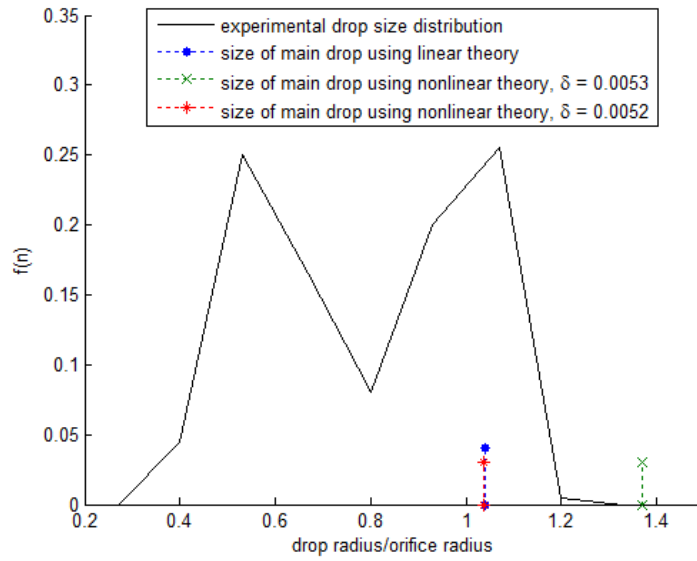
Figure 6.13: Graphs showing experimental drop size distribution for Jet 4, with theoretical drop size predictions for linear and nonlinear theory. $\delta = 0.0052$ and $\epsilon = 0.01$.
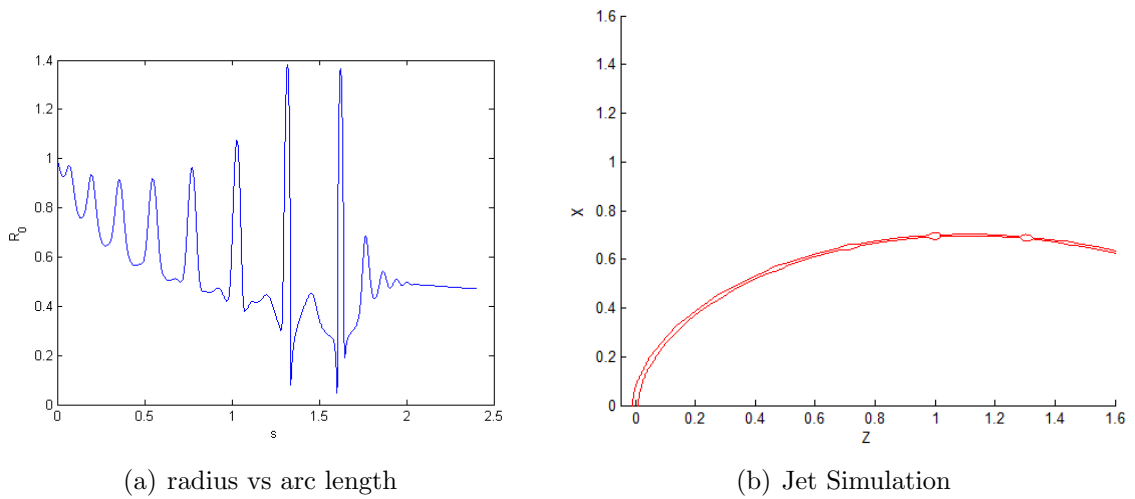

(a) radius vs arc length

(b) Jet Simulation

Figure 6.14: Theoretical results for Jet 5. $\delta = 0.0399$ and $\epsilon = 0.01$.

(a) experimental jet
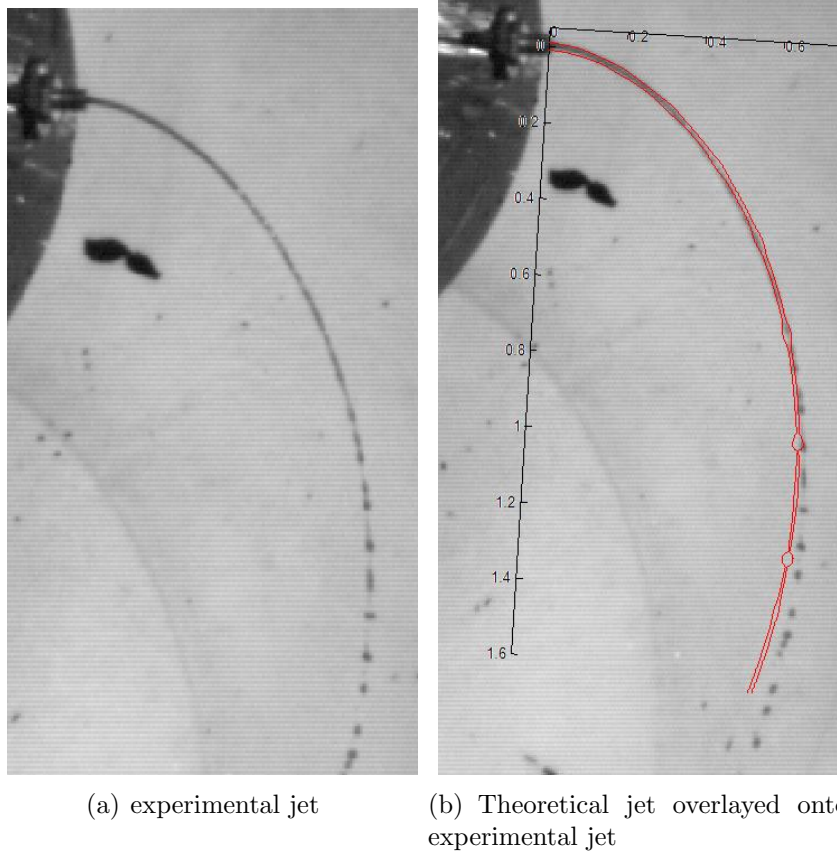
(b) Theoretical jet overlayed onto experimental jet

Figure 6.15: Results for Jet 5. $\delta = 0.0399$ and $\epsilon = 0.01$.

Figures 6.17 - 6.19 show results for Jet 6, displaying similar behaviour to Jet 5. However, Figure 6.19 shows that the nonlinear theory predicts a drop much larger than expected from experimental results, and the linear theory predicts a drop of size more typically observed. These results, in correlation with those presented in the previous section, illustrate that the two theories give different results for high rotation rates and viscosities, and show the nonlinear theory gives droplets much larger than what experiments suggest.

As a viscous jet has a longer break-up length and thins more than a less viscous jet, air resistance has a greater chance of impacting upon it, which has been excluded from our theoretical research. However, air resistance would act as a force resisting the forward movement of the jet, and so would have the effect of pushing the jet away
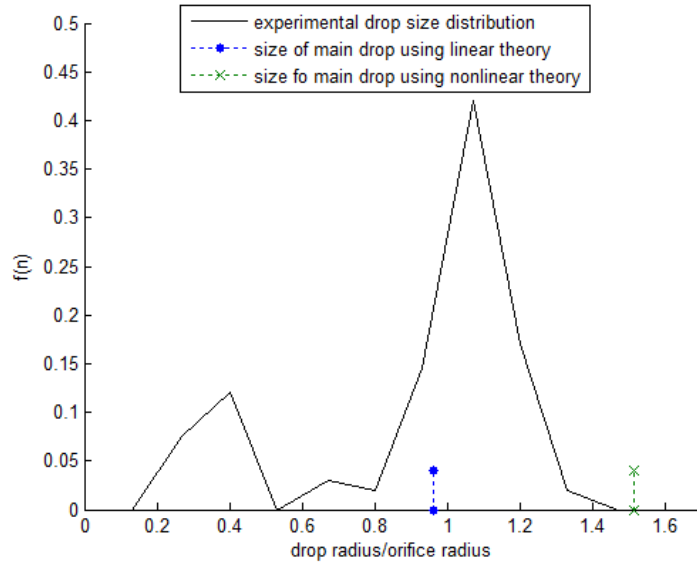
Figure 6.16: Graphs showing experimental drop size distribution for Jet 5, with theoretical drop size predictions for linear and nonlinear theory. $\delta = 0.0399$ and $\epsilon = 0.01$.

from its direction of movement. As a consequence, were air resistance an important factor in these experiments, we would expect the numerical simulation to be on the other side of the experimental image. As this is not the case, we can conclude that air resistance is not a defining factor for our simulations here.

Secondly, even though there is a greater rotation rate in Figure 6.15 and 6.18, break-up length is shorter than in Figure 6.12. It has been shown, [45], [33], that the effect of rotation is to increase the break-up length. However, this is not what is noted here in the experiments. It was necessary to raise δ by an order of magnitude to generate this shorter break-up length. This is an indication that something is occurring on the experimental scale creating this shorter break-up length when the rig is rotating more quickly. Perhaps this is due to instabilities caused by vibrations in the experimental apparatus. We shall investigate this possibility in the next chapter.

Figures 6.20 - 6.22 show simulated break-up for Jet 7. There is a vast difference between the trajectory of the simulated jet and the experimental image. Viscosity
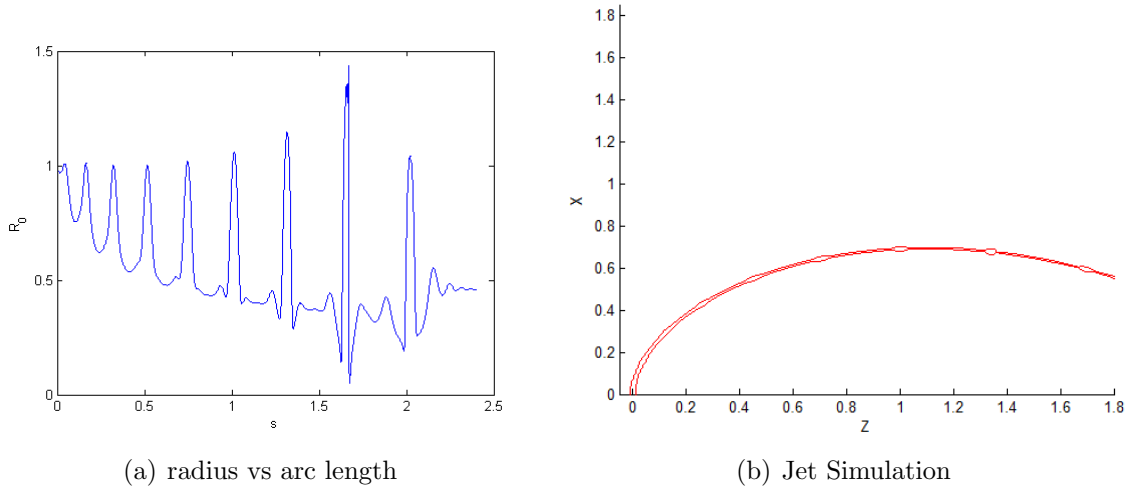
(a) radius vs arc length

(b) Jet Simulation

Figure 6.17: Theoretical results for Jet 6. $\delta = 0.065$ and $\epsilon = 0.01$.

causes the jet to thin dramatically and, with a large break-up length, makes the jet susceptible to the effects of gravity. This is noted through experimental observations as the jet is seen to fall significantly out of the plane of rotation. The main drop shows non-spherical formation and no satellite droplets are generated from the ligament. The inability to generate satellite droplets from ligaments for M2/3 and M3 break-up will create a major problem when comparing drop size distributions in the next chapter.

Similar results are noted for Jet 8 in Figures 6.23 - 6.25 though break-up length seems to be more consistent with the rotation rate as expected. Results could not be obtained for Jet 9 as the experimental break-up length was too long to be captured in a single frame, and thus trajectories cannot be matched.

6.3 Changing exit angle

We investigate the impact of the jet exit angle and discuss the implications it has upon the comparisons made in the previous section. Wong *et al.* [49] illustrated that the exit angle of the jet varies as the viscosity and rotation rate is altered. This is shown in Figure 6.26.
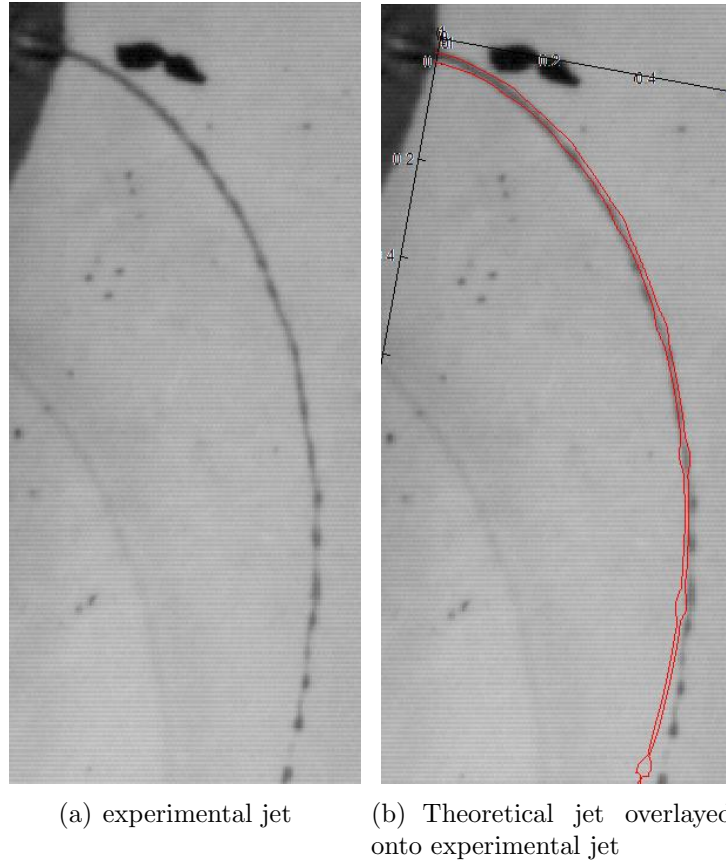
(a) experimental jet   (b) Theoretical jet overlayed onto experimental jet

Figure 6.18: Results for Jet 6. $\delta = 0.065$ and $\epsilon = 0.01$.

As the Rossby number is decreased, the angle at which the jet leaves the orifice becomes smaller. This also happens as the jet becomes more viscous. Therefore, for the jets we have considered, particularly the viscous jets at high rotation rates, our assumption that the jet is exiting perpendicularly to the orifice may become less valid. It is in this case that we found the least accurate comparison. We can modify the angle at which the jet leaves the orifice in the simulations by changing our steady state orifice conditions $X_s(s = 0) = 1$ and $Z_s(s = 0) = 0$. We must, however, maintain the arclength condition,
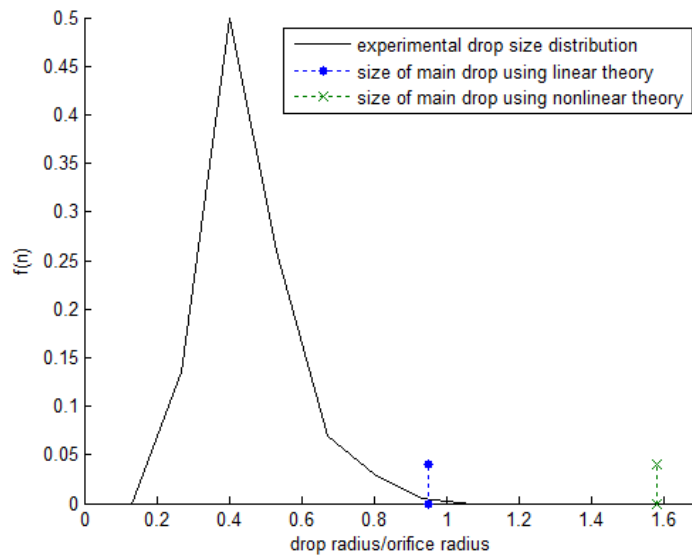
$$X_s(0)^2 + Z_s(0)^2 = 1.$$

84

Figure 6.19: Graphs showing experimental drop size distribution for Jet 6, with theoretical drop size predictions for linear and nonlinear theory. $\delta = 0.065$ and $\epsilon = 0.01$.

(a) radius vs arc length
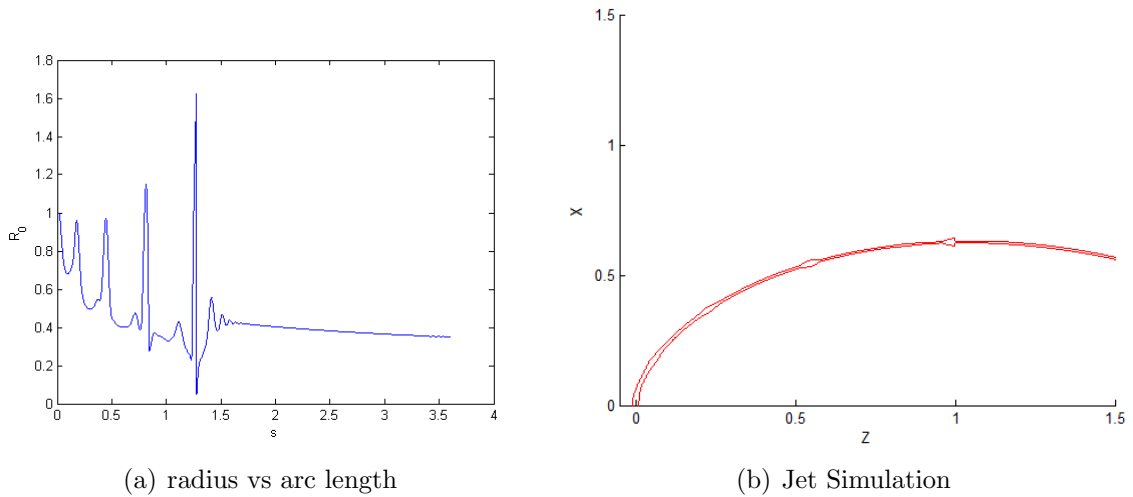
(b) Jet Simulation

Figure 6.20: Theoretical results for Jet 7. $\delta = 0.137$ and $\epsilon = 0.01$.

(a) experimental jet

(b) Theoretical jet overlayed onto experimental jet

Figure 6.21: Results for Jet 7. $\delta = 0.137$ and $\epsilon = 0.01$.

Figure 6.22: Graphs showing experimental drop size distribution for Jet 7. $\delta = 0.137$ and $\epsilon = 0.01$.

(a) radius vs arc length

(b) Jet Simulation

Figure 6.23: Theoretical results for Jet 8. $\delta = 0.058$ and $\epsilon = 0.01$.
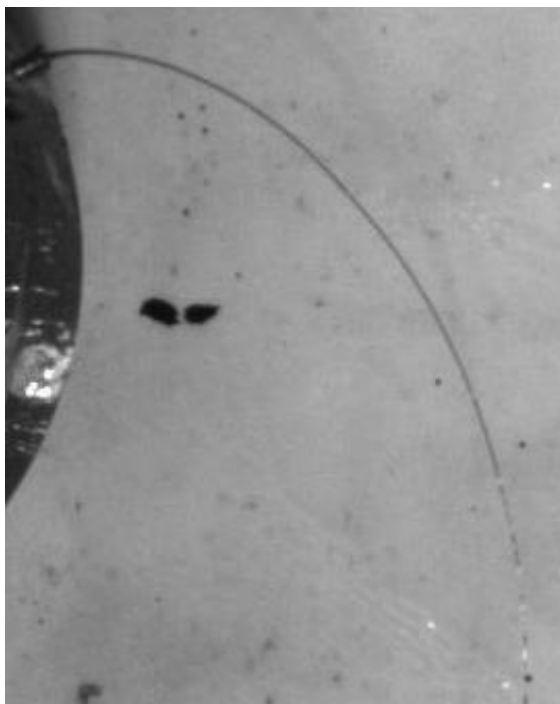
(a) experimental jet
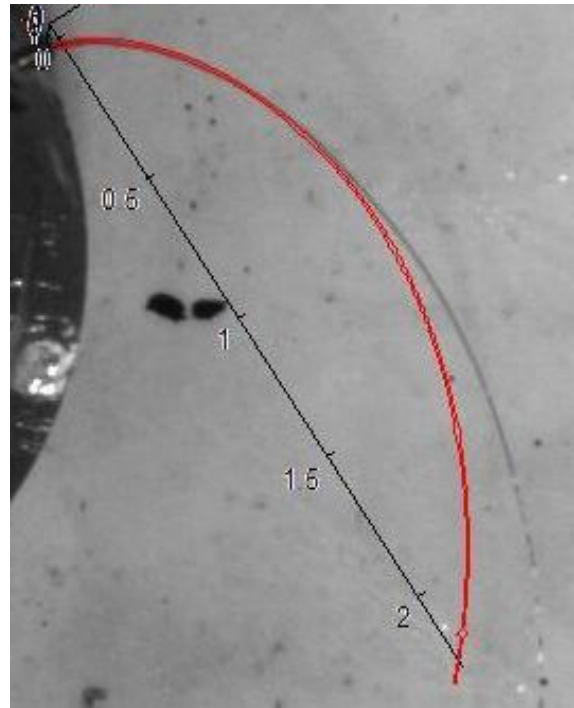
(b) Theoretical jet overlayed onto experimental jet

Figure 6.24: Results for Jet 8. $\delta = 0.058$ and $\epsilon = 0.01$.

87

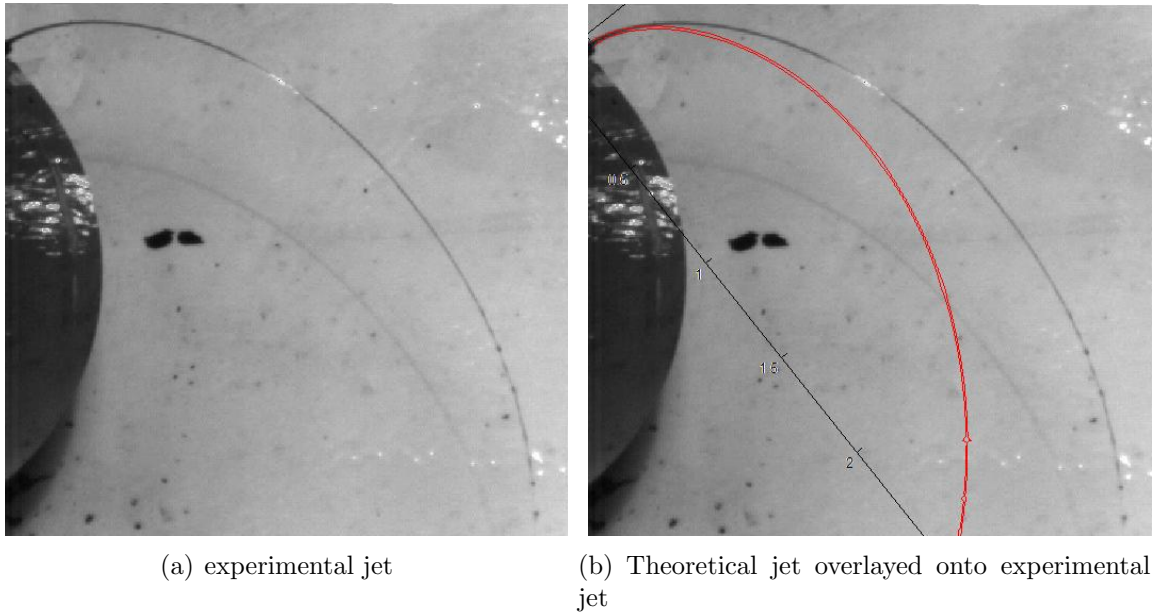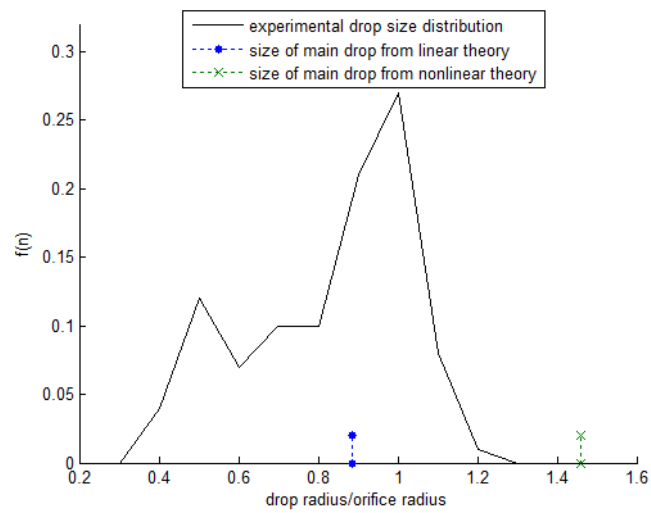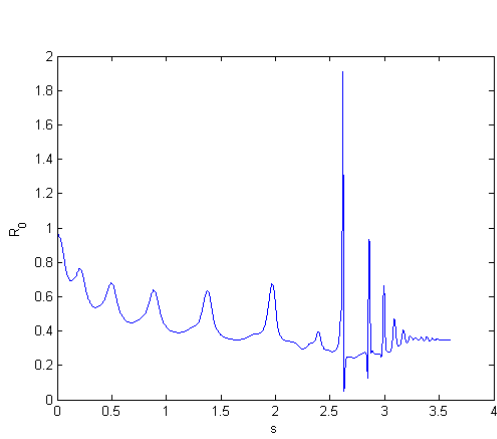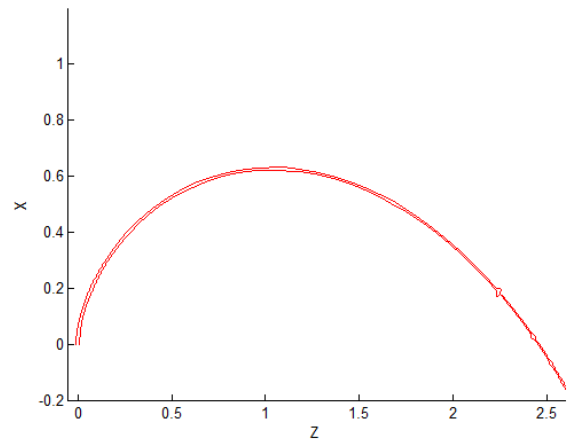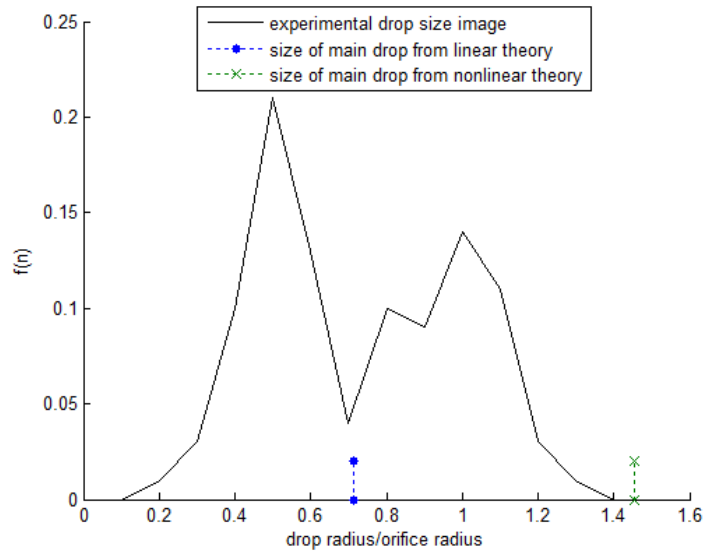Figure 6.25: Graphs showing experimental drop size distribution for Jet 8. $\delta = 0.058$ and $\epsilon = 0.01$.
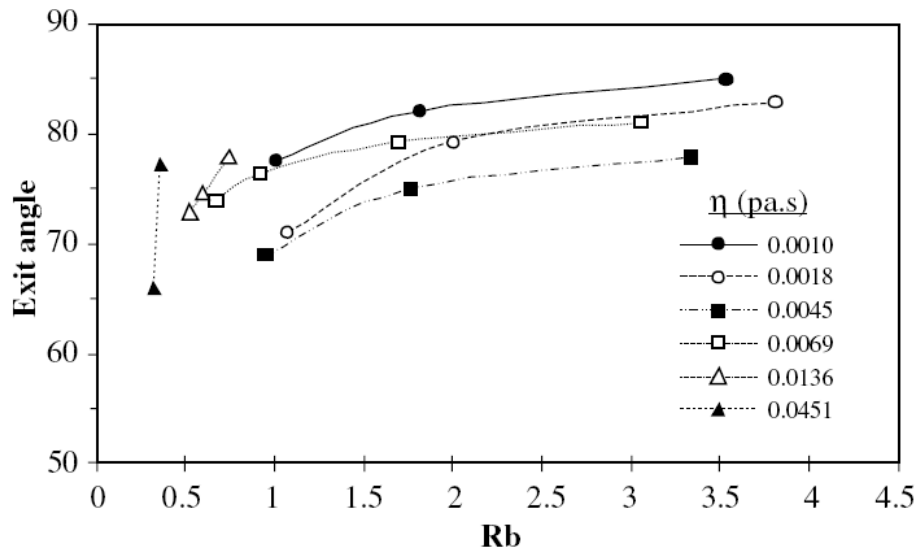
Figure 6.26: Graphs showing how the exit angle at the orifice is affected by rotation rate and viscosity of the fluid, reproduced from Wong *et al.* [49]
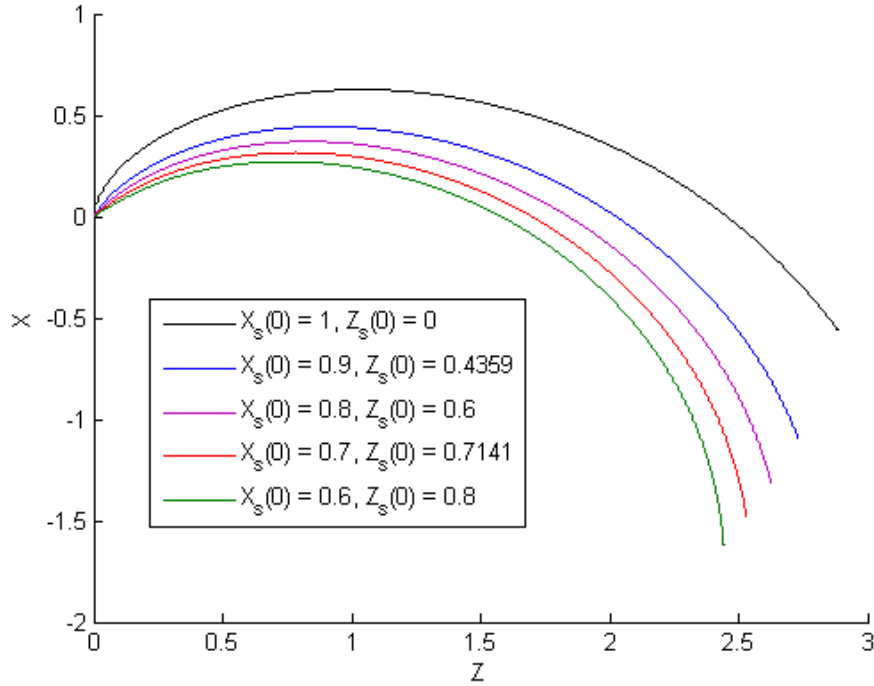
Figure 6.27: Graphs showing different trajectories for different values of $X_s(0)$ and $Z_s(0)$. The jet parameters used are $We = 28.676$, $Rb = 0.336$, $Re = 30$, $Oh = 0.1785$ and $\epsilon = 0.01$.

Figure 6.27 shows the affect of changing these initial conditions at $s = 0$, showing that the jet becomes more coiled as X_s is decreased. This illustrates the importance of the calculation of the steady state in the overall solution to the problem.

Figure 6.28, shows how these conditions affect the numerical simulations. Figure 6.28(a) and (b) show the original jet trajectory with the jet exiting perpendicularly to the orifice, as in the previous section. The orifice conditions are changed in 6.28(c) and (d) so the jet is no longer perpendicular and the same amplitude disturbance is applied. Break-up length is now shorter, and the main drop now forms after break-up with the ligament forming before break-up. This suggests that when the jet is emerging at an angle, it requires a different disturbance to generate the same break-up length.
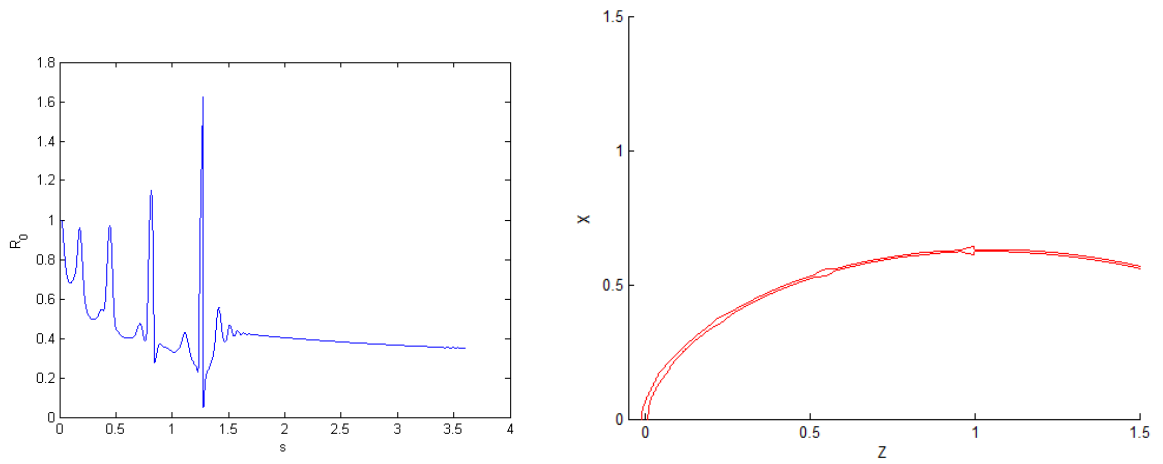
(a) $X_s(0) = 1$, $Z_s(0) = 0$, $\delta = 0.137$.
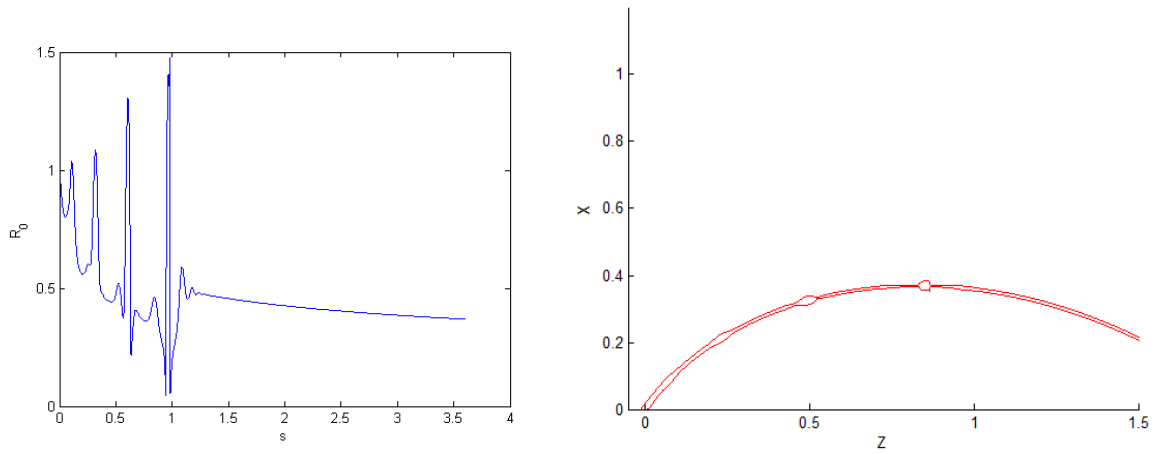
(b) $X_s(0) = 0.8$, $Z_s(0) = 0.6$, $\delta = 0.1$.
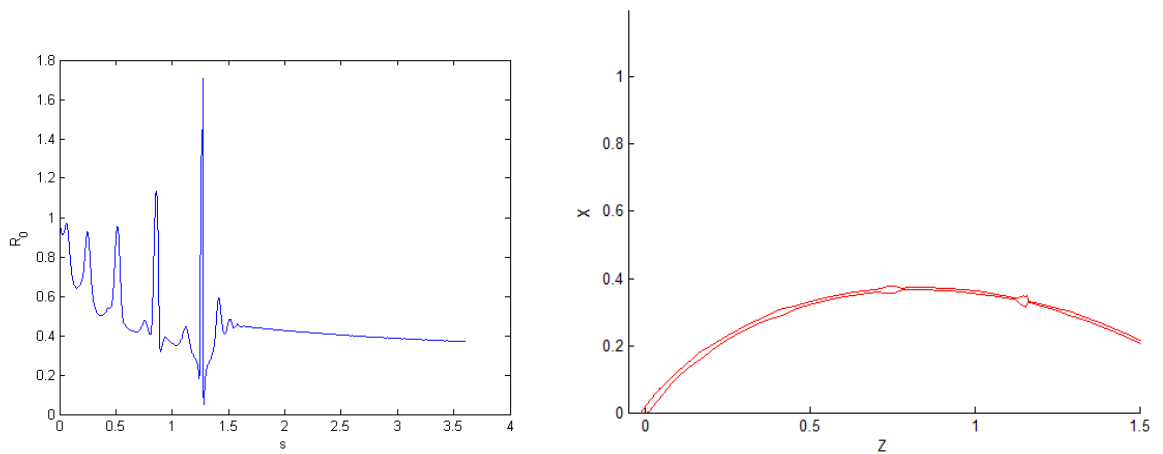
(c) $X_s(0) = 0.8$, $Z_s(0) = 0.6$, $\delta = 0.137$.

Figure 6.28: Numerical simulations used to show how $X_s(0)$ and $Z_s(0)$ changes break-up for Jet 7. $\epsilon = 0.01$.
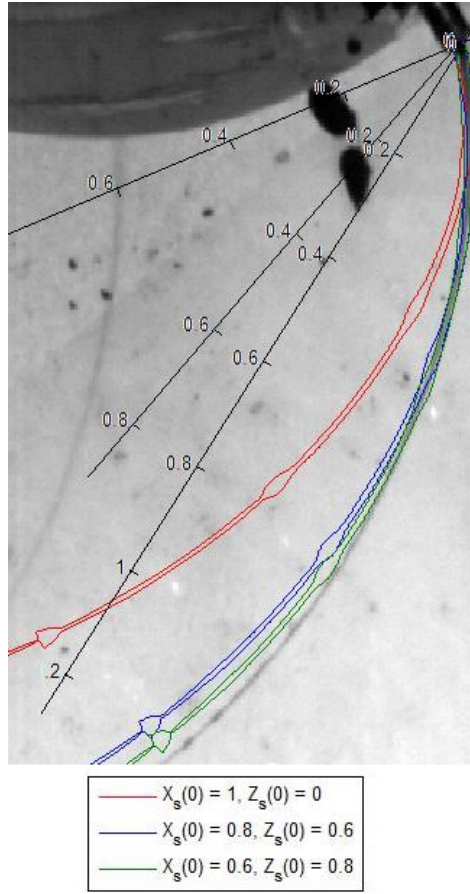
Figure 6.29: Graph showing additional jets added to Figure 6.21(b) with break-up length matched. (i) (blue) $X_s(0) = 0.8$, $Z_s(0) = 0.6$, $\delta = 0.1$ and (ii) (green) $X_s(0) = 0.6$, $Z_s(0) = 0.8$, $\delta = 0.075$ The parameters used are $We = 28.676$, $Rb = 0.336$, $Re = 30$, $Oh = 0.1785$, $\kappa = 0.6022$ and $\epsilon = 0.01$.

δ is modified in 6.28(e) and (f) such that break-up length is matched. Now break-up occurs in exactly the same way as in 6.28(a) and (b). Changing the angle has had no affect on the way the jet breaks up when the break-up length is the same. We can see in Figures, 6.28(b), (d) and (f) that although the break-up length has changed slightly, qualitative jet break-up is unaffected by changing the exit angle.

The numerical simulations are compared to an experimental image in Figure 6.29. With the modified orifice conditions, the numerical simulation shows a better comparison. However, the extent to which the simulation models the trajectory cannot

91
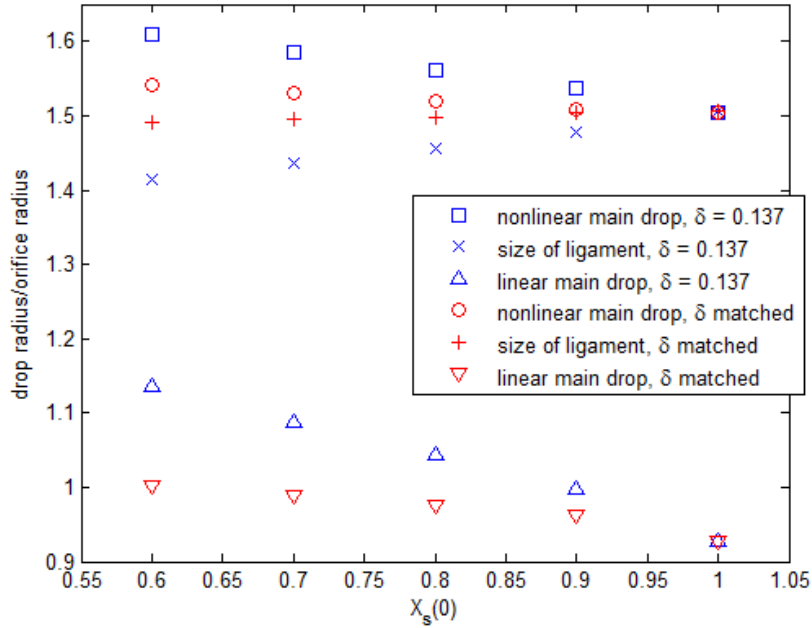
Figure 6.30: Graphs showing how changing $X_s(0)$ and $Z_s(0)$ affects drop sizes showing (i) nonlinear main drop prediction, (ii) nonlinear ligament size prediction and (iii) linear drop prediction for $\delta = 0.137$ and δ chosen to match break-up length. The jet parameters used are $We = 28.676$, $Rb = 0.336$, $Re = 30$, $Oh = 0.1785$ and $\epsilon = 0.01$.

be entirely quantified as the experimental jet falls out the plane of the experimental image.

Figure 6.30 shows the nonlinear and linear drop size predictions for changing jet angle with δ unmodified as well as with δ changing to match break-up. To generate the 'size of the ligament' we assume that the ligament contracts into a single drop. We then use the same technique as for calculating the radius of the main and satellite droplets described in Section 3.2.3 (That is, 'size of ligament' in Figure 6.30 refers to an equivalent drop radius produced if a ligament contracts into a single drop at rupture). The nonlinear theory predicts decreasing main drop size and increasing ligament size with increasing $X_s(0)$. These change only slightly when δ is chosen to match the break-up lengths, whilst they change more when δ is kept the same as for an exit angle of $90°$. Nonlinear theory still predicts drops which are larger than seen experimentally in

Figure 6.23, despite the changes in exit angle. Linear theory exhibits the same trends as identified for nonlinear theory whilst maintaining drop sizes comparable to that of experiments.

6.4 Conclusions

Throughout this chapter we have compared experimental results with theoretical predictions assuming break-up was generated by the most unstable wave. For less viscous fluids in the M2 regime we obtained a very good comparison between the theory and the experiments. However, we were unable to compare the trajectories for slower viscous jets as they fell out the plane of the experimental image, and quicker high viscosity jets as we could not ascertain break-up on an experimental scale as the jet was too long to be observed in a single frame.

The comparison with the experiments show that the linear theory provides an accurate drop size prediction. Whilst nonlinear theory can accurately predict the mode classification of a jet (providing ϵ is small), in more viscous situations where the jet thins, the theory appears less accurate. Perhaps the bunching of the wavepacket resulted in nonlinear supposition of waves close to pinch-off. Alternatively, inaccuracies could arise due to the use of the long wavelength approximation in the derivation of the nonlinear equations.

We also investigated the impact of jet exit angle and discovered that though the exit angle has a dramatic effect on the trajectory of the jet, qualitative behaviour is unaffected and drop sizes are only slightly affected.

Chapter 7

Introducing Another Disturbance

Up to this point, we have posed a periodic boundary condition at the orifice of the form,

$$u(0,t) = 1 + \delta \sin(\kappa t/\epsilon),$$

where δ is the amplitude of the disturbance, and κ chosen such that break-up is caused by the most unstable mode. However, experiments are seen to yield a distribution in drop sizes, and the above boundary condition will only produce a single drop size prediction. Partridge *et al.* [34] attributed discrepancies between the pilot scale rig and results from the laboratory scale rig from Wong *et al.* [49] to mechanical vibrations in the rig components, yet this could also account for distributions in drop sizes. A secondary disturbance is introduced through the boundary condition at the orifice,

$$u(0,t) = 1 + \delta \sin(\kappa t/\epsilon) + \gamma \sin(\omega t/\epsilon), \qquad (7.1)$$

where γ and ω are the amplitude and frequency of the additional disturbance. Clearly it is unlikely that a singular sinusoidal wave is representative of all vibrations in the rig; this approach merely allows the sensitivity of a jet to additional disturbances to
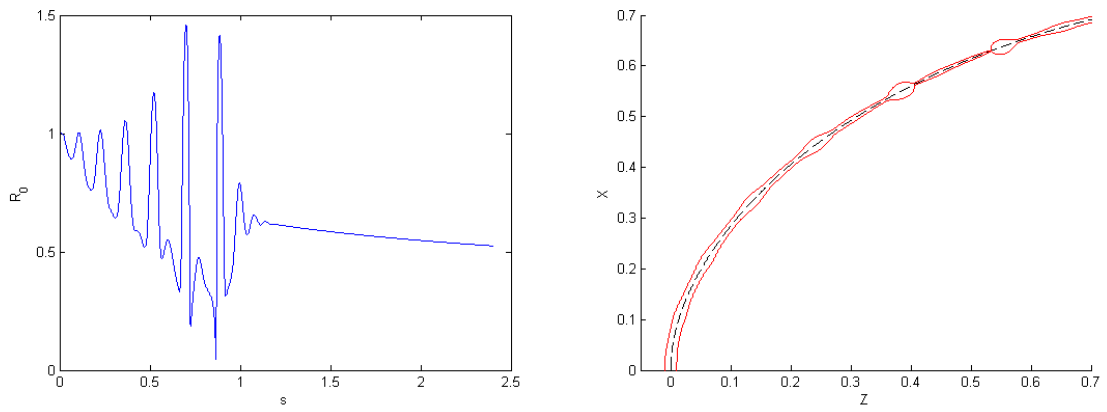
(a) no secondary disturbance
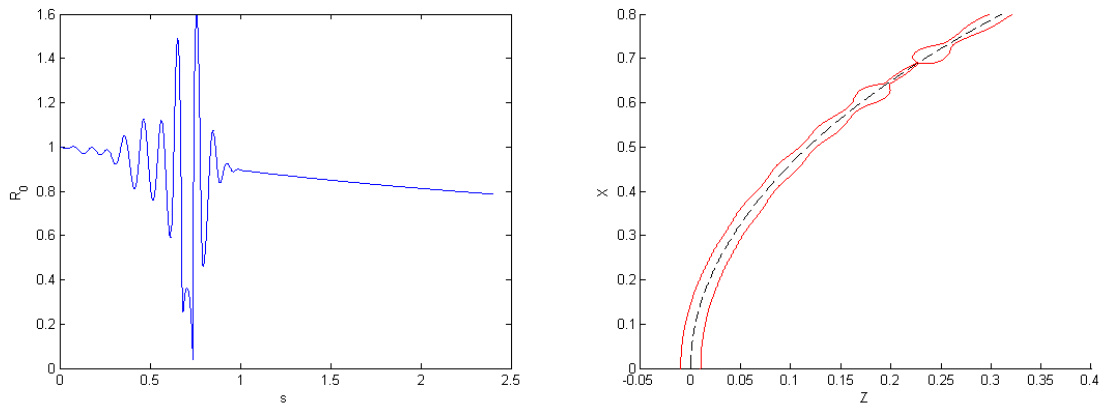
(b) $\gamma = 0.00199$ and $\omega = 0.5$
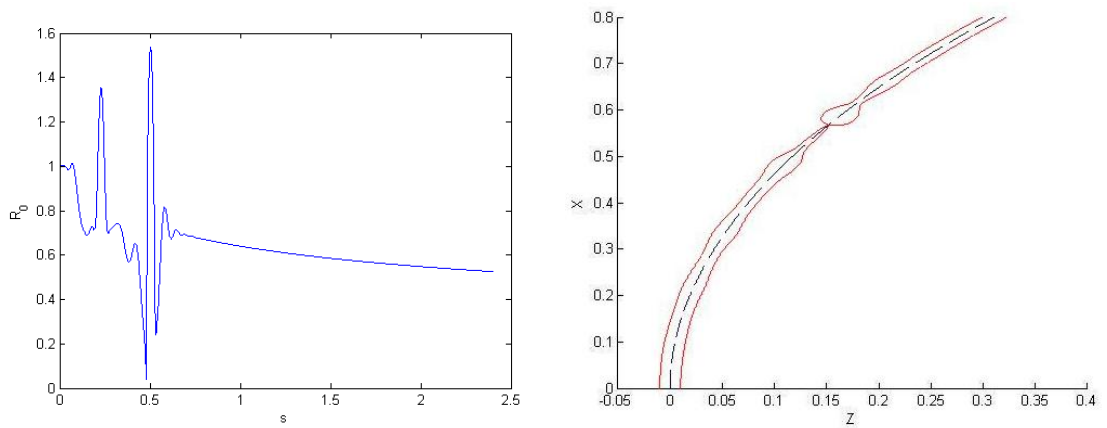
(c) $\gamma = 0.01$ and $\omega = 0.5$

Figure 7.1: Secondary disturbance applied to Jet 1. $\delta = 0.00199$ and $\epsilon = 0.01$.
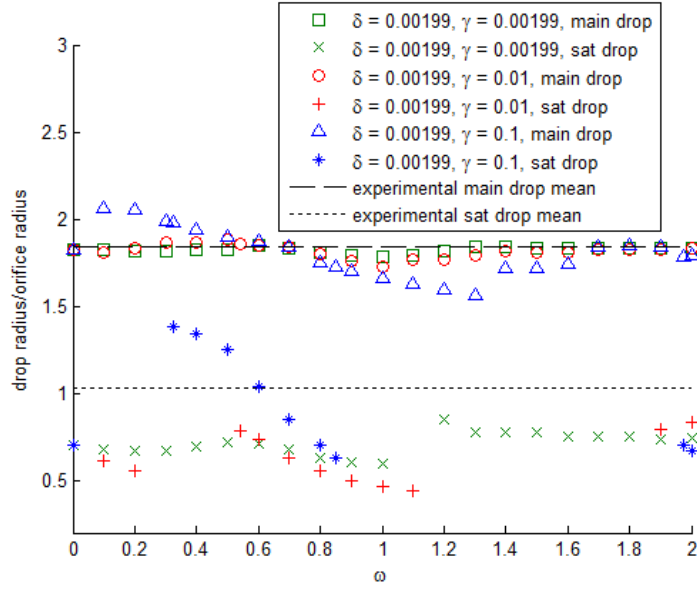
Figure 7.2: Graphs showing how the drop sizes with varying ω for three different disturbances, (1) $\delta = 0.00199, \gamma = 0.00199$, (2) $\delta = 0.00199, \gamma = 0.01$, and (3) $\delta = 0, \gamma = 0.00199$ for Jet 1. $\epsilon = 0.01$. The dotted line shows the experimental mean.

be demonstrated.

Figures 7.1(a) and (b) show a jet with no additional disturbances at the orifice. Figures 7.1(c) and (d) show a secondary disturbance with the same amplitude as the most unstable wave, and Figures 7.1(e) and (f) show a secondary disturbance with amplitude larger than that of the most unstable wave. As the size of the secondary disturbance is increased, the presence of satellite droplets is seen to be eradicated for this given secondary frequency $\omega = 0.5$. We apply additional frequencies to Jets 1-9 from Table 6.1 to generate drop size distributions and investigate changes of mode of break-up.

7.1 Water

Figure 7.2 examines the behaviour of Jet 1 when subjected to a three different secondary disturbances, one with a weak disturbance the same size as the most unstable mode, another a stronger secondary disturbance which is an order of magnitude in amplitude greater and one without the most unstable mode present ($\delta = 0$). Also plotted is the experimental mean for the main and satellite drop sizes. Although values of ω only go up to 2, greater frequencies could be investigated. However, for the purpose of our investigation we are examining regions around the most unstable wave frequency $\kappa = 0.7048$ and so we are not interested in very high frequency secondary disturbances.

There is very little quantitative difference for the main drop sizes for all frequencies and amplitudes. However, there is a difference with satellite droplet formation. For the low amplitude secondary disturbance, satellite droplet formation is largely unaffected. The most unstable wave frequency does indeed dominate the jet break-up over other frequencies applied to the jet, thus regulating break-up.

At a higher secondary amplitude, the additional frequencies can have a more dominant affect on the jet and in some cases eradicate the satellite drop formation. When $\delta = 0$ and there is no Rayleigh mode, the behaviour is equivalent to investigating a disturbance an order of magnitude greater than the most unstable wave, except at higher frequencies. We propose that for some jets, such as Jet 1, the most unstable mode can cause satellite droplets and it is necessary to force a jet to vibrate at a different frequency to reduce the presence of these smaller droplets.

In order to compare the behaviour of these imposed secondary disturbances with experimental drop size distributions and gain insight into the behaviour of the experimental setup, it is necessary to generate drop size distribution modelling a carefully selected range of frequencies.
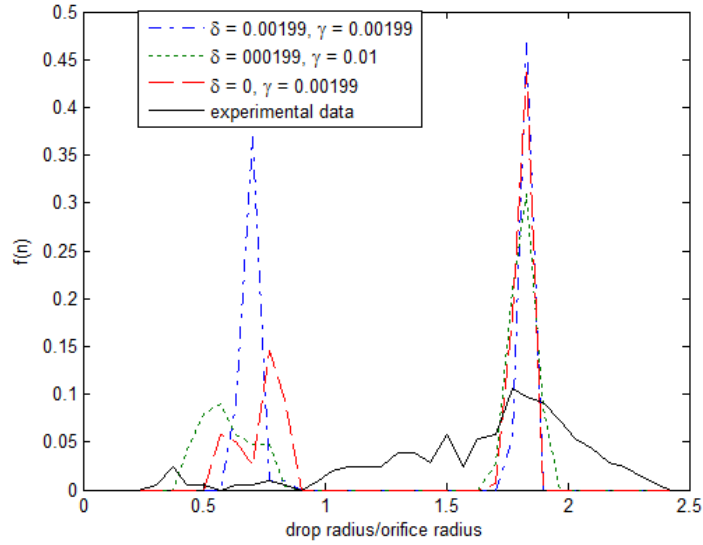
Figure 7.3: Theoretical drop size distributions produced for the different disturbances (1) $\delta = 0.00199, \gamma = 0.00199$, (2) $\delta = 0.00199, \gamma = 0.01$, and (3) $\delta = 0, \gamma = 0.00199$, taken about the frequency of the most unstable wave for Jet 1. $\epsilon = 0.01$. Also plotted is the experimental data.

To model a distribution in disturbance frequencies at the orifice, a (truncated) Gaussian profile is adopted with the mean chosen to be equal to the frequency of the most unstable wave, under the assumption that the Rayleigh mode is still a critical factor in jet break-up. The standard deviation of the Gaussian distribution is arbitrarily taken to be equal to the experimental standard deviation in drop size. 200 frequencies are studied to be consistent with the production of experimental distributions, generated using MATLAB's normal distribution function (normrnd).

Inputting 200 different frequencies into the nonlinear model is impractical, thus discrete values of ω are chosen (i.e. those shown in Figure 7.2). It is assumed that drop sizes generated by a given frequency fall on the gradient in between the discrete points. In cases where no satellite droplets are produced, such as $\omega = 1.3$, the jet is assumed to undergo M1 break-up. It is also assumed that no further satellite drops are generated in between the two discrete values.

98

Using this Gaussian profile, we obtain the theoretical drop size distribution shown in Figure 7.3. We conclude that if disturbances are of similar magnitude to the most unstable wave ($\gamma = \delta$) then there is a poor correlation with experimental results - there are too many satellite droplets and not enough variation in main drop size. Removing the most unstable wave from the jet had no improved effect upon the variation in main droplet sizes, but had a more dramatic effect on satellite droplets, in a similar fashion to increasing the amplitude of the secondary disturbance by an order of magnitude.

It is necessary for γ to increase by two orders of magnitude, to $\gamma = 0.1$ in Figure 7.4, before a good agreement is reached and a unimodal distribution is generated, indicating the impact of mechanical instabilities that dominate the classical dynamics of liquid jet break-up. (It is not suggested that the vibrations are this large in amplitude; in practice there would be a multitude of smaller disturbances interacting during break-up). As a consequence, this raises issues for experimental research. Would two independently engineered experimental setups yield the same results if the jets are so sensitive to vibrations, and does an engineered setup vibrate with similar amplitudes and frequencies to the industrial problem? Dimensionless parameters permit a scaling of the industrial problem, yet subtleties in engineering that lead to varying mechanical instabilities are not accounted for. In order to control jet break-up, it would be necessary to dominate the mechanical instabilities that arise as the rig rotates, regardless of its design. Similar trends are identified for the same fluid at a larger rotation rate, as shown by Figures 7.5 and 7.6 for Jets 2 and 3. However it appears that higher rotation rates in Figure 7.6 show less of an accurate comparison.

In addition, the concept of these experimentally induced vibrations may explain why there is less of a comparable distribution for higher rotation rates. Naturally, if there are instabilities in the rig then these will be more pronounced when the rig is rotating more rapidly. As a consequence, the experimental jet will be experiencing

99

higher amplitude vibrations at the orifice. This could cause jets to be shorter, and as such, it explains why in the previous chapter it was necessary for δ to be set larger to match to experimental images in these cases.

In addition, the jets generated during these simulations using additional disturbances naturally have varying break-up lengths. We see variations in break-up lengths on the experimental scale during visualisation of a single jet; perhaps these are related. Also, to reiterate an earlier statement, these secondary disturbances we have introduced here have not been used to model vibrations in the rig, rather to demonstrate the jet's sensitivity. In reality, we would have a whole range of different frequencies and amplitudes at the orifice, corresponding to nonlinear wavepackets moving down the jet.

7.1.1 Changing Modes

The previous section illustrated a jet's sensitivity to additional disturbances, and we proposed that such disturbances occurring in the experimental set-up could account for the observed distributions. However, we did not fully investigate the impact of these disturbances on the theoretical jet simulation. Increasing either γ or ω corresponds to increasing the amplitude or frequency of the secondary disturbance. We wish to see which has greater effect on the jet, increasing amplitude or frequency, and how these qualitatively effect break-up.

Figure 7.7 shows how low amplitude disturbances of different secondary frequencies affect jet break-up when compared with a jet with no secondary disturbance. Increasing the frequency of this small amplitude disturbance has little effect on the jet, apart from slightly reducing the break-up length. There is distinct satellite drop formation, and this has no effect on the mode of break-up; it is clearly M2. Note that each jet image is shifted along the Z axis, the orifice remains at $X = Z = 0$ during each simulation.
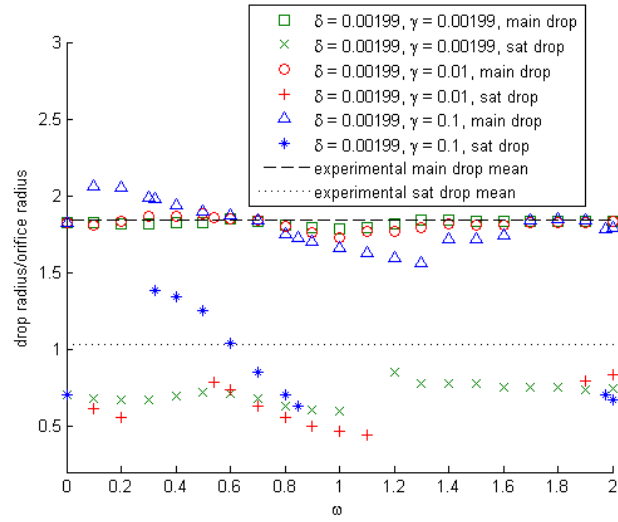
(a) drop sizes with varying ω
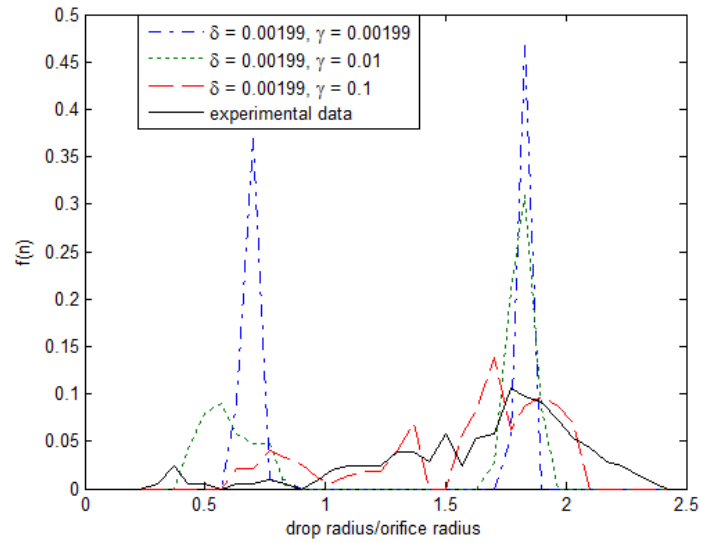
(b) drop size distribution

Figure 7.4: Effect of 3 secondary disturbances, (1) $\delta = 0.00199, \gamma = 0.00199$, (2) $\delta = 0.00199, \gamma = 0.01$ and (3) $\delta = 0.00199, \gamma = 0.1$ for Jet 1. $\epsilon = 0.01$.
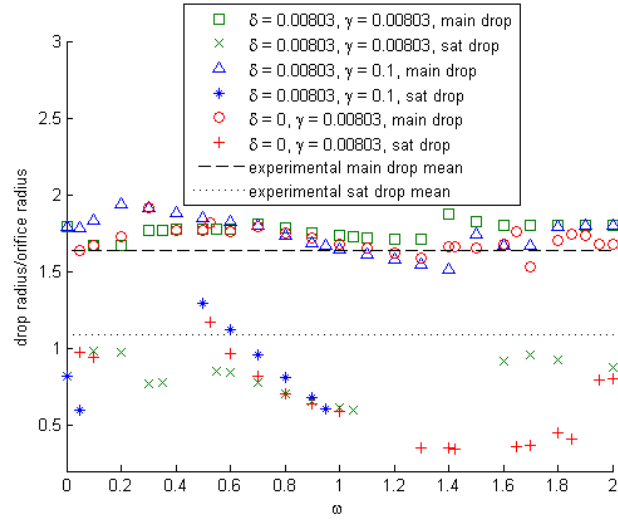
(a) drop sizes with varying ω
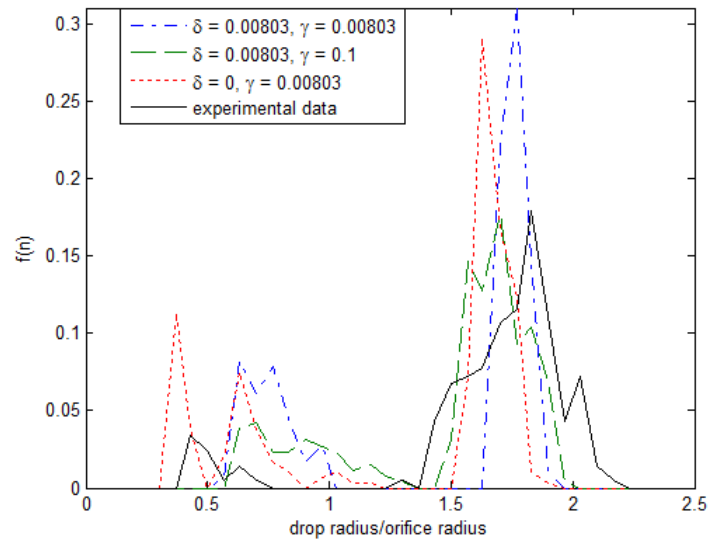
(b) drop size distribution

Figure 7.5: Effect of 3 secondary disturbances, (1) $\delta = 0.00803, \gamma = 0.00803$, (2) $\delta = 0.00803, \gamma = 0.01$ and (3) $\delta = 0.00803, \gamma = 0.1$ for Jet 2. $\epsilon = 0.01$. Also plotted is the experimental data.
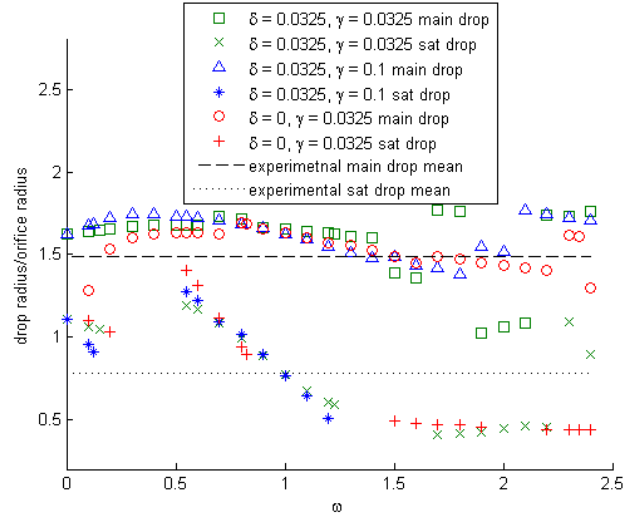
(a) drop sizes with varying ω
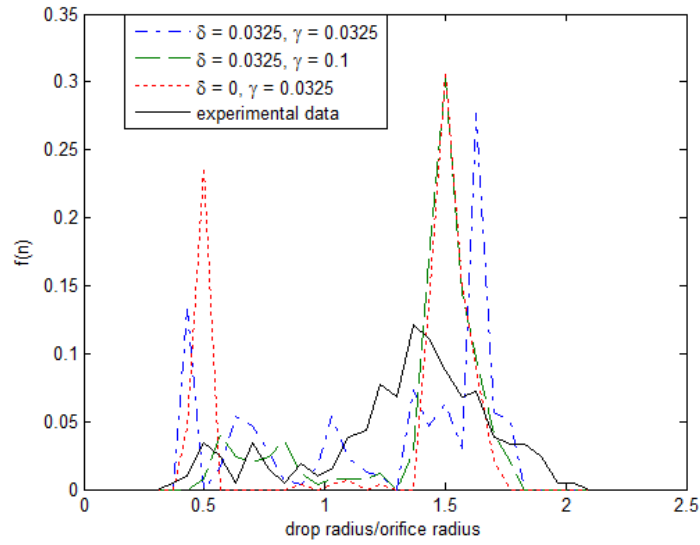
(b) drop size distribution

Figure 7.6: Effect of 3 secondary disturbances, (1) $\delta = 0.0325, \gamma = 0.0325$, (2) $\delta = 0.0325, \gamma = 0.1$ and (3) $\delta = 0, \gamma = 0325$ for Jet 3. $\epsilon = 0.01$. Also plotted is the experimental data.
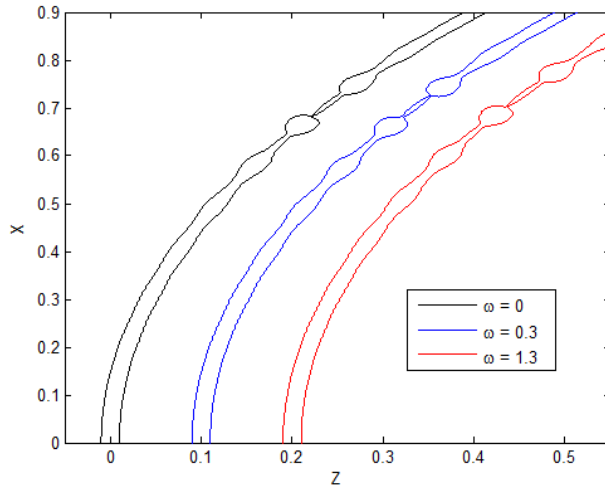
Figure 7.7: Graphs showing how the disturbance is affected by changing frequency of a low amplitude disturbance $\gamma = 0.00199$ for Jet 1. $\epsilon = 0.01$. Each jet image is shifted along the Z axis.

The amplitude is increased in Figure 7.8. There is markedly different behaviour as frequency is changed. For frequencies $\omega = 0.3$ and $\omega = 1.3$, it appears that satellite drop formation is eradicated, the high frequency disturbance causes very short jet break-up.

Figure 7.9 shows the different modes of break-up for different amplitude disturbances. We can see that for low amplitude disturbances we see little qualitative change in jet break-up, and it is the most unstable wave derived by Decent *et al.* [12] which dominates the behaviour. When the amplitude is increased, there are two areas of M1 break-up predicted, one in the low frequency range and a larger area in the high frequency range. The stability of different frequencies will be examined in the next chapter.

These areas of satellite drop eradication are of primary interest to prilling, and so we can propose useful frequencies for an experimental range in order to achieve the desired break-up, i.e. we propose that this feature could usefully be applied by forcing
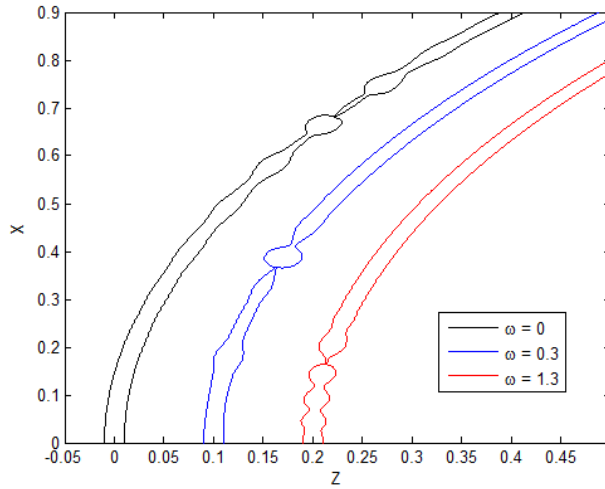
Figure 7.8: Graphs showing how the disturbance is affected by changing frequency of a high amplitude disturbance $\gamma = 0.1$ for Jet 1. $\epsilon = 0.01$. Each jet image is shifted along the Z axis.

the jet at given frequencies to control jet break-up, using either a vibrating nozzle or insonification. This is discussed further in Chapter 11. It would perhaps also be useful to search for higher frequency disturbances above those shown in the figures. However, we notice as ω approaches 2 that a very high frequency disturbance predicts M2 behaviour. In fact this break-up is very 'messy', and we shall investigate reasons why these very high frequencies generate disturbances yielding satellite drops in a later chapter.

As a side note, the jet break-up length can be controlled through the use of applied frequencies. Whilst the prilling industry is primarily focussed on droplet size, the length of a jet is an important factor in areas such as electrospinning, and the results obtained in this chapter could be used to generate jets of a desired break-up length.

105
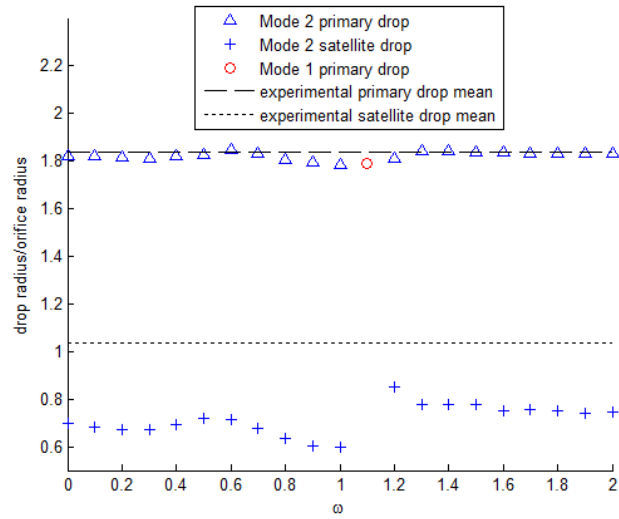
(a) low amplitude disturbance $\gamma = 0.00199$

(b) high amplitude disturbance $\gamma = 0.1$

Figure 7.9: Graphs showing how the mode of jet break-up changes with varying frequency for Jet 1. $\epsilon = 0.01$.

7.2 Low Viscosity Fluids

In this section we examine the effect of secondary disturbances on Jets 4-6, using the same analysis as for Jets 1-3. Figure 7.10 shows the impact of three different secondary disturbance amplitudes. The size of the ligament in Figure 7.10(a) refers to the effective radius if the ligament formed a single drop instead of multiple satellite drops.

Figure 7.10 presents results for Jet 4. Having a large amplitude disturbance of varying frequency can cause a large range of droplets. However, most of the main droplets produced theoretically are larger than seen experimentally. Ligaments have been neglected in Figure 7.10(b) since we do not feel able to predict whether they will contract into a single drop or break-up into multiple satellites. We return to this in more detail in Chapter 8.

Figure 7.11 and Figure 7.12 present distributions for Jets 5 and 6. They demonstrate that our uncertainty in dealing with the ligaments is producing poor agreement with experiments for drop size distributions.

7.2.1 Changing Modes

The mode of jet break-up is now investigated, first examining changes in frequency. Figure 7.13 shows little qualitative changes in the jet, although break-up length is noticeably reduced at higher frequencies. This effect is more noticeable than for Jet 1.

Amplitude is increased in Figure 7.14 and there are some very striking results. As the secondary frequency is increased, break-up moves through the mode boundaries; beginning with M3 with no additional disturbance; a low frequency result yields the behaviour characterised as M2/3; through M2; and finally the highest frequency disturbance predicts M1 behaviour. This suggests that high energy disturbances of both
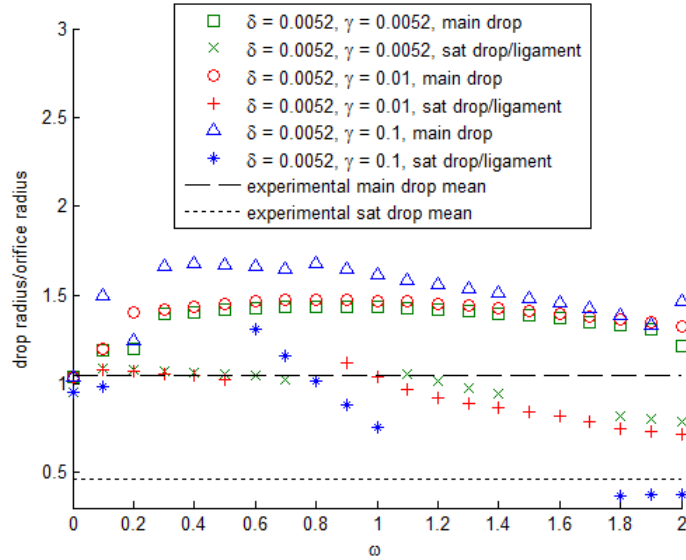
(a) drop sizes with varying ω
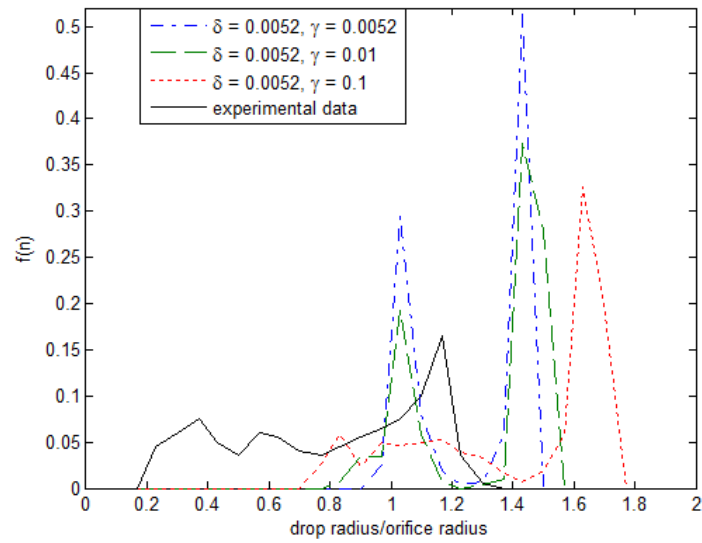
(b) drop size distribution

Figure 7.10: Effect of 3 secondary disturbances, (1) $\delta = 0.0052, \gamma = 0.0052$, (2) $\delta = 0.0052, \gamma = 0.01$ and (3) $\delta = 0.0052, \gamma = 0.1$ for Jet 4. $\epsilon = 0.01$. Also plotted is the experimental data.

108
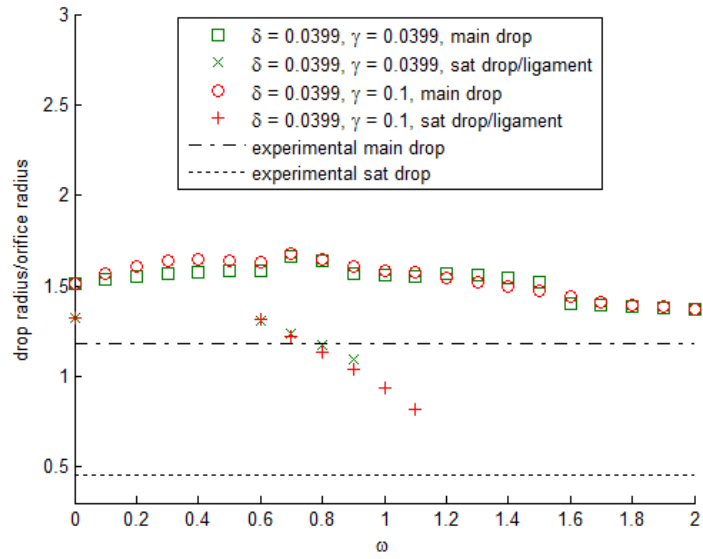
(a) drop sizes with varying ω
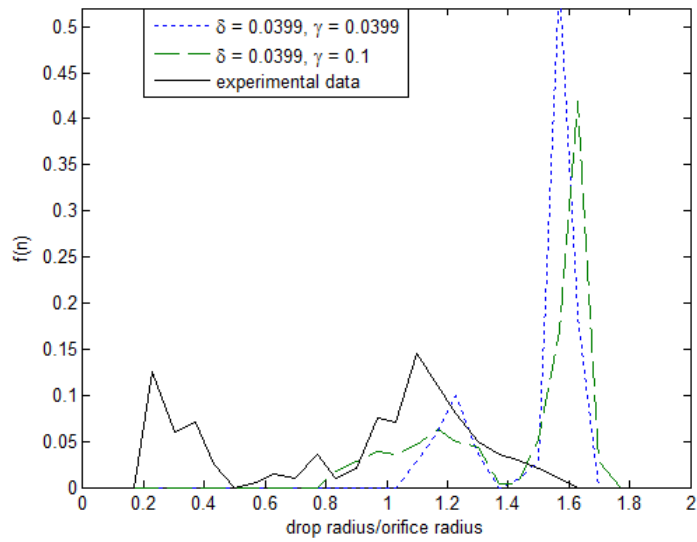
(b) drop size distribution

Figure 7.11: Effect of 3 secondary disturbances, (1) $\delta = 0.0399, \gamma = 0.0399$ and (2) $\delta = 0.0052, \gamma = 0.1$ for Jet 5. $\epsilon = 0.01$. Also plotted is the experimental data.
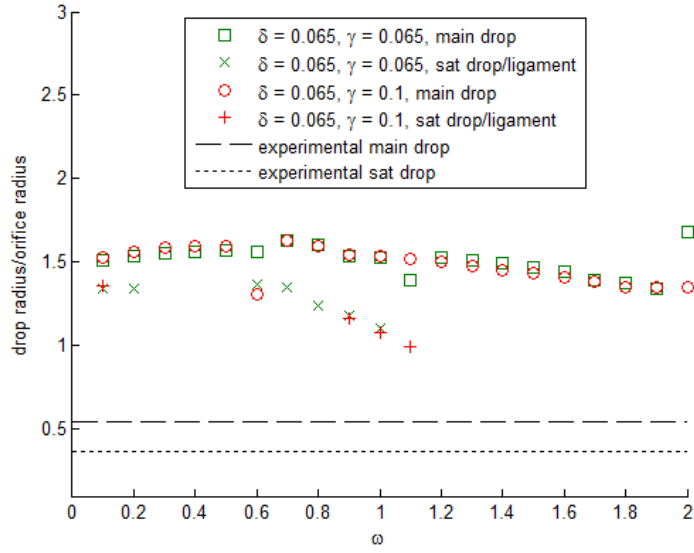
(a) drop sizes with varying ω
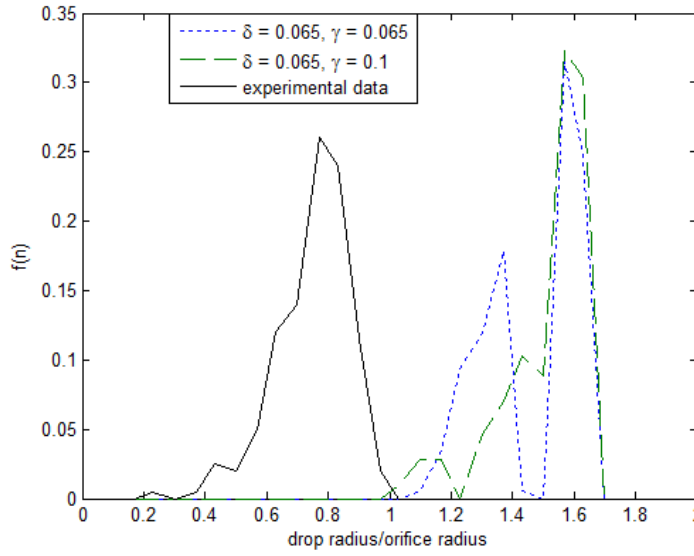
(b) drop size distribution

Figure 7.12: Effect of 3 secondary disturbances, (1) $\delta = 0.065, \gamma = 0.065$ and (2) $\delta = 0.065, \gamma = 0.1$ for Jet 6. $\epsilon = 0.01$. Also plotted is the experimental data.
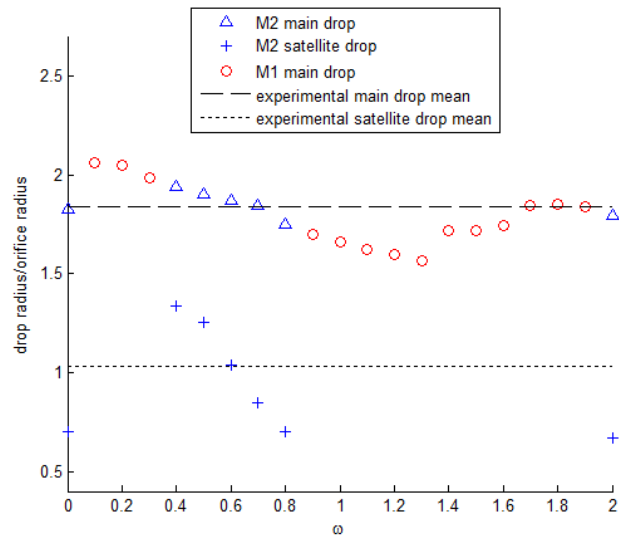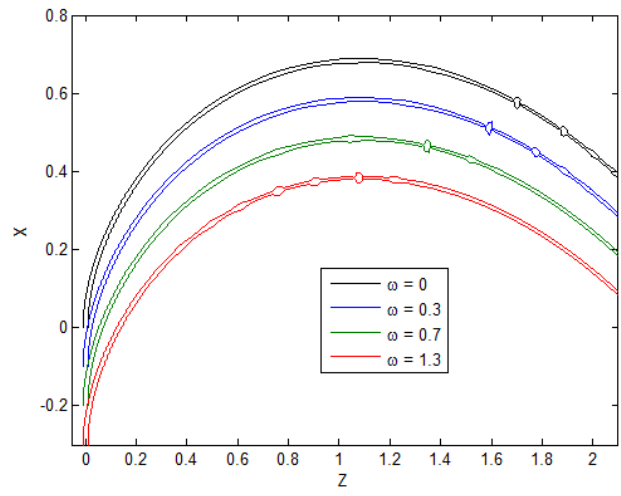
Figure 7.13: Graphs showing how the disturbance is affected by changing frequency of a low amplitude disturbance $\gamma = 0.0052$ for Jet 4. $\epsilon = 0.01$. Each jet image is shifted along the Z axis.
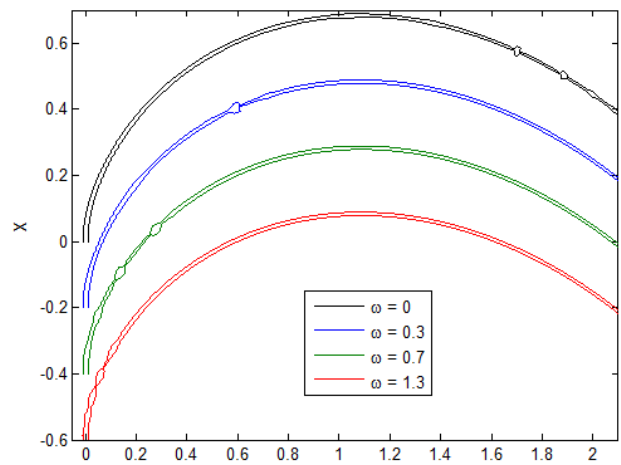
Figure 7.14: Graphs showing how the disturbance is affected by changing frequency of a high amplitude disturbance $\gamma = 0.1$ for Jet 4 $\epsilon = 0.01$. Each jet image is shifted along the Z axis.

111

high frequency and amplitude are required to generate M1 behaviour in a viscous fluid.

There is also a rather surprising result here. The disturbance frequency corresponding to $\omega = 0.7$ is very close to the most unstable frequency ($\kappa = 0.6979$ here). However, with a high amplitude secondary disturbance ($\gamma = 0.1$), at this frequency ($\omega = 0.7$) M2 behaviour is generated, not the M3 predicted which occurred with no additional disturbance (i.e. $\omega = 0$). This hints that mode break-up in the absence of secondary disturbances can be dependent on the amplitude of the most unstable wave at the orifice, contrary to what was previously thought in Chapter 5. We propose a reason for this behaviour in Chapter 10.

Figure 7.15 shows how the behaviour changes for varying frequencies, fully illustrating the movement through the mode boundaries for a high amplitude disturbance. For a very high frequency break-up reverts back to M2 behaviour. Also, M1 behaviour can be found in Figure 7.15(b).

7.3 High Viscosity Fluid

Jet 7 is now examined, though no drop size distributions are generated as it is known a priori that main droplets will be too big and satellite droplets cannot be generated from a ligament. Figure 7.16 shows the movement through the mode boundaries as the secondary disturbance is changed. However, for high amplitude high frequency disturbances there is still M2 behaviour. This may be because it was necessary to have a large δ chosen so that break-up length matches the experimental data with $\gamma = 0$, and so we cannot impose a secondary disturbance to completely dominate this unstable mode. It may also be the case that jets at this viscosity can not be forced to break-up in the M1 regime.

In the previous chapter, we discussed that the trajectory of the jet is affected

by changing the angle at the orifice, whilst qualitative behaviour remained largely unaffected. We wish to see whether this is the case for secondary disturbances. Figures 7.17 and 7.18 show how changing the orifice angle affects the growth of low and high frequency disturbances respectively. Break-up length changes with exit angle. The impact of orifice angle is further illustrated in Figure 7.19 where the full range of frequencies are examined. The exit angle has no effect on the mode of break-up on application of a secondary disturbance.

7.4   Conclusions

In this chapter we have modelled secondary disturbances in a jet using an additional sinusoidal wave. Though this does not model the mechanical vibrations in a rig, we used this to demonstrate the sensitivity of a jet to these vibrations. Through comparison with experimental data, we concluded that the experimental rig is subject to mechanical instabilities that cause such varied drop size distributions.

We also investigated the qualitative break-up of a jet as we varied the amplitude and frequency of a disturbance. We showed that as the disturbance amplitude was increased, break-up gradually moved through the mode boundaries and eradicate satellite droplets. We were unable to completely remove satellite droplets from a high viscosity fluid at a high rotation rate. We postulate that the effects described in this chapter can be used to industrial advantage. This will be discussed in Chapter 11.
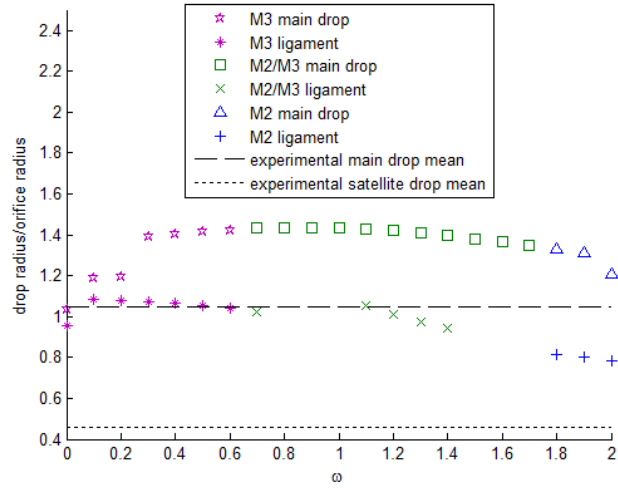
(a) low amplitude disturbance $\gamma = 0.0052$
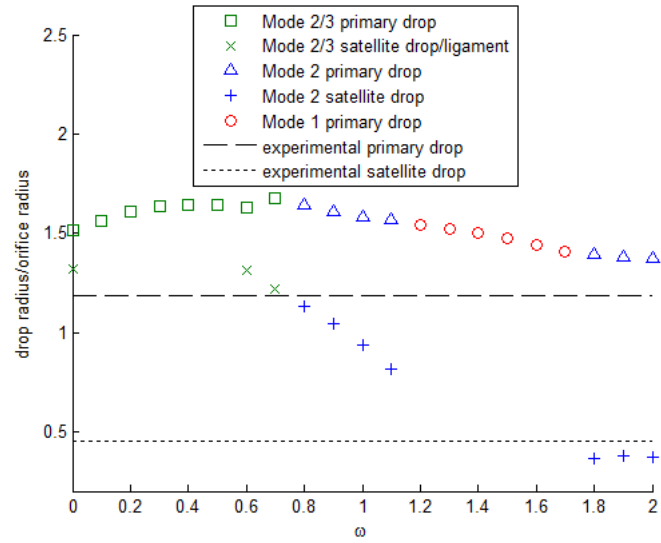
(b) high amplitude disturbance $\gamma = 0.1$

Figure 7.15: Graphs showing how the mode of jet break-up changes with varying frequency for Jet 4. $\epsilon = 0.01$.
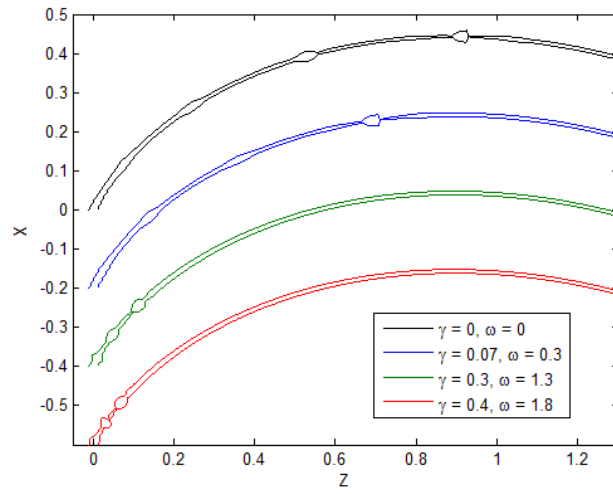
Figure 7.16: Graphs showing how the secondary disturbance is affected by changing frequency and amplitude for Jet 7. $\epsilon = 0.01$. Each jet image is shifted along the Z axis.
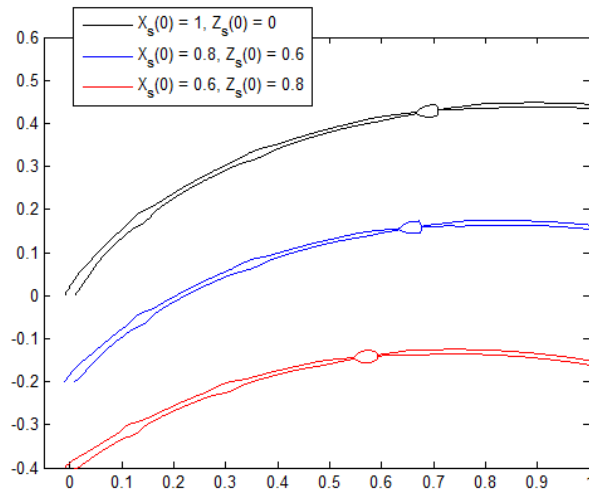
Figure 7.17: Graphs showing how the secondary disturbance affects a jet with different orifice angles with a low frequency disturbance $\omega = 0.3$ for Jet 7. $\epsilon = 0.01$. Each jet image is shifted along the Z axis.
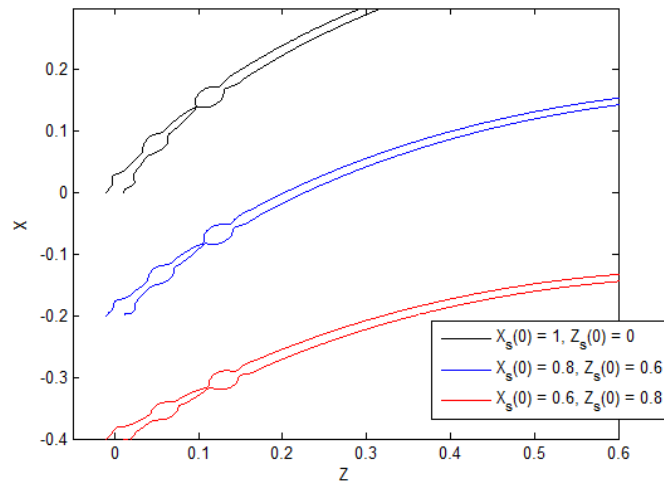
Figure 7.18: Graphs showing how the secondary disturbance affects a jet with different orifice angles with a high frequency disturbance $\omega = 1.3$ for Jet 7. $\epsilon = 0.01$.
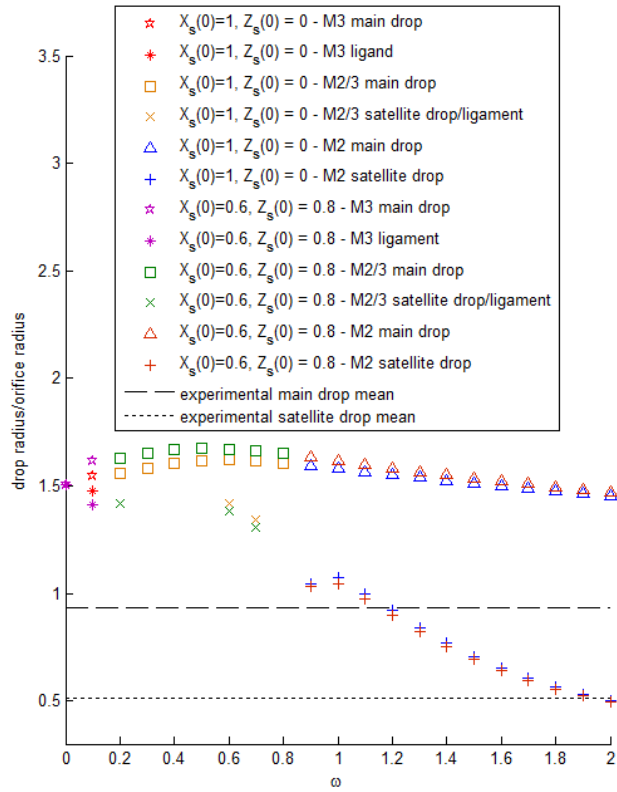
Figure 7.19: Graphs showing how the mode of jet break-up changes with varying secondary frequency for different orifice angles for Jet 7. $\epsilon = 0.01$. γ increases with increasing ω.

Chapter 8

Stability Analysis

In Chapter 6, we show that the nonlinear model can be used to accurately predict the mode of jet break-up. For Mode 2 break-up, occurring for low viscosity fluids at low rotation rates, the trajectory and drop sizes compare well to experimental data. As viscosity and rotation rate increase, however, the trajectory appeared displaced, primary drop sizes appear larger that expected and satellite droplets cannot be predicted post jet break-up.

In this chapter we investigate a local instability analysis of a jet, with the view to investigating the stability at any point on the jet at any time, in order to investigate the stability on the ligament at the time of break-up and estimate the sizes of satellite droplets.

Additionally, in Chapter 7 we imposed a secondary disturbance and showed a jet can be sensitive to disturbances other than the most unstable wave. The behaviour of different frequencies is examined by adopting a spatial instability analysis of the steady jet equations.

Firstly, we present the full equations for our problem here from [36] and [45]. In the bulk we have conservation of mass

$$\epsilon n \frac{\partial u}{\partial s} + (1 + \epsilon n \cos \phi (X_s Z_{ss} - X_{ss} Z_s)) \left(v + n \frac{\partial v}{\partial n} + \frac{\partial w}{\partial \phi} \right) \quad +$$

$$\epsilon n (X_s Z_{ss} - X_{ss} Z_s)(v \cos \phi - w \sin \phi) \quad = \quad 0,$$

and the Navier-Stokes equations

$$h_s \left(\epsilon \frac{\partial u}{\partial t} + \epsilon (v \cos \phi - w \sin \phi)(Z_{st} X_s - X_{st} Z_s) + v \frac{\partial u}{\partial n} + \frac{w}{n} \frac{\partial u}{\partial \phi} \right) + \epsilon u \frac{\partial u}{\partial s}$$

$$+ \epsilon u (X_s Z_{ss} - X_{ss} Z_s)(v \cos \phi - w \sin \phi) =$$

$$- \epsilon \frac{\partial p}{\partial s} + h_s \left(\frac{2\epsilon}{Rb} (v \cos \phi - w \sin \phi) + \frac{\epsilon}{Rb^2}((X+1)X_s + ZZ_s) \right)$$

$$+ \frac{1}{\epsilon Ren} \left[\frac{-\epsilon^3 n^2 \cos \phi (X_s Z_{sss} - Z_s X_{sss})}{h_s^2} \left(\frac{\partial u}{\partial s} + v \cos \phi (X_s Z_{ss} - Z_s X_{ss}) \right. \right.$$

$$- w \sin \phi (X_s Z_{ss} - Z_s X_{ss})) \frac{\epsilon^2 n}{h_s} \left(-u(X_s Z_{ss} - Z_s X_{ss})^2 + \frac{\partial^2 u}{\partial s^2} \right.$$

$$+ 2 \frac{\partial v}{\partial s} \cos \phi (X_s Z_{ss} - Z_s X_{ss}) + (v \cos \phi - w \sin \phi)(X_s Z_{sss} - Z_s X_{sss})$$

$$\left. - 2 \frac{\partial w}{\partial s} \sin \phi (X_s Z_{ss} - X_{ss} Z_s) \right) + (1 + 2 \epsilon n \cos \phi (X_s Z_{ss} - X_{ss} Z_s)) \frac{\partial u}{\partial n} + n h_s \frac{\partial^2 u}{\partial n^2}$$

$$\left. - \epsilon \frac{\partial u}{\partial \phi} \sin \phi (X_s Z_{ss} - Z_s X_{ss}) + \frac{h_s}{n} \frac{\partial^2 u}{\partial \phi^2} \right],$$

$$h_s \left(\epsilon \frac{\partial v}{\partial t} + \epsilon u \cos \phi (X_{st} Z_s - Z_{st} X_s) + v \frac{\partial v}{\partial n} + \frac{w}{n} \frac{\partial v}{\partial \phi} - \frac{w^2}{n} \right)$$

$$+ \epsilon u \frac{\partial v}{\partial s} - \epsilon \cos \phi (X_s Z_{ss} - Z_s X_{ss}) u^2$$

$$= \left(-\frac{\partial p}{\partial n} - \frac{2\epsilon}{Rb} u \cos \phi + \frac{h_s \epsilon \cos \phi}{Rb^2} ((X+1) Z_s - Z X_s + \epsilon n \cos \phi) \right) +$$

$$\frac{1}{\epsilon Ren} \left[\frac{-\epsilon^3 n^2 \cos \phi (X_s Z_{sss} - Z_s X_{sss})}{h_s^2} \left(\frac{\partial v}{\partial s} - u \cos \phi (X_s Z_{ss} - Z_s X_{ss}) \right) \right.$$

$$+ \frac{\epsilon^2 n}{h_s} \left(-v \cos^2 \phi (X_s Z_{ss} - Z_s X_{ss})^2 + \frac{\partial^2 v}{\partial s^2} - 2 \frac{\partial u}{\partial s} \cos \phi (X_s Z_{ss} - Z_s X_{ss}) \right.$$

$$\left. - u \cos \phi (X_s Z_{sss} - Z_s X_{sss}) + w \sin \phi \cos \phi (X_s Z_{ss} - Z_s X_{ss})^2 \right)$$

$$+ (1 + 2\epsilon n \cos \phi (X_s Z_{ss} - Z_s X_{ss})) \frac{\partial v}{\partial n} + n h_s \frac{\partial^2 v}{\partial n^2}$$

$$\left. - \epsilon \left(\frac{\partial v}{\partial \phi} - w \right) \sin \phi (X_s Z_{ss} - Z_s X_{ss}) + \frac{h_s}{n} \left(\frac{\partial^2 v}{\partial \phi^2} - v - 2 \frac{\partial w}{\partial \phi} \right) \right]$$

and

$$h_s \left(\epsilon \frac{\partial w}{\partial t} + \epsilon u \sin \phi (Z_{st} X_s - X_{st} Z_s) + v \frac{\partial w}{\partial n} + \frac{w}{n} \frac{\partial w}{\partial \phi} + \frac{wv}{n} \right)$$

$$+ \epsilon u \frac{\partial w}{\partial s} + \epsilon \sin \phi (X_s Z_{ss} - X_{ss} Z_s) u^2$$

$$= h_s \left(-\frac{1}{n} \frac{\partial p}{\partial \phi} + \frac{2\epsilon}{Rb} u \sin \phi + \frac{\epsilon \sin \phi}{Rb^2} (Z X_s - (X+1) Z_s - \epsilon n \cos \phi) \right)$$

$$+ \frac{1}{\epsilon n Re} \left[\frac{-\epsilon^3 n^2 \cos \phi (X_s Z_{sss} - Z_s X_{sss})}{h_s^2} \left(\frac{\partial w}{\partial s} \right. \right.$$

$$\left. + u \sin \phi (X_s Z_{ss} - X_{ss} Z_s) \right) + \frac{\epsilon^2 n}{h_s} \left(-w \sin^2 \phi (X_s Z_{ss} - X_{ss} Z_s)^2 + \frac{\partial^2 w}{\partial s^2} \right.$$

$$+ 2 \frac{\partial u}{\partial s} \sin \phi (X_s Z_{ss} - X_{ss} Z_s) + u \sin \phi (X_s Z_{sss} - Z_s X_{sss})$$

$$\left. + v \sin \phi \cos \phi (X_s Z_{ss} - Z_s X_{ss})^2 \right) + (1 + 2\epsilon n \cos \phi (X_s Z_{ss} - Z_s X_{ss})) \frac{\partial w}{\partial n}$$

$$\left. + n h_s \frac{\partial^2 w}{\partial n^2} - \epsilon \left(\frac{\partial w}{\partial \phi} + v \right) \sin \phi (X_s Z_{ss} - Z_s X_{ss}) + \frac{h_s}{n} \left(\frac{\partial^2 w}{\partial \phi^2} - w + 2 \frac{\partial v}{\partial \phi} \right) \right],$$

with boundary conditions on the free surface $n = R(s, \phi, t)$,

$$h_s \left(\epsilon \frac{\partial R}{\partial t} + \cos \phi (X_t Z_s - X_s Z_t) - v + \frac{w}{n} \frac{\partial R}{\partial \phi} + \frac{1}{n} \frac{\partial R}{\partial \phi} \sin \phi (X_t Z_s - X_s Z_t) \right)$$

$$+ \epsilon u \frac{\partial R}{\partial s} - \epsilon \frac{\partial R}{\partial s} (X_t Z_s + Z_t X_s + \epsilon n \cos \phi (X_s Z_{st} - X_{st} Z_s)) = 0,$$

$$\left(1 - \frac{\epsilon^2}{h_s^2} \left(\frac{\partial R}{\partial s} \right)^2 \right) \left(\epsilon \frac{\partial v}{\partial s} + h_s \frac{\partial u}{\partial n} - \epsilon u \cos \phi (X_s Z_{ss} - X_{ss} Z_s) \right) + 2\epsilon \frac{\partial R}{\partial s} \left(\frac{\partial v}{\partial n} \right.$$

$$\left. - \frac{\epsilon}{h_s} \frac{\partial u}{\partial s} - \frac{\epsilon (v \cos \phi - w \sin \phi)}{h_s} (X_s Z_{ss} - X_{ss} Z_s) \right) = 0,$$

$$\left(1 - \frac{1}{n^2} \left(\frac{\partial R}{\partial \phi} \right)^2 \right) \left(\frac{\partial w}{\partial n} - \frac{w}{n} + \frac{1}{n} \frac{\partial v}{\partial \phi} \right) + \frac{2}{n} \frac{\partial R}{\partial \phi} \left(\frac{\partial v}{\partial n} - \frac{1}{n} \left(\frac{\partial w}{\partial \phi} + v \right) \right) = 0,$$

and

$$p - \frac{2}{ReE^2} \left(\frac{\epsilon^2}{h_s^3} \left(\frac{\partial R}{\partial s} \right)^2 \left(\frac{\partial u}{\partial s} + (v \cos \phi - w \sin \phi)(X_s Z_{ss} - X_{ss} Z_s) \right) \right.$$

$$+ \frac{1}{\epsilon} \frac{\partial v}{\partial n} + \frac{1}{\epsilon R^3} \left(\frac{\partial R}{\partial \phi} \right)^2 \left(\frac{\partial w}{\partial \phi} + v \right) - \frac{\epsilon}{h_s} \frac{\partial R}{\partial s} \left(\frac{\partial v}{\partial s} + \frac{1}{\epsilon} \frac{\partial u}{\partial n} - \frac{u}{h_s} \cos \phi (X_s Z_{ss} - X_{ss} Z_s) \right)$$

$$- \frac{1}{\epsilon R} \frac{\partial R}{\partial \phi} \left(\frac{\partial w}{\partial n} - \frac{w}{R} + \frac{1}{R} \frac{\partial v}{\partial \phi} \right) + \frac{\epsilon}{h_s R} \frac{\partial R}{\partial s} \frac{\partial R}{\partial \phi} \left(\frac{1}{\epsilon R} \frac{\partial u}{\partial \phi} + \frac{u}{h_s} \sin \phi (X_s Z_{ss} - X_{ss} Z_s) \right.$$

$$\left. \left. + \frac{1}{h_s} \frac{\partial u}{\partial s} \right) \right) = \frac{\kappa}{We},$$

where

$$\kappa = \frac{1}{h_s} \left(\epsilon^2 \frac{\partial}{\partial s} \left(-\frac{1}{h_s E} \frac{\partial R}{\partial s} \right) + \frac{1}{n} \frac{\partial}{\partial n} \left(\frac{n h_s}{E} \right) + \frac{\partial}{\partial \phi} \left(-\frac{h_s}{n^2 E} \frac{\partial R}{\partial \phi} \right) \right),$$

$$h_s = (1 + \epsilon n \cos \phi (X_s Z_{ss} - X_{ss} Z_s)),$$

and

$$E = \left(1 + \frac{\epsilon^2}{h_s^2} \left(\frac{\partial R}{\partial s} \right)^2 + \frac{1}{n^2} \left(\frac{\partial R}{\partial \phi} \right)^2 \right)^{1/2}.$$

In addition we have the arclength condition

$$X_s^2 + Z_s^2 = 1$$

and centreline conditions

$$v = w = 0 \ \text{ on } \ n = 0.$$

8.1   Asymptotic Form of the Jet Equations

We examine small deformations to our variables by perturbing by a small parameter, δ, where we assume $0 < \delta << \epsilon << 1$, as follows

$$\left.\begin{aligned}
\mathbf{u} &= \hat{\mathbf{u}}(s,t,n,\phi,\epsilon) + \delta\tilde{\mathbf{u}}(s,\bar{s},n,\phi,t,\bar{t}), \\
R &= \hat{R}(s,t,\phi,\epsilon) + \delta\tilde{R}(s,\bar{s},\phi,t,\bar{t}) \\
p &= \hat{p}(s,t,n,\phi,\epsilon) + \delta\tilde{p}(s,\bar{s},n,\phi,t,\bar{t}) \\
\mathbf{X} &= \hat{\mathbf{X}}(s,t,\epsilon) + \delta\epsilon\tilde{\mathbf{X}}(s,\bar{s},t,\bar{t})
\end{aligned}\right\} \tag{8.1}$$

where $(\hat{\mathbf{u}}, \tilde{\mathbf{u}}) = (\hat{u}, \tilde{u})\mathbf{e_s} + (\hat{v}, \tilde{v})\mathbf{e_n} + (\hat{w}, \tilde{w})\mathbf{e_\phi}$, $(\hat{\mathbf{X}}, \tilde{\mathbf{X}}) = (\hat{X}, \tilde{X})\mathbf{i} + (\hat{Z}, \tilde{Z})\mathbf{k}$. (We note that we first tried $\mathbf{X} = \hat{\mathbf{X}}(s,t,\epsilon) + \delta\tilde{\mathbf{X}_0}(s,\bar{s},t,\bar{t}) + \delta\epsilon\tilde{\mathbf{X}}(s,\bar{s},t,\bar{t})$, but $\tilde{\mathbf{X}_0}$ was found to be identically equal to zero). The variables with a hat describe the solution to the leading order unsteady nonlinear equations, and the variables with a tilde denote the unsteady linear disturbances describing the perturbation. We have introduced a short lengthscale $\bar{s}$ and a short timescale $\bar{t}$, given by s/ϵ and t/ϵ respectively, in order to describe the shorter wave-like disturbances of $O(\epsilon)$, as in Chapter 3.

8.1.1 Unsteady Nonlinear Jet Equations

We apply the above asymptotic expansions to the jet equations, taking O(1) equations in δ in order to obtain $\hat{\mathbf{u}}, \hat{R}, \hat{p}$ and $\hat{\mathbf{X}}$. We then apply asymptotic Taylor series solutions of the form

$$
\left.
\begin{aligned}
\hat{\mathbf{u}} &= u_0(s,t)\mathbf{e_s} + (\epsilon n)\mathbf{u}_1(s,\phi,t) + (\epsilon n)^2\mathbf{u}_2(s,\phi,t) + O\left((\epsilon n)^3\right), \\
\hat{R} &= R_0(s,t) + (\epsilon n)R_1(s,\phi,t) + (\epsilon n)^2 R_2(s,\phi,t) + O\left((\epsilon n)^3\right), \\
\hat{p} &= p_0(s,\phi,t) + (\epsilon n)p_1(s,\phi,t) + (\epsilon n)^2 p_2(s,\phi,t) + O\left((\epsilon n)^3\right), \\
\hat{\mathbf{X}} &= \mathbf{X}_0(s) + (\epsilon n)\mathbf{X}_1(s,t) + (\epsilon n)^2\mathbf{X}_2(s,t) + O\left((\epsilon n)^3\right),
\end{aligned}
\right\} \tag{8.2}
$$

where $\mathbf{u}_i = u_i\mathbf{e_s} + v_i\mathbf{e_n} + w_i\mathbf{e}_\phi$ for $i = 1,2$ and $\mathbf{X}_i = X_i\mathbf{i} + Z_i\mathbf{k}$ for $i = 0,1,2$. We rewrite X_0 as X, Z_0 as Z, define $S = X_s Z_{ss} - Z_s X_{ss}$ and obtain the following equations (8.3) - (8.16). Taking the Continuity Equation at $O(\epsilon n)$:

$$
u_{0s} + 2v_1 + w_{1\phi} = 0, \tag{8.3}
$$

and at $O\left((\epsilon n)^2\right)$:

$$
u_{1s} + 3v_2 + w_{2\phi} + (3v_1 + w_{1\phi})S\cos\phi - w_1 S\sin\phi = 0. \tag{8.4}
$$

The first Navier-Stokes equation at $O(\epsilon)$:

$$
\begin{aligned}
u_{0t} + u_0 u_{0s} &= -p_{0s} + \frac{1}{Rb^2}((X+1)X_s + ZZ_s) \\
&+ \frac{1}{Re}\Big(-u_0 S^2 + u_{0ss}4u_2 + u_{2\phi\phi} + (2u_1 + u_{1\phi\phi})S\cos\phi - u_{1\phi}S\sin\phi\Big),
\end{aligned}
\tag{8.5}
$$

the second Navier-Stokes equation at $O(\epsilon)$:

$$
\begin{aligned}
-u_0^2 S \cos\phi \;=\;& -p_1 - \frac{2}{Rb} u_0 \cos\phi + \frac{\cos\phi}{Rb^2}((X+1)Z_s + ZX_s) \\
& + \frac{1}{Re}\Big(3v_2 + v_{2\phi\phi} - 2w_{2\phi}((-2u_{0s} + v_1 + v_{1\phi\phi} - 2w_{1\phi})S - u_0 S_S)\cos\phi \\
& - (w_1 - v_{1\phi})S\sin\phi\Big),
\end{aligned}
\tag{8.6}
$$

the third Navier-Stokes equation at $O(1)$:

$$
p_{0\phi} = 0,
\tag{8.7}
$$

and at $O(\epsilon)$:

$$
\begin{aligned}
u_0^2 S \sin\phi \;=\;& -p_{1\phi} + \frac{2}{Rb} u_0 \sin\phi - \frac{\sin\phi}{Rb^2}((X+1)Z_s + ZX_s) \\
& + \frac{1}{Re}\Big(3w_2 + w_{2\phi\phi} + 2v_{2\phi}(w_1 + w_{1\phi\phi} + 2v_{1\phi})S\cos\phi \\
& + ((2u_{0s} + v_1 - w_{1\phi\phi})S + u_0 S_S)\sin\phi\Big).
\end{aligned}
\tag{8.8}
$$

The Kinematic Condition at $O(\epsilon)$:

$$
R_{0t} - R_0 v_1 + u_0 R_{0s} = 0,
\tag{8.9}
$$

the first Tangential Stress Condition at $O(\epsilon)$:

$$
u_1 = u_0 S \cos\phi,
\tag{8.10}
$$

and at $O(\epsilon^2)$:

$$
R_0 v_{1s} + 2R_0 u_2 + R_{0s}(v_1 - u_{0s}) = 0.
\tag{8.11}
$$

124

The second Tangential Stress Condition at $O(\epsilon)$:

$$v_{1\phi} = 0, \tag{8.12}$$

and at $O(\epsilon^2)$:

$$R_0 w_2 + R_0 v_{2\phi} + \frac{2}{R_0} R_{1\phi} w_{1\phi} = 0. \tag{8.13}$$

The Normal Stress Condition to $O(1)$:

$$p_0 - \frac{2}{Re} v_1 = \frac{1}{We R_0}, \tag{8.14}$$

and at $O(\epsilon)$:

$$
\begin{aligned}
R_0 p_1 \quad - \quad & \frac{2}{Re}\left(2R_0 v_2 - \frac{1}{R_0} R_{1\phi} v_{1\phi} - R_{0s}(u_1 - u_0 S \cos\phi)\right) \\
= \quad & \frac{1}{We}\left(S\cos\phi - \frac{R_1 + R_{1\phi\phi}}{R_0^2}\right).
\end{aligned}
\tag{8.15}
$$

The final equation is the arclength condition, at leading order this is

$$X_s^2 + Z_s^2 = 1. \tag{8.16}$$

Equation (8.12) implies that $v_1 = v_1(s,t)$ and (8.7) implies $p_0 = p_0(s,t)$. Differentiating (8.3) with respect to ϕ gives

$$w_{1\phi\phi} = 0 \Rightarrow w_{1\phi} = C,$$

where C is a constant. As we require periodic solutions with respect to ϕ, $C = 0$ and

so $w_1 = w_1(s, t)$. Evaluating (8.3) we obtain

$$v_1 = \frac{-u_{0s}}{2}. \tag{8.17}$$

Differentiating (8.13) with respect to ϕ yields

$$w_{2\phi} = -v_{2\phi\phi}$$

and we substitute this result, along with (8.10), into (8.4) to get

$$v_{2\phi\phi} - 3v_2 = \left(-\frac{1}{2}u_{0s}S + u_0 S_s\right)\cos\phi - w_1 S \sin\phi. \tag{8.18}$$

The particular solution to (8.18) is

$$v_2 = \frac{1}{4}\left(\frac{1}{2}u_{0s}S - u_0 S_s\right)\cos\phi + \frac{1}{4}w_1 S \sin\phi, \tag{8.19}$$

and hence

$$w_2 = \frac{1}{4}\left(\frac{1}{2}u_{0s}S - u_0 S_s\right)\sin\phi - \frac{1}{4}w_1 S \cos\phi. \tag{8.20}$$

Substituting (8.19) and (8.20) into (8.6) and rearranging for p_1, gives

$$
\begin{aligned}
p_1 &= \left[u_0^2 S - \frac{2u_0}{Rb} + \frac{1}{Rb^2}((X+1)Z_s - ZX_s) - \frac{1}{Re}\left(\frac{5}{2}u_{0s}S + u_0 S_s\right)\right]\cos\phi \\
&+ \frac{1}{Re}w_1 S \sin\phi.
\end{aligned} \tag{8.21}
$$

We note that substituting (8.19) and (8.20) into (8.8) gives

$$
\begin{aligned}
p_{1\phi} &= -\left[u_0^2 S - \frac{2u_0}{Rb} + \frac{1}{Rb^2}((X+1)Z_s - ZX_s) - \frac{1}{Re}\left(\frac{5}{2}u_{0s}S + u_0 S_s\right)\right]\sin\phi \\
&+ \frac{1}{Re}w_1 S \cos\phi,
\end{aligned} \tag{8.22}
$$

126

which is (8.21) differentiated with respect to ϕ. We substitute (8.10), (8.19) and (8.21) into (8.15) and obtain the equation

$$\frac{R_1 + R_{1\phi\phi}}{R_0^3} = \left[u_0^2 S - \frac{2u_0}{Rb} + \frac{1}{Rb}((X+1)Z_s - ZX_s) - \frac{3}{Re}u_{0s}S - \frac{S}{WeR_0} \right] \cos\phi. \tag{8.23}$$

In order to remove the non periodic secular terms in (8.23), the right hand side must be identically equal to zero, and so

$$(X_s Z_{ss} - Z_s X_{ss})\left(u_0^2 - \frac{3}{Re}u_{0s} - \frac{1}{WeR_0} \right) - \frac{2u_0}{Rb} + \frac{1}{Rb}((X+1)Z_s - ZX_s) = 0. \tag{8.24}$$

This is the first equation describing the nonlinear evolution of the jet.

We substitute (8.17) into (8.11) and rearrange for u_2 yielding

$$u_2 = \frac{u_{0ss}}{4} - \frac{3}{2}\frac{u_{0s}R_{0s}}{R_0}. \tag{8.25}$$

Substituting (8.17) into (8.14) and differentiating with respect to s yields

$$p_{0s} = -\frac{1}{Re}u_{0ss} + \frac{1}{We}\left(\frac{1}{R_0} \right)_s. \tag{8.26}$$

We substitute u_2 and p_{0s}, along with (8.10), into (8.5) and obtain the second equation

$$u_{0t} + u_0 u_{0s} = -\frac{1}{We}\left(\frac{1}{R_0} \right)_s + \frac{1}{Rb^2}((X+1)X_s + ZZ_s) + \frac{3}{Re}\left(\frac{(u_{0s}R_0^2)_s}{R_0^2} \right). \tag{8.27}$$

Finally, we substitute (8.17) into (8.9) and obtain the third equation

$$R_{0t} + \frac{R_0 u_{0s}}{2} + u_0 R_{0s} = 0. \tag{8.28}$$

Equations (8.24), (8.27) and (8.28), along with (8.16) are our system of four equations

for the four unknowns R_0, u_0, X and Z. The conditions at the orifice are $X = Z = Z_s = 0$, $X_s = R_0 = u_0 = 1$ at $s = 0$. Note that we are assuming that X and Z are not time dependent, as demonstrated in calculations carried out in [35, 36].

Steady State Equations

The initial conditions for the temporal problem are given by the steady solutions to equations (8.24), (8.27), (8.28) and (8.16), namely

$$u_0 u_{0s} = -\frac{1}{2We}\frac{u_{0s}}{\sqrt{u_0}} + \frac{(X+1)X_s + ZZ_s}{Rb^2} + \frac{3}{Re}\left(u_{0ss} - \frac{u_{0s}^2}{u_0}\right),$$

$$(X_s Z_{ss} - Z_s X_{ss})\left(u_0^2 - \frac{3}{Re}u_{0s} - \frac{\sqrt{u_0}}{We}\right) - \frac{2u_0}{Rb} + \frac{((X+1)Z_s - ZX_s)}{Rb^2} = 0,$$

$$X_s^2 + Z_s^2 = 1, \quad (8.29)$$

where $u_0 = 1/R_0^2$, and the boundary conditions at $s = 0$ are given by $X = Z = Z_s = 0$ and $X_s = u_0 = 1$. Downstream boundary conditions are given by $u_0(\infty) = \infty$ and $R_0(\infty) = 0$ as described in Chapter 3.

Temporal Equations

The non-linear temporal system to be solved are equations (8.27) and (8.28) for u_0 and R_0. Here $\kappa = 1/R_0$ is the leading order curvature term obtained in the derivation of the nonlinear equations. Eggers and Villermaux [17] describe the importance of the full curvature in the nonlinear PDEs, and we must include the full radial and longitudinal components of curvature here before the asymptotic expansions in δ are

applied. Hence

$$
\begin{aligned}
\kappa &= \frac{1}{R(1+\epsilon^2 R_s^2)^{1/2}} - \frac{\epsilon^2 R_{ss}}{(1+\epsilon^2 R_s^2)^{3/2}} \\
&= (\hat{R}+\delta\tilde{R})^{-1}\left((1+\epsilon^2(\hat{R}+\delta\tilde{R})_s^2)^{1/2}\right) - \epsilon^2(\hat{R}+\delta\tilde{R})_{ss}\left((1+\epsilon^2(\hat{R}+\delta\tilde{R})_s^2)^{3/2}\right) \\
&= \frac{1}{\hat{R}(1+\epsilon^2\hat{R}_s^2)^{1/2}} - \frac{\epsilon^2\hat{R}_{ss}}{(1+\epsilon^2\hat{R}_s^2)^{3/2}} \\
&+ \delta\left[\frac{1}{\hat{R}(2\epsilon^2\hat{R}_s\tilde{R}_s + 2\epsilon\hat{R}_s\tilde{R}_{\bar{s}})^{1/2}} - \frac{\tilde{R}}{\hat{R}^2} - \frac{\epsilon^2\tilde{R}_{ss} + \epsilon\tilde{R}_{s\bar{s}} + \tilde{R}_{\bar{s}\bar{s}}}{(1+\epsilon^2\hat{R}_s^2)^{3/2}}\right. \\
&\left. - \frac{\epsilon^2\hat{R}_{ss}}{(2\epsilon^2\hat{R}_s\tilde{R}_s + 2\epsilon\hat{R}_s\tilde{R}_{\bar{s}})^{3/2}}\right]
\end{aligned}
$$

So, asymptotically, we retain the full curvature to leading order in δ and so the full temporal system we solve is given by

$$
\begin{aligned}
A_t + (Au)_s &= 0 \\
u_t + \left(\frac{u^2}{2}\right)_s &= -\frac{1}{We}\frac{\partial}{\partial s}\left(\frac{4(2A+(\epsilon A_s)^2 - \epsilon^2 AA_{ss})}{(4A+(\epsilon A_s)^2)^{3/2}}\right) + \frac{(X+1)X_s + ZZ_s}{Rb^2} \\
&+ \frac{3}{Re}\frac{(Au_s)_s}{A}.
\end{aligned} \tag{8.30}
$$

at $O(1)$ in δ. Here $A = R_0^2$, with initial conditions

$$
A(s, t=0) = R_0^2(s), \qquad u(s, t=0) = u_0(s),
$$

provided by the above steady state equations (8.29). Likewise X and Z in (8.30) are obtained from (8.29) at all times as in [35, 36]. The periodic boundary conditions at the orifice are

$$
A(s=0, t) = 1, \qquad u(s=0, t) = 1 + \delta\sin\left(\frac{\kappa t}{\epsilon}\right),
$$

129

where δ and κ are the amplitude and frequency of the disturbance.

8.1.2 Instability Equations

The equations describing the instability are obtained by taking the full equations to $O(\delta)$ and to leading order in ϵ, namely

$$n\frac{\partial \tilde{u}}{\partial \bar{s}} + \tilde{v} + n\frac{\partial \tilde{v}}{\partial n} + \frac{\partial \tilde{w}}{\partial \phi} = 0,$$

$$\frac{\partial \tilde{u}}{\partial \bar{t}} + u_0\frac{\partial \tilde{u}}{\partial \bar{s}} = -\frac{\partial \tilde{p}}{\partial \bar{s}} + \frac{Oh}{We^{1/2}}\left[\frac{\partial^2 \tilde{u}}{\partial \bar{s}^2} + \frac{1}{n}\frac{\partial \tilde{u}}{\partial n} + \frac{\partial^2 \tilde{u}}{\partial n^2} + \frac{1}{n^2}\frac{\partial^2 \tilde{u}}{\partial \phi^2}\right],$$

$$\frac{\partial \tilde{v}}{\partial \bar{t}} + u_0\cos\phi(\tilde{X}_{\bar{s}\bar{t}}Z_s - \tilde{Z}_{\bar{s}\bar{t}}X_s) + u_0\frac{\partial \tilde{v}}{\partial \bar{s}} - \cos\phi(X_s\tilde{Z}_{\bar{s}\bar{s}} - Z_s\tilde{X}_{\bar{s}\bar{s}})u_0^2 =$$

$$-\frac{\partial \tilde{p}}{\partial n} + \frac{Oh}{We^{1/2}}\left[\frac{\partial^2 \tilde{v}}{\partial \bar{s}^2} + u_0\cos\phi(X_s\tilde{Z}_{\bar{s}\bar{s}\bar{s}} - Z_s\tilde{X}_{\bar{s}\bar{s}\bar{s}})\right.$$

$$\left. +\frac{1}{n}\frac{\partial \tilde{v}}{\partial n} + \frac{\partial^2 \tilde{v}}{\partial n^2} + \frac{1}{n^2}\left(\frac{\partial^2 \tilde{v}}{\partial \phi^2} - \tilde{v} - 2\frac{\partial \tilde{w}}{\partial \phi}\right)\right],$$

$$\frac{\partial \tilde{w}}{\partial \bar{t}} + u_0\sin\phi(\tilde{Z}_{\bar{s}\bar{t}}X_s - \tilde{X}_{\bar{s}\bar{t}}Z_s) + u_0\frac{\partial \tilde{w}}{\partial \bar{s}} + \sin\phi(X_s\tilde{Z}_{\bar{s}\bar{s}} - \tilde{X}_{\bar{s}\bar{s}}Z_s)u_0^2 =$$

$$-\frac{1}{n}\frac{\partial \tilde{p}}{\partial \phi} + \frac{Oh}{We^{1/2}}\left[\frac{\partial^2 \tilde{w}}{\partial \bar{s}^2} + u_0\sin\phi(X_s\tilde{Z}_{\bar{s}\bar{s}\bar{s}} - Z_s\tilde{X}_{\bar{s}\bar{s}\bar{s}})\right.$$

$$\left. +\frac{1}{n}\frac{\partial \tilde{w}}{\partial n} + \frac{\partial^2 \tilde{w}}{\partial n^2} + \frac{1}{n^2}\left(\frac{\partial^2 \tilde{w}}{\partial \phi^2} - \tilde{w} + 2\frac{\partial \tilde{w}}{\partial \phi}\right)\right],$$

with conditions on $n = R_0$:

$$\frac{\partial \tilde{R}}{\partial \bar{t}} - \tilde{v} + \cos\phi(\tilde{X}_{\bar{t}}Z_s - X_s\tilde{Z}_{\bar{t}}) + u_0\frac{\partial \tilde{R}}{\partial \bar{s}} = 0,$$

$$\frac{\partial \tilde{v}}{\partial \bar{s}} + \frac{\partial \tilde{u}}{\partial n} - u_0\cos\phi(X_s\tilde{Z}_{\bar{s}\bar{s}} - \tilde{X}_{\bar{s}\bar{s}}Z_s) = 0,$$

$$\frac{\partial \tilde{w}}{\partial n} - \frac{\tilde{w}}{R_0} + \frac{1}{R_0}\frac{\partial \tilde{v}}{\partial \phi} = 0,$$

$$\tilde{p} - \frac{2Oh}{We}\frac{\partial \tilde{v}}{\partial n} = \frac{1}{We}\left(-\frac{1}{R_0^2}\left(\tilde{R} + \frac{\partial^2 \tilde{R}}{\partial \phi^2}\right)\right) + \cos\phi\left(X_s\frac{\partial^2 \tilde{Z}}{\partial \bar{s}^2} - Z_s\frac{\partial^2 \tilde{X}}{\partial \bar{s}^2}\right) - \frac{\partial^2 \tilde{R}}{\partial \bar{s}^2}\right),$$

$$X_s\tilde{X}_{\bar{s}\bar{s}} + Z_s\tilde{Z}_{\bar{s}\bar{s}} = 0,$$

and on $n = 0$

$$\tilde{v} = \tilde{w} = 0. \tag{8.31}$$

We search for solutions of the instability problem by searching for Fourier series solutions of the form

$$
\begin{aligned}
\tilde{\mathbf{u}} &= \exp\left(ik(s,t)\bar{s} + \lambda(s,t)\bar{t}\right)\left(\hat{\mathbf{u}}_1(s,n) + \sum_{m=1}^{\infty} \hat{\mathbf{u}}_{m0}(s,n)\cos(m\phi) + \hat{\mathbf{u}}_{m1}(s,n)\sin(m\phi)\right) + c.c., \\
\tilde{p} &= \exp\left(ik(s,t)\bar{s} + \lambda(s,t)\bar{t}\right)\left(\hat{p}_1(s,n) + \sum_{m=1}^{\infty} \hat{p}_{m0}(s,n)\cos(m\phi) + \hat{p}_{m1}(s,n)\sin(m\phi)\right) + c.c., \\
\tilde{R} &= \exp\left(ik(s,t)\bar{s} + \lambda(s,t)\bar{t}\right)\left(\hat{R}_1(s) + \sum_{m=1}^{\infty} \hat{R}_{m0}(s)\cos(m\phi) + \hat{R}_{m1}(s)\sin(m\phi)\right) + c.c., \\
\tilde{\mathbf{X}} &= \exp\left(ik(s,t)\bar{s} + \lambda(s,t)\bar{t}\right)\hat{\mathbf{X}}_1 + c.c.,
\end{aligned}
\tag{8.32}
$$

where $(\hat{\mathbf{u}}_1, \hat{\mathbf{u}}_{m0}, \hat{\mathbf{u}}_{m1}) = i(\hat{u}_1, \hat{u}_{m0}, \hat{u}_{m1})\mathbf{e_s} + (\hat{v}_1, \hat{v}_{m0}, \hat{v}_{m1})\mathbf{e_n} + (\hat{w}_1, \hat{w}_{m0}, \hat{w}_{m1})\mathbf{e_\phi}$ and $\hat{\mathbf{X}}_1 = \hat{X}_1\mathbf{i} + \hat{Z}_1\mathbf{k}$. The wavenumber and frequencies are functions of t as well as s, namely $k(s,t)$ and $\lambda(s,t)$, allowing both to be complex quantities. In addition $c.c.$ denotes the complex conjugate. Through inclusion of a temporally dependent mode, we can use stability analysis at the time of break-up to give an indication of post break-up behaviour. This is of special interest concerning ligament break-up.

After considerable work, the dispersion relation governing jet stability is given by

$$
\begin{aligned}
(\lambda + iu_0 k)^2 \quad &+ \quad \frac{2(\lambda + iu_0 k)}{Re I_m(kR_0)}\left[I_m''(kR_0) - \frac{2k^2 I_m'(kR_0)I_m''(\tilde{k}R_0)}{(k^2 + \tilde{k}^2)I_m'(\tilde{k}R_0)}\right] \\
&+ \quad \frac{1}{We}\left(k^2 - \frac{1}{R_0^2}(1 - m^2)\right)\left[\frac{(\tilde{k}^2 - k^2)I_m'(kR_0)}{(\tilde{k}^2 + k^2)I_m(kR_0)}\right] = 0, \tag{8.33}
\end{aligned}
$$

This derivation is given in Appendix A. For the unstable mode $m = 0$, the dispersion

131

relation is

$$
\begin{aligned}
We^{3/2}R_0^2 \ \lambda^2 k^2 I_0(kR_0)I_1(\tilde{k}R_0) \quad &+ \quad We^{3/2}R_0^2 \ \lambda^2 \tilde{k}^2 I_0(kR_0)I_1(\tilde{k}R_0) \\
+2iWe^{3/2}R_0^2 \ \lambda k^3 I_0(kR_0)I_1(\tilde{k}R_0) \quad &+ \quad 2iWe^{3/2}u_0 R_0^2 \ \lambda k \tilde{k}^2 I_0(kR_0)I_1(\tilde{k}R_0) \\
-We^{3/2}R_0^2 u_0^2 \ k^4 I_0(kR_0)I_1(\tilde{k}R_0) \quad &- \quad We^{3/2}R_0^2 u_0^2 \ k^2 \tilde{k}^2 I_0(kR_0)I_1(\tilde{k}R_0) \\
+2OhWeR_0^2 \ \lambda k^4 I_0(kR_0)I_1(\tilde{k}R_0) \quad &+ \quad 2OhWeR_0 \ \lambda k^3 I_1(kR_0)I_1(\tilde{k}R_0) \\
+2OhWeR_0^2 \ \lambda k^2 \tilde{k}^2 I_0(kR_0)I_1(\tilde{k}R_0) \quad &- \quad 2OhWeR_0 \ \lambda k \tilde{k}^2 I_1(kR_0)I_1(\tilde{k}R_0) \\
-4OhWe \ \lambda k^3 \tilde{k} I_1(kR_0)I_0(\tilde{k}R_0) \quad &+ \quad 2iOhWeR_0^2 u_0 \ k^5 I_0(kR_0)I_1(\tilde{k}R_0) \\
+2iOhWeR_0 u_0 \ k^4 I_1(kR_0)I_1(\tilde{k}R_0) \quad &+ \quad 2iOhWeR_0^2 u_0 \ k^3 \tilde{k}^2 I_0(kR_0)I_1(\tilde{k}R_0) \\
-2iOhWeR_0 u_0 \ k^2 \tilde{k}^2 I_1(kR_0)I_1(\tilde{k}R_0) \quad &- \quad 4iOhWeR_0^2 u_0 \ k^4 \tilde{k} I_1(kR_0)I_0(\tilde{k}R_0) \\
-\sqrt{We} \ k \tilde{k}^2 I_1(kR_0)I_1(\tilde{k}R_0) \quad &+ \quad \sqrt{We} \ k^3 I_1(kR_0)I_1(\tilde{k}R_0) \\
+\sqrt{We}R_0^2 \ k^3 \tilde{k}^2 I_1(kR_0)I_1(\tilde{k}R_0) \quad &- \quad \sqrt{We}R_0^2 \ k^5 I_1(kR_0)I_1(\tilde{k}R_0) = 0 \quad (8.34)
\end{aligned}
$$

where $Re = We^{1/2}/Oh$ and $\tilde{k}^2 = k^2 + We^{1/2}(\lambda + iu_0 k)/Oh$. This is the dispersion relation we solve for k (or λ) to investigate the jet stability. This is identical to the equation presented in Decent *et al.* [12], yet now we can investigate stability as the jet evolves with time, since in the above equation $R_0 = R_0(s,t)$ and $u_0 = u_0(s,t)$ obtained from (8.30).

8.2   Spatial Instability of the Steady State

From the previous chapter we saw the effect of the additional disturbances on jet break-up. On application of a low frequency disturbance, satellite droplets could be eradicated, whilst applying high frequencies always caused a change in jet break-up if it was applied with a large amplitude (though it did not always prevent satellite drop formation).
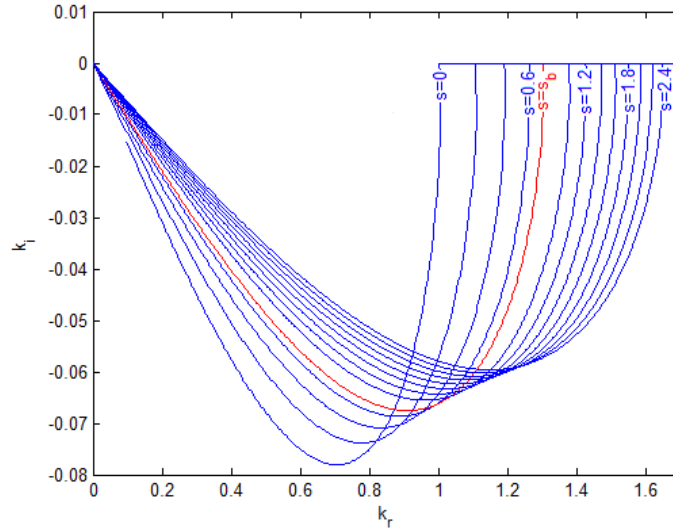
Figure 8.1: Graph showing the wavenumber k for $0 < \omega < 5$ for Jet 1. $\epsilon = 0.01$. Each curve corresponds to a different value of s. Along each curve, ω increases from 0 to 5.

We shall investigate the spatial instability of these additional disturbances and investigate the behaviour down the jet. The time dependence is removed from k and λ in the dispersion relation (8.34) and we use the steady state given by (8.29).

For spatial instability, $k = k_r + ik_i$ and $\lambda = -i\omega$ where ω is a real frequency. Thus k_i describes the growth rate of the disturbance, $k^* = k_r$ is the most unstable wavenumber found at $\min(k_i)$, and ω^* is the corresponding frequency. Figure 8.1 shows the stability at different points along Jet 1 (see Table 6.1). Each curve corresponds to a different value of s and along each curve, ω increases from 0 to 5. Here $s = s_b$ is the experimentally observed break-up length for these parameters. As s increases, the most unstable wave is generated by a larger wavenumber yielding shorter wavelength disturbances, and the growth rate of each disturbance is smaller. The most unstable wave in each case is at the minimum of each curve.

Figure 8.2 shows that the drop radius, found by integrating over a wavelength of the most unstable wave, decreases as s increases due to the shorter wavelength disturbances

133
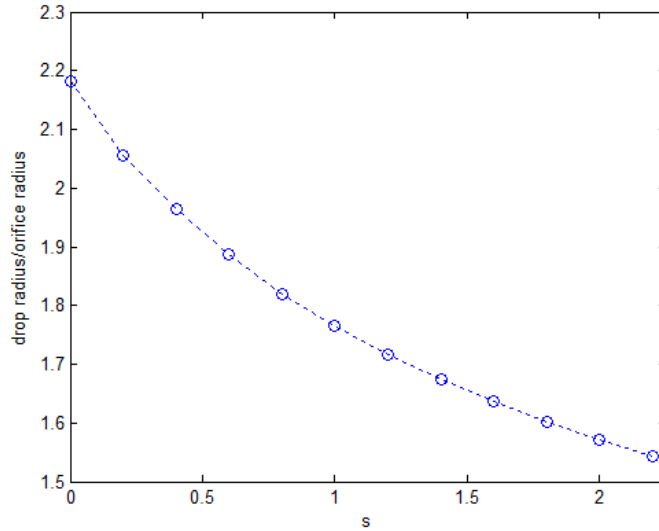
Figure 8.2: Graph showing the predicted drop sizes from linear theory produced by the most unstable wave for different values of s for Jet 1. $\epsilon = 0.01$.

along a thinner section of the jet. This describes the size of drops that will be produced given rupture at each point on the jet.

In Figure 8.3, the effect of different frequencies is investigated. It shows that the wave with the largest growth rate occurs for higher values of ω for larger s. The effect of different frequencies is shown to greater effect in Figure 8.4. There is a difference in behaviour between lower frequencies $\omega < 0.6065$, middle frequencies $\omega \approx 0.6065$ and higher frequencies $\omega > 0.6065$. $\omega = 0.6065$ corresponds to the frequency of the most unstable wave $\omega^*(s = 0)$ at the orifice.

The middle frequencies have the largest growth rate close to the orifice which decrease exponentially down the jet. The lower frequencies also have maximum growth rate at the orifice, though the growth rate is smaller than for the middle frequencies and low frequencies never correspond to the maximum growth rate. These also decrease exponentially down the jet. Higher frequencies however, have zero growth rate at the orifice. At a given value of s these disturbances suddenly become unstable and so disturbances of these high frequencies naturally grow at points away from the orifice,

134
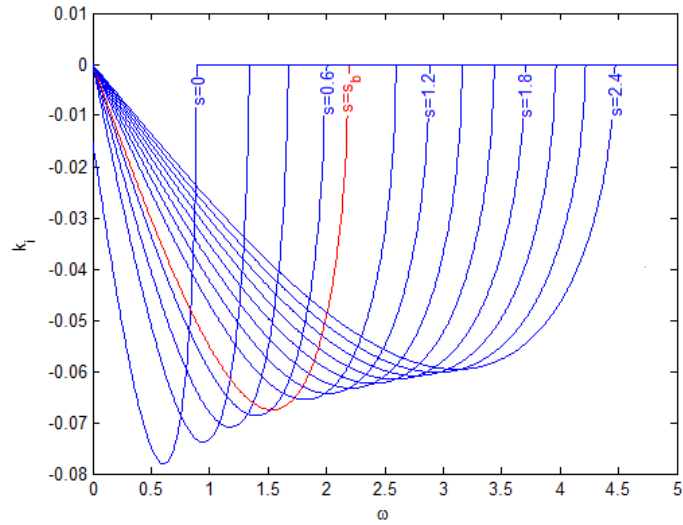
Figure 8.3: Graph showing the growth rate k_i plotted against ω for different values of s for Jet 1. $\epsilon = 0.01$.

and not at the orifice. Each discrete value of ω has growth rate at a maximum at a single point down the jet.

This perhaps explains some of the results in the previous chapter on the effect of secondary forced disturbances. Lower frequencies applied at small amplitudes had little effect, due to the smaller growth rate at all points down the jet for these waves. For higher frequencies at low amplitude there was minimal effect on the jet. These disturbance would become unstable down the jet, but as the growth rate is much smaller towards the orifice, the most unstable wave $k^*(s = 0)$ still grows more quickly and dominates the break-up. However, at high amplitudes, break-up occurred very close to the orifice as the disturbance suddenly became unstable.

This may explain why it was necessary to set a larger value of δ to match break-up for higher rotation rates. For the higher rotation rates we would expect larger vibrations in the rig, thus resulting in shorter jet break-up than if no disturbances were present. As a consequence, matching to experimental images it was necessary to choose a larger value of δ when there was no additional disturbance.
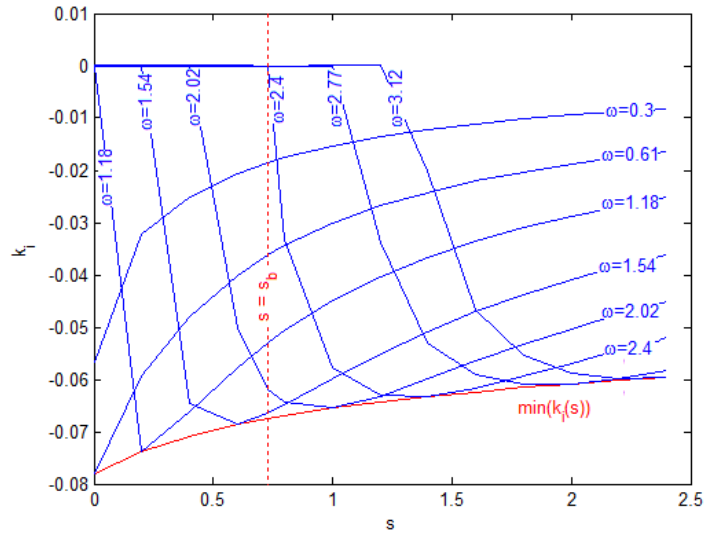
Figure 8.4: Graph showing the growth rate k_i for different values of ω for Jet 1. $\epsilon = 0.01$.

It would serve great value if we were able to verify this assumption experimentally. Though it would be impossible to remove any additional disturbances from the rig, it would be extremely useful to identify the frequencies present through vibration. The techniques used in this thesis could then be used to find particular modes which could be imposed onto a jet to counter or modify the effect of the instabilities naturally occurring, ultimately yielding the desired break-up.

Results for Jet 7 (see Table 6.1) are shown in Figure 8.5, showing similar behaviour: frequencies which are stable at the origin become unstable down the jet. This explains why having smaller amplitude additional disturbances had little or no effect for greater viscosity in the previous chapter. However, the frequency to generate the mode with greatest growth rate required is much larger than before.

In Chapter 6 we saw that for low viscosity fluids (40% Glycerol, 60% Water) jet's had a longer break-up length for low rotation rates than high rotation rates. This did not occur for high viscosity fluids (80% Glycerol, 20% Water). This could be explained by the above analysis. It mat be the case that the mechanical instabilities occur at

136
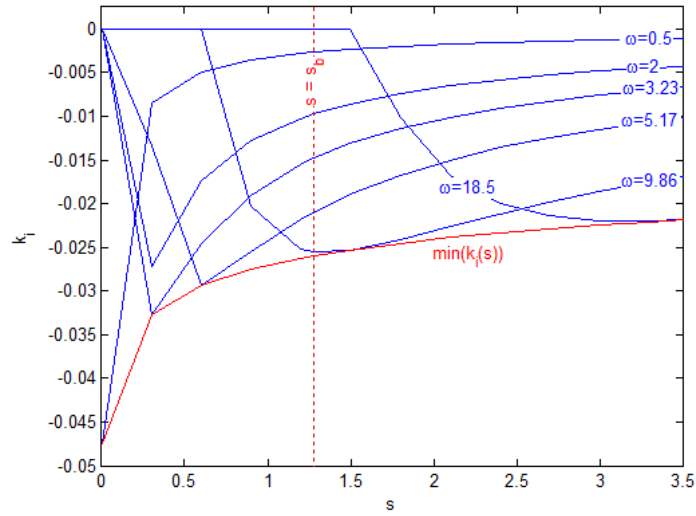
Figure 8.5: Graph showing the growth rate k_i for different values of ω for Jet 7. $\epsilon = 0.01$.

sufficient frequency such that they become unstable to break the jet, whilst at a lower viscosity the same frequency becomes unstable at a larger value of s.

We also note here that if we wished to force the jet at the very high frequency disturbances which are stable close to the orifice as seen in Figure 8.5, we would need to impose vibrations in the order of 10kHz at high amplitudes, a range we are unable to reach with the proposed experimental equipment. We shall explain this in greater detail in Chapter 11.

8.3 Time-dependent Instability

We examine the instability of our jet as time increases, where now k and λ are functions of t. (8.34) is solved computationally, with a temporal instability where the wavenumber k is real and $\lambda = \lambda_r + i\lambda_i$ is complex. u_0 and R_0 are obtained by solving the nonlinear equations (8.30). λ_r describes the growth rate, and we solve for k.

$R_0(s,t)$ for Jet 1 is shown in Figure 8.6, showing the approach to pinch off as time
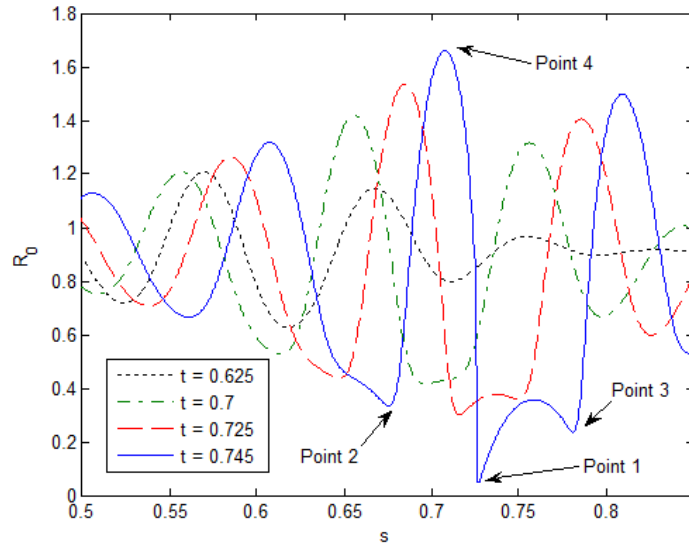
Figure 8.6: Graph showing $R_0(s,t)$ for Jet 1 at times approaching break-up. $\delta = 0.00199$ and $\epsilon = 0.01$.
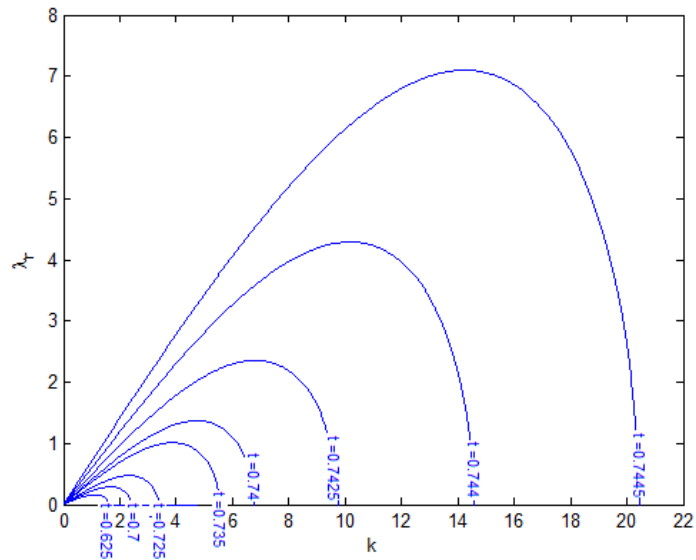
Figure 8.7: Graph showing the growth rate λ_r at times approaching break-up at Point 1 for Jet 1 for $0 < k < 20$. $\delta = 0.00199$ and $\epsilon = 0.01$.

progresses, and the gradual formation of the satellite droplet. Several points have been labelled on the figure as points for further evaluation. Point 1 occurs at the global minimum of R_0 at each time, and corresponds to the break-up up point s_b at the time of break-up. Points 2 and 3 are at the two local minima either side of the break-up point, namely at the points that we assume pinch off to form the droplets. Point 4 is taken at the maximum of R_0 on the main drop.

We first examine the instability at Point 1. We note that the value of s is different for each simulation. At the time of break-up this value of s is the break-up point s_b. Figure 8.7 shows that as time increases towards break-up, the wavenumber k of the most unstable wave increases dramatically. This shows that the original imposed long waves generate these short waves later on close to rupture, as seen experimentally [37]. We also see that the growth rate λ_r increases as break-up is approached, due to the jet becoming more unstable.

Examining the full complex values of λ, as shown in Figure 8.8, highlights some interesting results. As the growth rate λ_r increases, the frequency of the disturbance λ_i changes sign from negative to positive. This occurs at the point where u_0 becomes negative in the nonlinear simulation. At break-up, there is a very large positive frequency corresponding to the disturbance with greatest growth rate. This change of sign of λ_i corresponds to a change in direction of the unstable waves, with the waves at this point travelling towards the orifice.

In Figure 8.9, values of s close to s_b are examined. These solutions also have positive frequencies, and it is not the largest frequency disturbance which is generated at the break-up point. Perhaps these large modes of varying frequencies interact during the break-up process, thus resulting in complex behaviour close to pinch off.
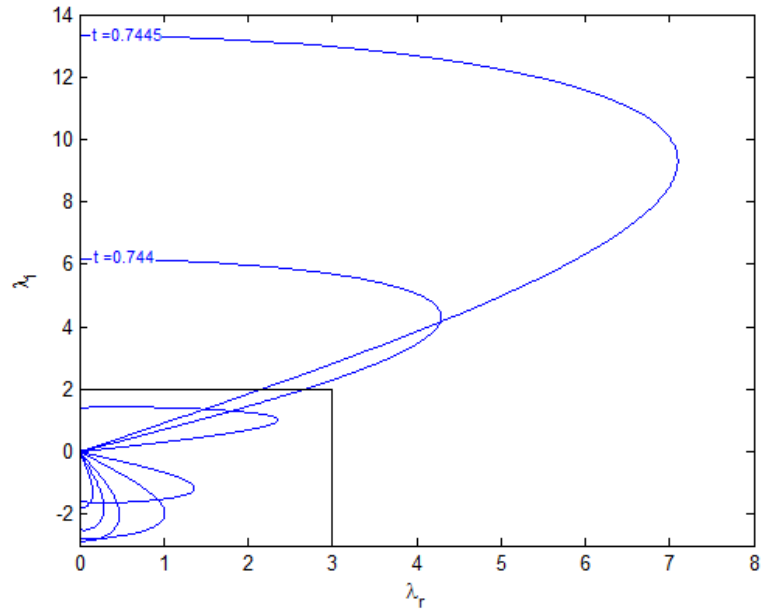
(a)
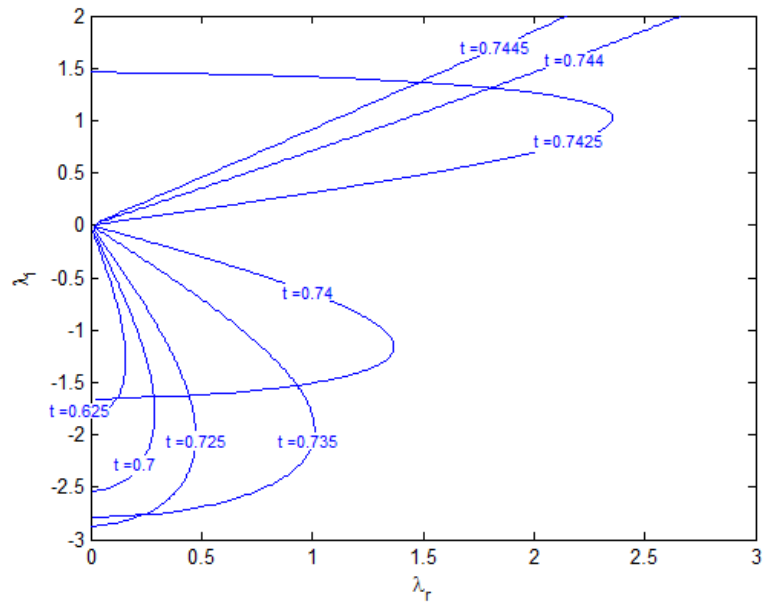
(b)

Figure 8.8: Graph showing the frequency λ at times approaching break-up for Jet 1 for $0 < k < 20$ for Point 1 in Figure 8.6. $\delta = 0.00199$ and $\epsilon = 0.01$. The lower graph is a zoomed in version of the upper graph.
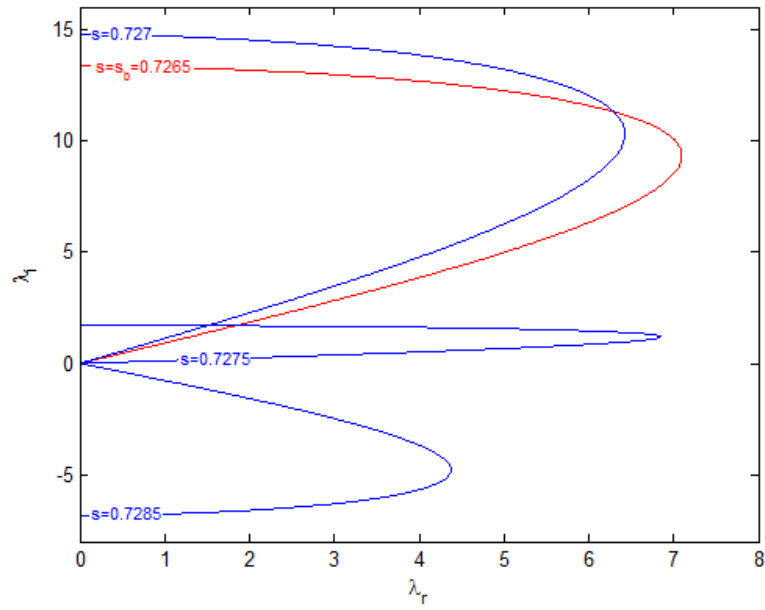
(a) frequency λ
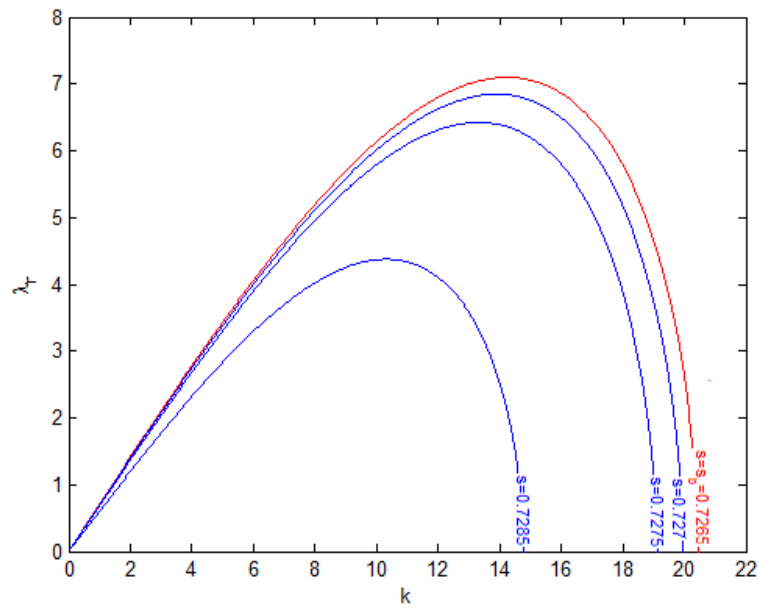
(b) growth rate λ_r

Figure 8.9: Wave behaviour at points near break-up of waves for Jet 1 for $0 < k < 20$. $\epsilon = 0.01$.

141
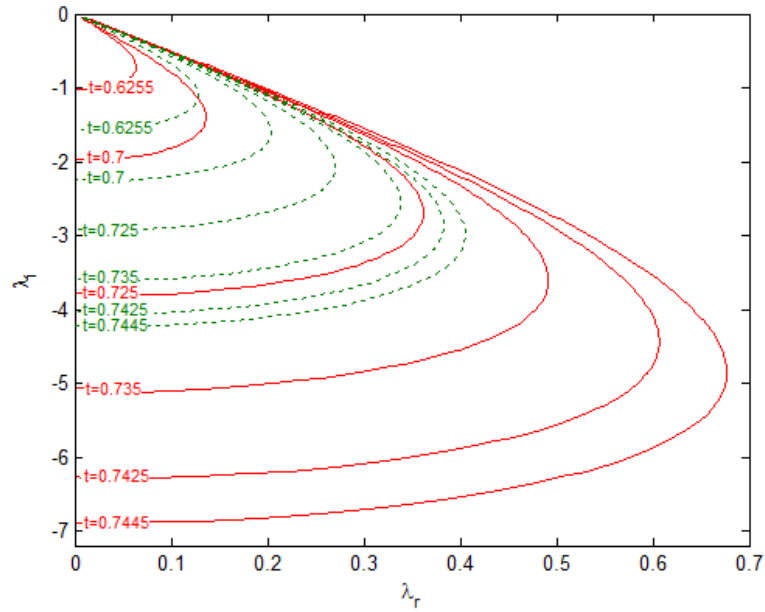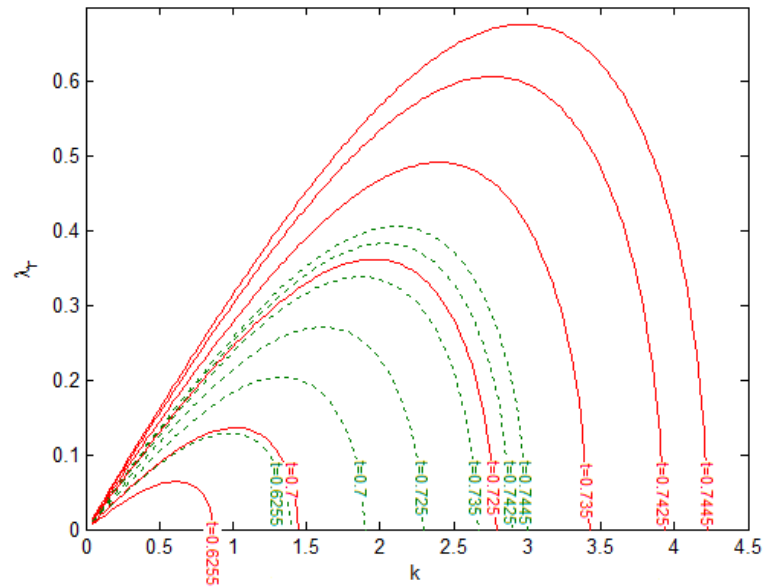
(a) frequency λ

(b) growth rate λ_r

Figure 8.10: Graph showing wave behaviour as the break-up time is approached for Jet 1 for $0 < k < 4.5$, for (i) Point 2 '$\cdots$' and (ii) Point 3 '$-$' in Figure 8.6. $\epsilon = 0.01$.

(a) frequency λ

(b) growth rate λ_r

Figure 8.11: Graph showing wave behaviour at times approaching break-up for Jet 1 for $0 < k < 4.5$ shown at Point 4 in Figure 8.6 $\epsilon = 0.01$.

Figure 8.10 shows the instability at Points 2 and 3. We see that both these points behave in a similar way, with an increase in growth rate and wavenumber as break-up is approached. Originally the first minima has larger growth rate, but then the later point becomes more unstable. This is as expected as it is a smaller radius which generates greater instability, and the radius decreased at a later time further down the jet on Figure 8.6.

In Figure 8.11 the instability at Point 4 is shown. The growth rate is much smaller than at other points along the jet, and gets smaller as the break-up time is approached, as the radius $R_0(s,t)$ increases and so the solution becomes more stable. In addition, the wavenumber decreases and remains less than 1. This shows that disturbances along a main droplet are long wave disturbances and the shorter waves generated at smaller radii are not seen here.

Increasing Viscosity

Figure 8.12 shows the temporal evolution of $R_0(s,t)$ for Jet 4 at times approaching break-up. We recall from Chapter 6 that when we changed δ from 0.0052 to 0.0053 we shifted break-up points, these are labelled Point 5 and 6 in Figure 8.12. Figure 8.13 shows the instability at Points 5 and 6 at each time as break-up is approached.

The growth rate does not change significantly as t increases at Point 5. However, the growth rate of Point 6 increases dramatically as break-up is approached. There is also an increase in wavenumber at the break-up point and the generation of very short waves. Unlike Jet 1, there are no negative frequencies.

Figure 8.12 also shows Point 7, which is a point taken on the ligament in betweens Points 5 and 6. The wave behaviour is shown in Figure 8.14. The growth rate is not as large as at the break-up point so the ligament is far more stable, but there are short wave disturbances present. We can use these short wave disturbances to predict post

144
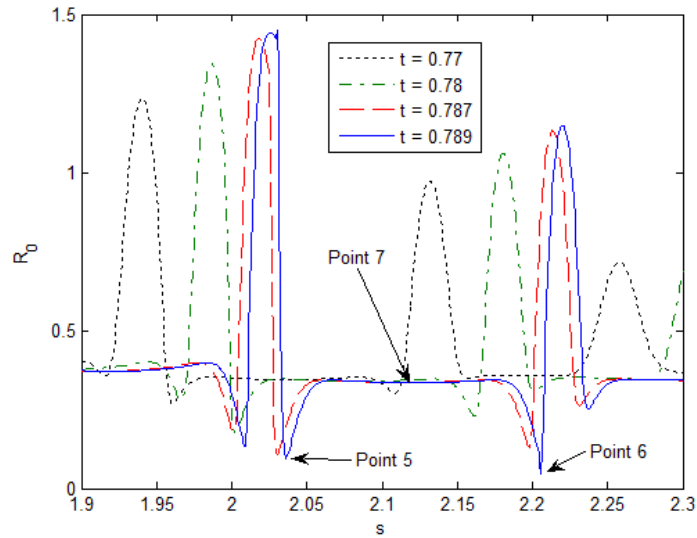
Figure 8.12: Graph showing $R_0(s,t)$ for Jet 4 at times approaching break-up. The parameters used are $We = 22.26$, $Rb = 0.512$, $Re = 375$, $Oh = 0.012354$, $\delta = 0.0052$ and $\epsilon = 0.01$.

break-up behaviour on the ligament by assuming that satellite droplets form over the wavelengths of these modes.

We integrate over these wavelengths on the ligament in the same way as for the main drops from the linear theory (see Chapter 3). Figure 8.15 shows the radius of the predicted satellites droplets on the ligament using this theory added to the drop size distributions for two different viscous fluids, namely Jets 4 and 7. We can see that the satellite droplets predicted using this technique fall within the droplet range we see in experiments. We also see a greater variety in satellite droplets for Jet 7, as the ligament has a greater variation in R_0 at break-up.
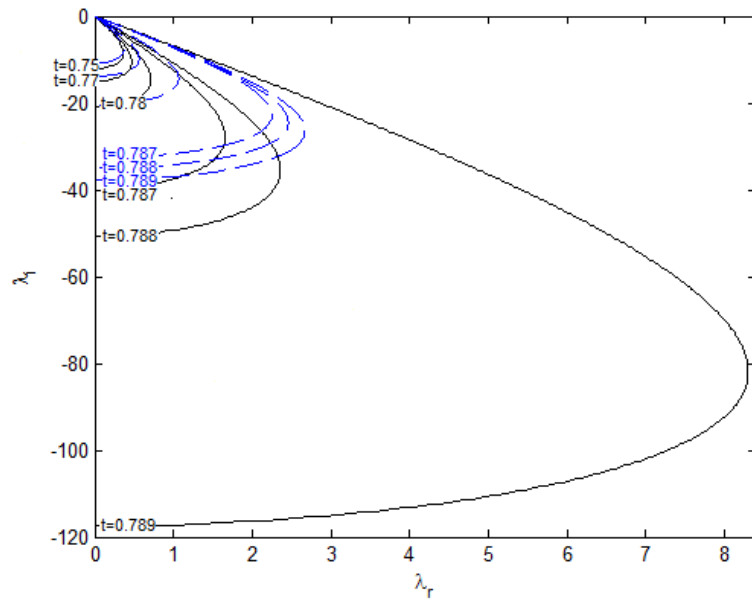
(a)
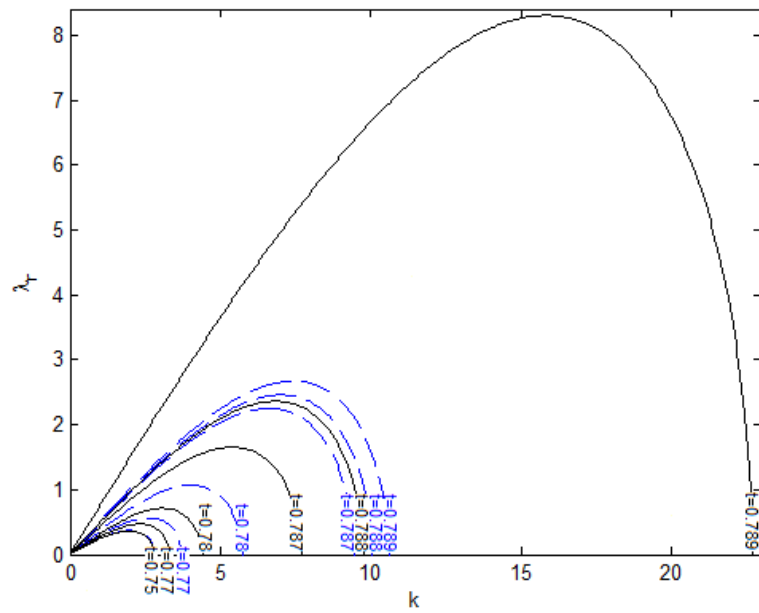
(b)

Figure 8.13: Graph showing the frequency λ at times approaching break-up for Jet 4 for $0 < k < 25$, shown at (i) Point 5 '$-$' and (ii) Point 6 '$--$' from Figure 8.12. $\delta = 0.00199$ and $\epsilon = 0.01$.

146
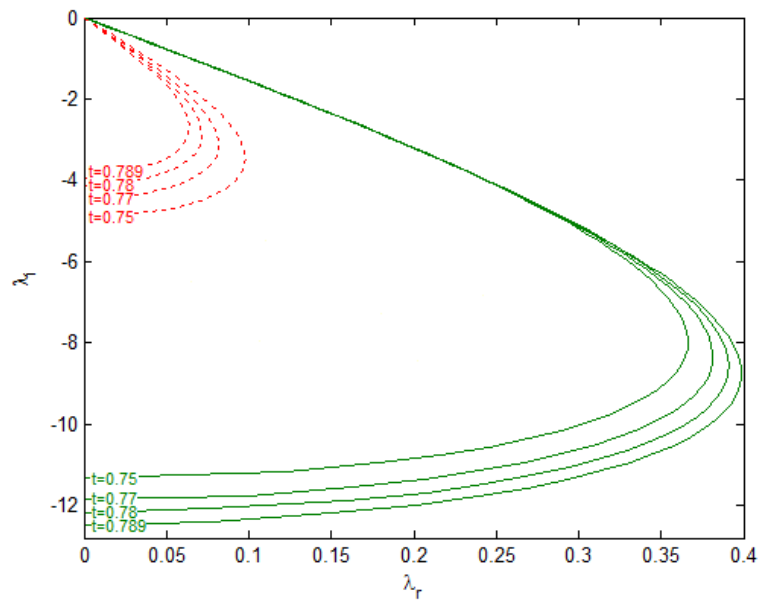
(a) frequency λ
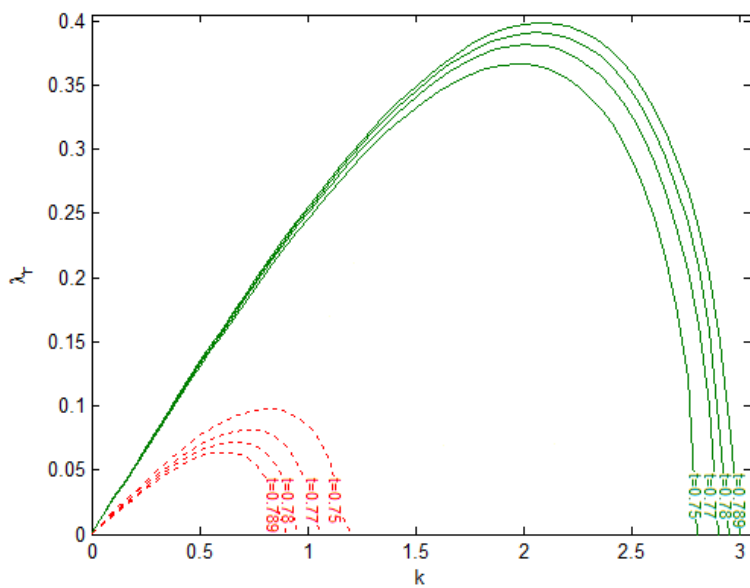
(b) growth rate λ_r

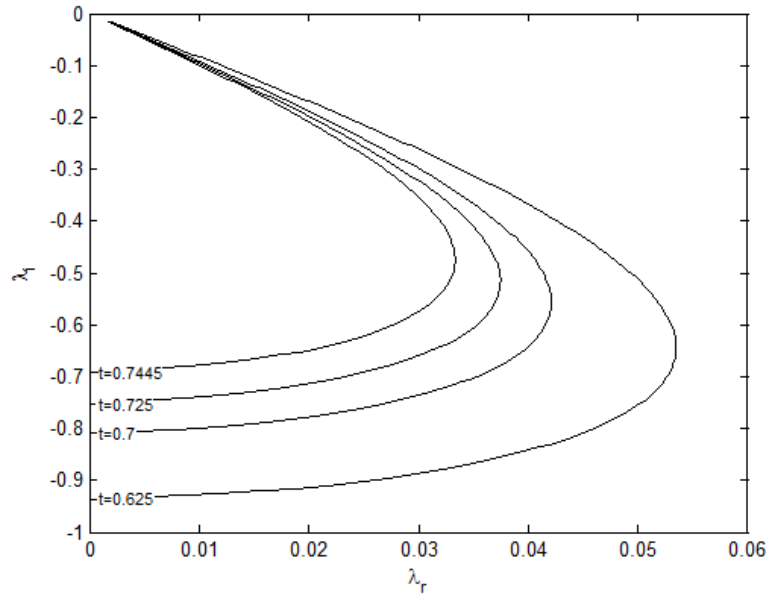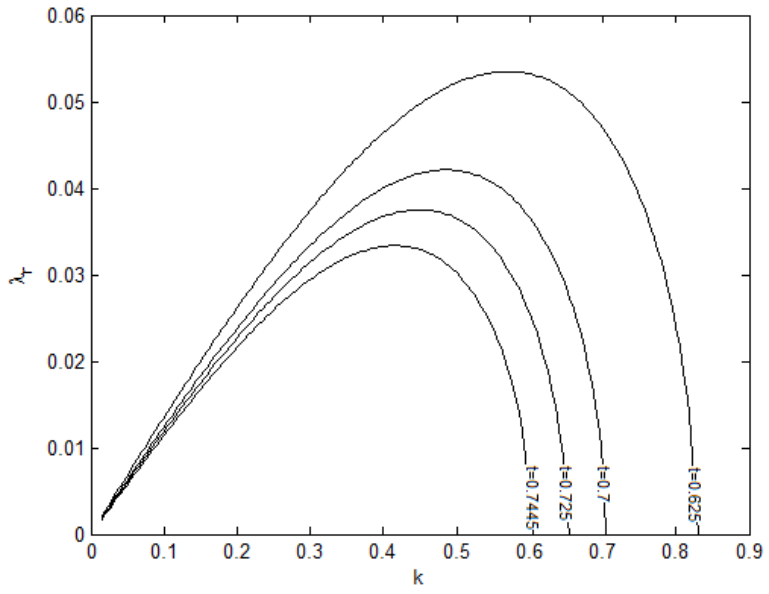Figure 8.14: Graph showing wave behaviour at times approaching break-up for Jet 4 for $0 < k < 5$ for Point 7 in Figure 8.12. $\epsilon = 0.01$.
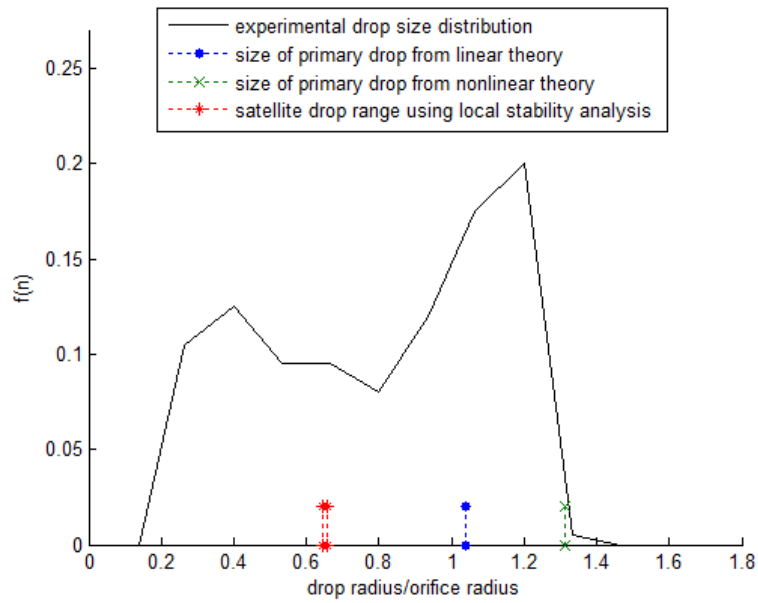
(a) Jet 4
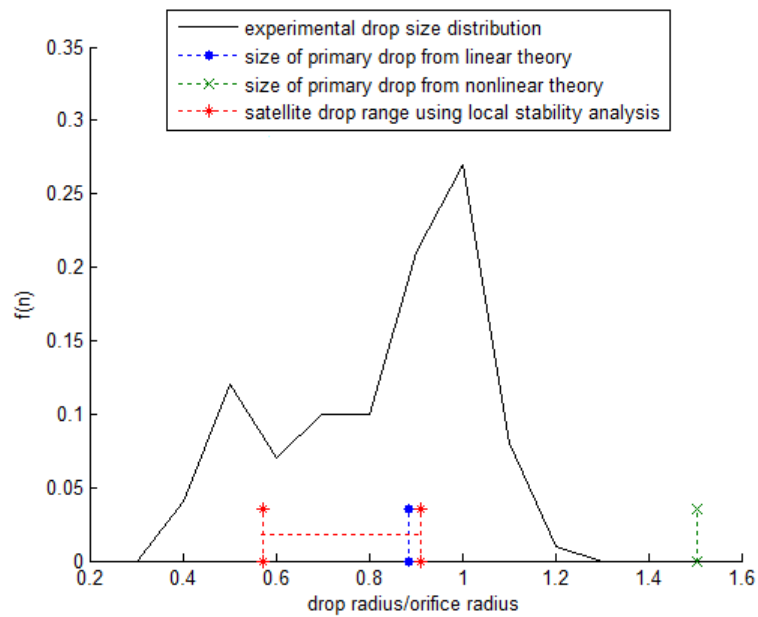
(b) Jet 7

Figure 8.15: Graph showing the satellite drop size prediction using the local stability analysis on the ligament added to experimental drop size distributions.

8.4 Long-wavelength Dispersion Relation

In order to describe the instability of the jet as time evolves, we have used values for u_0 and R_0 obtained from the nonlinear simulation of the jet. We now wish to analyse the instability of this long wavelength model and investigate the comparison between the resulting dispersion relations and the dispersion relation (8.34) for short waves. We take our nonlinear equations (8.30), namely

$$
\begin{aligned}
A_t + (Au)_s &= 0, \\
u_t + \left(\frac{u^2}{2}\right)_s &= \frac{-1}{We}\frac{\partial}{\partial s}\left(\frac{4(2A + (\epsilon A_s)^2 - \epsilon^2 AA_{ss})}{(4A + (\epsilon A_s)^2)^{3/2}}\right) + \frac{(X+1)X_s + ZZ_s}{Rb^2} \\
&\quad + \frac{3}{Re}\frac{(Au_s)_s}{A},
\end{aligned}
\tag{8.35}
$$

where $A = R^2$, and perturb them by unsteady quantities

$$
\begin{aligned}
R &= R_0(s) + \delta\tilde{R}(s, \bar{s}, \phi, t, \bar{t}), \\
u &= u_0(s) + \delta\tilde{u}(s, \bar{s}, \phi, t, \bar{t}),
\end{aligned}
$$

where δ is a small parameter and $\bar{s}$ and $\bar{t}$ are short length and timescales defined in the same way as Section 8.1. Note the absence of n here, due to the use of asymptotic Taylor expansions in the derivation of (8.35). To first order in δ and leading order in ϵ we obtain the equations

$$
\begin{aligned}
\tilde{R}_{\bar{t}} + \frac{1}{2}R_0\tilde{u}_{\bar{s}} + u_0\tilde{R}_{\bar{s}} &= 0, \\
\tilde{u}_{\bar{t}} + u_0\tilde{u}_{\bar{s}} &= \frac{1}{We}\left(\frac{1}{R_0^2}\tilde{R}_{\bar{s}} + \tilde{R}_{\bar{s}\bar{s}\bar{s}}\right) + \frac{3}{\tilde{Re}}\tilde{u}_{\bar{s}\bar{s}},
\end{aligned}
$$

where $\tilde{Re} = \epsilon Re$ is a scaled Reynolds number allowing the effect of viscosity at leading order. We search for a solution of the form

$$\begin{aligned}
\tilde{R} &= \hat{R}(s,\phi,t)\exp(ik(s,t)\bar{s} + \lambda(s,t)\bar{t}), \\
\tilde{u} &= \hat{u}(s,\phi,t)\exp(ik(s,t)\bar{s} + \lambda(s,t)\bar{t}),
\end{aligned}$$

and obtain the dispersion relation

$$\lambda = -iu_0 k - \frac{3k^2}{2Re} \pm \frac{k}{2}\sqrt{\frac{9k^2}{Re^2} - \frac{2R_0}{We}\left(k^2 - \frac{1}{R_0^2}\right)}. \tag{8.36}$$

Note here that the derived equation (8.36) is the long-wavelength approximation $k \to 0$ of the full dispersion relation (8.34). This approximation was derived and verified by Decent *et al.* [12] by taking this long-wavelength limit of (8.34) in the simpler case of $\lambda = \lambda(s)$ and $k = k(s)$. Here $\lambda = \lambda(s,t)$ and $k = k(s,t)$. This result is as expected, as we used the long wavelength asymptotic Taylor expansions during the derivation of (8.35).

This result is compared to full dispersion relation (8.34). Figure 8.16 shows a comparison for Jet 4 at $t = 0$; Figure 8.17 at the break-up point for Jet 1 for times approaching break-up and Figure 8.18 shows a comparison at the break-up point for Jet 4 for times approaching break-up.

In all cases, there is a good comparison in the unstable region, though the long-wavelength theory predicts a slightly larger growth rate. In addition, in regions where the full dispersion relation predicts modes of zero growth rate, the long wavelength theory predicts stable modes. For Jet 1, the frequency λ_i changes signs as k increases in the stable region $\lambda_r < 0$, yet for Jet 4 they become more negative. Overall however, as we focus on the region for unstable modes, the excellent correlation between the two results means that we can take the long wavelength approximation in future to predict

our break-up, thus saving computation time whilst solving the dispersion relation.

8.5   Conclusions

In this chapter we developed a dispersion relation which could be used to calculate the instability not only at points down the jet, but at points in time as the jet evolves. We could use this to calculate the post break-up instability of a ligament and obtain the satellite droplets; something that cannot be achieved using only the nonlinear model. The sizes of these droplets compare well to the experimental drop size distributions.

We also used this dispersion relation to explain the very short break-up we encountered in Chapter 7. We were forcing a jet to break-up with mode of zero growth rate at the orifice which became unstable down the jet dominating the break-up. These had less of an effect for a more viscous fluid. We also derived the long wavelength dispersion relation and the corresponding instability analysis of both these dispersion relations showed an excellent agreement in regions where the jet is unstable.
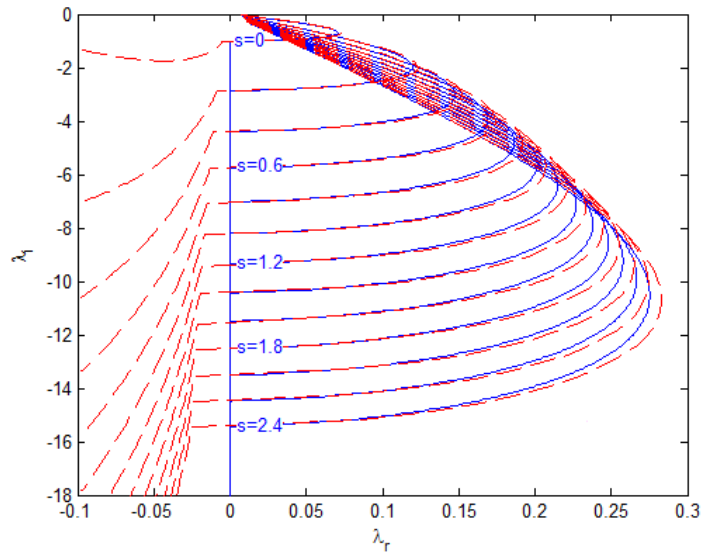
(a) frequency λ
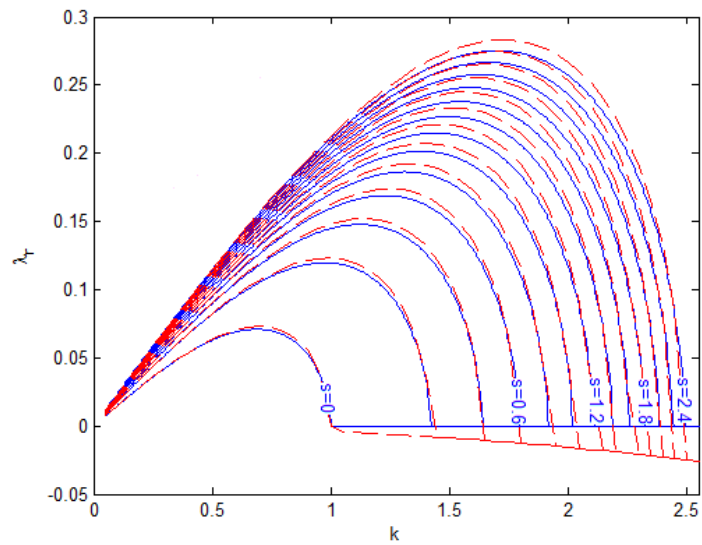
(b) growth rate λ_r

Figure 8.16: Graph showing for Jet 4 for $0 < k < 5$ at $t = 0$, shown for (i) the full dispersion relation '$-$' and (ii) the longwavelength dispersion relation '$--$'. $\epsilon = 0.01$.
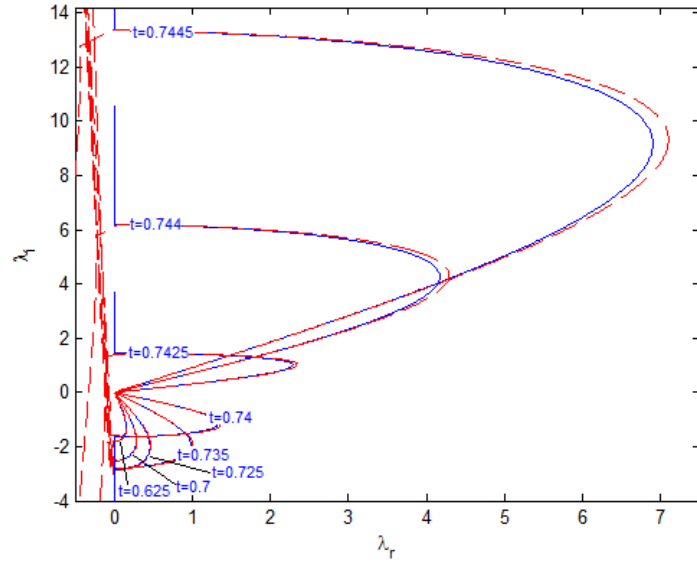
(a) frequency λ
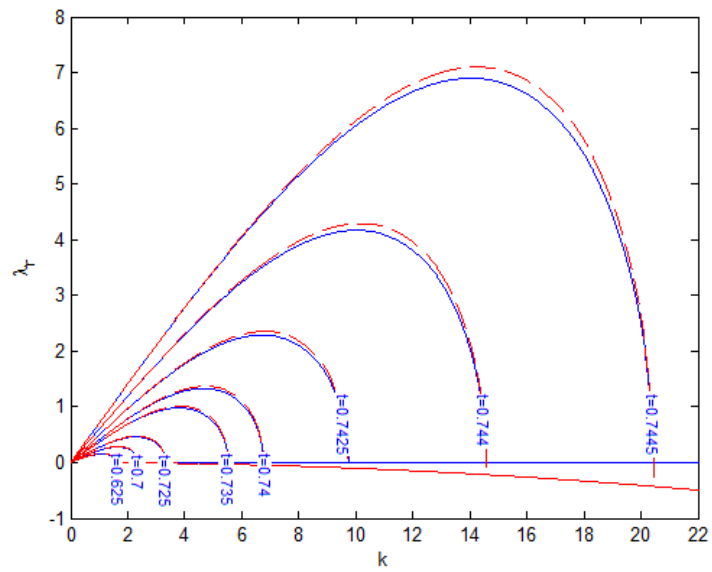
(b) growth rate λ_r

Figure 8.17: Graph showing for Jet 1 for $0 < k < 25$ at $t = 0$, shown for (i) the full dispersion relation '$-$' and (ii) the longwavelength dispersion relation '$--$'. $\epsilon = 0.01$.

153
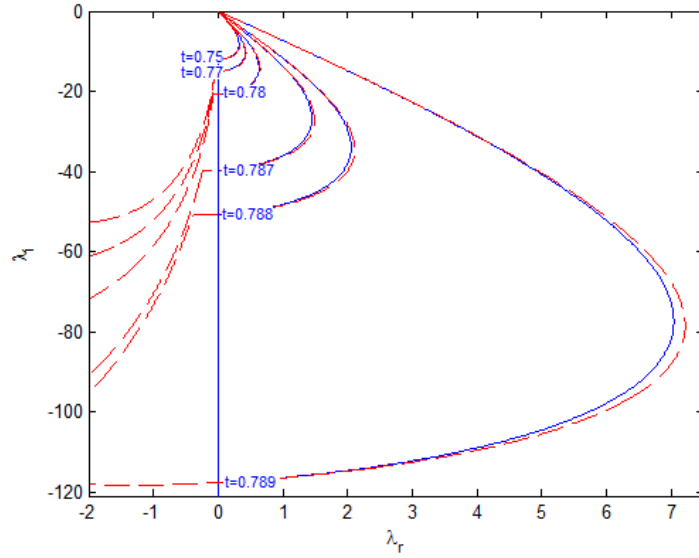
(a) frequency λ
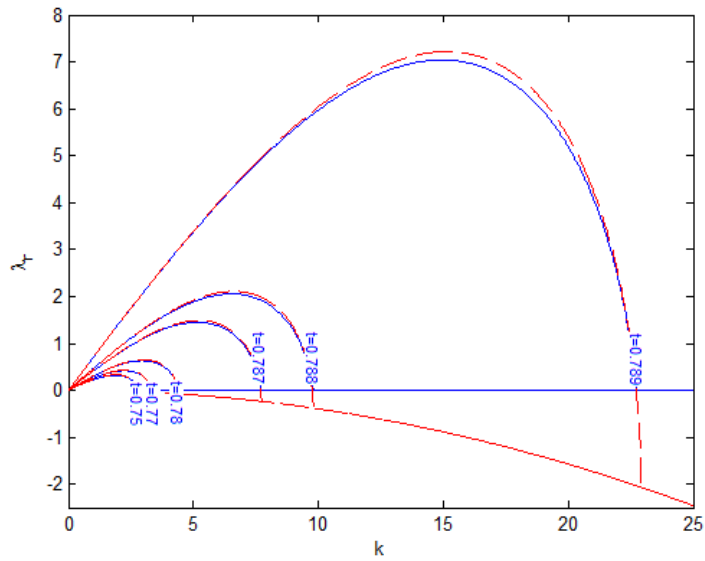
(b) growth rate λ_r

Figure 8.18: Graph showing for Jet 4 for $0 < k < 25$ at $t = 0$, shown for (i) the full dispersion relation '$-$' and (ii) the longwavelength dispersion relation '$--$'. $\epsilon = 0.01$.

154

Chapter 9

An asymptotic solution to the jet equations

In previous chapters we showed that it is possible to control a liquid jet's break-up by applying an additional disturbance at the orifice using a chosen frequency. Mode 1 break-up, that is break-up classified by the absence of satellite droplets, more commonly occurred when a jet had shorter break-up length. This occurred as the initial linear perturbation had not developed extensive nonlinearities and mode competition which may cause the satellite drop formation. When the jet break-up is longer, these nonlinearities can have a greater effect. An asymptotic method is adopted here to gain further understanding of the nonlinear jet equations and the nonlinearities that arise in jet break-up. This chapter details a large time and space asymptotic analysis in order to determine when the jets naturally become nonlinear. We begin be examining an inviscid straight jet, with the effects of rotation appearing in the next chapter.
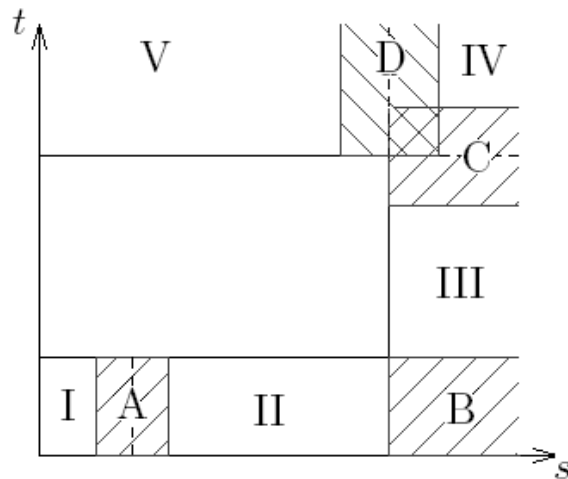
Figure 9.1: Diagrammatic representation showing the regions for the Needham-Leach Method for liquid jet break-up.

9.1 The Needham-Leach Method

The Needham-Leach Method [22] was originally developed to analyse the large time solutions to reaction diffusion equations. Is was later used to develop understanding of other PDEs, such as the Korteweg-de Vries equation. The method involves developing asymptotic solutions in different regions of s and t using matched asymptotics; these regions for liquid jet break-up are shown in Figure 9.1.

Solutions to the jet equations are obtained near the orifice in Region I where $s \to 0$ and $t \to 0$, using the initial conditions at $t = 0$ and boundary conditions at $s = 0$. The solutions obtained in Region I are used to generate an expansion in Region II, where $s = O(1)$ and $t \to 0$, and the solutions are matched in Region A. Region II is a region arising through the presence of a temporal boundary layer due to the initial conditions. The solution in Region II drives the expansion in Region III where $s \to \infty$ and $t = O(1)$, with the solutions from Region II and III asymptotically matched in Region B. The large time and large spatial ($s \to \infty$ and $t \to \infty$) solutions are given in Region IV, which are driven by matching in Region C with Region III. Region IV

156

describes nonlinear waves. Region V describes growing waves where $s = O(1)$ and $t \to \infty$, with matching in Region D. The solutions in Region IV and V will give an indication into the jet behaviour as break-up is approached.

The equations governing straight inviscid jet break-up are

$$R_t + uR_s + \frac{u_s R}{2} = 0, \tag{9.1}$$

$$u_t + uu_s = \frac{-1}{We} \left(\frac{1}{R(1 + R_s^2)^{\frac{1}{2}}} - \frac{R_{ss}}{(1 + R_s^2)^{\frac{3}{2}}} \right)_s \tag{9.2}$$

subject to

$$R(s, t = 0) = 1 \qquad u(s, t = 0) = 1 \tag{9.3}$$

$$R(s = 0, t) = 1 \qquad u(s = 0, t) = 1 + \delta \sin(\omega t) \tag{9.4}$$

In addition, it is necessary to adopt the following conditions in the spatial far field

$$R \to 1 \qquad u \to 1 \qquad \text{as} \qquad s \to \infty$$

(9.1) and (9.2) are equivalent to (3.11), with $Rb \to \infty$ and $Re \to \infty$ and $A = R^2$ in (3.11). The above initial conditions (9.3) and boundary conditions (9.4) are the equivalent to (3.12) and (3.13) with $R_0(s) = u_0(s) = 1$. These are the straight inviscid limits of the equations used to date in this thesis. We examine the behaviour of these equations in Regions I-V.

9.2 Asymptotic region for $s \to 0$, $t \to 0$

We examine the behaviour in Region I close the orifice with $s \to 0$ and $t \to 0$.

9.2.1 Existence of an inner region

We first try the following naive expansions and subsititute into (9.1) and (9.2),

$$R = 1 + tp(s) + O(t^2), \qquad u = 1 + tq(s) + O(t^2) \quad \text{as} \quad t \to 0.$$

Then (9.1) yields $p = 0$ as $t \to 0$ and (9.2) gives $q = $ constant as $t \to 0$. This means that the boundary conditions at $s = 0$ and $s \to \infty$ cannot both be satisfied. Hence there is a temporal boundary layer close to the orifice and it is necessary to have two asymptotic regions as $t \to 0$ as already indicated. Hence we abandon the above expansions for R and u and adopt something less naive.

9.2.2 Inner Solution

The solution in this region $s \to 0$ and $t \to 0$ drives the asymptotic behaviour in all future matching regions and so the solutions must be found in detail. We expand by writing

$$u = 1 + t^m F_0(\eta) + t^{m+p} F_1(\eta) + t^{m+2p} F_2(\eta) + O(t^{m+3p})$$

$$R = 1 + t^c G_0(\eta) + t^{c+p} G_1(\eta) + t^{c+2p} G_2(\eta) + O(t^{c+3p}) \tag{9.5}$$

where $\eta = st^{-a}$ and $a, c, m, p \geq 0$. Here $\eta = O(1)$ as $s \to 0$ and $t \to 0$. This expansion satisfies the initial conditions at $t = 0$ (9.3). Decent [11] solved the equivalent viscous problem for a straight jet and showed that the higher order terms can be neglected in the asymptotic expansion, and so we neglect F_i and G_i for $i = 1, 2....$ From the boundary conditions (9.4),

$$u(s = 0, t) = 1 + \delta \sin(\omega t) = 1 + \delta \omega t + O(t^3) \quad \text{as} \quad t \to 0,$$

and so

$$m = 1, \qquad F_0(0) = \delta\omega.$$

Substituting (9.5) into (9.1) and (9.2), and looking for the distinguished limits, we obtain $c = 3/2$ and $a = 1/2$. This yields the equations

$$3G_0 - \eta G_0' + F_0' + O\left(t^{1/2}\right) = 0, \tag{9.6}$$

$$F_0 - \frac{1}{2}\eta F_0' - \frac{1}{We}G_0''' + O\left(t^{1/2}\right) = 0, \tag{9.7}$$

where $' \equiv \frac{d}{d\eta}$, $\eta = s/\sqrt{t}$ and the boundary conditions are

$$F_0(0) = \delta\omega, \qquad F_0(\infty) = 0, \qquad G_0(0) = 0, \qquad G_0(\infty) = 0.$$

Differentiating (9.7) and substituting (9.6) we obtain

$$G_0'''' + \frac{1}{2}We\eta^2 G_0'' - \frac{3}{2}We\eta G_0' + \frac{3}{2}WeG_0 = 0. \tag{9.8}$$

As $G_0 = \eta$ is a solution to (9.8) (satisfying $G_0(0) = 0$) we can use the method of reduction of order where $G_0(\eta) = \eta\bar{G}_0(\eta)$ and $\bar{G}_0$ is the solution to the equation

$$\eta\bar{G}_0'''' + 4\bar{G}_0''' + \frac{1}{2}We\eta^3\bar{G}_0'' - \frac{1}{2}We\eta^2\bar{G}_0' = 0.$$

159

This ODE is solved for $\bar{G}_0$ which yields the solution for G_0, namely

$$
\begin{aligned}
G_0 &= C_1\eta + \frac{1}{2}C_2\eta^3 + \left[-2C_3 + \sqrt{We}C_4\eta^2\right]\cos\left(\frac{\sqrt{2We}}{4}\eta^2\right) \\
&+ \left[-\frac{\sqrt{2We}}{2}C_3\eta^2 - 2^{3/2}C_4\right]\sin\left(\frac{\sqrt{2We}}{4}\eta^2\right) \\
&+ \left[-\frac{3We^{1/4}\sqrt{\pi}}{2^{1/4}}C_3\eta + \frac{We^{3/4}\sqrt{\pi}}{2^{1/4}}C_4\eta^3\right] F_s\left(\frac{We^{1/4}}{2^{1/4}\sqrt{\pi}}\eta\right) \\
&+ \left[\frac{We^{3/4}\sqrt{\pi}}{2^{3/4}}C_3\eta^3 + 3\,2^{1/4}We^{1/4}\sqrt{\pi}C_4\eta\right] F_c\left(\frac{We^{1/4}}{2^{1/4}\sqrt{\pi}}\eta\right), \quad\quad (9.9)
\end{aligned}
$$

where

$$
F_s(x) = \int_0^x \sin\left(\frac{\pi\tau^2}{2}\right) d\tau, \qquad F_c(x) = \int_0^x \cos\left(\frac{\pi\tau^2}{2}\right) d\tau.
$$

are Fresnel Integrals that are also seen in Fresnel diffraction phenomena in optics [2]. Here C_i for $i = 1...4$ are constants of integration. Applying the boundary condition $G_0(0) = 0$ yields

$$
C_3 = 0.
$$

Using (9.6) we obtain an expression for F_0,

$$
\begin{aligned}
F_0 &= -C_1\eta^2 + 3\sqrt{2}C_4\eta\sin\left(\frac{\sqrt{2We}}{4}\eta^2\right) + \frac{3\,2^{3/4}\sqrt{\pi}}{We^{1/4}}C_4 F_s\left(\frac{We^{1/4}}{2^{1/4}\sqrt{\pi}}\eta\right) \\
&- 3\,2^{1/4}We^{1/4}\sqrt{\pi}C_4\eta^2 F_c\left(\frac{We^{1/4}}{2^{1/4}\sqrt{\pi}}\eta\right) + C_5, \quad\quad (9.10)
\end{aligned}
$$

where C_5 is a further constant of integration. Applying the boundary condition $F_0(0) = \delta\omega$ implies

$$
C_5 = \delta\omega.
$$

Comparing the coefficients of the largest terms of (9.9) and (9.10) as $\eta \to \infty$, and using the identities $F_s(\eta) = F_c(\eta) = \frac{1}{2}$ as $\eta \to \infty$, we use the boundary conditions $F_0(\infty) = 0$

160

and $G_0(\infty) = 0$ to obtain

$$C_1 = -\frac{3We^{1/4}\sqrt{\pi}}{2^{3/4}}C_4 + \delta\omega \quad \text{and} \quad C_4 = -\frac{2^{1/4}}{We^{3/4}\sqrt{\pi}}C_2,$$

We use equation (9.7) to evaluate the final constant, namely

$$C_2 = \frac{We}{3}\delta\omega,$$

and thus

$$C_1 = \frac{\sqrt{2We}}{2}\delta\omega, \qquad C_4 = -\frac{2^{1/4}We^{1/4}}{3\sqrt{\pi}}\delta\omega,$$

so that

$$\begin{aligned}
G_0 &= \delta\omega\left[\frac{\sqrt{2We}}{2}\eta + \frac{We}{6}\eta^3 - \frac{2^{1/4}We^{3/4}}{3\sqrt{\pi}}\eta^2\cos\left(\frac{\sqrt{2We}}{4}\eta^2\right)\right.\\
&\quad + \left.\frac{2^{7/4}We^{1/4}}{3\sqrt{\pi}}\sin\left(\frac{\sqrt{2We}}{4}\eta^2\right) - \frac{We}{3}\eta^3 F_s\left(\frac{We^{1/4}}{2^{1/4}\sqrt{\pi}}\eta\right) - \sqrt{2We}\eta F_c\left(\frac{We^{1/4}}{2^{1/4}\sqrt{\pi}}\eta\right)\right]
\end{aligned}$$

(9.11)

and

$$\begin{aligned}
F_0 &= \delta\omega\left[1 - \frac{\sqrt{2We}}{2}\eta^2 - \frac{2^{3/4}We^{1/4}}{\sqrt{\pi}}\eta\sin\left(\frac{\sqrt{2We}}{4}\eta^2\right) - 2F_s\left(\frac{We^{1/4}}{2^{1/4}\sqrt{\pi}}\eta\right)\right.\\
&\quad + \left.\sqrt{2We}\eta^2 F_c\left(\frac{We^{1/4}}{2^{1/4}\sqrt{\pi}}\eta\right)\right].
\end{aligned}$$

(9.12)

Matching with the next region occurs in Region A, where $s = O(1)$ and $t \to 0$, i.e.

as $\eta = s/\sqrt{t} \to \infty$. Therefore, as $\eta \to \infty$,

$$
\begin{aligned}
F_0 &= \frac{\alpha}{\eta^3} \sin\left(\beta\eta^2\right) + O\left(\frac{1}{\eta^5}\right), \\
G_0 &= \frac{\alpha}{\eta^4} \sin\left(\beta\eta^2\right) + O\left(\frac{1}{\eta^6}\right),
\end{aligned}
\tag{9.13}
$$

where

$$
\alpha = -\frac{4\,2^{3/4}}{We^{3/4}\sqrt{\pi}}\delta\omega, \qquad \beta = \frac{\sqrt{2We}}{4}.
$$

We see algebraic decay here. In the viscous case, in Decent [11], the solution in Region I was found to decay exponentially with η.

9.3 $s = O(1)$, $t \to 0$ asymptotic region

In region (ii), using (9.13) we pose

$$
\begin{aligned}
u = 1 \;+\;& \sin\left(\frac{\sqrt{2We}}{4}\frac{s^2}{t}\right)\frac{t^{5/2}}{s^3}\left(u_0(s) + tu_2(s) + O\left(t^2\right)\right) \\
+\;& \cos\left(\frac{\sqrt{2We}}{4}\frac{s^2}{t}\right)\frac{t^{5/2}}{s^3}\left(u_1(s) + tu_3(s) + O\left(t^2\right)\right) \\
R = 1 \;+\;& \sin\left(\frac{\sqrt{2We}}{4}\frac{s^2}{t}\right)\frac{t^{7/2}}{s^4}\left(R_0(s) + tR_2(s) + O\left(t^2\right)\right) \\
+\;& \cos\left(\frac{\sqrt{2We}}{4}\frac{s^2}{t}\right)\frac{t^{7/2}}{s^4}\left(R_1(s) + tR_3(s) + O\left(t^2\right)\right)
\end{aligned}
\tag{9.14}
$$

as $t \to 0$.

Substituting into equation (9.1) gives

$$
u_0 = R_0, \qquad u_1 = R_1,
\tag{9.15}
$$

162

$$u_2 = \frac{4}{\sqrt{2We}s^2} \left(\frac{\sqrt{2We}}{4} s^2 R_2 - \frac{1}{2} s R_1' - 2R_1 - \frac{\sqrt{2We}}{2} s R_0 \right) \tag{9.16}$$

and

$$u_3 = \frac{4}{\sqrt{2We}s^2} \left(\frac{\sqrt{2We}}{4} s^2 R_3 - \frac{\sqrt{2We}}{2} s R_1 + \frac{1}{2} s R_0' + 2R_0 \right). \tag{9.17}$$

Equation 2 (9.2) yields

$$R_0 = A \sin\left(\sqrt{\frac{We}{2}} s \right) + B \cos\left(\sqrt{\frac{We}{2}} s \right) \tag{9.18}$$

and

$$R_1 = A \cos\left(\sqrt{\frac{We}{2}} s \right) - B \sin\left(\sqrt{\frac{We}{2}} s \right). \tag{9.19}$$

Note that u_0 to u_3 are used in the derivation of (9.18) and (9.19); u_2, u_3, R_2 and R_3 appear in the derivation of (9.18) and (9.19) but these terms cancel on substitution of (9.16) and (9.17). Matching with the previous region occurs as $s \to 0$. This gives $A = 0$ and $B = \alpha$. Hence

$$u = 1 + \alpha \sin\left(\frac{\sqrt{2We}}{4} \frac{s^2}{t} - \sqrt{\frac{We}{2}} s \right) \frac{t^{5/2}}{s^3} + h.o.t$$

$$R = 1 + \alpha \sin\left(\frac{\sqrt{2We}}{4} \frac{s^2}{t} - \sqrt{\frac{We}{2}} s \right) \frac{t^{7/2}}{s^4} + h.o.t \tag{9.20}$$

as $t \to 0$ and $s = O(1)$, where $h.o.t.$ denotes higher-order terms in the expansion.

9.4   Large spatial asymptotics

In region (iii) we consider $t = O(1)$ and $s \to \infty$. Driven by (9.20), we expand using

$$u = 1 \; + \; \sin\left(\frac{\sqrt{2We}}{4}\frac{s^2}{t} - \sqrt{\frac{We}{2}}s \right) \frac{t^{5/2}}{s^3} \left(U_0(t) + \frac{U_2(t)}{s} + \frac{U_4(t)}{s^2} + O\left(\frac{1}{s^3}\right) \right)$$

$$+ \; \cos\left(\frac{\sqrt{2We}}{4}\frac{s^2}{t} - \sqrt{\frac{We}{2}}s \right) \frac{t^{5/2}}{s^3} \left(U_1(t) + \frac{U_3(t)}{s} + \frac{U_5(t)}{s^2} + O\left(\frac{1}{s^3}\right) \right) + h.o.t$$

$$R = 1 \; + \; \sin\left(\frac{\sqrt{2We}}{4}\frac{s^2}{t} - \sqrt{\frac{We}{2}}s \right) \frac{t^{7/2}}{s^4} \left(r_0(t) + \frac{r_2(t)}{s} + \frac{r_4(t)}{s^2} + O\left(\frac{1}{s^3}\right) \right)$$

$$+ \; \cos\left(\frac{\sqrt{2We}}{4}\frac{s^2}{t} - \sqrt{\frac{We}{2}}s \right) \frac{t^{7/2}}{s^4} \left(r_1(t) + \frac{r_3(t)}{s} + \frac{r_5(t)}{s^2} + O\left(\frac{1}{s^3}\right) \right) + h.o.t$$

as $s \to \infty$ and $h.o.t.$ denotes the higher order terms. Substituting into equation (9.1),

$$U_0 = r_0, \qquad U_1 = r_1, \tag{9.21}$$

$$U_2 = r_2 - tr_0, \qquad U_3 = r_3 - tr_1, \tag{9.22}$$

$$U_4 = \frac{4}{\sqrt{2We}} \left(\frac{1}{4}\sqrt{2We}r_4 - \frac{1}{2}\sqrt{2We}tr_2 - t^2r_1' - 2tr_1 + \frac{1}{4}\sqrt{2We}t^2r_0 \right) \tag{9.23}$$

and

$$U_5 = \frac{4}{\sqrt{2We}} \left(\frac{1}{4}\sqrt{2We}r_5 - \frac{1}{2}\sqrt{2We}tr_3 + \frac{1}{4}\sqrt{2We}t^2r_1 + t^2r_0' + 2tr_0 \right). \tag{9.24}$$

Substituting into equation (9.2), using U_0 to U_5 gives

$$[r_0 = C \sin\left(\frac{1+We}{2\sqrt{2We}}t \right) + D \cos\left(\frac{1+We}{2\sqrt{2We}}t \right) \tag{9.25}$$

and

$$r_1 = -C \cos\left(\frac{1+We}{2\sqrt{2We}}t \right) + D \sin\left(\frac{1+We}{2\sqrt{2We}}t \right). \tag{9.26}$$

Note that in the derivation of (9.25) and (9.26) we have used (9.22) - (9.24) with higher

order terms cancelling.

Asymptotic matching with the solution in the previous region gives $C = 0$ and $D = \alpha$. Hence

$$u = 1 \;+\; \alpha \sin\left(\frac{\sqrt{2We}}{4}\frac{s^2}{t} - \sqrt{\frac{We}{2}}s + \frac{1+We}{2\sqrt{2We}}t\right)\frac{t^{5/2}}{s^3} + h.o.t$$

$$R = 1 \;+\; \alpha \sin\left(\frac{\sqrt{2We}}{4}\frac{s^2}{t} - \sqrt{\frac{We}{2}}s + \frac{1+We}{2\sqrt{2We}}t\right)\frac{t^{7/2}}{s^4} + h.o.t \qquad (9.27)$$

These expressions remain uniformly valid as $t \to \infty$ providing $s \gg t$, and become non-uniform when $t = O(s)$ as $t \to \infty$. The above results correspond to the inviscid large Reynolds number limit $Re \to \infty$ of the viscous results in Decent [11].

9.5 $\;\; s \to \infty,\; t \to \infty$ asymptotics

Using (9.27), we propose using the following expansions

$$u = 1 \;+\; \sum_{j=1}^{2} \exp\left((-1)^j t g_0(z)\right)\left[\frac{h_{11}^{(j)}(z)}{t^{1/2}} + \frac{h_{21}^{(j)}(z)}{t} + \frac{h_{31}^{(j)}(z)}{t^{3/2}}\right]$$

$$+ \; \sum_{j=1}^{2} \exp\left(2(-1)^j t g_0(z)\right)\left[\frac{h_{22}^{(j)}(z)}{t} + \frac{h_{32}^{(j)}(z)}{t^{3/2}}\right]$$

$$+ \; \sum_{j=1}^{2} \exp\left(3(-1)^j t g_0(z)\right)\left[\frac{h_{33}^{(j)}(z)}{t^{3/2}}\right] + O\left(\frac{1}{t^2}\right) + h.o.t., \qquad (9.28)$$

165

$$R = 1 + \sum_{j=1}^{2} \exp\left((-1)^j t g_0(z)\right) \left[\frac{\zeta_{11}^{(j)}(z)}{t^{1/2}} + \frac{\zeta_{21}^{(j)}(z)}{t} + \frac{\zeta_{31}^{(j)}(z)}{t^{3/2}} \right]$$

$$+ \sum_{j=1}^{2} \exp\left(2(-1)^j t g_0(z)\right) \left[\frac{\zeta_{22}^{(j)}(z)}{t} + \frac{\zeta_{32}^{(j)}(z)}{t^{3/2}} \right]$$

$$+ \sum_{j=1}^{2} \exp\left(3(-1)^j t g_0(z)\right) \left[\frac{\zeta_{33}^{(j)}(z)}{t^{3/2}} \right] + O\left(\frac{1}{t^2}\right) + h.o.t. \quad (9.29)$$

in this region where $s \to \infty$, $t \to \infty$ and $z = s/t = O(1)$. This expansion is equivalent to that presented in Decent [11]. However, higher order exponential terms $(\exp(2tg_0)$, $\exp(3tg_0)$ ...) that are neglected due to viscous damping in Decent [11] are included here as they are the same order of magnitude for an inviscid jet. These expansions remain uniformly valid providing g_0 is purely imaginary.

It is necessary to distinguish between the coefficients of $\exp(tg_0)$ and $\exp(-tg_0)$ in the above, and so we include, for example, both $h_{11}^{(1)}(z)$ and $h_{11}^{(2)}(z)$ terms. However, we will find that the expansions (9.28) and (9.29) are incomplete, as they fail to generate a solution that matches with the far-field in the previos asymptotic region. The full correct expansions will be found in Section 9.5.3, but it is important to understand what happens when we use (9.28) and (9.29) to appreciate their deficiency.

9.5.1 The Lower Order Terms in the Expansion

Substitution of the expansions (9.28) and (9.29) into equation (9.1) yields

$$h_{11}^{(j)} = 2 \left(\frac{(z-1)g_0' - g_0}{g_0'} \right) \zeta_{11}^{(j)}. \quad (9.30)$$

Equation (9.2) yields a first order nonlinear ODE for g_0,

$$(g_0')^4 + (g_0')^2 + 2We \left[(z-1)^2 (g_0')^2 - 2(z-1)g_0 g_0' + g_0^2 \right] = 0. \quad (9.31)$$

Equation (9.31) has 3 sets of solutions. The first are the set of linear solutions

$$g_0 = M_0 + M_1 z$$

which are linked by the algebraic equation

$$M_1^4 + M_1^2 + 4WeM_1M_0 + 2WeM_0^2 + 2WeM_1^2 = 0. \tag{9.32}$$

This equation describes spatial instability and will be discussed in Section 9.6. The remaining solutions are given by $g_0 = g^+$ and $g_0 = g^-$ where

$$g^+ = \frac{(-1)^j}{4\sqrt{We}} \left(-We^2(z-1)^4 \quad - \quad 10We(z-1)^2 + 2 \right.$$
$$\left. + \quad \sqrt{We(z-1)^2 \left(We(z-1)^2 - 4 \right)^3} \right)^{1/2} \tag{9.33}$$

and

$$g^- = \frac{(-1)^j}{4\sqrt{We}} \left(-We^2(z-1)^4 \quad - \quad 10We(z-1)^2 + 2 \right.$$
$$\left. - \quad \sqrt{We(z-1)^2 \left(We(z-1)^2 - 4 \right)^3} \right)^{1/2} \tag{9.34}$$

We take the asymptotic limit as $z \to \infty$ of the above, namely,

$$g^+ = i(-1)^j (z-1) + O\left(\frac{1}{z}\right)$$
$$g^- = i(-1)^j \left(\frac{\sqrt{2We}}{4} z^2 - \sqrt{\frac{We}{2}} z + \frac{We+1}{2\sqrt{2We}} \right) + O\left(\frac{1}{z}\right) \qquad \text{as} \qquad z \to \infty.$$

Clearly it is the solution given by g^- that could be matched with the solution in region (iii) (9.27) as $z \to \infty$. The behaviour of (9.34) is examined in more detail in

9.5.2 Higher Order Terms

It is necessary to go to higher order to obtain an expression for the wave amplitude $\zeta_{11}^{(j)}$ ($h_{11}^{(j)}$ is given by (9.30)). Substituting the expansions into equation (9.1) yields

$$h_{21}^{(j)} = 2\left(\frac{(z-1)g_0' - g_0}{g_0'}\right)\zeta_{21}^{(j)}. \tag{9.35}$$

$$h_{22}^{(j)} = 2\left(\frac{(z-1)g_0' - g_0}{g_0'}\right)\zeta_{22}^{(j)} - \frac{3}{2}h_{11}^{(j)}\zeta_{11}^{(j)} \tag{9.36}$$

$$h_{31}^{(j)} = 2\left(\frac{(z-1)g_0' - g_0}{g_0'}\right)\zeta_{31}^{(j)} + (-1)^j\frac{2(z-1)(\zeta_{11}^{(j)})' + \zeta_{11}^{(j)} - (h_{11}^{(j)})'}{g_0'} - 3h_{11}^{(\bar{j})}\zeta_{22}^{(j)}. \tag{9.37}$$

$$h_{32}^{(j)} = 2\left(\frac{(z-1)g_0' - g_0}{g_0'}\right)\zeta_{32}^{(j)} - \frac{3}{2}\left(\zeta_{11}^{(j)}h_{21}^{(j)} + h_{11}^{(j)}\zeta_{21}^{(j)}\right) \tag{9.38}$$

$$h_{33}^{(j)} = 2\left(\frac{(z-1)g_0' - g_0}{g_0'}\right)\zeta_{33}^{(j)} - \frac{1}{3}\left(4\zeta_{11}^{(j)}h_{22}^{(j)} + 5h_{11}^{(j)}\zeta_{22}^{(j)}\right). \tag{9.39}$$

where $\bar{j} = 3 - j$.

Substituting into equation (9.2), we obtain

$$\zeta_{22}^{(j)} = \left[-\frac{1 + 2(g_0')^2}{2(g_0')^2}\right](\zeta_{11}^{(j)})^2. \tag{9.40}$$

$$\zeta_{32}^{(j)} = \left[\frac{1 + 2(g_0')^2}{(g_0')^2}\right]\zeta_{11}^{(j)}\zeta_{21}^{(j)}, \tag{9.41}$$

$$\zeta_{33}^{(j)} = \left[\frac{3 + 23(g_0')^2 + 25(g_0')^4 + 3(g_0')^6}{16(g_0')^2}\right](\zeta_{11}^{(j)})^3. \tag{9.42}$$

Additionally two ODEs for $\zeta_{11}^{(j)}$ are obtained

$$(-1)^j \frac{1}{2} \left[-3(g_0)^2 - 15(g_0)^4 - 11(g_0)^6 + 3(g_0)^8 \right] \zeta_{11}^{(\bar{j})} (\zeta_{11}^{(j)})^2$$

$$+ \left[2We g_0^2 g_0'' + 2We(z-1)^2(g_0')^3 + (g_0')^3 + 3(g_0')^5 \right] (\zeta_{11}^{(j)})'$$

$$+ \left[2We(g_0)^2 g_0'' + 2We(z-1)(g_0')^3 - 2We g_0(g_0')^2 + 3(g_0')^4 g_0'' \right] \zeta_{11}^{(j)} = 0 \quad (9.43)$$

for $f = 1, 2$, where the value of g_0 is given by $g_0 = g^-$ in (9.34). In the viscous case, the equivalent ODE for ζ was satisfied automatically by using the equivalent solution for g_0. The solution for ζ was then obtained through asymptotic matching with region (iii). However, the coefficients for the cubic term in $\zeta_{11}^{(j)}$ in (9.43) do not equal zero when g_0 is given by (9.34). Therefore the only solution to (9.43) is $\zeta_{11}^{(j)} = 0$, which is clearly not a valid solution because of matching with hte previous asymptotic region.

Cubic nonlinearities such as these appear in many physical systems, such as the vibration of strings, beams and membranes, or in the motion of masses connected by nonlinear springs [32]. The interactions of higher order harmonics in the system are indicative of resonance [9, 48]. These have also been shown to occur for capillary waves by Wilton [20] in his classical work. Details of these ripples in shallow water waves can be seen in many works, [30, 31], amongst others.

9.5.3 Extended Multiple Scales Expansion

Following experience of these cubic nonlinearities (e.g [9]), we introduce a secondary scale to generate a solution for $\zeta_{11}^{(j)}$, given by $Z = z \ln(t)^1$. It is then necessary to include an additional term in the expansions (9.28) and (9.29) to balance the terms of $\ln(t)/t^{3/2}$, given by $\bar{h}_{31}^{(j)}$ and $\bar{\zeta}_{31}^{(j)}$, in additional to the secondary scale. The correct expansions in region (iv) are given by

---

[1]We note that we first tried $Z = zt^p$ but no rational value of p generated the necessary terms.

$$u = 1 \ + \ \sum_{j=1}^{2} \exp\left((-1)^j t g_0(z)\right) \left[\frac{h_{11}^{(j)}(z, Z)}{t^{1/2}} + \frac{h_{21}^{(j)}(z, Z)}{t} + \frac{h_{31}^{(j)}(z, Z) + \ln(t)\bar{h}_{31}^{(j)}(z, Z)}{t^{3/2}}\right]$$

$$+ \ \sum_{j=1}^{2} \exp\left(2(-1)^j t g_0(z)\right) \left[\frac{h_{22}^{(j)}(z, Z)}{t} + \frac{h_{32}^{(j)}(z, Z)}{t^{3/2}}\right]$$

$$+ \ \sum_{j=1}^{2} \exp\left(3(-1)^j t g_0(z)\right) \left[\frac{h_{33}^{(j)}(z, Z)}{t^{3/2}}\right] + O\left(\frac{1}{t^2}\right) + h.o.t., \tag{9.44}$$

$$R = 1 \ + \ \sum_{j=1}^{2} \exp\left((-1)^j t g_0(z)\right) \left[\frac{\zeta_{11}^{(j)}(z, Z)}{t^{1/2}} + \frac{\zeta_{21}^{(j)}(z, Z)}{t} + \frac{\zeta_{31}^{(j)}(z, Z) + \ln(t)\bar{\zeta}_{31}^{(j)}(z, Z)}{t^{3/2}}\right]$$

$$+ \ \sum_{j=1}^{2} \exp\left(2(-1)^j t g_0(z)\right) \left[\frac{\zeta_{22}^{(j)}(z, Z)}{t} + \frac{\zeta_{32}^{(j)}(z, Z)}{t^{3/2}}\right]$$

$$+ \ \sum_{j=1}^{2} \exp\left(3(-1)^j t g_0(z)\right) \left[\frac{\zeta_{33}^{(j)}(z, Z)}{t^{3/2}}\right] + O\left(\frac{1}{t^2}\right) + h.o.t. \tag{9.45}$$

where $Z = z \ln(t)$. Note there will also be $\ln(t)$ terms in the expansion to $O(1/t^2)$ and higher order terms in the expansion. It is important to note that this secondary scale does not affect the solution for g_0, and thus all the results in Section 9.5.1 are retained.

On substitution of (9.44) and (9.44) into (9.2), the terms for h_{11}, h_{21}, h_{22}, h_{32} and h_{33} are identical to before (namely (9.30), (9.35), (9.36), (9.38) and (9.39)). In addition, we obtain

$$\frac{\partial h_{11}^{(j)}}{\partial Z} = 2(z-1)\frac{\partial \zeta_{11}^{(j)}}{\partial Z}, \tag{9.46}$$

$$\bar{h}_{31}^{(j)} = 2\left(\frac{(z-1)g_0' - g_0}{g_0'}\right)\bar{\zeta}_{31}^{(j)} + (-1)^j \frac{2(z-1)\frac{\partial \zeta_{11}^{(j)}}{\partial Z} - \frac{\partial h_{11}^{(j)}}{\partial Z}}{g_0'} - 3h_{11}^{(\bar{j})}\zeta_{22}^{(j)}. \tag{9.47}$$

170

and

$$h_{31}^{(j)} = 2\left(\frac{(z-1)g_0' - g_0}{g_0'}\right)\zeta_{31}^{(j)} + (-1)^j \frac{2(z-1)\frac{\partial \zeta_{11}^{(j)}}{\partial z} + \zeta_{11}^{(j)} - \frac{\partial h_{11}^{(j)}}{\partial z} - 2z\frac{\partial \zeta_{11}^{(j)}}{\partial Z}}{g_0'} - 3h_{11}^{(\bar{j})}\zeta_{22}^{(j)},$$

(9.48)

Equations (9.46) and (9.47) are new equations arising from the need to balance $\ln(t)$ terms; equation (9.48) replaces equation (9.37).

Substituting into equation (9.2), we obtain the same ODE to solve for g_0, namely (9.31). Therefore, the solution for g_0 is unaffected by the secondary scale. In addition, ζ_{22}, ζ_{32} and ζ_{33} remain unchanged, (given by (9.40), (9.41) and (9.42)). We also obtain

$$\left[[2((z-1)^2(g_0')^2 - g_0^2)]We + 3(g_0')^4 + (g_0')^2\right]\frac{\partial \zeta_{11}^{(j)}}{\partial Z}$$
$$+(g_0')^5 + (g_0')^3 + 2Weg_0'\left[(z-1)^2(g_0')^2 - 2(z-1)g_0g_0' + g_0^2\right] = 0.$$

(9.49)

and

$$(-1)^j\left[-3(g_0)^2 - 15(g_0)^4 - 9(g_0)^6 + 3(g_0)^8\right]\zeta_{11}^{(\bar{j})}(\zeta_{11}^{(j)})^2$$
$$+ \left[2Weg_0^2g_0'' + 2We(z-1)^2(g_0')^3 + (g_0')^3 + 3(g_0')^5\right]\frac{\partial \zeta_{11}^{(j)}}{\partial z}$$
$$+ \left[2We(g_0)^2g_0'' + 2We(z-1)(g_0')^3 - 2Weg_0(g_0')^2 + 3(g_0')^4g_0''\right]\zeta_{11}^{(j)}$$
$$-8Wez(g_0')^2((z-1)g_0' - g_0)\frac{\partial \zeta_{11}^{(j)}}{\partial Z} = 0. \quad (9.50)$$

Equation (9.49) is a new equation arising from the need to balance $\ln(t)$ terms; equation (9.50) replaces equation (9.43). Equation (9.49) is satisfied automatically when g_0 is given by $g_0 = g^-$ in (9.34).

Hence,

$$\frac{\partial \zeta_{11}^{(j)}}{\partial Z} = (-1)^j A(z)\zeta_{11}^{(\bar{j})}(\zeta_{11}^{(j)})^2.$$

(9.51)

where

$$A(z) = \frac{[-3(g_0)^2 - 15(g_0)^4 - 9(g_0)^6 + 3(g_0)^8]}{-8Wez(g_0')^2((z-1)g_0' - g_0)} \neq 0,$$

and g_0 is given by $g_0 = g^-$ in (9.34). This arises due to the fact that the coefficients of $\partial\zeta_{11}^{(j)}/\partial z$ and $\zeta_{11}^{(j)}$ in (9.50) equal zero when g_0 is given by $g_0 = g^-$ in (9.34). Taking the limit as $z \to \infty$

$$A(z) \to -\frac{3\sqrt{2}}{32} iW e^{3/2} z^3.$$

Hence $A(z)$ is purely imaginary as $z \to \infty$.

Equation (9.51) consists of two equations, namely

$$\frac{\partial\zeta_{11}^{(1)}}{\partial Z} = -A(z)\zeta_{11}^{(2)}(\zeta_{11}^{(1)})^2 \qquad \frac{\partial\zeta_{11}^{(2)}}{\partial Z} = A(z)\zeta_{11}^{(1)}(\zeta_{11}^{(2)})^2 \tag{9.52}$$

Through matching with the far field in region (iii) as $z \to \infty$ it becomes clear that the solution is required to behave as

$$\zeta_{11}^{(1)} \to \frac{i\alpha}{2z^4} \qquad \zeta_{11}^{(2)} \to -\frac{i\alpha}{2z^4} \tag{9.53}$$

where α is a constant obtained in region (i). Solving (9.52), we obtain

$$\zeta_{11}^{(1)} = C_1(z)\exp\left(C_2(z)Z\right) \qquad \zeta_{11}^{(2)} = -\frac{C_2(z)}{A(z)C_1(z)}\exp\left(-C_2(z)Z\right).$$

Matching with the previous region is obtained if

$$C_2(z) = A(z)C_1(z)^2.$$

and

$$C_1(z) \to \frac{i\alpha}{2z^4} \qquad \text{as} \quad z \to \infty.$$

172

Hence

$$\zeta_{11}^{(1)} \rightarrow \frac{i\alpha^2}{2z^4} \exp\left(-\frac{A(z)\alpha^2}{4z^8}Z\right) \qquad \zeta_{11}^{(2)} \rightarrow -\frac{i\alpha}{2z^4} \exp\left(\frac{A(z)\alpha}{4z^8}Z\right).$$

as $z \rightarrow \infty$ and $Z \rightarrow \infty$, as so this matches with region (iii). This solution also agrees with the viscous solution obtained in Decent [11] in the large Reynolds number limit $Re \rightarrow \infty$.

9.6   Linear waves with $t \rightarrow \infty$ and $s = O(1)$.

In region (v), $s = O(1)$ and $t \rightarrow \infty$. We search for linear wave solutions, expanding with

$$
\begin{aligned}
u &= 1 + \delta \exp(i\omega t)\left(\Omega_0(s) + \frac{\Omega_1(s)}{t^{1/2}} + O\left(\frac{1}{t}\right)\right) + c.c + h.o.t. \\
R &= 1 + \delta \exp(i\omega t)\left(\Gamma_0(s) + \frac{\Gamma_1(s)}{t^{1/2}} + O\left(\frac{1}{t}\right)\right) + c.c + h.o.t.
\end{aligned}
$$

where $c.c$ denotes the complex conjugate and higher order terms encompass the $\ln(t)$ terms in the multiple scales expansion used in region (iv). ω is given by the boundary condition at $s = 0$, and δ small indicates a small perturbation at the orifice.

Taking equations (9.1) and (9.2) to $O(1)$ gives

$$i\omega\Omega_0 + \Gamma_0' + \frac{1}{2}\Omega' = 0 \tag{9.54}$$

and

$$i\omega\Gamma_0 + \Gamma_0' = \frac{-1}{We}\left(-\Omega_0' - \Omega_0'''\right) \tag{9.55}$$

Hence

$$\Omega_0'''' + (1 + 2We)\Omega_0'' + 4iWe\omega\Omega_0' - 2We\omega^2\Omega_0 = 0$$

173

and

$$\Omega_0 = \sum_{j=1}^{4} \omega_j e^{m_j s}$$

where m_j are the solutions to the equation

$$m^4 + (1 + 2We)m^2 + 4iWe\omega m - 2We\omega^2 = 0. \tag{9.56}$$

This equation describes spatial instability (as can be seen in Keller *et al.* [21]) and corresponds to the linear wave solution found in Section 9.5.1 where $M_0 = -m$ and $M_1 = -i\omega$.

Equation (9.54) yields

$$\Gamma_0 = \sum_{j=1}^{4} \gamma_j \exp^{m_j s}$$

where

$$\gamma_j = -\frac{2\omega_j(i\omega + m_j)}{m_j} \qquad \text{for} \quad j = 1, 2, 3, 4. \tag{9.57}$$

Substitution into the boundary condition $R(s = 0, t) = 1$ gives

$$\omega_1 + \omega_2 + \omega_3 + \omega_4 = 0$$

and $u(s = 0, t) = 1 + \delta \sin(\omega t)$ gives

$$\gamma_1 + \gamma_2 + \gamma_3 + \gamma_4 \quad = \quad -\frac{i}{2}.$$

Taking equations (9.1) and (9.2) to $O(t)$, we obtain similar to equations (9.54) and (9.55), though with solution

$$\Omega_1 = \sum_{j=5}^{8} \omega_j e^{m_j s}, \qquad \text{and} \qquad \Gamma_1 = \sum_{j=5}^{8} \gamma_j e^{m_j s},$$

174

where m_j are solutions to (9.56) and γ_j are given by (9.57) for $j = 5, 6, 7, 8$, and

$$\omega_5 + \omega_6 + \omega_7 + \omega_8 = 0$$
$$\gamma_5 + \gamma_6 + \gamma_7 + \gamma_8 = 0.$$

9.7   Discussion

In Section 9.5, we used the expansions (9.44) and (9.45) to generate the solution in Region IV where $s \to \infty$ and $t \to \infty$. The correct solution g_0 that matched to the farfield in Region III is given by (9.34). We now examine the behaviour of this solution.

Figure 9.2 shows g_0, given by (9.34), plotted along the jet for varying Weber numbers. It can be seen in Figure 9.2(a) that for values of $z_1 < z < z_2$, for some value of z_1 and z_2, the real part of g_0 ($\Re(g_0)$) is positive, and therefore the expansions (9.44) and (9.45) become non-uniform for large t. In this region, the asymptotics cannot fully capture the behaviour of the waves and only a full computational solution can do it. $\Re(g_0)$ is the temporal growth rate of the nonlinear wave, and the most unstable temporal mode occurs at $z = 1$. The imaginary part of g_0 ($\Im(g_0)$) is the local frequency, and this is shown in Figure 9.2(b). It can be seen that the frequency changes sign at $z = 1$.

By considering a Taylor expansion of $g_0(z)$, and comparing with terms to an expression describing a linear wave ($\exp(iks + \omega t)$, we can also obtain the spatial growth rate, given by $\Re(g_0)'$, and the local wavenumber, given by $k = \Im(g_0)'$. These are plotted in Figure 9.3. The spatial growth rate changes sign at $z = 1$. The minimum in local wavenumber also occurs at this point.

175

The local wave speed is given by

$$v = z - \frac{\Im(g_0)}{\Im(g_0)'}.$$

This is plotted in Figure 9.4, and we notice that $v = 1$ as $z = 1$. The local wavespeed increases with z.

Adopting a Taylor expansion about $z = 1$ we obtain

$$
\begin{aligned}
\Re(g_0) &= \frac{\sqrt{2}}{4\sqrt{We}} - \frac{\sqrt{2We}}{8}(z-1)^2 + \frac{\sqrt{2}We^{3/2}}{32}(z-1)^4 + O((z-1)^6) \\
\Im(g_0) &= -\frac{\sqrt{2}}{2}(z-1) - \frac{\sqrt{2}We}{16}(z-1)^3 + O((z-1)^5) \\
v &= 1 + \frac{We}{4}(z-1)^3 + O((z-1)^4) \\
k &= \Im(g_0)' = \frac{\sqrt{2}}{2} + \frac{3\sqrt{2}We}{16}(z-1)^2 + O((z-1)^4)
\end{aligned}
$$

as $z \to 1$. We notice that as $z \to 1$ the values for the temporal growth rate and wavenumber, $\Re(g_0)$ and k, correspond to the longwavelength results of temporal instability of a the straight jet dispersion relation (2.3). This suggests that when the nonlinear wave is growing at its fastest, it behaves in a similar fashion to an unstable linear wave.

In Section 9.6, we obtained a linear wave solution which was spatially unstable. This grows as it propagates, becoming nonlinear, but is driven by the frequency ω arising from the vibration at the orifice. At point z_1, which corresponds to the point at which the real part of g_0 becomes unstable, this linear wave interacts with the unstable nonlinear disturbance for $z_1 < z < z_2$. In this region the expansions are non-uniform and the full solution can only be captured computationally. The expansions are uniform for $z > z_2$ and it is the solution given by (9.34) that matches with the far-field in Region III. The aforementioned regions where linear waves are dominant,

nonlinear waves are dominant, and where linear and nonlinear waves undergo mode are shown in Figure 9.5.

After some algebra, we can evaluate z_1 and z_2 as

$$z_1 = \max\left(1 - \frac{2}{\sqrt{We}}, 0\right) \qquad z_2 = 1 + \frac{2}{\sqrt{We}}.$$

It is postulated that in order to regulate jet break-up it is necessary to break the jet in regions where linear waves dominate break-up and nonlinear waves are stable ($z < z_1$). This suggests that when $We \leq 4$, $z_1 = 0$ and nonlinear waves are dominant at the orifice and the jets are more difficult to control. As We increases, the region at which the jet is more easily controllable increases.

If the jet is allowed, either for $We < 4$ or δ sufficiently small, to break up for $z > z_1$ nonlinearities are present which cause satellite droplets, shown in Figure 9.6(a) and (b). If the jet is forced to break-up for $z < z_1$ then it is possible to remove satellite droplets if the correct frequency is used (as discussed in Chapter 7 for the case of a rotating jet). This is shown in Figure 9.6(c).

9.8   Conclusions

In this chapter we have used the Needham Leach method to develop an asymptotic solution in the large time region to describe the behaviour of the jet evolution equations. We illustrate the difference in behaviour between an inviscid jet and viscous jet, highlighting the more complex dynamics in the solution for nonlinear waves for inviscid fluids, drawing comparisons with other areas of fluid dynamics such as shallow water waves.

We have used a multiple scales expansion to generate the asymptotic expansions in order to describe nonlinear waves as $s \to \infty$ and $t \to \infty$. This allowed us to describe

the regions in which linear waves are more dominant, nonlinear waves dominated jet break-up and a region where both modes undergo competition. We postulate that if the jet can be forced to break in a region where linear waves are more dominant, then satellite droplets are less likely to appear.
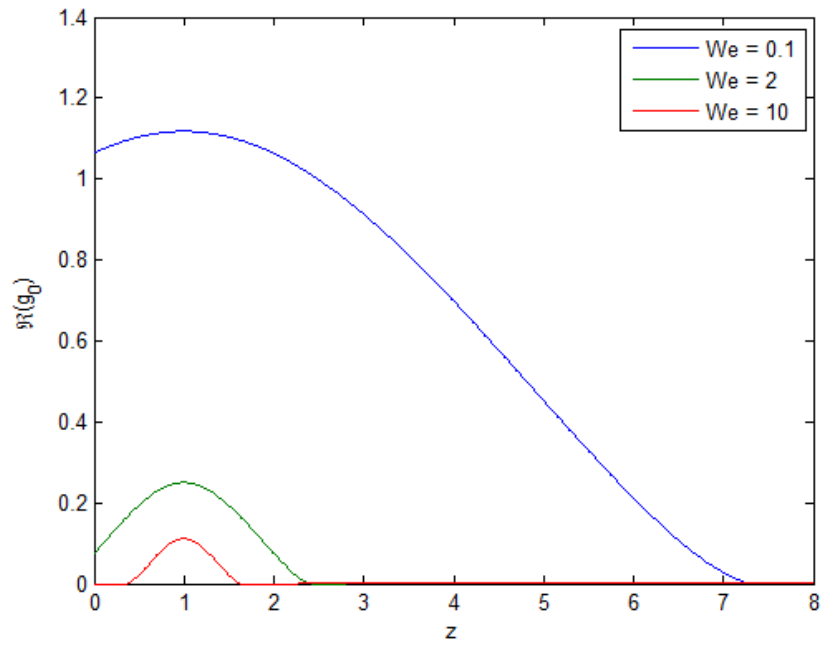
(a) temporal growth rate $\Re(g_0)$
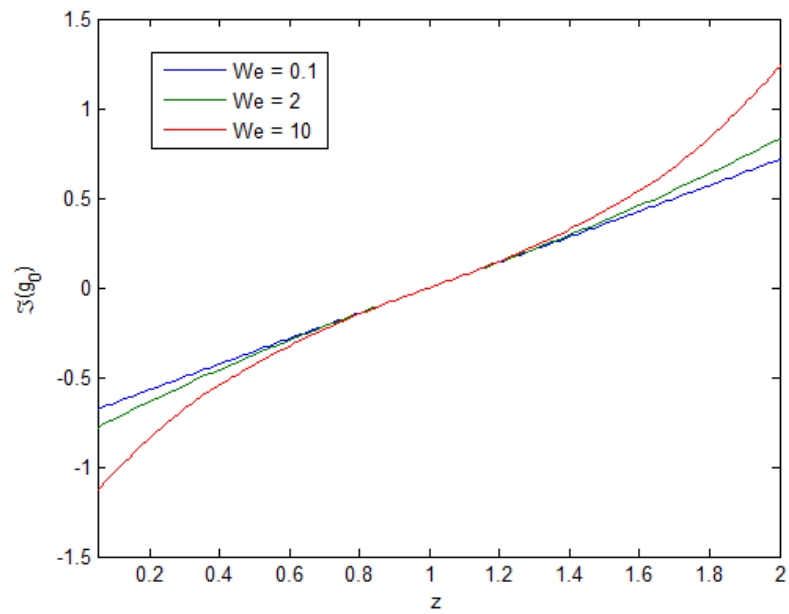
(b) $\Im(g_0)$

Figure 9.2: Plot showing g_0 with z.

179
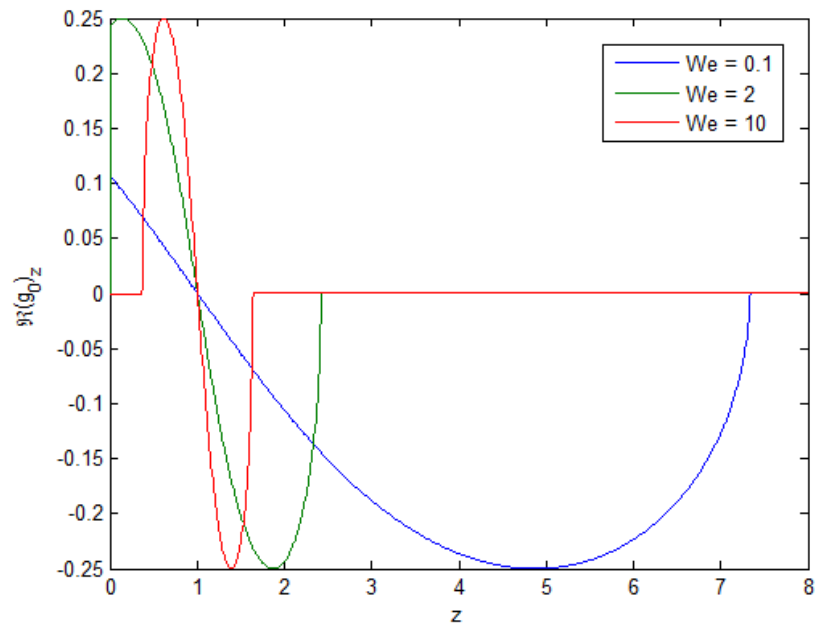
(a) spatial growth rate $\Re(g_0)'$
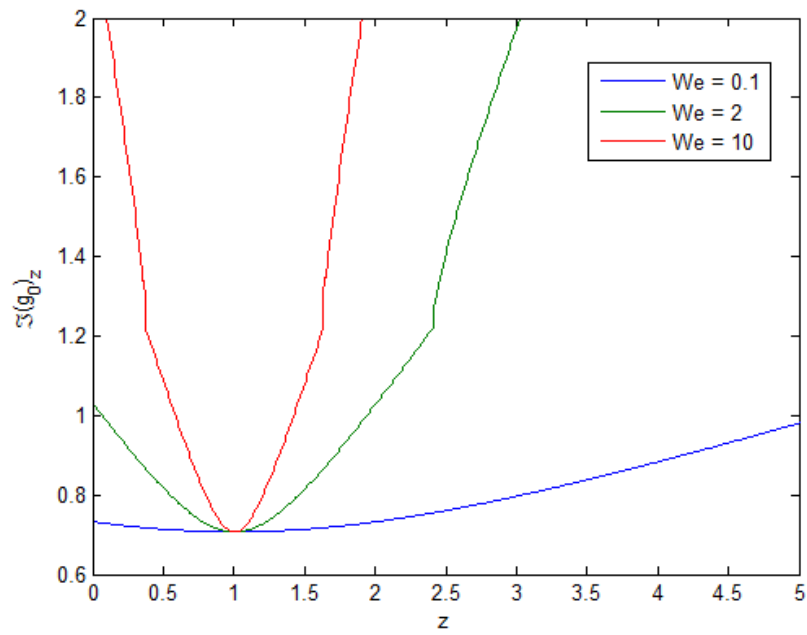
(b) local wavenumber $k = \Im(g_0)'$

Figure 9.3: Plot showing wave behaviour with z.
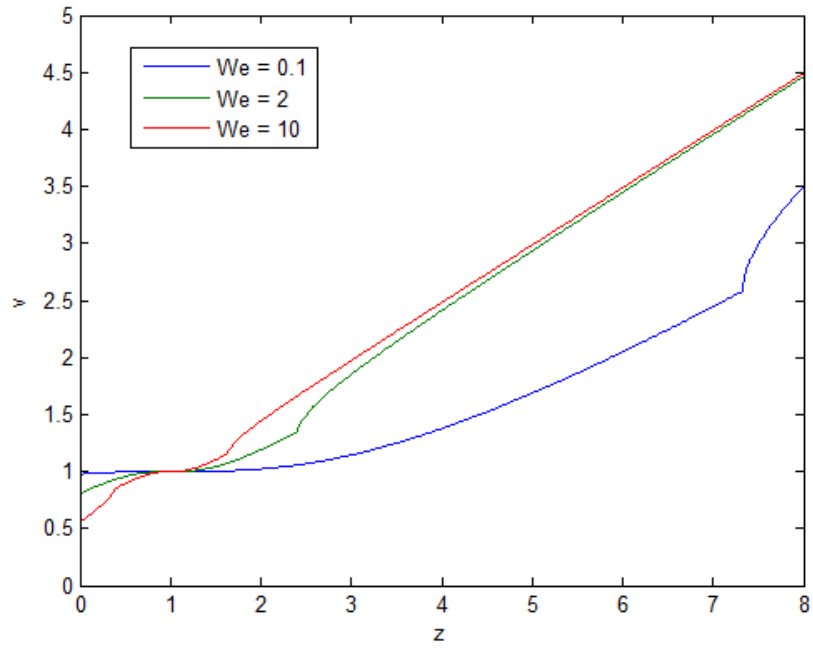
Figure 9.4: Plot showing wave speed v with z.
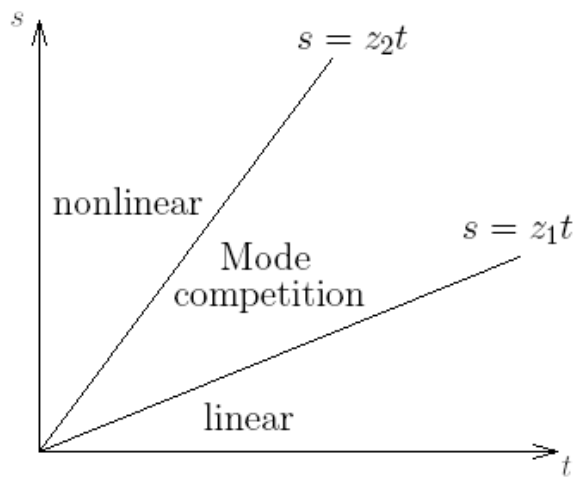
Figure 9.5: Diagrammatic representation showing the regions of wave behaviour.
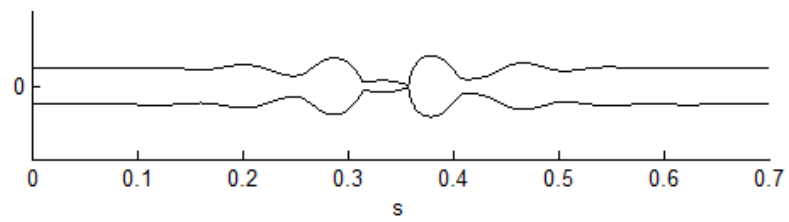
(a) $We = 2$, $\delta = 0.001$, $\omega = 0.7048$
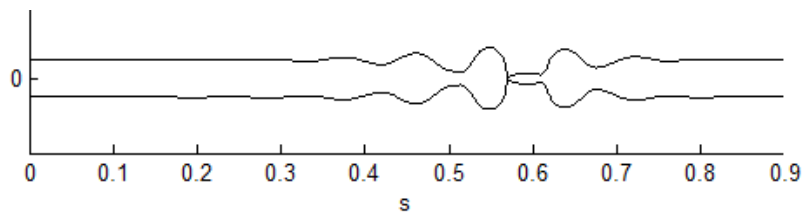
(b) $We = 50$, $\delta = 0.001$, $\omega = 0.7048$
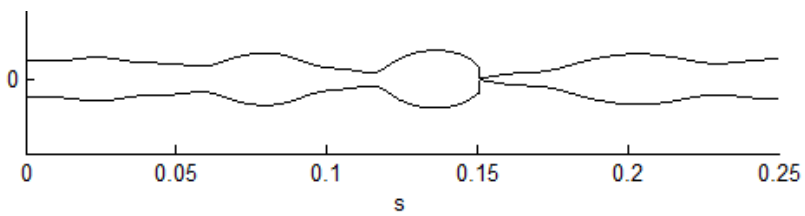
(c) $We = 50$, $\delta = 0.1$, $\omega = 1.1$

Figure 9.6: Straight jet break-up.

Chapter 10

The effect of rotation on an asymptotic solution to the jet equations

In the last chapter we used the Needham-Leach Method to investigate the asymptotic behaviour of a straight liquid jet in the large spatial and temporal limits. This chapter extends the analysis to describe the behaviour of a curved liquid jet. The asymptotic regions are the same as for a straight jet, namely those shown in Figure 9.1.

The equations describing curved liquid jet break-up are

$$R_t + uR_s + \frac{u_s R}{2} = 0, \tag{10.1}$$

$$u_t + uu_s = \frac{-1}{We}\left(\frac{1}{R(1+R_s^2)^{\frac{1}{2}}} - \frac{R_{ss}}{(1+R_s^2)^{\frac{3}{2}}}\right)_s + \frac{(X+1)X_s + ZZ_s}{Rb^2} \tag{10.2}$$

where u is the jet velocity, R is the jet radius and X and Z are the jet centreline

coordinates. These equations were derived by Pǎrǎu *et al.* [36] and are equivalent to (3.11) with $Re \to \infty$. These are subject to

$$R(s, t = 0) = 1 \qquad u(s, t = 0) = 1$$

$$R(s = 0, t) = 1 \qquad u(s = 0, t) = 1 + \delta \sin(\omega t)$$

$$R \to \bar{R}(s) \qquad u \to \bar{u}(s) \qquad \text{as} \qquad s \to \infty \qquad (10.3)$$

where $\bar{u}(s)$ and $\bar{R}(s)$ are the steady state solutions obtained from the solutions to the equations

$$\bar{u}\bar{u}_s = \frac{1}{We}\kappa_s + \frac{(\bar{X} + 1)\bar{X}_s + \bar{Z}\bar{Z}_s}{Rb^2},$$

$$\frac{1}{2}\bar{R}\bar{u}_s + \bar{u}\bar{R}_s = 0$$

$$(\bar{X}_s\bar{Z}_{ss} - \bar{Z}_s\bar{X}_{ss})\left(\bar{u}^2 - \frac{1}{We\bar{R}}\right) - \frac{2\bar{u}}{Rb} + \frac{((\bar{X} + 1)\bar{Z}_s - \bar{Z}\bar{X}_s)}{Rb^2} = 0,$$

$$\bar{X}_s\bar{X}_{ss} + \bar{Z}_s\bar{X}_{ss} = 1. \qquad (10.4)$$

where κ is the curvature of the jet. These are subject to $\bar{X} = \bar{Z} = \bar{Z}_s = 0$ and $\bar{X}_s = \bar{R} = \bar{u} = 1$ at $s = 0$. In addition, we have the boundary condition

$$R(s, t = 0) = \hat{R}(s) \qquad u(s, t = 0) = \hat{u}(s) \qquad \text{as} \qquad s \to 0$$

where $\hat{R}(s)$ and $\hat{u}(s)$ are the small s expansions of the steady state (10.4).

10.1 Asymptotic region for $s \to 0$, $t \to 0$

As with a straight jet, there exists an inner region as $s \to 0$. The expansion in Region I is given by

$$
\begin{aligned}
u &= \hat{u}(s) + tF_0(\eta) + O(t^{3/2}) \\
R &= \hat{R}(s) + t^{3/2}G_0(\eta) + O(t^3)
\end{aligned}
\tag{10.5}
$$

where $\eta = s/\sqrt{t}$ and $\hat{u}(s)$ and $\hat{R}(s)$ are the small s expansions of $\bar{u}(s)$ and $\bar{R}(s)$. This is the same expansion as in Chapter 9, but for the presence of the steady state. Substitution into (10.1) and (10.2) yields

$$
\frac{1}{\sqrt{t}}\left(\hat{u}\hat{R}_s + \frac{\hat{u}_s\hat{R}}{2}\right) + 3G_0 - \eta G_0' + \frac{1}{2}\check{R}F_0' + O\left(t^{1/2}\right) = 0,
\tag{10.6}
$$

and

$$
\begin{aligned}
F_0 - \frac{1}{2}\eta F_0' + \hat{u}\hat{u}_s \; - \; & \frac{1}{We}\left(\frac{-\hat{R}_s}{\hat{R}^2(1+\hat{R}_s^2)^{\frac{1}{2}}} - \frac{\hat{R}_s\hat{R}_{ss} + \hat{R}\hat{R}_{sss} + \hat{R}G_0'''}{(1+\hat{R}_s^2)^{\frac{3}{2}}} + \frac{3\hat{R}_s\hat{R}_{ss}^2}{(1+\hat{R}_s^2)^{\frac{5}{2}}}\right) \\
& - \frac{(\hat{X}+1)\hat{X}_s + \hat{Z}\hat{Z}_s}{Rb^2} + O\left(t^{1/2}\right) = 0,
\end{aligned}
\tag{10.7}
$$

where $\hat{X}(s)$ and $\hat{Z}(s)$ are the small s expansions of steady state solutions $\bar{X}(s)$ and $\bar{Z}(s)$. The hatted quantities are given by the small s asymptotic solution to the steady state equations (10.4). After considerable work investigating the small s behaviour of the steady state equations, details of which can be found in Appendix B, this can be reduced to

$$
\begin{aligned}
3G_0 - \eta G_0' + F_0' + O\left(t^{1/2}\right) + O(s) &= 0, \\
F_0 - \frac{1}{2}\eta F_0' - \frac{1}{\gamma}G_0''' + O\left(t^{1/2}\right) + O(s) &= 0,
\end{aligned}
$$

where $' \equiv \frac{d}{d\eta}$, $\eta = s/\sqrt{t}$ and

$$
\begin{aligned}
\gamma &= We\left(1 + \left(\check{R}'\right)^2\right)^{3/2} \\
&= \frac{We\left(Rb^4(2We + 1)^2 + We^2\right)^{3/2}}{Rb^6(2We + 1)^3} \quad \text{as} \quad s \to 0.
\end{aligned}
\tag{10.8}
$$

We note that taking the limit $Rb \to \infty$, $\gamma \to We$ and we simplify to the case of a straight jet. We maintain boundary conditions

$$
F_0(0) = \delta\omega, \qquad F_0(\infty) = 0, \qquad G_0(0) = 0, \qquad G_0(\infty) = 0.
$$

Following the same analysis as in the previous chapter we obtain

$$
\begin{aligned}
G_0 &= \delta\omega\left[\sqrt{\frac{\gamma}{2}}\eta + \frac{\gamma}{6}\eta^3 - \frac{2^{1/4}\gamma^{3/4}}{3\sqrt{\pi}}\eta^2\cos\left(\frac{\sqrt{2\gamma}}{4}\eta^2\right)\right. \\
&\quad + \left.\frac{2^{7/4}\gamma^{1/4}}{3\sqrt{\pi}}\sin\left(\frac{\sqrt{2\gamma}}{4}\eta^2\right) - \frac{\gamma}{3}\eta^3 F_s\left(\frac{\gamma^{1/4}}{2^{1/4}\sqrt{\pi}}\eta\right) + \sqrt{2\gamma}\eta F_c\left(\frac{\gamma^{1/4}}{2^{1/4}\sqrt{\pi}}\eta\right)\right]
\end{aligned}
\tag{10.9}
$$

and

$$
\begin{aligned}
F_0 &= \delta\omega\left[1 - \sqrt{\frac{\gamma}{2}}\eta^2 - \frac{2^{3/4}\gamma^{1/4}}{\sqrt{\pi}}\eta\sin\left(\frac{\sqrt{2\gamma}}{4}\eta^2\right) - 2F_s\left(\frac{\gamma^{1/4}}{2^{1/4}\sqrt{\pi}}\eta\right)\right. \\
&\quad + \left.\sqrt{2\gamma}\eta^2 F_c\left(\frac{\gamma^{1/4}}{2^{1/4}\sqrt{\pi}}\eta\right)\right].
\end{aligned}
\tag{10.10}
$$

As $\eta \to \infty$,

$$
\begin{aligned}
F_0 &= \frac{\alpha}{\eta^3}\sin\left(\beta\eta^2\right) + O\left(\frac{1}{\eta^5}\right), \\
G_0 &= \frac{\alpha}{\eta^4}\sin\left(\beta\eta^2\right) + O\left(\frac{1}{\eta^6}\right),
\end{aligned}
\tag{10.11}
$$

186

where

$$\alpha = \frac{4 \, 2^{3/4} \delta \omega}{\gamma^{3/4} \sqrt{\pi}}, \qquad \beta = \frac{\sqrt{2\gamma}}{4}.$$

This solution is identical to the solution describing a straight jet, but for the constant γ.

10.2 $s = O(1)$, $t \to 0$ **asymptotics**

In Region II, we consider $s = O(1)$ and $t \to 0$. Driven by matching in Region A as $\eta \to \infty$, we use (10.11) in (10.5) to pose the following expansions

$$
\begin{aligned}
u = \bar{u}(s) \;\; + \;\; & \sin\left(\frac{\sqrt{2\gamma}}{4}\frac{s^2}{t}\right) \frac{t^{5/2}}{s^3} \left(u_0(s) + tu_2(s) + O\left(t^2\right)\right) \\
+ \;\; & \cos\left(\frac{\sqrt{2\gamma}}{4}\frac{s^2}{t}\right) \frac{t^{5/2}}{s^3} \left(u_1(s) + tu_3(s) + O\left(t^2\right)\right) + h.o.t \\
R = \bar{R}(s) \;\; + \;\; & \sin\left(\frac{\sqrt{2\gamma}}{4}\frac{s^2}{t}\right) \frac{t^{7/2}}{s^4} \left(R_0(s) + tR_2(s) + O\left(t^2\right)\right) \\
+ \;\; & \cos\left(\frac{\sqrt{2\gamma}}{4}\frac{s^2}{t}\right) \frac{t^{7/2}}{s^4} \left(R_1(s) + tR_3(s) + O\left(t^2\right)\right) + h.o.t
\end{aligned}
$$

as $t \to 0$, $h.o.t.$ denotes the higher order terms in the expansion of F_0 and G_0 and $\bar{u}(s)$ and $\bar{R}(s)$ are the steady values for u and R.

Substituting into equation (10.1) we obtain,

$$\frac{1}{2}\bar{R}\bar{u}_s + \bar{u}\bar{R}_s = 0$$

which is satisfied by the steady state, and

$$u_0 = \frac{R_0}{\bar{R}} \quad \text{and} \quad u_1 = \frac{R_1}{\bar{R}},$$

187

$$u_2 = \frac{4}{\sqrt{2\gamma}s^2\bar{R}}\left(\frac{\sqrt{2\gamma}}{4}s^2R_2 - \frac{1}{2}sR_1' - \frac{1}{2}sR_1\frac{\bar{R}'}{\bar{R}} - 2R_1 - \frac{\sqrt{2\gamma}}{2}sR_0\right)$$

and

$$u_3 = \frac{4}{\sqrt{2\gamma}s^2\bar{R}}\left(\frac{\sqrt{2\gamma}}{4}s^2R_3 - \frac{\sqrt{2\gamma}}{2}sR_1 + \frac{1}{2}sR_0' + \frac{1}{2}sR_0\frac{\bar{R}'}{\bar{R}} + 2R_0\right).$$

Substituting into equation (10.2) we obtain,

$$\bar{u}\bar{u}' + \frac{1}{We}\left(\frac{-\bar{R}'}{\bar{R}^2(1+(\bar{R}')^2)^{\frac{1}{2}}} - \frac{\bar{R}'\bar{R}'' + \bar{R}\bar{R}'''}{\bar{R}(1+(\bar{R}')^2)^{\frac{3}{2}}} + \frac{3\bar{R}'\bar{R}''^2}{(1+(\bar{R}')^2)^{\frac{5}{2}}}\right) + \frac{(\bar{X}+1)\bar{X}' + \bar{Z}\bar{Z}'}{Rb^2} = 0$$

which is satisfied by the steady state with the full curvature included, and

$$-\frac{\beta}{s}u_0 + \frac{8\beta^3}{sWe(1+(\bar{R}')^2)^{3/2}}R_0 \tag{10.12}$$

and

$$\frac{\beta}{s}u_1 + \frac{8\beta^3}{sWe(1+(\bar{R}')^2)^{3/2}}R_1 = 0, \tag{10.13}$$

where $\beta = \sqrt{2\gamma}/4$. This is not satisfied with

$$\gamma = We(1+(\bar{R}')^2)^{3/2}$$

as defined by (10.8). However, if γ is defined as

$$\gamma = \frac{We(1+(\bar{R}')^2)^{3/2}}{\bar{R}},$$

(10.12) and (10.13) are satisfied. This new value of γ does indeed match with (10.8) in Region A as $\bar{R} = 1$ at $s = 0$. We also obtain

$$R_1' + \frac{\sqrt{2\gamma}}{2}\bar{u}R_0 + \Sigma R_1 = 0$$

and

$$R_0' - \frac{\sqrt{2\gamma}}{2}\bar{u}R_1 + \Sigma R_0$$

where

$$\Sigma = \frac{\bar{R}'(1 + (\bar{R}')^2) - 3\bar{R}\bar{R}'\bar{R}''}{2\bar{R}^2(1 + (\bar{R}')^2)} > 0.$$

This yields

$$R_0'' + 2\Sigma R_0' + \left(\frac{\gamma\bar{u}^2}{2} + \Sigma^2\right)R_0 = 0$$

and hence

$$R_0(s) = A\exp(-\Sigma s)\sin\left(\frac{\sqrt{2\gamma}\bar{u}}{2}s\right) + B\exp(-\Sigma s)\cos\left(\frac{\sqrt{2\gamma}\bar{u}}{2}s\right) \qquad (10.14)$$

and

$$R_1(s) = A\exp(-\Sigma s)\cos\left(\frac{\sqrt{2\gamma}\bar{u}}{2}s\right) - B\exp(-\Sigma s)\sin\left(\frac{\sqrt{2\gamma}\bar{u}}{2}s\right) \qquad (10.15)$$

Matching occurs in Region A, with $\eta = s/\sqrt{t}$ and $s \to 0$, yielding $A = 0$ and $B = \alpha$. The expansions become

$$u = \bar{u} + \frac{\alpha\exp(-\Sigma s)}{\bar{R}}\sin\left(\frac{\sqrt{2\gamma}}{4}\frac{s^2}{t} - \frac{\sqrt{2\gamma}\bar{u}}{2}s\right) + h.o.t$$

$$R = \bar{R} + \alpha\exp(-\Sigma s)\sin\left(\frac{\sqrt{2\gamma}}{4}\frac{s^2}{t} - \frac{\sqrt{2\gamma}\bar{u}}{2}s\right) + h.o.t$$

as $t \to 0$ and $s = O(1)$. The exponential term suggests that as s increases R decreases, indicating the jet thins with s.

10.3   Large spatial asymptotics

In Region III we consider $t = O(1)$ and $s \to \infty$. It is extremely difficult to obtain the full solution in Region III in terms of $\bar{R}$ and $\bar{u}$, so we scale out the complex algebraic terms for the steady state and concentrate on the asymptotic behaviour of (10.1) and (10.2). The impact of rotation will appear through a numerical solution to the steady state. We introduce a second variable $\bar{s} = s\epsilon$, with $\epsilon \to 0$ such that $\bar{s} = O(1)$. We extend the solution in Region II by

$$
\begin{aligned}
u = \bar{u}(\bar{s}) \;+\; & \frac{\exp(-\Sigma s)}{\bar{R}(\bar{s})} \left[\sin\left(\frac{\sqrt{2\gamma}}{4}\frac{s^2}{t} - \sqrt{\frac{\gamma}{2}}\bar{u}s \right) \frac{t^{5/2}}{s^3} \left(U_0(t) + \frac{U_2(t)}{s} + \frac{U_4(t)}{s^2} + O\left(\frac{1}{s^3}\right) \right) \right. \\
+\; & \left. \cos\left(\frac{\sqrt{2\gamma}}{4}\frac{s^2}{t} - \sqrt{\frac{\gamma}{2}}\bar{u}s \right) \frac{t^{5/2}}{s^3} \left(U_1(t) + \frac{U_3(t)}{s} + \frac{U_5(t)}{s^2} + O\left(\frac{1}{s^3}\right) \right) \right] + h.o.t. \\
R = \bar{R}(\bar{s}) \;+\; & \exp(-\Sigma s) \left[\sin\left(\frac{\sqrt{2\gamma}}{4}\frac{s^2}{t} - \sqrt{\frac{\gamma}{2}}\bar{u}s \right) \frac{t^{7/2}}{s^4} \left(r_0(t) + \frac{r_2(t)}{s} + \frac{r_4(t)}{s^2} + O\left(\frac{1}{s^3}\right) \right) \right. \\
+\; & \left. \cos\left(\frac{\sqrt{2\gamma}}{4}\frac{s^2}{t} - \sqrt{\frac{\gamma}{2}}\bar{u}s \right) \frac{t^{7/2}}{s^4} \left(r_1(t) + \frac{r_3(t)}{s} + \frac{r_5(t)}{s^2} + O\left(\frac{1}{s^3}\right) \right) \right] + h.o.t.
\end{aligned}
\tag{10.16}
$$

as $s \to \infty$, where now $\bar{R}$, $\bar{u}$ and γ depend on $\bar{s}$. $h.o.t.$ denotes the higher order terms.

Substituting the above expansions into (10.1), we obtain the steady state equations

$$
\bar{u}\bar{R}' + \frac{\bar{u}'\bar{R}}{2} = 0
\tag{10.17}
$$

and

$$
\begin{aligned}
\epsilon\bar{u}\bar{u}' \;=\; & \frac{-1}{We}\left(\frac{-\epsilon\bar{R}'}{\bar{R}^2(1+\epsilon^2(\bar{R}')^2)^{\frac{1}{2}}} - \frac{\epsilon^3\bar{R}'\bar{R}'' + \epsilon^3\bar{R}\bar{R}'''}{\bar{R}(1+\epsilon^2(\bar{R}')^2)^{\frac{3}{2}}} + \frac{3\epsilon^5\bar{R}'(\bar{R}'')^2}{(1+\epsilon^2(\bar{R}')^2)^{\frac{5}{2}}} \right) \\
+\; & \frac{(X+1)X_s + ZZ_s}{Rb^2},
\end{aligned}
\tag{10.18}
$$

190

where $' \equiv \frac{d}{d\bar{s}}$. The large s behaviour of X and Z is found to be

$$
\begin{aligned}
Z &= \left(\sqrt{2Rbs} - \frac{\sqrt{2}Rb^{3/2}}{8} \frac{\log s}{\sqrt{s}} + \cdots \right) \sin \left(\sqrt{\frac{2s}{Rb}} - \frac{\sqrt{2Rb}}{8} \frac{\log s}{\sqrt{s}} + \cdots \right) \\
X &= -1 + \left(\sqrt{2Rbs} - \frac{\sqrt{2}Rb^{3/2}}{8} \frac{\log s}{\sqrt{s}} + \cdots \right) \cos \left(\sqrt{\frac{2s}{Rb}} - \frac{\sqrt{2Rb}}{8} \frac{\log s}{\sqrt{s}} + \cdots \right)
\end{aligned}
$$

as $s \to \infty$. This calculation is given in Appendix C. Hence

$$
\frac{(X+1)X_s + ZZ_s}{Rb^2} \to \frac{1}{Rb} \quad \text{as} \quad s \to \infty.
$$

Scaling Rb by $\tilde{R}b/\epsilon$, we adopt the following expansions

$$
u_0 = \check{u}_0 + \epsilon \check{u}_1 + \epsilon^2 \check{u}_2 + O(\epsilon^3)
$$

$$
R_0 = \check{R}_0 + \epsilon \check{R}_1 + \epsilon^2 \check{R}_2 + O(\epsilon^3)
$$

and apply them to (10.17) and (10.18). We obtain the following leading order equations for the jet stady state as $s \to \infty$,

$$
\begin{aligned}
\check{u}_0 \check{R}_0' + \frac{\check{u}_0' \check{R}_0}{2} &= 0, \\
\check{u}_0 \check{u}_0' &= \frac{-1}{We} \left(\frac{-\check{R}_0'}{\check{R}_0^2} \right) + \tilde{R}b.
\end{aligned}
\tag{10.19}
$$

A numerical solution to these equations is shown in Figure 10.1.

The behaviour of the parameters from the previous section is given as follows

$$
\gamma = \frac{We(1 + \bar{R}_s^2)^{3/2}}{\bar{R}} = \frac{We(1 + \epsilon^2 \bar{R}_{\bar{s}}^2)^{3/2}}{\bar{R}} \to \frac{We}{\check{R}_0} \quad \text{as} \quad \epsilon \to 0,
$$

and

$$\Sigma = \frac{\bar{R}_s(1 + \bar{R}_s^2) - 3\bar{R}\bar{R}_s\bar{R}_{ss}}{\bar{R}(1 + \bar{R}_s^2)} = \frac{\epsilon\bar{R}_{\bar{s}}(1 + \epsilon^2\bar{R}_{\bar{s}}^2) - 3\epsilon^3\bar{R}\bar{R}_{\bar{s}}\bar{R}_{\bar{s}\bar{s}}}{\bar{R}(1 + \epsilon^2\bar{R}_{\bar{s}}^2)} \to 0 \quad \text{as} \quad \epsilon \to 0.$$

It is then possible to continue the Needham-Leach asymptotic analysis with the effect of rotation appearing through $\check{u}_0$ and $\check{R}_0$. Substitution of (10.16) into (10.1)

$$U_0 = r_0 \quad \text{and} \quad U_1 = r_1,$$

and

$$U_2 = r_2 - \check{u}_0 t r_0 \quad \text{and} \quad U_3 = r_3 - \check{u}_0 t r_1,$$

and

$$U_4 = \frac{4\check{R}_0}{\sqrt{2We}}\left(\frac{1}{4}\sqrt{\frac{2We}{\check{R}_0}}r_4 - \frac{1}{4}\sqrt{\frac{2We}{\check{R}_0}}\check{u}_0 t r_2 - t^2 r_1' - 2tr_1 + \frac{1}{4}\sqrt{\frac{2We}{\check{R}_0}}\check{u}_0^2 t^2 r_0\right)$$

and

$$U_5 = \frac{4\check{R}_0}{\sqrt{2We}}\left(\frac{1}{4}\sqrt{\frac{2We}{\check{R}_0}}r_5 - \frac{1}{4}\sqrt{\frac{2We}{\check{R}_0}}\check{u}_0 t r_3 + \frac{1}{4}\sqrt{\frac{2We}{\check{R}_0}}\check{u}_0^2 t^2 r_1 + t^2 r_0' + 2tr_0\right).$$

Substitution of (10.16) into equation (10.2) the $O\left(1/s\right)$ and $O\left(1/s^2\right)$ are satisfied automatically. To $O\left(1/s^3\right)$, using $U_0 - U_5$, we obtain,

$$r_1' = \frac{\sqrt{2}(1 + \check{u}_0^2\check{R}We)}{4\sqrt{2\check{R}_0^3 We}}r_0$$

and

$$r_0' = -\frac{\sqrt{2}(1 + \check{u}_0^2\check{R}We)}{4\sqrt{2\check{R}_0^3 We}}r_1.$$

Hence

$$r_0'' + \frac{(1 + \check{u}_0^2 \check{R}We)^2}{8We\check{R}_0^3} r_0 = 0$$

and

$$r_0 = C \sin\left(\frac{\sqrt{2}(1 + \check{u}_0^2 \check{R}We)}{4\sqrt{2\check{R}_0^3 We}} t\right) + D \cos\left(\frac{\sqrt{2}(1 + \check{u}_0^2 \check{R}We)}{4\sqrt{2\check{R}_0^3 We}} t\right),$$

and

$$r_1 = -C \cos\left(\frac{\sqrt{2}(1 + \check{u}_0^2 \check{R}We)}{4\sqrt{2\check{R}_0^3 We}} t\right) + D \sin\left(\frac{\sqrt{2}(1 + \check{u}_0^2 \check{R}We)}{4\sqrt{2\check{R}_0^3 We}} t\right)$$

Matching occurs in Region B, with $t \to 0$ and $s = O(1)$, and therefore $C = 0$, $D = \alpha$, $\Sigma \to 0$ and $\gamma \to We/\check{R}_0$, and the expansions become

$$u = \check{u}_0 + \frac{\alpha}{\check{R}} \sin\left(\frac{\sqrt{2We}}{4\sqrt{\check{R}_0}} \frac{s^2}{t} - \sqrt{\frac{We}{2\check{R}_0}} \check{u}_0 s + \frac{\sqrt{2}(1 + \check{u}_0^2 \check{R}We)}{4\sqrt{2\check{R}_0^3 We}} t\right) \frac{t^{5/2}}{s^3} + h.o.t$$

$$R = \check{R}_0 + \alpha \sin\left(\frac{\sqrt{2We}}{4\sqrt{\check{R}_0}} \frac{s^2}{t} - \sqrt{\frac{We}{2\check{R}_0}} \check{u}_0 s + \frac{\sqrt{2}(1 + \check{u}_0^2 \check{R}We)}{4\sqrt{2\check{R}_0^3 We}} t\right) \frac{t^{7/2}}{s^4} + h.o.t$$

Taking the asymptotic limit as $t \to \infty$ we obtain

$$u = \frac{\alpha}{\check{R}_0} \left(\frac{\sqrt{2We}}{4\sqrt{\check{R}_0}} \left(\frac{s}{t}\right)^2 - \sqrt{\frac{We}{2\check{R}_0}} \check{u}_0 \frac{s}{t} + \frac{1 + \check{u}_0^2 We}{2\sqrt{2\check{R}_0 We}}\right) \left(\frac{t}{s}\right)^3 \frac{1}{t^{1/2}} + h.o.t$$

$$R = \alpha \left(\frac{\sqrt{2We}}{4\sqrt{\check{R}_0}} \left(\frac{s}{t}\right)^2 - \sqrt{\frac{We}{2\check{R}_0}} \check{u}_0 \frac{s}{t} + \frac{1 + \check{u}_0^2 We}{2\sqrt{2\check{R}_0 We}}\right) \left(\frac{t}{s}\right)^4 \frac{1}{t^{1/2}} + h.o.t$$

$$(10.20)$$

Taking the limit of a straight jet $Rb \to \infty$, $\check{u}_0 = \check{R}_0 = 1$ and this corresponds to the result obtained in Chapter 9 in the far-field as $s \to \infty$ and $t \to \infty$.

10.4 $s \to \infty$, $t \to \infty$ asymptotics

The above expression generates the form of the expansion in Region IV, where higher order exponential terms are included as the jet is inviscid (c.f. Chapter 9). However, in this section we shall not examine the higher order terms to obtain the expression for $\zeta_{11}^{(j)}$, and will focus on the behaviour of the nonlinear waves through the solution of g_0. However, the multiple scale $Z = z \ln(t)$ is included such that the expression for $\zeta_{11}^{(j)}$ could be found by examining higher orders. We note the secondary scale $\bar{s} = s\epsilon$ has also been included. The expansion in Region IV are

$$
\begin{aligned}
u = u(\bar{s}) \; + \; & \sum_{j=1}^{2} \exp\left((-1)^j t g_0(z,\bar{s})\right) \left[\frac{h_{11}^{(j)}(z,\bar{s},Z)}{t^{1/2}} + \frac{h_{21}^{(j)}(z,\bar{s},Z)}{t} \right. \\
& \left. + \frac{h_{31}^{(j)}(z,\bar{s},Z) + \ln(t)\bar{h}_{31}^{(j)}(z,\bar{s},Z)}{t^{3/2}} \right] \\
+ \; & \sum_{j=1}^{2} \exp\left(2(-1)^j t g_0(z,\bar{s})\right) \left[\frac{h_{22}^{(j)}(z,\bar{s},Z)}{t} + \frac{h_{32}^{(j)}(z,\bar{s},Z)}{t^{3/2}} \right] \\
+ \; & \sum_{j=1}^{2} \exp\left(3(-1)^j t g_0(z,\bar{s},Z)\right) \left[\frac{h_{33}^{(j)}(z,\bar{s},Z)}{t^{3/2}} + O\left(\frac{1}{t^2}\right) \right] + h.o.t.,
\end{aligned}
$$

$$
\begin{aligned}
R = R(\bar{s}) \; + \; & \sum_{j=1}^{2} \exp\left((-1)^j t g_0(z,\bar{s})\right) \left[\frac{\zeta_{11}^{(j)}(z,\bar{s},Z)}{t^{1/2}} + \frac{\zeta_{21}^{(j)}(z,\bar{s},Z)}{t} \right. \\
& \left. + \frac{\zeta_{31}^{(j)}(z,\bar{s},Z) + \ln(t)\bar{\zeta}_{31}^{(j)}(z,\bar{s},Z)}{t^{3/2}} \right] \\
+ \; & \sum_{j=1}^{2} \exp\left(2(-1)^j t g_0(z,\bar{s},Z)\right) \left[\frac{\zeta_{22}^{(j)}(z,\bar{s},Z)}{t} + \frac{\zeta_{32}^{(j)}(z,\bar{s},Z)}{t^{3/2}} \right] \\
+ \; & \sum_{j=1}^{2} \exp\left(3(-1)^j t g_0(z,\bar{s})\right) \left[\frac{\zeta_{33}^{(j)}(z,\bar{s},Z)}{t^{3/2}} + O\left(\frac{1}{t^2}\right) \right] + h.o.t.
\end{aligned}
$$

Substituting into equation (10.1) we obtain

$$h_{11}^{(j)} = \frac{2(z - \check{u}_0)g_{0z} - 2g_0}{\check{R}_0 g_{0z}} \zeta_{11}^{(j)},$$

where $\check{u}_0$ and $\check{R}_0$ are given by the solution to equations (10.19). Substitution into equation (10.2) yields the ODE for g_0

$$g_{0z}^4 \check{R}_0^2 + g_{0z}^2 + 2We\check{R}_0 \left[(z - \check{u}_0)g_{0z} - g_0\right]^2 = 0. \tag{10.21}$$

Taking the limit of a straight jet with $\check{u}_0(s) = \check{R}_0(s) = 1$ gives

$$h_{11}^{(j)} = 2\left(\frac{(z - 1)g_0' - g_0}{g_0'}\right)\zeta_{11}^{(j)},$$

and

$$(g_0')^4 + (g_0')^2 + 2We\left[(z - 1)g_0' - g_0\right]^2 = 0;$$

namely (9.30)-(9.31) obtained in the previous chapter for a straight jet.

As in Chapter 9, (10.21) has 3 sets of solutions. The first are the set of linear solutions

$$g_0 = M_0 + M_1 z$$

which are linked by the equation

$$\check{R}_0^2 M_1^4 + M_1^2 + 4\check{R}_0 \check{u}_0 We M_1 M_0 + 2\check{R}_0 We M_0^2 + 2\check{R}_0 \check{u}_0^2 We M_1^2 = 0. \tag{10.22}$$

This is the spatial instability result analogous to a straight jet. The remaining solutions

are

$$g^+ = \frac{(-1)^j}{4\sqrt{We}\check{R}_0^{3/2}}\left(-We^2\check{R}_0^2(z-\check{u}_0)^4 - 10We\check{R}_0(z-\check{u}_0)^2 + 2\right.$$

$$\left. +\sqrt{We\check{R}_0(z-\check{u}_0)^2\left(We\check{R}_0(z-\check{u}_0)^2-4\right)^3}\right)^{1/2}$$

$$g^- = \frac{(-1)^j}{4\sqrt{We}\check{R}_0^{3/2}}\left(-We^2\check{R}_0^2(z-\check{u}_0)^4 - 10We\check{R}_0(z-\check{u}_0)^2 + 2\right.$$

$$\left. -\sqrt{We\check{R}_0(z-\check{u}_0)^2\left(We\check{R}_0(z-\check{u}_0)^2-4\right)^3}\right)^{1/2}$$
$$(10.23)$$

We take the asymptotic limit as $z \to \infty$ of the above, namely,

$$g^+ = i(-1)^j\left(\frac{z}{\check{R}_0} - \frac{\check{u}_0}{\check{R}_0}\right) + O\left(\frac{1}{z}\right)$$

$$g^- = i(-1)^j\left(\frac{\sqrt{2We}}{4\sqrt{\check{R}_0}}z^2 - \sqrt{\frac{We}{2\check{R}_0}}\check{u}_0 z + \frac{\sqrt{2}(\check{R}_0\check{u}_0^2 We + 1)}{4\sqrt{We\check{R}_0^3}}\right) + O\left(\frac{1}{z}\right) \qquad \text{as} \qquad z \to \infty.$$

The solution that matches with the farfield (10.20) is given by $g_0 = g^-$. The behaviour of this solution will be discussed in Section 10.6.

10.5 Linear waves with $t \to \infty$ and $s = O(1)$.

In Region V we consider $s = O(1)$ and $t \to \infty$. We examine linear wave solutions of the form

$$
\begin{aligned}
u &= \bar{u}(\bar{s}) + \delta \exp(i\omega t) \left(\Omega_0(s) + \frac{\Omega_1(s)}{t^{1/2}} + O\left(\frac{1}{t}\right) \right) + c.c + h.o.t. \\
R &= \bar{R}(\bar{s}) + \delta \exp(i\omega t) \left(\Gamma_0(s) + \frac{\Gamma_1(s)}{t^{1/2}} + O\left(\frac{1}{t}\right) \right) + c.c + h.o.t.
\end{aligned}
$$

where $\bar{s} = s\epsilon$, $c.c$ denotes the complex conjugate and ω is given by the boundary condition at $s = 0$. $h.o.t.$ denote the higher order terms which include the $\ln(t)$ terms in the expansion in Region IV.

Taking equations (10.1) and (10.2) to $O(1)$ in δ and ϵ, we obtain the equations

$$
i\omega\Omega_0 + \check{u}_0\Omega_0' + \frac{1}{2}\check{R}\Gamma_0' = 0 \tag{10.24}
$$

$$
i\omega\Gamma_0 + \check{u}_0\Gamma_0' = \frac{-1}{We}\left(-\frac{\Omega_0'}{\check{R}_0^2} - \Omega_0''' \right) \tag{10.25}
$$

where $\check{u}_0$ and $\check{R}_0$ are solutions to equations (10.19). This yields

$$
\check{R}_0^2\Omega_0'''' + (1 + 2\check{u}_0^2\check{R}_0 We)\Omega_0'' + 4iWe\check{u}_0\check{R}_0\omega\Omega_0' - 2We\check{R}_0\omega^2\Omega_0 = 0
$$

$$
\Rightarrow \Omega_0 = \sum_{j=1}^{4} \omega_j e^{m_j s}
$$

where m_j are the solutions to the equation

$$
\check{R}_0^2 m^4 + (1 + 2\check{u}_0^2\check{R}_0 We)m^2 + 4i\check{u}_0\check{R}_0 We\omega m - 2We\check{R}_0\omega^2 = 0. \tag{10.26}
$$

This equation describes spatial instability and matches with the linear solution appear-

ing in Region IV (c.f. Chapter 9). (9.54) yields

$$\Gamma_0 = \sum_{j=1}^{4} \gamma_j \exp^{m_j s}$$

where

$$\gamma_j = -\frac{2\omega_j(i\omega + \check{u}_0 m_j)}{\check{R}_0 m_j} \qquad \text{for} \quad j = 1, 2, 3, 4. \tag{10.27}$$

We have set the constant of integration equal to zero as it does not yield wave solutions in the expansion.

Substitution into the boundary condition $R = 1$ gives

$$\omega_1 + \omega_2 + \omega_3 + \omega_4 = 0$$

and $u = 1 + \delta \sin(\omega t)$

$$\gamma_1 + \gamma_2 + \gamma_3 + \gamma_4 = -\frac{i}{2}.$$

Taking equations (10.1) and (10.2) to $O(t)$, we obtain similar to equations (9.54) and (10.25), though with solution

$$\Omega_1 = \sum_{j=5}^{8} \omega_j e^{m_j s}, \qquad \text{and} \qquad \Gamma_1 = \sum_{j=5}^{8} \gamma_j e^{m_j s},$$

where m_j are solutions (10.26) and γ_j given by (10.27) for $j = 5, 6, 7, 8$, and

$$\omega_5 + \omega_6 + \omega_7 + \omega_8 = 0$$
$$\gamma_5 + \gamma_6 + \gamma_7 + \gamma_8 = 0.$$

10.6 Discussion

As in the previous chapter, we can analyse (10.23) to find the region $z_1 < z < z_2$ where these nonlinear waves grow. z_1 and z_2 are given by

$$z_1 = \max\left(\check{u}_0 - \frac{2}{\sqrt{\check{R}_0 We}}, 0\right) \qquad z_2 = \check{u}_0 + \frac{2}{\sqrt{\check{R}_0 We}}.$$

Figure 10.2 shows the temporal growth rate, given by the ral part of g_0 ($\Re(g_0)$) given by (10.23), for different jets at different rotation rates. It shows that as Rb decreases, for a given value of $\bar{s}$, the maximum of $\Re(g_0)$ occurs for a larger value of z. This is because the maximum occurs at $z = \check{u}_0$, and for a given value of $\bar{s}$, $\check{u}_0$ is larger if the jet is rotating more quickly. The value of z_1 also increases with $\bar{s}$. Consequently, a given value of z_1 would occur for a smaller value of s for a jet rotating more rapidly. Therefore, nonlinearities are unstable for smaller values of s. This coincides with results obtained earlier in this thesis, as it was noted that it is easier to generate Mode 1 break-up for slower rotation rates. At $\bar{s} = 0$, the curves are identical for different Rossby numbers, as $\check{u} = \check{R} = 1$.

The local wavespeeds, spatial growth rates and wavenumbers are shown in Figures 10.3, 10.4 and 10.5 respectively. The wavespeed increases with decreasing Rb and is larger for a given $\bar{s}$. For a larger Rb, the region of z for which the jet is spatially unstable is smaller, and occurs for a smaller value of z. Therefore, at higher rotation rates the range of z for which nonlinearities grow spatially is larger. The minimum of the local wavenumber occurs for a larger value of z for increased rotation rate and for a larger $\bar{s}$. Again, at $\bar{s} = 0$, the curves are identical for different Rossby numbers, as $\check{u} = \check{R} = 1$.

Many of the above results can be explained by taking a Taylor expansion about

$z = \check{u}_0,$

$$\Re(g_0) = \frac{\sqrt{2}}{4\sqrt{We\check{R}_0^3}} - \frac{\sqrt{2We}}{8\sqrt{\check{R}_0}}(z - \check{u}_0)^2 + \frac{\sqrt{2\check{R}_0}We^{3/2}}{32}(z - \check{u}_0)^4 + O((z - \check{u}_0)^6)$$

$$\Re(g_0)' = -\frac{\sqrt{2We}}{4\sqrt{\check{R}_0}}(z - \check{u}_0) + \frac{\sqrt{2\check{R}_0}We^{3/2}}{8}(z - \check{u}_0)^3 + O((z - \check{u}_0)^5)$$

$$v = \check{u}_0 + \frac{We\check{R}_0}{4}(z - \check{u}_0)^3 + O((z - \check{u}_0)^4)$$

$$k = \Im(g_0)' = \frac{\sqrt{2}}{2\check{R}_0} + \frac{3\sqrt{2}We}{16}(z - \check{u}_0)^2 + O((z - \check{u}_0)^4)$$

as $z \to \check{u}_0$. $\check{u}_0$ increases (and $\check{R}_0$ decreases) as the rotation rate increases and is larger ($\check{R}_0$ is smaller) for a given value of $\bar{s}$. This illustrates the trends presented in Figures 10.2 - 10.5, with the dominant behavior of the solution occurring at $z = \check{u}_0$. The temporal growth rate increases with $\check{R}_0^{-3/2}$, wavespeed increases with $\check{u}_0$ and wavenumber increases with $\check{R}_0^{-1}$. The Taylor expansion for spatial growth rate also illustrates that for $z < \check{u}_0$, the waves are spatially unstable and for $z > \check{u}_0$ they are spatially stable.

Figure 10.6 displays the z values at the time of break-up of 4 different disturbances and where they fall on a temporal growth rate curve. We note that the temporal growth rate used here is for the purposes of an example, it does not correspond to any of the jets shown. The point labelled Z_1 on Figure 10.6 occurs for $z < z_1$. This yields Mode 1 break-up, as shown in Figure 10.7(a). The point labelled Z_2 in Figure 10.6 occurs for $z_1 < z < z_2$, but occurs for a value of z significantly smaller than $z = \check{u}_0$ (where the growth rate is at a maximum). Consequently, there is clear linear and nonlinear mode competition in Figure 10.7(b). We assume this break-up is Mode 1, as it is unclear whether there will be any satellite drop formation.

Z_3 in Figure 10.6 occurs for a small amplitude disturbance. The value of z is quite similar to $\check{u}_0$ and the break-up regime is clearly M2. The frequency in Figure 10.7 and

Figure 10.8(a) ($\omega = 1.3$) is chosen such that it is stable at the orifice and becomes unstable for a value of s (see Chapter 8). In Figure 10.7, when δ is larger forcing the jet at higher amplitudes, z is smaller and we see M1 break-up. In Figure 10.8(a), with lower amplitude, nonlinearities dominate as z is larger. This corresponds to results found in Chapter 7. Figure 10.8(b) shows a disturbance generated by an unstable linear frequency at the orifice, corresponding to Z_4 in Figure 10.6. $z_1 < z < z_2$ and the nonlinearity causes the satellite droplet. No values of $z > u_0$ were found at the point of break-up.

The relationship between the mode of break-up and the value of z at break-up compared to z_1 and $\check{u}_0$ seems to be an interesting area of study, requiring a much more thorough investigation.

10.7   Conclusion

In this chapter we have extended the Needham-Leach method to account for rotational forces on the jet. For $s = O(1)$, a solution could be obtained in terms of the steady state values for $\bar{R}$ and $\bar{u}$. In Region III however, where $s \to \infty$, it was necessary to scale the steady state by an additional scale $\bar{s} = s\epsilon$. This secondary scale was then used in Regions IV and V to examine the linear and nonlinear wave behaviour.

An ODE was obtained for g_0 which could be used to investigate nonlinear wave stability. This was dependent on leading order values for the scaled steady state $\check{u}_0$ and $\check{R}_0$. In the limit of $Rb \to \infty$, the equations reduced to the equations for a straight jet.

We examined the impact of rotation rate on the stability of the nonlinear waves. As the rotation rate increases, the value of z at which the nonlinearities become unstable decreases. We performed a brief investigation into the impact of these nonlinearities

on the mode of jet break-up. Preliminary results suggest that as z approached the local steady state velocity $\check{u}_0$, Mode 2 break-up is more likely. This work needs further investigation to fully understand the impact of these nonlinearities. A comparison with the results in Chapters 6 - 8 would also be interesteing.
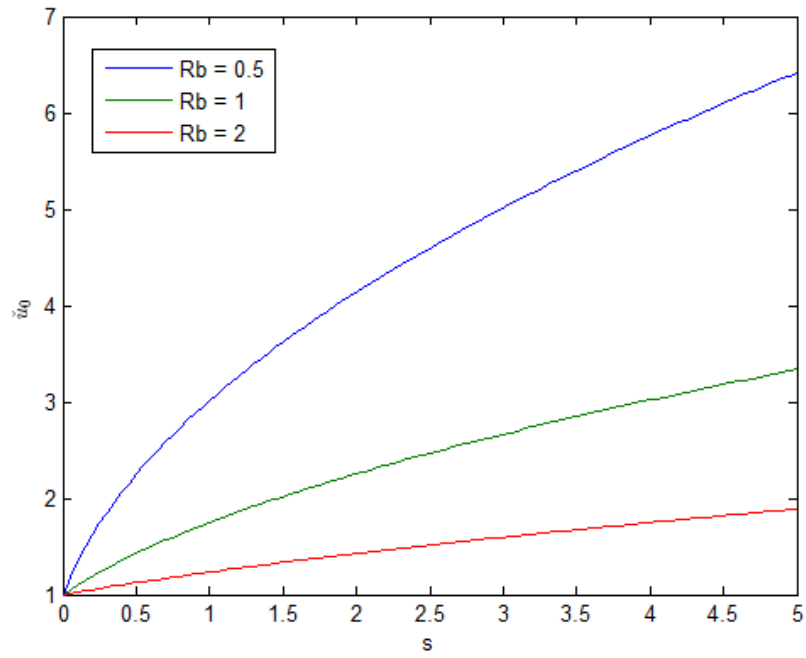
(a) $\check{u}_0$ vs s
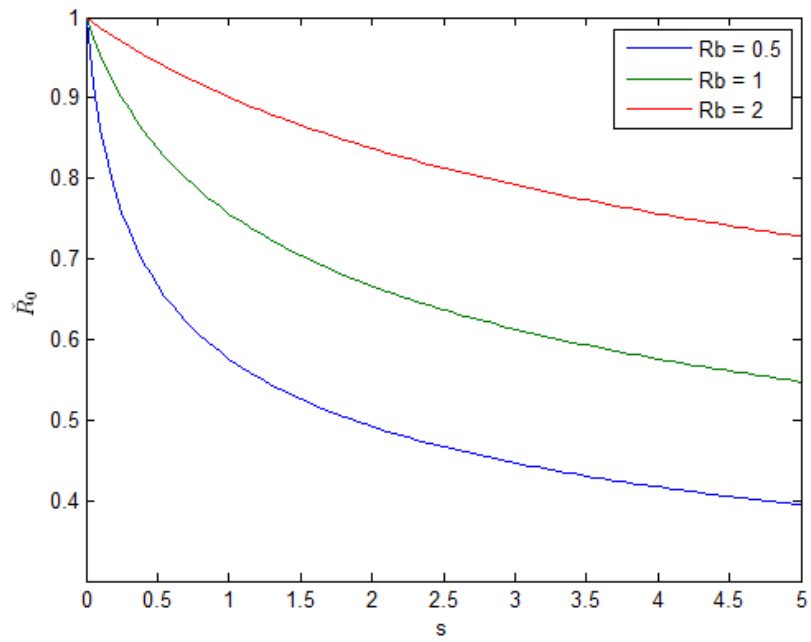
(b) $\check{R}_0$ vs s

Figure 10.1: Graph showing the solution to (10.19) for $Rb = 0.5, 1$ and 2.
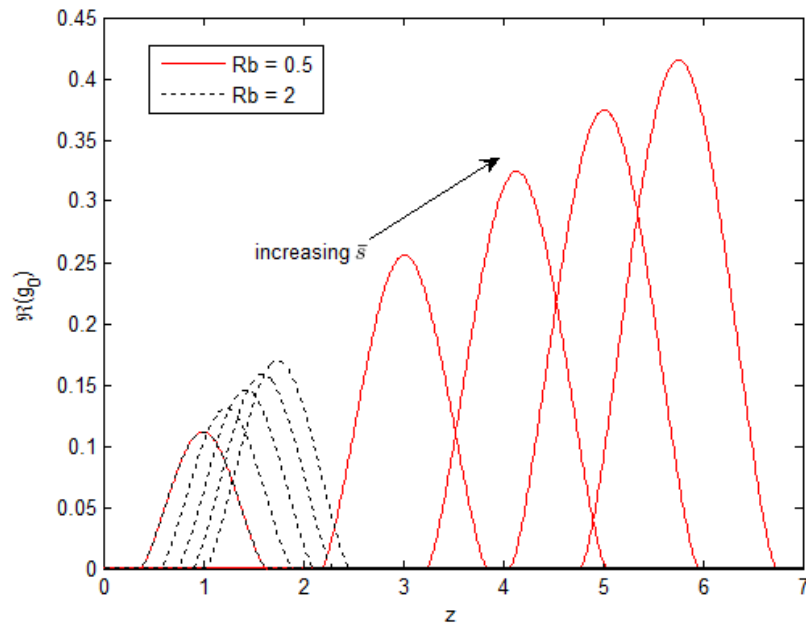
Figure 10.2: Plot showing temporal growth rate $\Re(g_0)$ with z. $We = 10$
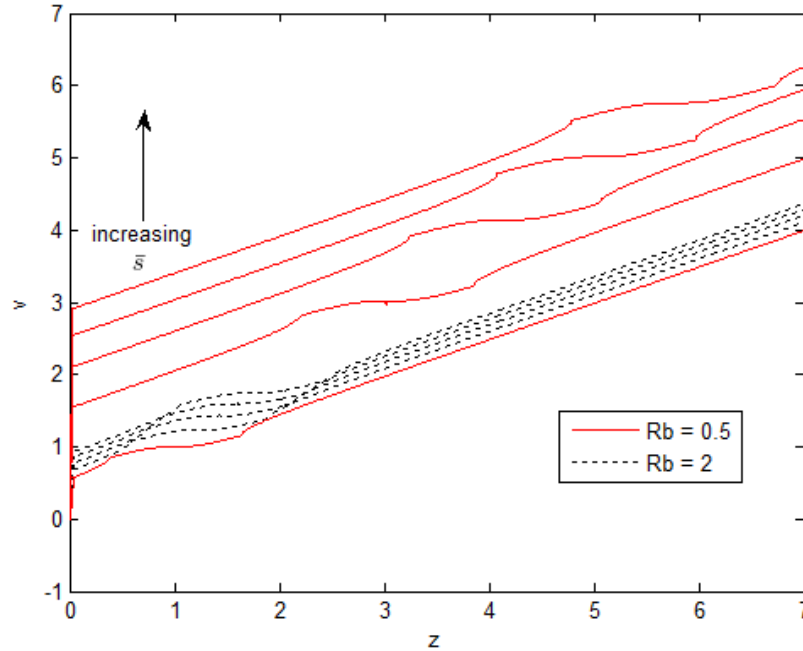
Figure 10.3: Plot showing wavespeed v with z. $We = 10$.
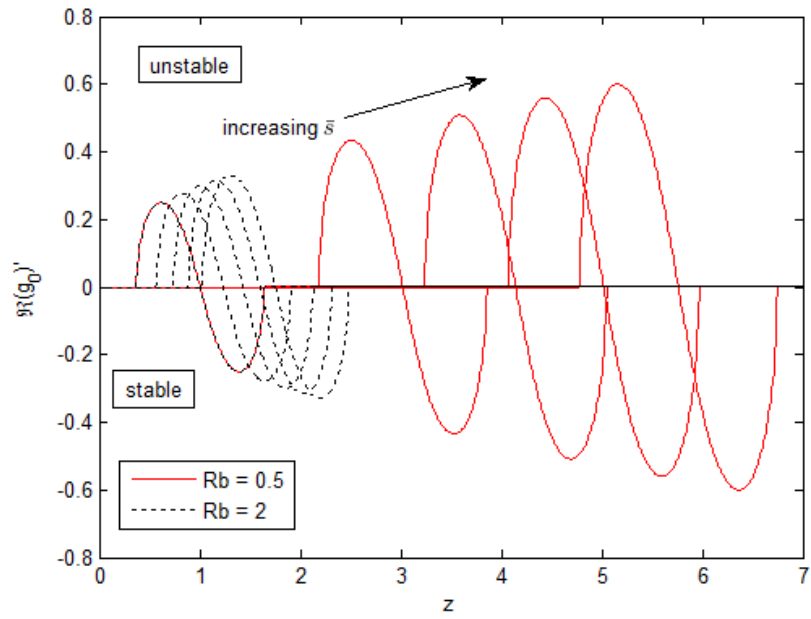
Figure 10.4: Plot showing spatial growth rate $\Re(g_0)'$ with z. $We = 10$
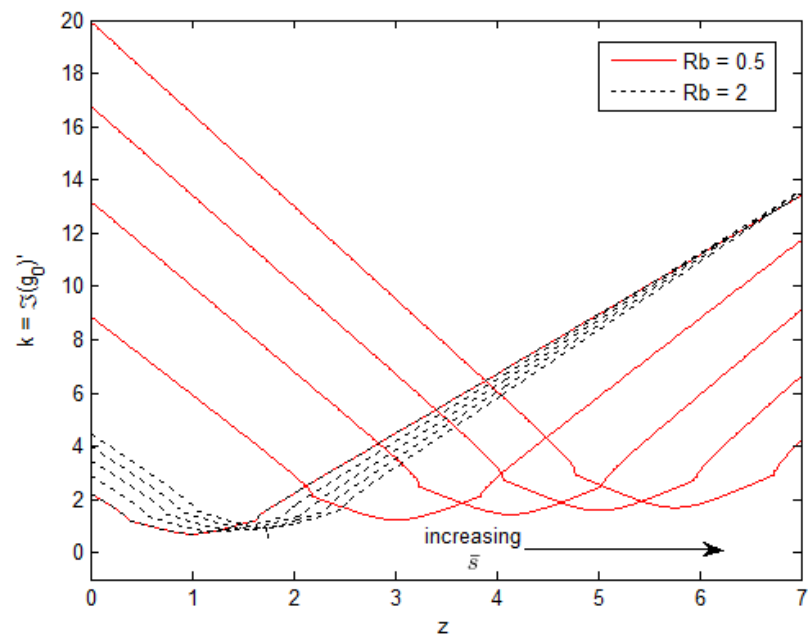
Figure 10.5: Plot showing local wavenumber k with z. $We = 10$
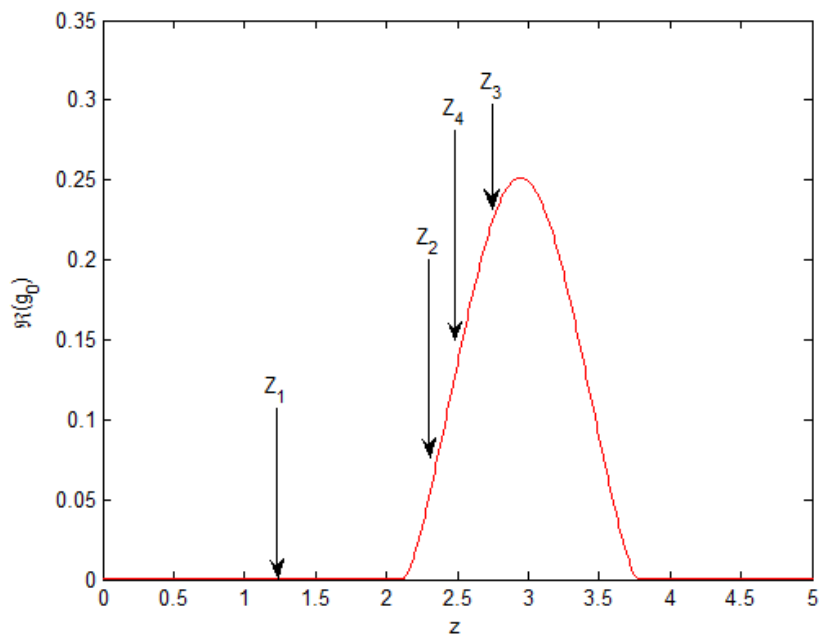
Figure 10.6: Plot illustrating z values of 4 different orifice disturbances compared to a temporal growth rate curve. $We = 50$, $Rb = 5$.
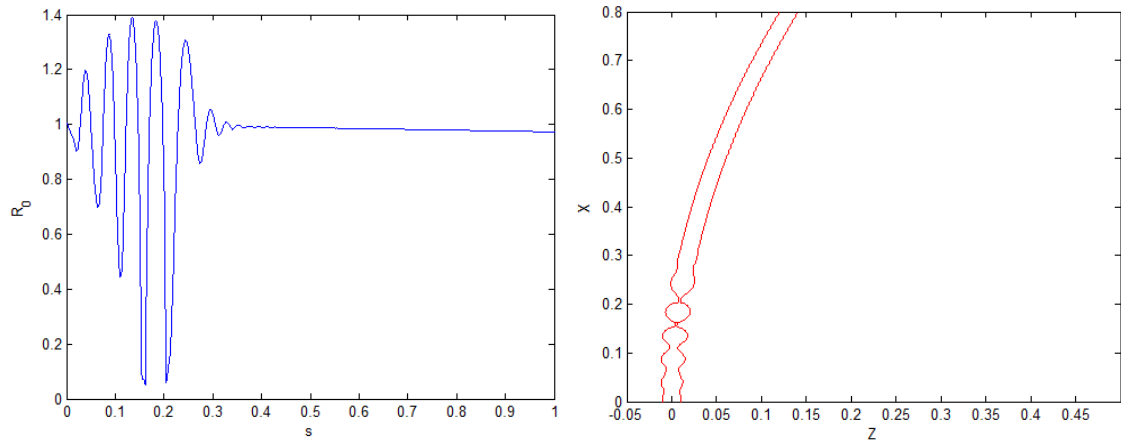
(a) Mode 1 break-up in the linear wave regime, corresponding to Z_1 in Figure 10.6. $\delta = 0.075$ and $\omega = 1.3$.
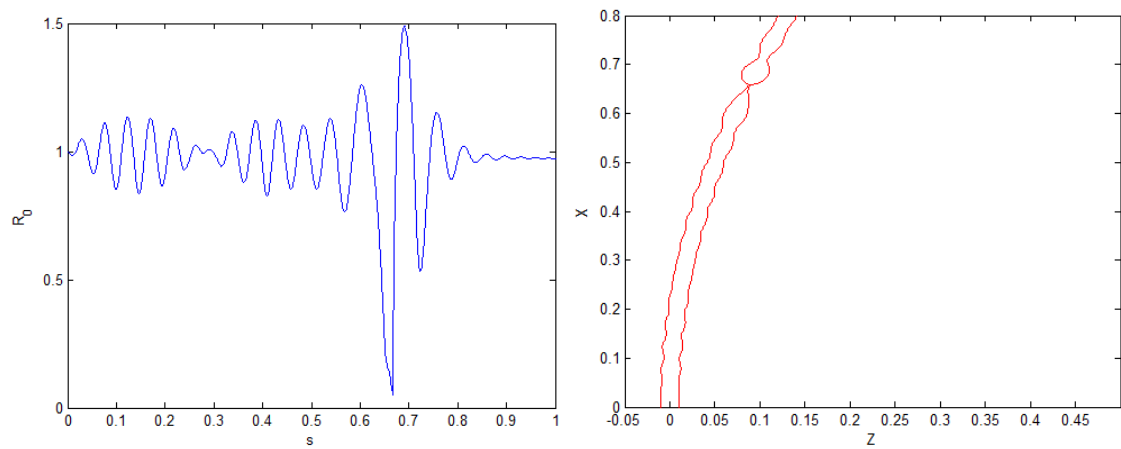
(b) Mode 1 break-up with linear and nonlinear mode competition, corresponding to Z_2 in Figure 10.6. $\delta = 0.025$ and $\omega = 1.3$.

Figure 10.7: Break-up in different wave regimes. $We = 50$, $Rb = 1$.
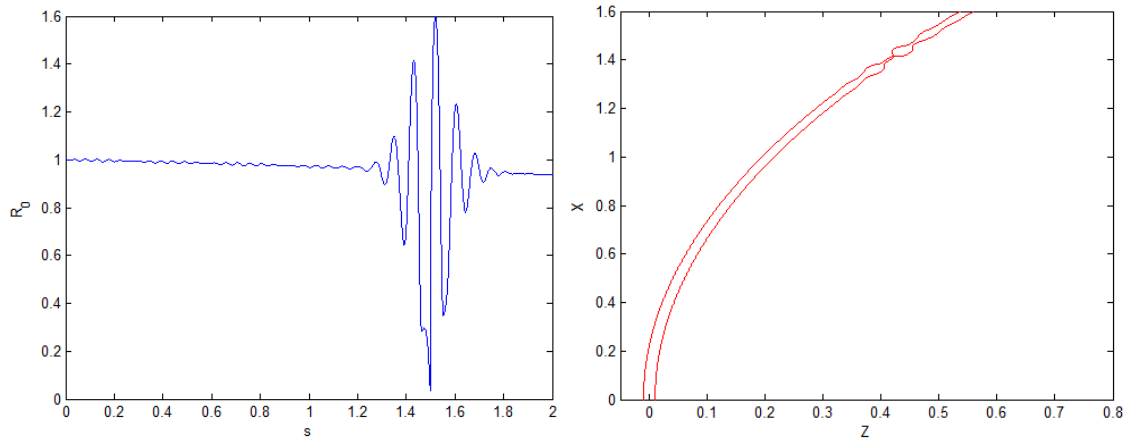
(a) Mode 2 break-up with linear and nonlinear mode competition, corresponding to Z_3 in Figure 10.6. $\delta = 0.001$ and $\omega = 1.3$.
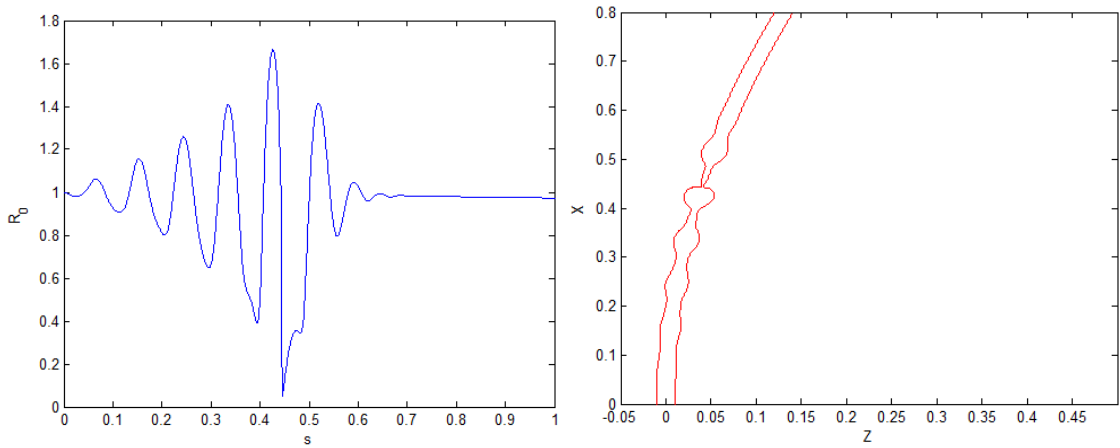
(b) Mode 2 break-up with linear and nonlinear mode competition, corresponding to Z_4 in Figure 10.6. $\delta = 0.025$ and $\omega = 0.7$.

Figure 10.8: Break-up in different wave regimes. $We = 50$, $Rb = 1$.

Chapter 11

Controlling Jet Break-up

This chapter details an attempt to control liquid jet break-up, motivated by the results in this thesis. In Chapter 10, it was deduced that the nonlinearities that are the cause of the smaller satellite droplets can be avoided if the jet is forced to break-up in the region where linear waves dominate and the nonlinear waves are stable. This typically occurs for small s. In Chapter 7, it was discovered that to cause shorter jet break-up and obtain Mode 1 behaviour it is necessary to apply an additional disturbance which has a high amplitude and frequency $\omega \approx 1 - 1.5$ in dimensionless units. This research has aided the production of a device that can attach to the experimental rig. The preliminary results are summarised in this chapter.

11.1 Obtaining the frequency and amplitude on dimensional units

In Chapter 7, jet break-up was cause by applying the following orifice boundary condition

$$u(0, t) = 1 + \delta \sin(\kappa t/\epsilon) + \gamma \sin(\omega t/\epsilon), \tag{11.1}$$

where δ and κ were the amplitude and frequency of the most unstable wave and γ and ω were the amplitude and frequency of the secondary disturbance. This is a perturbation to the velocity of the jet, yet a vibrating orifice would cause perturbations to the jet by vibrating in the plane of gravity (up and down). Thus, we need to discuss what the values of γ and ω mean physically.

Consider the problem in terms of the full model equations in three dimensions before any asymptoic expansions are applied. We perturb gravity by a small parameter $g = \bar{g} + G\sin(\omega t)$ such that $G/g << 1$. Therefore, a perturbation expansion in terms of G/g gives to leading order the unperturbed long wavelength equations which have a steady solution given by the solution to the three dimensional steady ODEs (c.f. Chapter 8 for the two dimensional counterpart).

To next order in G/g, we obtain a linearised system of equations describing a perturbation of frequency ω. This yields the viscous dispersion relation (8.34) for a given frequency ω. As long as $G/g << 1$, these linear spatial instability results remain valid. Nonlinear theory can be used to get an impression of the behaviour as G/g increases from 0^+, taking a long wavelength approximation of the linear results to a long wavelength dispersion relation (8.36). Therefore G/g is small.

If we were to apply a small δ expansion, as in Chapter 8, we would obtain the same results as above. Hence, δ would be the amplitude of the velocity perturbation in the above boundary condition. Therefore, a perturbation in the plane of gravity and a perturbation of the velocity are equivalent. Therefore, we only need to dimensionalise γ and ω.

In Chapter 7, the largest regions of M1 break-up occurred for $\gamma = O(0.1)$ and $\omega = O(1)$. Recalling the dimensionless parameters introduced in Chapter 3,

$$t = \frac{U\bar{t}}{s_0} \quad \text{and} \quad \epsilon = \frac{a}{s_0}$$

where t is the dimensionless time, $\bar{t}$ is the dimensional time, U is the jet exit velocity, a is the orifice radius and s_0 is the radius of the can. Therefore, from (11.1),

$$\frac{\omega}{\epsilon}t = \frac{\omega U}{a}\bar{t}$$

and so the dimensional frequency would be given by

$$\bar{f} = \frac{\omega U}{a}.$$

As $a = O(1\text{ mm})$, $U = O(1\text{ ms}^{-1})$ and $\omega = O(1)$, $\bar{f} = O(kHZ)$.

As the perturbation in the plane of gravity and the perturbation in the velocity can be considered equivalent, the amplitude of the perturbation is simply given by

$$\bar{\gamma} = \gamma a,$$

and so $\bar{\gamma} = O(0.1\text{ mm})$ for $\gamma = O(0.1)$ and $a = O(1\text{ mm})$. Therefore to control liquid jet break-up, 0.1 mm amplitude disturbances of the order of kHz should be applied to the jet. The details of a vibrating nozzle which works in those regimes is given in the next section.

11.2   A Vibrating Nozzle

Modifications were made to the pilot scale rig such that a vibrating nozzle could be attached to the can in place of the original nozzle. The amplitude and frequency of the vibration could be applied such that the Rayleigh mode and any mechanical instabilities are dominated by a more controlled disturbance. An image of the nozzle is shown in Figure 11.1.
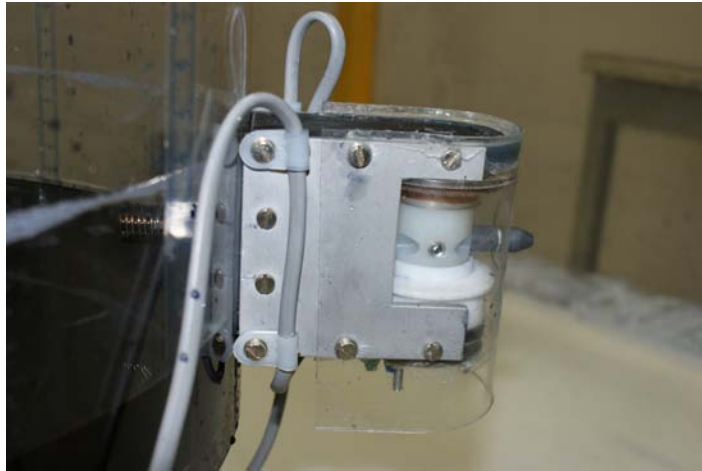
Figure 11.1: Graph showing the impact of a secondary disturbance on Jet 4.

Figure 11.2 shows a schematic of this nozzle added to the rig. Through the application of an AC electric signal, the electromagnet attracts and repels causing a vibration to the transporter tube. The liquid flows from the drum, through the tube to the nozzle, and the vibration is controlled through the electric signal. There is also a hall sensor that acts as a feedback to control the amplitude. As can also be seen in the figure, an accelerometer has been added to the rig in order to measure the mechanical instabilities arising through rotation.

11.3   Preliminary results

In this section we present some preliminary results of the work by Victoria Hawkins using the vibrating nozzle. Figure 11.3 shows a drop size distribution displaying a high amplitude and high frequency disturbance applied to Jet 1 from Table 6.1. Satellite droplets are reduced, and there is a decreased standard deviation in main drop sizes. A high amplitude and frequency disturbance is applied to Jet 4 in Figure 11.4 and we see a more dramatic reduction in the number of satellite droplets, changing break-up from Mode 2/3 to Mode 1. It should be noted that the vibrating nozzle reduces
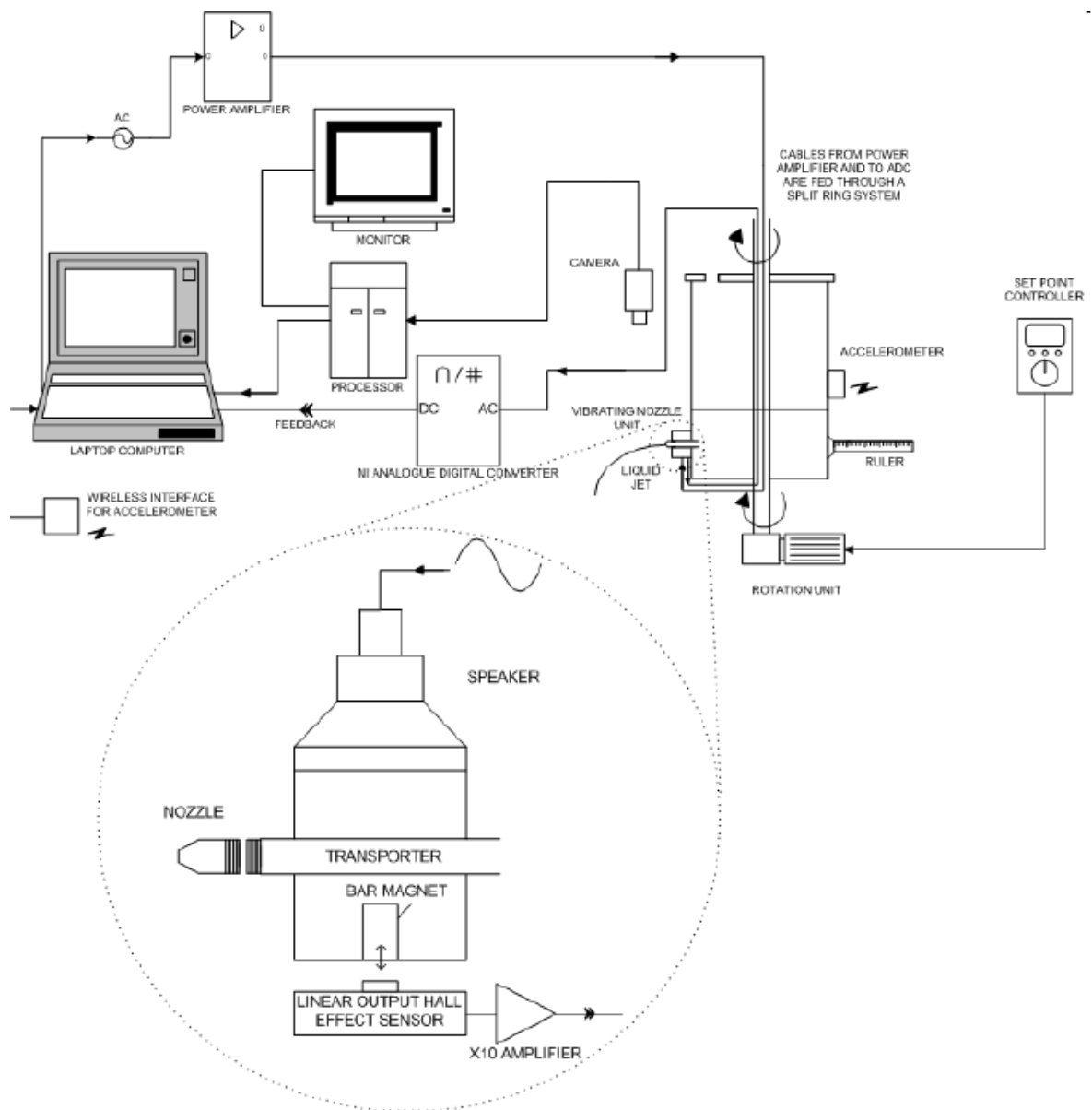
Figure 11.2: Sketch of the vibrating nozzle set-up.
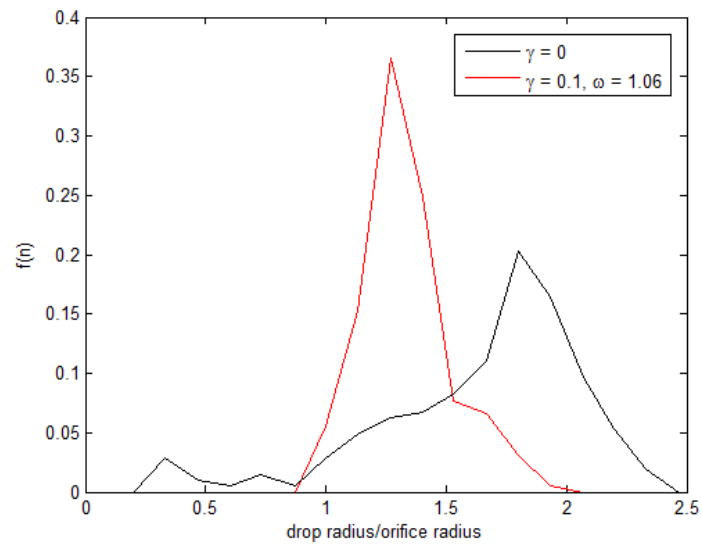
Figure 11.3: Graph showing the impact of a secondary disturbance on Jet 1.

the exit velocity of the fluid, and so the dimensionless parameters will differ with the additional disturbances. A greater comparison between the theoretical insonification and experimental results is the subject of current work, but these preliminary results are very encouraging.
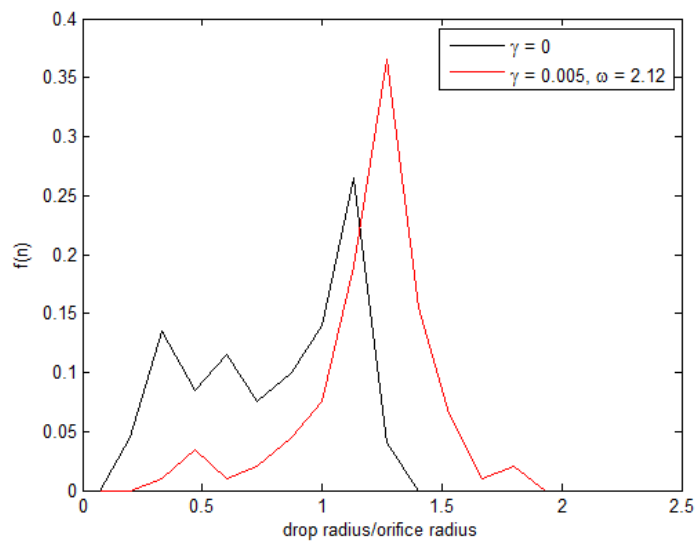
Figure 11.4: Graph showing the impact of a secondary disturbance on Jet 4.

Chapter 12

Conclusions and Future Work

Over the course of this thesis we have investigated the break-up dynamics of a curved liquid jet as seen in the prilling process. The primary aim of the study was to investigate methods of reducing satellite droplets which are the source of waste to the industrial process. These satellite droplets were typically seen for viscous jets emerging from the can rotating at higher speeds.

Chapters 2 - 4 gave an in depth review of the previous works on straight jets and curved jets, both theoretical and experimental. We presented linear stability analysis of a curved viscous jet derived by Decent *et al.*[12], and the nonlinear equations derived by Părău *et al.*[35].

In Chapter 5 we fully analyzed the mathematical model, illustrating the differences between the linear and nonlinear theories. For a viscous fluid at higher rotation rates, the nonlinear theory can predict a droplet over twice the radius of the linear theory. In addition, the nonlinear model breaks down at the time of break-up, and subsequent satellite droplets can not be generated after the ligament forms.

Despite extensive work theoretically and experimentally on curved liquid jets, there had never previously been a full and thorough comparison. In Chapter 6, we showed

the nonlinear model could be used to accurately predict the mode of jet break-up, although identifying the mode close to the mode boundary becomes more difficult due to the subjective nature of classifying break-up. There was an excellent correlation between the nonlinear theory and the experimental image in the M2 regime, matching the trajectory and predicting main and satellite drop radii that compare well to experiments. As viscosity is increased, the nonlinear theory showed less of an accurate comparison; the trajectory appeared displaced, and the droplet we could predict was much larger than experimental droplets. Linear theory predicted drops of a more comparable size. We changed the exit angle of the jet in the nonlinear simulations and noted the trajectory can be modelled to a greater degree of accuracy, though the main drop remained too large.

In Chapter 7 we added a secondary wave at the orifice and investigated the effects. We generated drop size distributions for our theoretical jet by varying this additional disturbance. We showed that these distributions displayed a better comparison to experimental drop size distributions when the amplitude of this disturbance is larger, and concluded that experimentally engineered setups have mechanical instabilities present that dominate the Rayleigh mode. These results have major implications; whilst dimensionless parameters can be used to scale down an industrial setup, subtleties in design engineering that cause mechanical instabilities are not picked up by the experimental modelling. These instabilities are more noticeable at higher rotation rates. We also showed that it was possible to reduce the presence of satellite droplets if a disturbance was applied with sufficient amplitude and at a chosen frequency.

In Chapter 8 we developed a local stability analysis of the jet. We derived a linear dispersion relation that can be used to calculate the instability at any point along the jet at any time. With this method, we generate very short waves at break-up point, noting that at break-up we see the presence of negative frequencies, indicating wave

motion in both directions. For higher rotation rates we did not see these negative frequencies.

We also generated short waves on a ligament and showed that satellite droplets that form over these wavelengths fall within a drop size distribution, suggesting this local stability analysis is a suitable way of predicting post ligament break-up. Through a combination of nonlinear analysis, linear stability and the new local stability technique, droplets can be accurately predicted for jets consisting of a wide range of viscosities at varying rotation rates.

We also investigated the spatial instability of a steady jet, and showed that some frequencies are initially stable at the orifice and then suddenly become unstable further down the jet. The use of initially stable disturbances that become unstable down the jet can be used to control the break-up length, which has implications to industries other than prilling. This shorter break-up length also coincided with the M1 break-up seen in Chapter 7. The onset of unstable disturbances of (dimensionless) frequencies greater than one is a feature unique to curved jet break-up.

In Chapter 9 we used the Needham Leach asymptotic technique to investigate the behaviour of the the straight inviscid jet in the large time and space limits. This was used to develop understanding of linear and nonlinear behaviour of the capillary instabilities in liquid jets. For small s the wave grows linearly, but for some value of $z = s/t$, nonlinearities became unstable and dominate the jet behaviour. To regulate droplet production, it is necessary to break a jet in regions where the nonlinear waves are stable. For $We < 4$, nonlinear waves are unstable at the orifice and there is no region where the jet can be forced to break linearly.

In addition, through investigation of the nonlinear wave region, we found some exciting results. We discovered the prescence of cubic nonlinearities, an example of Wilton's ripples, in the equation describing wave amplitude. These nonlinearities are

seen in other areas of fluid dynamics such as shallow water waves, but have not been seen to be a feature of liquid jet break-up.

The technique was extended in Chapter 10 to examine the behaviour of a curved inviscid jet. The critical region for the onset on nonlinear wave instability was seen to be a function of the steady state values for radius and velocity, and so is largely dependent on rotation rate. Nonlinearities occur for smaller values of s for higher rotation rates. M1 behaviour is more likely to be obtained if the jet is forced to break-up before nonlinearities become unstable.

In Chapter 11 we used knowledge obtained throughout the majority of this thesis to design a method of droplet control. A vibrating nozzle was designed such that it could vibrate at sufficient amplitude to break the jet in the linear wave regime, as motivated by Chapters 9 and 10, vibrating in frequency ranges suggested by work in Chapter 7. The preliminary results are extremely encouraging, with the significant reduction of satellite droplets in a viscous fluid.

12.1   Further Work

There are many further questions still to be answered on jet break-up. The work previewed in Chapter 11 needs to be examined in greater detail for an increased range of fluid rheologies and rotation rates. This needs to be compared thoroughly with the work predicted by the nonlinear model in Chapter 7 and the regions of linear and nonlinear wave growth predicted in Chapter 10.

There is also limited understanding in the behaviour of the cubic nonlinearity that arose in Chapter 9. Through techniques used in examining shallow water waves, greater understanding of jet nonlinearities could be obtained.

In addition, the work in Chapter 8 highlighted the complex dynamics governing

jet break-up. The numerical model predicted negative values for jet velocity and this resulted in waves propagating back down the jet in the local stability analysis. It could be that the one-dimensional model fails to capture the full dynamics of jet break-up and it is necessary to include a radial dependence on jet velocity to capture these dynamics. This would involve some very complicated mathematical and numerical modelling.

Appendix A

Derivation of the linear dispersion relation

This section details the derivation of the linear dispersion relation governing jet instability. Subtitution of (8.32) into the instability equations (8.31) yields the following set of equations

$$
(-kn\hat{u}_1 + \hat{v}_1 + n\hat{v}_{1,n}) + \sum_{m=1}^{\infty} \left(-kn\hat{u}_{m0} + \hat{v}_{m0} + \hat{v}_{m0,n} + m\hat{w}_{m1} \right) \cos m\phi
$$
$$
+ \sum_{m=1}^{\infty} \left(-kn\hat{u}_{m1} + \hat{v}_{m1} + \hat{v}_{m1,n} - m\hat{w}_{m0} \right) \sin m\phi, \qquad \text{(A.1)}
$$

$$
\left(-(\lambda + iu_0 k)\hat{u}_1 - k\hat{p}_1 + \frac{1}{Re} \left(-k^2 \hat{u}_1 + \frac{1}{n}\hat{u}_{1,n} + \hat{u}_{1,nn} \right) \right)
$$
$$
+ \sum_{m=1}^{\infty} \left[-(\lambda + iu_0 k)\hat{u}_{m0} - k\hat{p}_{m0} + \frac{1}{Re} \left(-k^2 \hat{u}_{m0} + \frac{1}{n}\hat{u}_{m0,n} \right. \right.
$$
$$
\left. \left. + \; \hat{u}_{m0,nn} - \frac{m^2}{n^2}\hat{u}_{m0} \right) \right] \cos m\phi + \sum_{m=1}^{\infty} \left[- (\lambda + iu_0 k)\hat{u}_{m1} - k\hat{p}_{m1} \right.
$$
$$
\left. + \frac{1}{Re} \left(-k^2 \hat{u}_{m1} + \frac{1}{n}\hat{u}_{m1,n} + \hat{u}_{m1,nn} - \frac{m^2}{n^2}\hat{u}_{m1} \right) \right] \sin m\phi, \quad = \quad 0
$$
$$
\text{(A.2)}
$$

$$\left[-(\lambda + iu_0 k)\hat{v}_1 - \hat{p}_{1,n} + \frac{1}{Re}\left(-k^2\hat{v}_1 + \frac{1}{n}\hat{v}_{1,n} + \hat{v}_{1,nn} - \frac{1}{n^2}\hat{v}_1 \right) \right]$$

$$+ \sum_{m=1}^{\infty}\left[-(\lambda + iu_0 k)\hat{v}_{m0} - \hat{p}_{m0,n} + \frac{1}{Re}\left(-k^2\hat{v}_{m0} + \frac{1}{n}\hat{v}_{m0,n} \right. \right.$$

$$\left. \left. + \hat{v}_{m0,nn} - \frac{m^2}{n^2}\hat{v}_{m0} - \frac{1}{n^2}\hat{v}_{m0} - \frac{2m}{n^2}\hat{w}_{m1} \right) \right]\cos m\phi + \sum_{m=1}^{\infty}\left[-(\lambda + iu_0 k)\hat{v}_{m1} - \hat{p}_{m1,n} \right.$$

$$\left. + \frac{1}{Re}\left(-k^2\hat{v}_{m1} + \frac{1}{n}\hat{v}_{m1,n} + \hat{v}_{m1,nn} - \frac{m^2}{n^2}\hat{v}_{m1} - \frac{1}{n^2}\hat{v}_{m1} + \frac{2m}{n^2}\hat{w}_{m0} \right) \right]\sin m\phi$$

$$+ (Z_s\hat{X}_1 - X_s\hat{Z}_1)\left(k\lambda u_0 - k^2 u_0^2 - \frac{1}{Re}ik^3 u_0 \right)\cos\phi \;\; = \;\; 0,$$

(A.3)

and

$$\left[-(\lambda + iu_0 k)\hat{w}_1 - \frac{1}{n}\hat{p}_1 + \frac{1}{Re}\left(-k^2\hat{w}_1 + \frac{1}{n}\hat{w}_{1,n} + \hat{w}_{1,nn} - \frac{1}{n^2}\hat{w}_1 \right) \right]$$

$$+ \sum_{m=1}^{\infty}\left[-(\lambda + iu_0 k)\hat{w}_{m0} - \frac{1}{n}\hat{p}_{m0} + \frac{1}{Re}\left(-k^2\hat{w}_{m0} + \frac{1}{n}\hat{w}_{m0,n} \right. \right.$$

$$\left. \left. + \hat{w}_{m0,nn} - \frac{m^2}{n^2}\hat{w}_{m0} - \frac{1}{n^2}\hat{w}_{m0} + \frac{2m}{n^2}\hat{v}_{m1} \right) \right]\cos m\phi + \sum_{m=1}^{\infty}\left[-(\lambda + iu_0 k)\hat{w}_{m1} - \frac{1}{n}\hat{p}_{m1} \right.$$

$$\left. + \frac{1}{Re}\left(-k^2\hat{w}_{m1} + \frac{1}{n}\hat{w}_{m1,n} + \hat{w}_{m1,nn} - \frac{m^2}{n^2}\hat{w}_{m1} - \frac{1}{n^2}\hat{w}_{m1} - \frac{2m}{n^2}\hat{v}_{m0} \right) \right]\sin m\phi$$

$$- (Z_s\hat{X}_1 - X_s\hat{Z}_1)\left(k\lambda u_0 - k^2 u_0^2 - \frac{1}{Re}ik^3 u_0 \right)\sin\phi \;\; = \;\; 0,$$

(A.4)

and on $n = R_0$

$$\left((\lambda + iu_0 k)\hat{R}_1 - v_1 \right) + \sum_{m=1}^{\infty}\left((\lambda + iu_0 k)\hat{R}_{m0} - v_{m0} \right)\cos m\phi$$

$$+ \sum_{m=1}^{\infty}\left((\lambda + iu_0 k)\hat{R}_{m1} - v_{m1} \right)\sin m\phi + \lambda(Z_s\hat{X}_1 - X_s\hat{Z}_1)\cos\phi \;\; = \;\; 0, \quad \text{(A.5)}$$

$$(ik\hat{v}_1 + i\hat{u}_{1,n}) + \sum_{m=1}^{\infty}(ik\hat{v}_{m0} + i\hat{u}_{m0,n})\cos m\phi$$

$$+ \sum_{m=1}^{\infty}(ik\hat{v}_{m1} + i\hat{u}_{m1,n})\sin m\phi + k^2 u_0(Z_s\hat{X}_1 - X_s\hat{Z}_1)\cos\phi \;\; = \;\; 0, \qquad \text{(A.6)}$$

222

$$\left(\hat{w}_{1,n} - \frac{1}{R_0}\hat{w}_1 \right) + \sum_{m=1}^{\infty} \left(\hat{w}_{m0,n} - \frac{1}{R_0}\hat{w}_{m0} + \frac{m}{R_0}\hat{v}_{m1} \right) \cos m\phi$$

$$+ \sum_{m=1}^{\infty} \left(\hat{w}_{m1,n} - \frac{1}{R_0}\hat{w}_{m1} - \frac{m}{R_0}\hat{v}_{m0} \right) \sin m\phi \;=\; 0, \qquad \text{(A.7)}$$

$$\left(\hat{p}_1 - \frac{2}{Re}\hat{v}_{1,n} - \frac{1}{We}\left(k^2 - \frac{1}{R_0^2} \right) \hat{R}_1 \right) + \sum_{m=1}^{\infty} \left(\hat{p}_{m0} - \frac{2}{Re}\hat{v}_{m0,n} \right.$$

$$\left. - \frac{1}{We}\left(k^2 - \frac{1}{R_0^2} + \frac{m^2}{R_0^2} \right) \hat{R}_{m0} \right) \cos m\phi + \sum_{m=1}^{\infty} \left(\hat{p}_{m1} - \frac{2}{Re}\hat{v}_{m1,n} \right.$$

$$\left. - \frac{1}{We}\left(k^2 - \frac{1}{R_0^2} + \frac{m^2}{R_0^2} \right) \hat{R}_{m1} \right) \sin m\phi + k^2(Z_s\hat{X}_1 - X_s\hat{Z}_1)\cos\phi \;=\; 0, \quad \text{(A.8)}$$

$$X_s\hat{X}_1 + Z_s\hat{Z}_1 = 0, \qquad \text{(A.9)}$$

$$\hat{v}_1 + \sum_{m=1}^{\infty} \hat{v}_{m0}\cos m\phi + \hat{v}_{m1}\sin m\phi = 0 \quad \text{on} \quad n = 0, \qquad \text{(A.10)}$$

$$\hat{w}_1 + \sum_{m=1}^{\infty} \hat{w}_{m0}\cos m\phi + \hat{w}_{m1}\sin m\phi = 0 \quad \text{on} \quad n = 0. \qquad \text{(A.11)}$$

From equation (A.2) we obtain expressions for the pressure

$$\hat{p}_1 \;=\; \frac{1}{k}\left[-(\lambda + iu_0 k)\hat{u}_1 + \frac{1}{Re}\left(-k^2\hat{u}_1 + \frac{1}{n}\hat{u}_{1,n} + \hat{u}_{1,nn} \right) \right],$$

$$\hat{p}_{m0} \;=\; \frac{1}{k}\left[-(\lambda + iu_0 k)\hat{u}_{m0} + \frac{1}{Re}\left(-\left(k^2 + \frac{m^2}{n^2} \right)\hat{u}_{m0} + \frac{1}{n}\hat{u}_{m0,n} + \hat{u}_{m0,nn} \right) \right],$$

$$\hat{p}_{m1} \;=\; \frac{1}{k}\left[-(\lambda + iu_0 k)\hat{u}_{m1} + \frac{1}{Re}\left(-\left(k^2 + \frac{m^2}{n^2} \right)\hat{u}_{m1} + \frac{1}{n}\hat{u}_{m1,n} + \hat{u}_{m1,nn} \right) \right],$$

$$\text{(A.12)}$$

and from equation (A.1),

$$-kn\hat{u}_1 + \hat{v}_1 + n\hat{v}_{1,n} \;=\; 0,$$
$$-kn\hat{u}_{m0} + \hat{v}_{m0} + \hat{v}_{m0,n} + m\hat{w}_{m1} \;=\; 0,$$
$$-kn\hat{u}_{m1} + \hat{v}_{m1} + \hat{v}_{m1,n} - m\hat{w}_{m0} \;=\; 0, \qquad \text{(A.13)}$$

for $m \geq 1$. Substituting (A.12) into (A.3) and (A.4), and using (A.13) and (A.9) we

obtain (after considerable algebra)

$$u_1 = A_1(s)I_0(kn) - A_2(s)\tilde{k}I_0(\tilde{k}n), \quad v_1 = A_1(s)\frac{1}{k}\frac{d}{dn}I_0(kn) - A_2(s)\frac{k}{\tilde{k}}\frac{d}{dn}I_0(\tilde{k}n)$$

$$w_1 = 0, \quad p_1 = -A_1(s)\frac{\lambda + iu_0k}{k}I_0(kn)$$

$$u_{m0} = A_3(s)I_m(kn) - A_4(s)\tilde{k}I_m(\tilde{k}n), \quad v_{m0} = A_3(s)\frac{1}{k}\frac{d}{dn}I_m(kn) - A_4(s)\frac{k}{\tilde{k}}\frac{d}{dn}I_m(\tilde{k}n)$$

$$w_{m1} = -A_3(s)\frac{mI_m(kn)}{kn} + A_4(s)\frac{kmI_m(\tilde{k}n)}{\tilde{k}n}, \quad p_{m0} = -A_3(s)\frac{\lambda + iu_0k}{k}I_m(kn)$$
$$\text{for} \quad m > 1$$

$$u_{m1} = A_5(s)I_m(kn) - A_6(s)\tilde{k}I_m(\tilde{k}n), \quad v_{m1} = A_5(s)\frac{1}{k}\frac{d}{dn}I_m(kn) - A_6(s)\frac{k}{\tilde{k}}\frac{d}{dn}I_m(\tilde{k}n)$$

$$w_{m0} = -A_5(s)\frac{mI_m(kn)}{kn} + A_6(s)\frac{kmI_m(\tilde{k}n)}{\tilde{k}n}, \quad p_{m1} = -A_5(s)\frac{\lambda + iu_0k}{k}I_m(kn)$$
$$\text{for} \quad m \geq 1$$

$$u_{10} = A_7(s)I_1(kn) - A_8(s)\tilde{k}I_1(\tilde{k}n),$$

$$v_{10} = A_7(s)\frac{1}{k}\frac{d}{dn}I_1(kn) - A_8(s)\frac{k}{\tilde{k}}\frac{d}{dn}I_1(\tilde{k}n) - \frac{iku_0\hat{Z}_1}{X_s}$$

$$w_{11} = -A_7(s)\frac{I_1(kn)}{kn} + A_8(s)\frac{kI_1(\tilde{k}n)}{\tilde{k}n} + \frac{iku_0\hat{Z}_1}{X_s}, \quad p_{m0} = -A_7(s)\frac{\lambda + iu_0k}{k}I_1(kn).$$

where $\tilde{k}^2 = k^2 + Re(\lambda + iu_0k)$, $A_1 - A_8$ are constants and I_0, I_1 and I_m are zeroth, first and mth order modified Bessel functions respectively.

Substituting the above into the boundary condition (A.5) yields

$$R_1 = \frac{1}{\lambda + iu_0k}\left(A_1(s)\frac{1}{k}I_0'(kR_0) - A_2(s)\frac{k}{\tilde{k}}I_0'(\tilde{k}R_0)\right)$$

$$R_{m0} = \frac{1}{\lambda + iu_0k}\left(A_3(s)\frac{1}{k}I_m'(kR_0) - A_4(s)\frac{k}{\tilde{k}}I_m'(\tilde{k}R_0)\right) \quad \text{for} \quad m > 1$$

$$R_{m1} = \frac{1}{\lambda + iu_0k}\left(A_5(s)\frac{1}{k}I_m'(kR_0) - A_6(s)\frac{k}{\tilde{k}}I_m'(\tilde{k}R_0)\right) \quad \text{for} \quad m \geq 1$$

$$R_{10} = \frac{1}{\lambda + iu_0k}\left(A_5(s)\frac{1}{k}I_m'(kR_0) - A_6(s)\frac{k}{\tilde{k}}I_m'(\tilde{k}R_0)\right) - \frac{Z_1}{X_s}$$

where $I_m'(kR_0) \equiv \left(\frac{d}{dn}(I_m(kn))\right)\big|_{n=R_0}$. Using the boundary condition (A.6) we obtain the following relationships;

$$A_2(s) = \frac{2A_1(s)\tilde{k}I_0'(kR_0)}{(k^2 + \tilde{k}^2)I_0'(\tilde{k}R_0)}, \qquad A_4(s) = \frac{2A_3(s)\tilde{k}I_m'(kR_0)}{(k^2 + \tilde{k}^2)I_m'(\tilde{k}R_0)},$$

$$A_6(s) = \frac{2A_5(s)\tilde{k}I_m'(kR_0)}{(k^2 + \tilde{k}^2)I_m'(\tilde{k}R_0)}, \qquad A_8(s) = \frac{2A_7(s)\tilde{k}I_1'(kR_0)}{(k^2 + \tilde{k}^2)I_1'(\tilde{k}R_0)},$$

Substituting these relations into (A.8) yields (after considerable algebra) the dispersion relation for the stable modes with $m \geq 1$

$$(\lambda + iu_0k)^2 \;+\; \frac{2(\lambda + iu_0k)}{ReI_m(kR_0)}\left[I_m''(kR_0) - \frac{2k^2I_m'(kR_0)I_m''(\tilde{k}R_0)}{(k^2 + \tilde{k}^2)I_m'(\tilde{k}R_0)}\right]$$

$$+\; \frac{1}{We}\left(k^2 - \frac{1}{R_0^2}(1 - m^2)\right)\left[\frac{(\tilde{k}^2 - k^2)I_m'(kR_0)}{(\tilde{k}^2 + k^2)I_m(kR_0)}\right] = 0, \quad \text{(A.14)}$$

Appendix B

The solution in Region I for a curved jet

This appendix details the small s expansion in Chapter 10, showing that it is necessary to use the full curvature in the steady state equations to obtain the solution in region I, ((10.9) and (10.10)). The steady state equations are

$$\bar{u}\bar{u}_s = \frac{1}{We}\kappa_s + \frac{(\bar{X}+1)\bar{X}_s + \bar{Z}\bar{Z}_s}{Rb^2},$$

$$\frac{1}{2}\bar{R}\bar{u}_s + \bar{u}\bar{R}_s = 0$$

$$(\bar{X}_s\bar{Z}_{ss} - \bar{Z}_s\bar{X}_{ss})\left(\bar{u}^2 - \frac{1}{We\bar{R}}\right) - \frac{2\bar{u}}{Rb} + \frac{((\bar{X}+1)\bar{Z}_s - \bar{Z}\bar{X}_s)}{Rb^2} = 0,$$

$$\bar{X}_s\bar{X}_{ss} + \bar{Z}_s\bar{X}_{ss} = 1. \tag{B.1}$$

where κ is the curvature of the jet, subject to $\bar{X} = \bar{Z} = \bar{Z}_s = 0$ and $\bar{X}_s = \bar{R} = \bar{u} = 1$ at $s = 0$.

We first tried using the leading order term for the curvature,

$$\kappa = \frac{1}{\bar{R}}.$$

As we have up to third derivatives with respect to s in $\bar{R}$ in (10.2), we must expand our steady quantities up to $O(s^3)$, and so we expand by

$$\hat{\mathbf{F}} = \mathbf{F}_0 + s\mathbf{F}_1 + s^2\mathbf{F}_2 + s^3\mathbf{F}_3 + O(s^4),$$

where $\mathbf{F}_i = (u_i, R_i, X_i, Z_i)$ for $i = 0, 1, 2...$ as $s \to 0$.

We obtain

$$
\hat{u} = 1 + \frac{2We}{Rb^2(2We+1)}s - \left(\frac{We}{Rb^2(2We+1)} - \frac{We^2(4We-1)}{Rb^4(2We+1)^3}\right)s^2
$$
$$
- \left(\frac{We^2(4We-1)}{Rb^4(2We+1)^3} + \frac{2We^3(8We^4+121We^3+3We^2+31We+1)}{3Rb^6(We-1)^2(2We+1)^5}\right)s^3 + O(s^4),
$$
$$
\hat{R} = 1 - \frac{We}{Rb^2(2We+1)}s - \left(\frac{We}{2Rb^2(2We+1)} - \frac{We^2(5We+1)}{Rb^4(2We+1)^3}\right)s^2
$$
$$
+ \left(\frac{We^2(5We+1)}{Rb^4(2We+1)^3} - \frac{2We^3(29We^4+107We^3-6We^2+We+2)}{3Rb^6(We-1)^2(2We+1)^5}\right)s^3 + O(s^4),
$$
$$
\hat{X} = s - \frac{2We^2}{3Rb^2(We-1)^2}s^3 + \frac{We^3}{Rb^6(We-1)^3}s^4 + O(s^5),
$$
$$
\hat{Z} = \frac{We}{Rb(We-1)^2}s^2 - \frac{2We^2}{3Rb^2(We-1)^2}s^3
$$
$$
+ \left(-\frac{We^2}{6Rb^4(We-1)^2} + \frac{We^3(10We^2-1)}{6Rb^6(We-1)^3(2We+1)^2}\right)s^4 + O(s^5). \tag{B.2}
$$

as $s \to 0$.

Substituting into (10.6) and (10.7) we obtain

$$
3G_0 - \eta G_0' + F_0' + O\left(t^{1/2}\right) + O(s) = 0, \tag{B.3}
$$
$$
F_0 - \frac{1}{2}\eta F_0' - \frac{1}{\gamma}G_0''' + \chi + O\left(t^{1/2}\right) + O(s) = 0 \tag{B.4}
$$

where $' \equiv \frac{d}{d\eta}$ and $\eta = s/\sqrt{t}$ and

$$
\gamma = \frac{We((2We+1)^2Rb^4 + We^2)^{3/2}}{Rb^6(2We+1)^3}
$$
$$
\chi = \frac{\Gamma}{Rb^2((2We+1)^2Rb^4 + We^2)^{5/2}(We-1)^2(2We+1)}
$$

where

$$
\Gamma = (We-1)^2(2We+1)^5Rb^{10} - We(7+32We)(We-1)^2(2We+1)^3Rb^8
$$
$$
+ 3We^2(2We+1)(44We^4-150We^3-9We^2+4We+3)Rb^6
$$
$$
+ We^3(2We+1)(28We+5)(We-1)^2Rb^4 - We^4(80We^3-51We^2+78We+1)Rb^2
$$
$$
- ((2We+1)^2Rb^4 + We^2)^{5/2}(We-1)^2.
$$

We note that taking the limit in $Rb \to \infty$ in the above, $\gamma \to We$ and $\chi \to 0$ and (B.4) reduces to the case of a straight jet. Following the method used in Chapter 9,

we obtain

$$
\begin{aligned}
G_0 &= (\delta\omega - \chi)\left[\sqrt{\frac{\gamma}{2}}\eta + \frac{\gamma}{6}\eta^3 - \frac{2^{1/4}\gamma^{3/4}}{3\sqrt{\pi}}\eta^2\cos\left(\frac{\sqrt{2\gamma}}{4}\eta^2\right)\right.\\
&+ \left.\frac{2^{7/4}\gamma^{1/4}}{3\sqrt{\pi}}\sin\left(\frac{\sqrt{2\gamma}}{4}\eta^2\right) - \frac{\gamma}{3}\eta^3 F_s\left(\frac{\gamma^{1/4}}{2^{1/4}\sqrt{\pi}}\eta\right) + \sqrt{2\gamma}\eta F_c\left(\frac{\gamma^{1/4}}{2^{1/4}\sqrt{\pi}}\eta\right)\right]
\end{aligned}
$$

(B.5)

and

$$
\begin{aligned}
F_0 &= (\delta\omega - \chi)\left[-\sqrt{\frac{\gamma}{2}}\eta^2 - \frac{2^{3/4}\gamma^{1/4}}{\sqrt{\pi}}\eta\sin\left(\frac{\sqrt{2\gamma}}{4}\eta^2\right) - 2F_s\left(\frac{\gamma^{1/4}}{2^{1/4}\sqrt{\pi}}\eta\right)\right.\\
&+ \left.\sqrt{2\gamma}\eta^2 F_c\left(\frac{\gamma^{1/4}}{2^{1/4}\sqrt{\pi}}\eta\right)\right] + \delta\omega.
\end{aligned}
$$

(B.6)

As $\eta \to \infty$,

$$
\begin{aligned}
F_0 &= \chi + \frac{\alpha}{\eta^3}\sin\left(\beta\eta^2\right) + O\left(\frac{1}{\eta^5}\right),\\
G_0 &= \frac{\alpha}{\eta^4}\sin\left(\beta\eta^2\right) + O\left(\frac{1}{\eta^6}\right),
\end{aligned}
$$

(B.7)

where

$$
\alpha = \frac{4\,2^{3/4}}{\gamma^{3/4}\sqrt{\pi}}\left(\delta\omega - \chi\right), \qquad \beta = \frac{\sqrt{2\gamma}}{4}.
$$

As $Rb \to \infty$, $\chi \to 0$ and the above equations reduce to the equations describing a straight jet. However, through this term χ, we have an extra term in the large η behaviour of the velocity. This appears as though the velocity is been driven by a constant term, which should not be the case. This arises as a result of the full curvature term used in (9.2). This is not a problem for a straight jet as $u = R = 1$ at the orifice. Therefore, we must perform our small s asymptotics for steady state equations with the full curvature.

Using the full curvature in the small s asymptotics

We now use the full curvature in the problem, namely

$$
\kappa = \frac{1}{R(1 + R_s^2)^{\frac{1}{2}}} - \frac{R_{ss}}{(1 + R_s^2)^{\frac{3}{2}}}
$$

We have new modified steady state equations

$$\bar{u}\bar{u}_s = \frac{1}{We}\left(\frac{-R_s}{R^2(1+R_s^2)^{\frac{1}{2}}} - \frac{R_sR_{ss}+RR_{sss}}{R(1+R_s^2)^{\frac{3}{2}}} + \frac{3R_sR_{ss}^2}{(1+R_s^2)^{\frac{5}{2}}}\right) + \frac{(\bar{X}+1)\bar{X}_s+\bar{Z}\bar{Z}_s}{Rb^2},$$

$$\frac{1}{2}\bar{R}\bar{u}_s + \bar{u}\bar{R}_s = 0$$

$$(\bar{X}_s\bar{Z}_{ss}-\bar{Z}_s\bar{X}_{ss})\left(\bar{u}^2-\frac{1}{We\bar{R}}\right) - \frac{2\bar{u}}{Rb} + \frac{((\bar{X}+1)\bar{Z}_s-\bar{Z}\bar{X}_s)}{Rb^2} = 0,$$

$$\bar{X}_s\bar{X}_{ss}+\bar{Z}_s\bar{X}_{ss} = 1. \tag{B.8}$$

and expand as above.

We obtain

$$\hat{u} = 12R_1s - (3R1-2R_2)s^2 + O(s^3)$$
$$\hat{R} = 1 + R_1s + R_2s^2 \tag{B.9}$$
$$- \frac{1}{6}\left(\frac{We(2Rb^2R_1+1)(1+R_1^2)(3/2)}{Rb^2} + R_1(1+R_1^2) + 2R_1R_2 - \frac{12R_1R_2^2}{1+R_1^2}\right)s^3 + O(s^4),$$
$$\hat{X} = s - \frac{2We^2}{3Rb^2(We-1)^2}s^3 + \frac{We^3}{Rb^6(We-1)^3}s^4 + O(s^5),$$
$$\hat{Z} = \frac{We}{Rb(We-1)^2}s^2 + \left(\frac{R_1We(2We+1)}{3Rb^2(We-1)^2} - \frac{We^2}{3Rb^4(We-1)^2}\right)$$
$$+ \left(\frac{R_2We(2We+1)}{6Rb^2(We-1)^2} - \frac{We^2}{12Rb^4(We-1)^2} + \frac{We^4(4+5We)}{6Rb^6(We-1)^3(2We+1)^2}\right)s^4 + O(s^5). \tag{B.10}$$

as $s \to 0$. As we have introduced the full curvature into our steady state (B.8), we get contributions from R_1, R_2 and R_3 to leading order in s. Hence we are unable to determine R_1 and R_2. Substitution into (9.1) and (9.2) yields

$$3G_0 - \eta G_0' + F_0' + O\left(t^{1/2}\right) + O(s) = 0,$$
$$F_0 - \frac{1}{2}\eta F_0' - \frac{1}{\gamma}G_0''' + O\left(t^{1/2}\right) + O(s) = 0,$$

where $' \equiv \frac{d}{d\eta}$ and $\eta = s/\sqrt{t}$ and

$$\gamma = We(1+R_1^2)^{3/2}$$

is not a function of s, but it must be necessary that $R_1 \to 0$ as $Rb \to \infty$. If we assume the centreline position is unaffected by the full curvature, R_1 and R_2 can be caluclated

by matching X and Z in (B.8) and (B.10). This yields

$$\hat{u} = 1 + \frac{2We}{Rb^2(2We+1)}s - \left(\frac{We}{Rb^2(2We+1)} - \frac{We^2(4We-1)}{Rb^4(2We+1)^3}\right)s^2$$

$$\hat{R} = 1 - \frac{We}{Rb^2(2We+1)}s - \left(\frac{We}{2Rb^2(2We+1)} - \frac{We^2(5We+1)}{Rb^4(2We+1)^3}\right)s^2$$

$$+ \left(-\frac{(Rb^4(2We+1)^2+We^2)^{3/2}}{6Rb^8(2We+1)^4}\right.$$

$$+ \left.\frac{WeRb^2(2We+1) - We^2 + \frac{We^3(8We+1)}{Rb^2(2We+1)^2} + \frac{We^4(58We+11)}{Rb^4(2We+1)^3} - \frac{3We^5(92We^2+34We+3)}{Rb^6(2We+1)^5}}{6\left(Rb^4(2We+1)^2+We^2\right)}\right)s^3 + O(s^4),$$

$$\hat{X} = s - \frac{2We^2}{3Rb^2(We-1)^2}s^3 + \frac{We^3}{Rb^6(We-1)^3}s^4 + O(s^5),$$

$$\hat{Z} = \frac{We}{Rb(We-1)^2}s^2 - \frac{2We^2}{3Rb^2(We-1)^2}s^3$$

$$+ \left(-\frac{We^2}{6Rb^4(We-1)^2} + \frac{We^3(10We^2-1)}{6Rb^6(We-1)^3(2We+1)^2}\right)s^4 + O(s^5).$$

as $s \to 0$. Hence

$$3G_0 - \eta G_0' + F_0' + O\left(t^{1/2}\right) + O(s) = 0,$$

$$F_0 - \frac{1}{2}\eta F_0' - \frac{1}{\gamma}G_0''' + O\left(t^{1/2}\right) + O(s) = 0,$$

where $' \equiv \frac{d}{d\eta}$, $\eta = s/\sqrt{t}$ and

$$\gamma = We\left(1 + \left(\check{R}'\right)^2\right)^{3/2}$$

$$= \frac{We\left(Rb^4(2We+1)^2 + We^2\right)^{3/2}}{Rb^6(2We+1)^3} \quad \text{as} \quad s \to 0.$$

Taking the limit $Rb \to \infty$, $\gamma \to We$ and we reduce to the case of a straight jet.

Appendix C

Large s asymptotics of jet equations

Expanding u, R, X and Z in (10.4) by $1/s$ as $s \to \infty$ doesn't yield a valid expansion, so clearly the large s expansion is more complicated. As $s \to \infty$, we have a coiled solution, so we adopt plane polar coordinates where $Z = r(s)\sin(\theta(s))$ and $X = -1 + r(s)\cos(\theta(s))$ placing the centre of the coordinate system at the cnetre of the can. Substituting this into the steady state equations (10.4) we obtain

$$uu_s - \frac{R_s}{WeR^2} - \frac{rr'}{Rb^2} = 0, \qquad (C.1)$$

$$\frac{1}{2}Ru_s + uR_s = 0, \qquad (C.2)$$

$$\left(-r\theta'r'' + r^2(\theta')^3 + 2(r')^2\theta' + rr'\theta''\right)\left(u^2 - \frac{1}{WeR}\right) - \frac{2u}{Rb} + \frac{r^2\theta'}{Rb} = 0, \qquad (C.3)$$

$$r^2(\theta')^2 + (r')^2 = 1. \qquad (C.4)$$

Differentiating (C.4) we get

$$\theta'\theta'' = -\frac{r'r''}{r^2} + \frac{(r')^3}{r^3} - \frac{r'}{r^3}.$$

Substituiting this and (C.4) into (C.3) yields after some simplification

$$\frac{r''}{r} + \frac{(r')^2}{r^2} - \frac{1}{r^2} + \frac{1}{u^2 - \frac{1}{WeR}}\left(\frac{2u}{Rb}\sqrt{\frac{1 - (r')^2}{r^2}} - \frac{1 - (r')^2}{Rb^2}\right) = 0. \qquad (C.5)$$

From (C.1), using $R = u = 1$ and $r = 0$ at $s = 0$, we obtain

$$u = \left(1 + \frac{2}{We}\left(1 - \frac{1}{R}\right) + \frac{r^2}{Rb^2}\right)^{1/2}. \qquad (C.6)$$

Hence, to give a balance it is necessary that $u \sim r/Rb$. Substituting (C.6) into (C.5)

yields

$$+\frac{1}{1+\frac{2}{We}-\frac{3}{WeR}+\frac{r^2}{Rb^2}}\left(\frac{2}{Rb}\sqrt{\frac{1-(r')^2}{r^2}}\left(1+\frac{2}{We}\left(1-\frac{1}{R}\right)+\frac{r^2}{Rb^2}\right)^{1/2}-\frac{1-(r')^2}{Rb^2}\right)\begin{array}{c}\frac{r''}{r}+\frac{(r')^2}{r^2}-\frac{1}{r^2}\\[6pt]\end{array}=0.$$

Evaluating (C.2), using $R = u = 1$ at $s = 0$ gives $u = 1/R^2$. Substituting this and (C.2) into the above yields

$$+\frac{1}{1+\frac{2}{We}-\frac{3\sqrt{u}}{We}+\frac{r^2}{Rb^2}}\left(\frac{2}{Rb}\sqrt{\frac{1-(r')^2}{r^2}}\left(1+\frac{2}{We}\left(1-\sqrt{u}\right)+\frac{r^2}{Rb^2}\right)^{1/2}-\frac{1-(r')^2}{Rb^2}\right)\begin{array}{c}\frac{r''}{r}+\frac{(r')^2}{r^2}-\frac{1}{r^2}\\[6pt]\end{array}=0$$

Using $u \sim r/Rb$

$$+\frac{1}{1+\frac{2}{We}-\frac{3\sqrt{r}}{We\sqrt{Rb}}+\frac{r^2}{Rb^2}}\left(\frac{2}{Rb}\sqrt{\frac{1-(r')^2}{r^2}}\left(1+\frac{2}{We}\left(1-\frac{\sqrt{r}}{\sqrt{Rb}}\right)+\frac{r^2}{Rb^2}\right)^{1/2}-\frac{1-(r')^2}{Rb^2}\right)\begin{array}{c}\frac{r''}{r}+\frac{(r')^2}{r^2}-\frac{1}{r^2}\\[6pt]\end{array}=0.$$

$$\text{(C.7)}$$

We adopt an algebraic expansion for r,

$$r \sim \alpha s^n + \beta s^m + ...$$

where $0 < m < n < 1$, $\alpha, \beta \in \Re$ and $\alpha > 0$. Substituting into (C.7) it is necessary that

$$(n(n-1)+n^2)s^{-2} = \frac{1}{\alpha^2}s^{-2n} + \frac{2Rb(3\sqrt{Rb}-1)}{We\alpha^{7/2}}s^{-7n/2} \qquad \text{(C.8)}$$

To match the above

(i) $n = 4/7$ balancing the first and third terms in s. In this case, α is not real.

(ii) $n = 1$ to match the first and second terms. In this case, the third term is larger.

(iii) $n = 1/2$ to make the first term identically equal to zero. The second and third terms don't match.

It appears that an algebraic expansion is not possible for $r(s)$. However, if a higher order expansion were to remove the second term, in case (iii) there would be a match if $We \to \infty$. This is realistic, as for a finite Weber number the jet returns to the orifice.

So a large s expansion will not be valid for finite Weber number. Taking the limit $We \to \infty$,

$$\frac{r''}{r} + \frac{(r')^2}{r^2} - \frac{1}{r^2} + \frac{1}{1 + \frac{r^2}{Rb^2}}\left(\frac{2}{Rb}\sqrt{\frac{1 - (r')^2}{r^2}}\left(1 + \frac{r^2}{Rb^2}\right)^{1/2} - \frac{1 - (r')^2}{Rb^2}\right) = 0. \quad \text{(C.9)}$$

The limit $We \to \infty$ corresponds to zero surface tension, so we can consider the classical mechanics problem considering the motion of a particle on the centreline of the jet.

Consider a rotating can with radius a in a rotating frame of reference $\mathbf{r}(t) = (x(t), y(t), z(t))$ with rotation $\omega = (0, 0, \omega)$. The fixed axis is given by $\mathbf{r}'(t) = (x'(t), y'(t), z'(t))$. A particle leaves the orifice with speed v in the x-direction. As there are no body forces, Newton's second law states that the acceleration is zero, hence

$$\frac{d^2\mathbf{r}}{dt^2} = 0$$

and

$$\frac{d^2\mathbf{r}'}{dt^2} + 2\omega \wedge \frac{d\mathbf{r}'}{dt} + \frac{d\omega}{dt} \wedge \mathbf{r} + \omega \wedge (\omega \wedge \mathbf{r}) = 0$$

This yields

$$\begin{aligned} x'' - 2\omega y' - \omega^2 x &= 0, \\ y'' + 2\omega x' - \omega^2 y &= 0, \\ z'' &= 0, \end{aligned}$$

where $' \equiv d/dt$, subject to the initial conditions $x = a$, $x' = v$ and $y = y' = z = z' = 0$. Defining $\xi = x + iy$ yields

$$\xi'' + 2i\xi' - \omega^2\xi = 0,$$

subject to $\xi = a$ and $\xi' = v$. This yields

$$\xi = e^{-i\omega t}[(v + ai\omega)t + a]$$

and hence

$$\begin{aligned} x &= vt\cos(\omega t) + at\omega\sin(\omega t) + a\cos(\omega t) \\ y &= -vt\sin(\omega t) + at\omega\cos(\omega t) - a\sin(\omega t) \end{aligned}$$

In polar cooridinates, where $\xi = re^{i\theta}$, this gives

$$r = \sqrt{a^2\omega^2 t^2 + v^2 t^2 + 2vta + a^2}. \quad \text{(C.10)}$$

It is the aim to obtain $r(s)$, where s is the arclength along the centre of the jet. This

can be done by obtaining $t(r)$ and $t(s)$ and removing t as a parameter. Rearranging (C.10), and keeping the physical positive root

$$t = \frac{-av + \sqrt{v^2r^2 + \omega^2a^2r^2 - \omega^2a^4}}{v^2 + \omega^2a^2}.$$

(C.11)

In terms of s,

$$s = \int \sqrt{\left(\frac{dx}{dt}\right)^2 + \left(\frac{dy}{dt}\right)^2}\, dt = \int \sqrt{v^2t^2\omega^2 + a^2t^2\omega^4 + 2atv\omega^2 + v^2}\, dt$$

yielding

$$s = \frac{((v^2\omega^2 + \omega^4a^2)t + 2av\omega^2)\sqrt{(v^2\omega^2 + \omega^4a^2)t^2 + 2av\omega^2t + v^2}}{2\omega^2(v^2 + \omega^2a^2)}$$

$$+ \frac{\omega^2v^4 \log\left(\frac{a\omega^2 + \omega^2(v^2 + \omega^2a^2)t}{\sqrt{\omega^2(v^2 + \omega^2a^2)}} + \sqrt{(v^2\omega^2 + \omega^4a^2)t^2 + 2av\omega^2t + v^2}\right)}{2(\omega^2(v^2 + \omega^2a^2))^{3/2}}$$

(C.12)

As we wish to examine $s \to \infty$ and $t \to \infty$, taking the large t expansion of above we get terms to $O\left(t^2\right)$. Taking the terms up to $O(1)$, we can solve the expansion as a quadratic for t,

$$t \sim \frac{-2av\omega + \sqrt{8\sqrt{v^2 + a^2\omega^2}(sa^2\omega^3 + s\omega v^2) - 2v^4}}{2\omega(v^2 + \omega^2a^2)}.$$

(C.13)

Using (C.11) and (C.13), we can eliminate t to get

$$r \sim \frac{\sqrt{4a^4\omega^4 - 2v^4 + 8s(v^2\omega + \omega^3a^2)\sqrt{v^2 + a^2\omega^2}}}{2\omega\sqrt{v^2 + \omega^2a^2}}.$$

(C.14)

Expanding this asymptotically gives $r = O(\sqrt{s})$ to leading order. This backs up the findings from case (iii) setting $n = 1/2$ in (C.8) matching when $We \to \infty$. However, the higher order behaviour has not yer been determined. Taking the limit $a \to 0$ in (C.10) and (C.12), this corresponds to the radius of the drum tending to zero which is a reasonable approximation in the large s limit, we obtain

$$s = \frac{1}{2}tv\sqrt{t^2\omega^2 + 1} + \frac{v\log(\omega t)}{2\omega},$$
$$r = tv$$

Eliminating t from the above, we obtain $r(s)$ in terms of the Lambert W function, defined as the solution $y = \text{LambertW}(x)$ as a solution to $ye^y = x$. Taking the

asymptotic limit of this solution we obtain

$$r \sim C_0 \sqrt{s} + C_1 \frac{\log s}{\sqrt{s}}.$$

Substituting this into the equation for r (C.9), the terms now balance. We obtain an expression linking the constants

$$C_1 = -\frac{1}{64}C_0^3 - \frac{1}{8}\frac{Rb^2}{C_0} - \frac{1}{4}\frac{Rb^4}{C_0^5}.$$

It is still necessary to determine the value of C_0. Examining the largest term in (C.14), with $a \to 0$, gives

$$r \sim \sqrt{\frac{2sv}{\omega}}.$$

Given that the Rossby number in the problem is $v/\omega s$, $C_0 = \sqrt{2Rb}$, and the expansion becomes

$$r \sim \sqrt{2Rbs} - \frac{\sqrt{2}Rb^{3/2}}{8}\frac{\log s}{\sqrt{s}} + \cdots .$$

This gives, using (C.4),

$$\theta \sim \sqrt{\frac{2s}{Rb}} - \frac{\sqrt{2Rb}}{8}\frac{\log s}{\sqrt{s}},$$

and the large s asymptotics are complete.

List of References

[1] G.K. Batchelor. *An Introduction to Fluid Dynamics*. Cambridge Univ. Press, 1970.

[2] M. Born and E. Wolf. *Principle of Optics*. Cambridge Univ. Press, 1964.

[3] M. P. Brenner, J. Eggers, K. Joseph, R.N. Sidney, and X.D. Shi. Breakdown of scaling in droplet fission at high reynolds number. *Phys. Fluids.*, 9:1573–1590, 1997.

[4] S. Chandrasekhar. *Hydrodynamic and Hydromagnetic Stability*. Oxford Univ. Press, 1961.

[5] K.C. Chaudhary and T. Maxworthy. The nonlinear capillary instability of a liquid jet. part 2. experiments on jet behaviour before droplet formation. *J. Fluid Mech.*, 96:275–286, 1980.

[6] K.C. Chaudhary and T. Maxworthy. The nonlinear capillary instability of a liquid jet. part 3. experiments on satellite drop formation and control. *J. Fluid Mech.*, 96:287–298, 1980.

[7] K.C. Chaudhary and L.G. Redekopp. The nonlinear capillary instability of a liquid jet. part 1. theory. *J. Fluid Mech.*, 96:257–274, 1980.

[8] A. Chauhan, C. Maldarelli, D.S. Rumschitzki, and D.T. Papageorgiou. An experimental investigation of the convective instability of a jet. *Chem. Eng. Sci*, 58:2421–2432, 2003.

[9] A.D.D. Craik. *Wave interactions and fluid flows*. Cambridge Univ. Press, 1985.

[10] L. Crane, S. Birch, and P.D. McCormack. The effect of mechanical vibration on the break-up of a cylindrical water jet in air. *Br. J. Appl. Phys.*, 15:743–750, 1964.

[11] S. P. Decent. Asymptotic solution of slender viscous jet break-up. *IMA J. Appl. Math.*, pages 1–41, 2009.

[12] S. P. Decent, A. C. King, M. J. H. Simmons, E. I. Părău, I. M. Wallwork, C. J. Gurney, and J. Uddin. The trajectory and stability of a spiralling liquid jet: Viscous theory. *Applied Math. Modelling*, 2009.

[13] S. P. Decent, A.C. King, and I.M. Wallwork. Free jets spun from a prilling tower. *J. Eng. Math.*, 42:265–282, 2002.

[14] R.J. Donnelly and W. Glaberson. Experiments on the capillary instability of a liquid jet. *Proc. R. Soc. Lond. A.*, 290:547–556, 1966.

[15] J. Eggers. Theory of drop formation. *Phys. Fluids.*, 7:941–953, 1994.

[16] J. Eggers and T.F. Dupont. Drop formation in a one-dimensional approximation of the navier-stokes equation. *J. Fluid. Mech.*, 262:205–221, 1994.

[17] J. Eggers and E. Villermaux. Physics of liquid jets. *Rep. Prog. Phys.*, 71, 2008.

[18] V.M. Entov and A.L. Yarin. The dynamics of thin liquid jets in air. *J. Fluid Mech.*, 140:91–111, 1984.

[19] E.F. Goedde and M.C. Yuen. Experiments on liquid jet instability. *J. Fluid Mech.*, 40:495–511, 1970.

[20] Wilton J.R. On ripples. *Phil. Mag.*, 29:688–700, 1915.

[21] J.B. Keller, S.I. Rubinow, and Y.O. Tu. Spatial instability of a jet. *Phys. Fluids.*, 16:2052–2055, 1973.

[22] J.A. Leach and D.A. Needham. *Matched Asymptotic Expansions in Reaction-Diffusion Theory.* Springer-Verlag London, 1991.

[23] S.J. Leib and M.E. Goldstein. The generation of capillary instabilities on a liquid jet. *J. Fluid Mech.*, 168:479–500, 1986.

[24] D. Leppinen and J.R. Lister. Capillary pinch-off in inviscid fluids. *Phys. Fluids.*, 15:568–578, 2003.

[25] S.P. Lin. *Regimes of Jet Breakup and Breakup Mechanisms (Mathematical Aspects). Appeared in Recent Advances in Spray Combustion, Spray Atomization and Drop Burning. Edited by K.K. Kuo.* American Institute of Aeronautics and Astronautics, Inc., 1996.

[26] S.P. Lin. *Break-up of Liquid Jets and Sheets.* Cambridge University Press, 2003.

[27] S.P. Lin and Z.W. Lian. Absolute instability of a liquid jet in a gas. *Phys. Fluids A.*, 1:490–499, 1989.

[28] S.P. Lin and R.D. Reitz. Drop and spray formation from a liquid jet. *Ann. Rev. Fluid Mech.*, 30:85–105, 1998.

[29] N.R. Lindblad and J.M. Schneider. Production of uniform-sized liquid droplets. *J. Sci. Instrum.*, 42:635–638, 1965.

[30] L.F. McGoldrick. Resonant interactions among capillary-gravity waves. *J. Fluid Mech.*, 21:305–331, 1965.

[31] L.F. McGoldrick. On the rippling of small waves: a harmonic nonlinear nearly resonant interaction. *J. Fluid Mech.*, 52:725–751, 1972.

[32] A.H. Nayfeh and D.T. Mook. *Nonlinear Oscillations*. John Wiley & Sons, New York, 1979.

[33] L. Partridge. An experimental and theoretical investigation into the break-up of curved liquid jets in the prilling process. *PhD thesis. University of Birmingham.*, 2006.

[34] L. Partridge, D.C. Wong, Simmons M.J.H., E.I. Pӑrӑu, and S.P. Decent. Experimental and theoretical description of the break-up of curved liquid jets in the prilling process. *Chem. Eng. Res Des.*, 83:1267–1275, 2005.

[35] E.I. Pӑrӑu, S.P. Decent, A.C. King, M.J.H. Simmons, and Wong D.C.Y. Nonlinear travelling waves on a spiralling liquid jet. *Wave Motion*, 43:599–618, 2006.

[36] E.I. Pӑrӑu, S.P. Decent, M.J.H. Simmons, Wong D.C.Y., and A.C. King. Nonlinear viscous jets emerging from a rotating orifice. *J. Eng. Math.*, 57:159–179, 2007.

[37] D.H. Pergrine, G. Shoker, and A. Symon. The bifurcation of liquid bridges. *J. Fluid Mech.*, 212:25–39, 1990.

[38] J. Plateau. *Statique Expérimentale et Théoretique des Liquides Soumis aux Seules Forces Moléculaires.* Gauthier Villars, 1870.

[39] Lord J.W.S. Rayleigh. On the capillary phenomena of jets. *Proc. Roy. Soc. London.*, 29:4–13, 1879.

[40] O. Reynolds. *Phil. Trans. Roy. Soc.*, 177:157, 1886.

[41] D.F. Rutland and G.J. Jameson. A non-linear effect in the capillary instability of liquid jets.

[42] F Savart. *Ann. de chemie.*, 53:337–398, 1833.

[43] A. Sierou and J.R. Lister. Self-similar solutions for viscous capillary pinch-off. *J. Fluid Mech.*, 497:381–403, 2003.

[44] J. Uddin. An investigation into methods to control break-up and droplet formation in single and compound liquid jets. *PhD thesis. University of Birmingham.*, 2007.

[45] I.M. Wallwork. The trajectory and stability of a spiralling liquid jet. *PhD thesis. University of Birmingham.*, 2002.

[46] I.M. Wallwork, S. P. Decent, A.C. King, and R.M.S.M. Schulkes. The trajectory and stability of a spiralling liquid jet. part 1. inviscid theory. *J. Fluid Mech.*, 459:43–65, 2002.

[47] C. Weber. Zum zerfall eines flussigkeitsstrahles. *Z. Angew. Math. Mech.*, 11:36–41, 1931.

[48] G.B Whitham. *Linear and Nonlinear Waves.* John Wiley & Sons, New York, 1974.

[49] D.C.Y. Wong, M.J.H. Simmons, S.P. Decent, E.I. Părău, and A.C. King. Break-up dynamics and drop size distributions created from spiralling liquid jets. *Int. J. Multiphase Flow*, 30:499–520, 2004.

[50] A.L. Yarin. *Free Liquid Jets and Films: Hydrodynamics and Rheology.* Longman, 1993.

[51] M.C Yuen. Non-linear capillary instability of a liquid jet. *J. Fluid Mech.*, 33:151–163, 1968.